Imperial College London

Plasma Physics Group

The Blackett Laboratory

Imperial College London

Experimental Study of Reverse Shock Structure in Magnetised High Energy Density Plasma Flows Driven by an Inverse Wire Array Z Pinch

Lee George Suttle

Submitted in partial fulfilment of the requirements for the degree of Doctor of Philosophy of Imperial College London

July 2014

Supervisor: Prof. Sergey Lebedev

Declaration

I hereby declare that this thesis describes my own original work, except where explicitly stated. No part of this work has previously been submitted, either in the same or different form, to this or any other university in connection with a higher degree or qualification.

Lee George Suttle

29 June 2014

The copyright of this thesis rests with the author and is made available under a Creative Commons Attribution - Non Commercial - No Derivatives licence. Researchers are free to copy, distribute or transmit the thesis on the condition that they attribute it, that they do not use it for commercial purposes and that they do not alter, transform or build upon it. For any reuse or distribution, researchers must make clear to others the licence terms of this work.

Abstract

The thesis reports on the design and data from a new experimental platform, which uses the supersonic ablated plasma flow from an inverse wire array z pinch to create a highly diagnosed interaction geometry for studying magnetised reverse shocks. The flow ($v\sim 10^7 cm/s, M_S\sim 4-5$) is generated with a frozen in magnetic field ($B\sim 1-2T, Re_M\sim 100$) at a level sufficient to affect the structure of the shocks created by its collision with a stationary planar obstacle.

In addition to the expected accumulation of stagnated plasma material in a thin, high density (strong shock) layer at the obstacle surface, a separate detached shock-like transition is also observed upstream of the obstacle, first observed at a distance $\sim c/\omega_{pi}$. Measurements of the reverse shock profile from Thomson scattering, interferometry, and local magnetic field probes, show that this "sub-shock" feature displays unusually small discontinuities in the plasma properties (velocity, density, temperature) despite the high Mach numbers of the flow. Analysis shows that this feature, which is weakly collisional during its formation phase, appears to be a consequence of the pile-up of magnetic flux brought by the flow, which accumulates at the obstacle surface and acts on the magnetised electrons of the flow.

An apparent discrepancy between the field strength measured at the sub-shock and the magnetic pressure required to support it against the ram pressure of the flow is addressed towards the end of the thesis. Preliminary results using a newly fielded Faraday rotation diagnostic to measure the field distribution within the reverse shock structure suggests that a pressure balance is achieved via the generation of current loops within the region, which locally enhance the field strength.

Future work is set out for continued investigation, including improvements to the diagnostic, and a proposal to adapt the wire array setup to study magnetic reconnection in colliding plasma flows.

Acknowledgements

It is my pleasure to thank the many wonderful colleagues and collaborators who I have had the honour of working with throughout my PhD, and without whom this project would not have been made possible.

First and foremost in this list is my supervisor Professor Sergey Lebedev, whose golden nuggets of experience and advice have been invaluable. His knowledge and passion for experimental science have been an inspiration and I consider myself immensely proud and fortunate to be a member of his group.

I would also like to give thanks to my fellow MAGPIE team members who, despite numerous experimental difficulties and mishaps (oil spills, vacuum leaks, MARX bank failures, broken wire arrays, and oh so many more...) have always made working in the lab a fun and spirited experience. They are: George Swadling, (Adam) Harvey-Thompson, Francisco Suzuki-Vidal, Gareth Hall, Simon Bland, Guy Burdiak, Phillip de Grouchy, Louisa Pickworth, Essa Khoory, Jon Skidmore, "James" Peitian Cong, Matthew Bennett, Liang Sheng, Nadine Kalmoni and Jack Hare.

Further acclaim must also go to:

Alan Finch and Paul Brown's workshop team for their constant struggle against a barrage of inevitably last-minute calls for apparatus and hardware modifications, the plasma physics football team for their valiant pursuit of the indoor 5-aside trophy, the combined efforts of South Kensington's Oriental Canteen and the Stick & Bowl to fuel world leading research with delicious Chinese food, and the wider Imperial Plasma & QOLS groups for generally being a superb bunch.

Lastly, but by no means least, I would like to give a whole-hearted thanks to all my family, friends and the people who I have met during this time for making the past four years so incredible, and London such a great place to live. Man cannot live on physics alone, so here's to all the hiking trips, summer picnics, games of tennis, bike rides, experimental cooking, visits to Sam Smith's, Christmas dinners, wanders through parks, travels and adventures that have seen me through.

Contents

Declaration 1
Abstract 3
Acknowledgements 4
List of figures 7
1 Introduction 12
1.1 Laboratory astrophysics and context of the thesis 12
1.2 Relating laboratory experiments with astrophysical phenomena 15
1.3 Scaling invariants 18
1.4 Outline of the thesis and the author's contribution 24
2 The physics of shocks 29
2.1 Shock waves 30
2.2 Radiative shocks 33
2.3 Magneto-hydrodynamic shocks 37
2.4 Shocks in astrophysics and the laboratory 43
2.5 Wire arrays as a platform for magnetised shock experiments 45
3 The MAGPIE generator and plasma diagnostics 51
3.1 The pulsed power generator 51
3.2 The MAGPIE experiment chamber 56
3.3 Current diagnostics 57
3.4 Laser probing 58
3.5 XUV and optical self-emission imaging 77
3.6 Local magnetic field probes 81
4 Characterisation of the plasma flow from an inverse wire array z pinch 83
4.1 Overview 83
4.2 The inverse wire array setup 84
4.3 Structure of the plasma flow from a pair of ablating wires 88
4.4 Density profile of the flow 90
4.5 Velocity and temperature properties of the flow 95
4.6 Magnetic measurements of the flow 98
4.7 Parameterisation of the flow 100
5 The structure of reverse shocks formed in the collision of a magnetised, supersonic plasma flow with a planar foil obstacle 105

5.1 Introduction 105
5.2 Setup for the reverse shock experiments 106
5.3 Overview of the flow-obstacle interaction 109
5.4 Spatial profiles of the plasma properties through the reverse shocks 119
5.5 Discussion: scale lengths relevant to the shock structure and pressure balance at the sub-shock 133
6 Investigation of the magnetic field in the reverse shock sub-structure 139
6.1 Introduction 139
6.2 Preliminary measurements of the magnetic field distribution in the reverse shock structure using a Faraday rotation technique 141
6.3 Experiments exploring the current structure of the sub-shock region 149
7 Conclusions & proposals for future study 154
7.1 Conclusions 154
7.2 Future work 156
References 162

List of figures

2.1 Diagram of an idealised steady-state shock wave, shown in the frame of reference moving with the shock front.

2.2 Regimes of radiative effects as a function of flow density and shock velocity in xenon and CH gases.

2.3 The schematic structure of radiative shock features in (a) an optically thick system, and (b) an optically thin system.

2.4 Schematic of a MHD shock.

2.5 Comparison of the magnetic field lines for fast and slow mode shocks.

2.6 Measurements taken by a spacecraft passing through the Earth's bow shock.

2.7 (a) An arc-shaped nebula near the star R Hydrae is the first bow shock ever seen around a pulsating red giant. (b) Bow shock around the very young star, LL Ori, in the Great Nebula.

2.8 Schematic of the radial foil load, showing the current path through the foil, the toroidal field and the force acting on the plasma produced by the foil.

2.9 The cylindrical wire array z pinch, showing the current applied to the array and the axial implosion of ablated plasma, which is directed by the J×B force of the global field. (a) A side-on cross-section of a wire array. (b) A 3D simulation of the plasma flow during the ablation stage of the implosion.

2.10 End-on electron density maps of the ablation phase for cylindrical 8 wire and 32 wire arrays.

2.11 Schematic of the inverse (exploding) wire array.

3.1 A drawing of the MAGPIE pulse power generator.

3.2 Circuit diagram of the Marx bank capacitors.

3.3 The interface of the VTL and MITL generator sections and their connection to the chamber load.

3.4 Overview of the MAGPIE chamber and its diagnostic layout.

3.5 Cross-section of the Rogowski groove which monitors the current through the load.

3.6 Geometrical relation of the Thomson scattering vectors.

3.7 Schematic diagram of the ion and electron components of the Theoretical Thomson scattered spectrum.

3.8 Optical setup for the shadowgraphy (laser-backlit) imaging system.

3.9 Gradients in the refractive index lateral to the direction of propagation of a light beam cause it to deflect.

3.10 Schematic of the Mach-Zehnder interferometer.

3.11 The misalignment of the probing and reference fringes causes their wavefronts to intersect, producing an interference pattern at the detector image plane.

3.12 Diagram of the geometrical resolution limit of the pinhole camera.

3.13 Illustration of how the pinhole camera images onto four independently time-gated quadrants of an MCP detector.

3.14 Diagram of the double image (telescope) setup for the optical emission camera.

4.1 (a) A schematic diagram of the inverse wire array with (end-on) laser probing of the shock-target interaction region. (b) A 3D design drawing of the array hardware.

4.2 A schematic diagram of the angular perturbation of wires in the array to produce a parallel flow from adjacent wires.

4.3 The global field components acting at the position of a single wire in an 8 wire inverse array.

4.4 An optical emission timeline showing the evolution of plasma flow from a single pair of ablating wires in the inverse array.

4.5 (a) An end-on (r-θ plane) interferogram showing the flow structure created by a pair of wires of the inverse array. (b) A schematic diagram of the flow trajectory in this structure.

4.6 A side-on (r-z plane) interferogram of ablation flow from the inverse wire array, shown are the raw data (a) background and (b) experimental images, as well as the traced fringe distributions from these in (c) and (d).

4.7 Images showing the steps in the areal density calculation process using the interferometry data in Fig. 4.6.

4.8 Vertically averaged, radial profiles of the areal electron density in the flow from a wire pair, taken from the side-on interferometry data.

4.9 Experimental setup for Thomson Scattering measurements of the plasma flow.

4.10 A typical fibre spectrum obtained from the Thomson scattering system, showing the ion feature of the spectrum.

4.11 Plot of $Z(T_e)$ at NLTE against the measured constraints of the ZT_e product from Thomson scattering.

4.12 The magnetic field measured by inductive probes positioned at a distance of 8.5mm from the wires.

5.1 A photo of two planar aluminium foil shock targets, mounted on support posts and positioned externally to an inverse wire array.

5.2 An example of the diagnostic setup for the reverse shock experiments, demonstrating the use of the array symmetry to create multiple flow-obstacle interaction regions to collect simultaneous data from different diagnostics.

5.3 An optical, self-emission timeline of the flow-obstacle interaction, recorded from an end-on perspective over multiple experiments.

5.4 A (false-colour) XUV self-emission timeline of the flow-obstacle interaction, recorded from a side-on perspective over multiple experiments.

5.5 (a) Side-on (532nm) laser interferometry data showing the full array-foil reverse shock interaction region at t=250ns, accompanied by (b) the pre-shot interference pattern for comparison, and (c) the areal density map from the fringe shift calculation.

5.6 (a) Modulations in the stagnation layer shock front and fluctuations in the wire ablation. (b) High magnification image of the reverse shock front modulations from a different experiment.

5.7 Side-on shadowography / light-frame Schlieren image of the reverse shock region showing the narrow transition thickness of the sub-shock.

5.8 End-on perspective interferometry data taken at t=225ns, showing the raw data and calculated electron density map.

5.9 Scale drawings of the probing and scattering geometry used for Thomson scattering experiments of the reverse shock interaction, shown from an end-on perspective.

5.10 End-on areal electron density maps from two experiments with simultaneous interferometry and TS measurements.

5.11 Images of the Thomson scattering spectrometer CCD, showing the spectral peaks for each of the fibre positions in Fig. 5.10.

5.12 Gaussian fits to the spectrometer data in Fig. 5.11a.

5.13 Plots of the plasma flow velocity profiles measured from TS at (a) t=180ns and (c) 225ns, as well as, (b) and (d), profiles of electron density (interferometry) and relative mass density calculated from the velocity profiles at these times.

5.14 End-on interferogram with accompanying TS positions and spectrometer CCD images of the scattered spectra for the two fibre bundles.

5.15 Velocity vector calculations using the 14 fibre TS data shown in Fig. 5.14.

5.16 The ion feature of the TS spectra measured in the upstream flow and after the sub-shock.

5.17 A pre-experiment, side-on interferogram showing the magnetic field probe placed ahead of the foil for measurements of the post-sub-shock flux compression.

5.18 The magnetic field measured by inductive probes centred at a distance of 8.5mm from the wires (1.5mm from foil).

6.1 Side-on intensity maps of a reverse shock experiment as measured by the two channels of the Faraday rotation diagnostic.

6.2 Normalised (I_C/I_B) intensity images from each channel of the Faraday system.

6.3 Secondary background image from the Faraday rotation camera showing an overlaid mesh grid for image alignment of the separate channels.

6.4 Map showing the measured Faraday rotation angle as a function of position for the full area of the probing beam.

6.5 Data from the Faraday rotation interferometry channel.

6.6 Diagram illustrating the aberration caused by a spherical lens.

6.7 (a) Map of the magnetic field as a function of position for the reverse shock region, together with (b) a line profile taken from this along y=0.

6.8 Faraday rotation map with an overlaid section of the interferometry data showing the offset in the positions of highest rotation (magnetic field) and electron density for the sub-shock front.

6.9 Side-on XUV image time-line showing the development of the sub-shock in an experiment where a plastic foil obstacle has been used instead of the original aluminium foil.

6.10 Side-on XUV and interferometry images of an experiment where two separate, vertically aligned foil obstacles were used with a 6mm gap between the two.

6.11 Side-on interferometry data from an experiment where the obstacle used is a linear array of 21×10μm copper wires with an inter-wire spacing of ~0.7mm.

6.12 Side-on XUV image taken in the same experiment as Fig. 6.11.

7.1 Diagram of the monochromatic x-ray backlighter diagnostic.

7.2 Radiograph of the reverse shock stagnation layer formed with a tungsten plasma.

7.3 Shadowgraphy image showing the reverse shock structure produced using a tungsten plasma.

7.4 End-on optical emission image of the interaction between two counter-streaming tungsten plasma flows.

Chapter 1:

Introduction

1.1 Laboratory astrophysics and context of the thesis

Our understanding of astrophysical systems suffers from a number of limitations associated with the observations we can make of them. Their great distances mean they are both spatially and spectroscopically difficult to resolve, and their long dynamic timescales, which often span up to 10^3 years, ensure that in most cases their evolution cannot be directly tracked. Add to this the fact that only two dimensional projections can be observed, and are subject to various line-of-sight aberrations, the dataset is inherently constrained.

Experimental studies supplementary to observations can however provide a new and enlightening perspective. By creating a laboratory representation of the physical conditions relevant to an astrophysical object, measurements can be made and an insight gained from the comparison. Previously such experiments have been confined to the contexts of spectroscopic, atomic and particle physics, providing data on opacities and cross-sections of various interactive processes; the focus being on material make up and microscopic behaviour, rather than global dynamics. Now however with the invention of modern high energy density physics (HEDP) facilities, such as powerful lasers and pulsed-power (z pinch) machines, extreme regimes are accessible inside the laboratory. Higher temperatures, pressures and densities than ever before can be repeatedly and reliably reproduced. These allow the exploration of domains including intense plasma flows (~100km/s), high Mach number and super-Alfvénic shocks, turbulence, photo-ionised plasmas, x-ray sources, radiation hydrodynamics and high ratios of magnetic to thermal pressures, to name but a few. The scope of applicability

therefore extends to a wide range of phenomena. Jets from young stars and active galactic nuclei, accretion disks, interactions of the interstellar medium, photo-evaporation of molecular clouds, planetary obstructions to solar wind, and even supernovae explosions are all amongst the potential for study.

It should be mentioned that the field of laboratory astrophysics is still in its infancy. Consequently it is an exciting and very much active area of scientific development, and as such the extent of its applicability may not yet be fully realised. Experiments tend to have a "maturity timescale", from conception, through design, modelling, testing, preliminary results and analysis, in the region of $\sim 3-5$ years [1]. Since the majority of HEDP experiments presently have an approximate age of 10 years they are evidently at an early stage of their natural fruition.

The range of methods is diverse and they are being employed to the simulation of an ever increasing number of astrophysical scenarios. Remington's 2006 paper [2] offers a comprehensive overview on the subject and details many examples of the experimental techniques in use; although in an ever advancing field this review is perhaps already behind the times with many further developments since first going to print. This is reflected by regular international conferences devoted to laboratory astrophysics [3,4], as well its frequent appearance as a hot topic in meetings on both plasma physics and HEDP.

Despite the diversity of application and methods, the facilities can for the most part be grouped into two kinds: high powered lasers, which can be focused down to small length scales with short, intense pulse shapes, as well as pulsed power machines, which deliver large and fast currents, and are used most commonly to drive the implosions of conducting loads via a strong magnetic pinching effect (known as a z pinch). As a tool, lasers thrive in experiments where energy needs to be delivered on a compressed timescale to achieve extreme temperatures; whereas pulsed power is best suited where a more relatively prolonged energy release is of interest. The scope of parameter space available in each case however is extensive and these methods entail their own catalogue of advantages and challenges.

This thesis reports on the design and analysis of results from one such HEDP experiment carried out at the Mega Ampere pulsed power Generator for Plasma Implosion Experiments (MAGPIE) [5] at Imperial College London. The project utilises a new and novel adaptation of the inverse wire array z pinch [6,7] to generate a stream of supersonic and magnetised plasma flow, which is used in a study of the structure of

perpendicular reverse shocks, formed on the collision of this flow with a stationary and planar obstacle. The experimental platform is unique in providing a well-defined and highly diagnosable, 1D interaction geometry, in combination with a comprehensive suite of diagnostic instruments which allows the direct measurement of a wide range of the plasma parameters relevant to the physical regimes of the shocks and their applicability to various astrophysical scenarios.

Shocks formed by supersonic plasma flows are ubiquitous in astrophysics and include environments such as accretion shocks [8], internal shocks in the jets from young stars [9] and other violent outbursts e.g. supernovae, and more locally in the interaction of the solar wind with spacecraft and planets [10–12]. In systems such as these our understanding of the dynamics of reverse shock formation and of their properties is currently far from complete despite considerable computational, observational and experimental efforts. This is particularly true in relation to shocks where the magnetic environment plays a key role in the evolution of the shock structure, affecting many of the fundamental fluid properties of the plasma e.g. inertial properties, dispersion, compressibility. Results presented in this thesis show that the generated plasma flows carry a significant level of frozen-in magnetic field, and there is strong evidence to suggest that the pile-up of this field in a thin layer at the surface of the obstacle leads to the formation of further amplification mechanisms of the field, which result in an additional, detached density-jump feature in the reverse shock structure that would not normally be present in an unmagnetised shock.

This opening chapter provides the context for the thesis as a laboratory astrophysics investigation. It begins with a discussion of the formalism of scaling – a concept at the heart of laboratory astrophysics which provides a quantitative framework for the comparison of systems whose state variables (e.g. temperature, density, time-scale) may vary wildly, but ensures that despite their differences, the results of laboratory experiments remain valid to their astrophysical counterparts. Examples are thereby given of the system parameters which must remain invariant in order for the two systems to scale under a variety of physical regimes. The chapter ends with an outline of the work presented in the thesis; summarising the main experimental results and findings, and highlighting the contribution of both the author and other collaborators – without whom a large scale project such as this could not have been made possible.

1.2 Relating laboratory experiments with astrophysical phenomena

The premise of laboratory astrophysics is to explain astrophysical observations on the basis of results from experiments. To do this formalism is required for determining the relevance of laboratory plasmas to their astrophysical counterparts, in terms of the important physical properties which dictate the degree to which a comparison is representative and valid. Such formalism can be achieved by utilising a technique known as scaling. This is not an original method, and has been established in many fields and for many applications. Models of stellar structure for instance are described by equations of a "homologous" form [13]; that is, they are written in terms only of fractional masses. Hence it does not matter if the state variables (temperature, density, pressure etc) of the stars being considered are many orders of magnitude apart; solutions between stars of different masses can be interpolated, because their state equations scale as a function of this dimensionless parameter. Another example of scaling is that of the simulations used for aerodynamic testing, such as parts for planes and other objects which have to sustain a high fluid velocity. It is often impractical or too expensive to directly test full sized replicas. Instead a model of reduced dimensions or flow speeds may be used and the equations of fluid dynamics scaled to account for the difference and recover the performance in the appropriate parameter range.

Essentially the approach of scaling is to take the key characteristics from one system and map them to another. The equations of the scaling have no explicit dependence on the individual variables of a system. Instead they use a combination of variables to derive quantities which describe these key characteristics. If all the scaled quantities are then found to be invariant between systems then there is an equivalence of physics and the laboratory experiment can act as a model to the subject. From this consideration laboratory experiments can be designed with the necessary scaling quantities in mind to study properties of astrophysical interest.

It should be noted however, the more physics that are relevant to the overall dynamics of the astrophysical system, the more quantities must be included and invariant under the scaling. This determines the regime under which the systems have been described, and under which the comparison is applicable. For example if scaling laws were derived using the equations of hydrodynamics, then correctly scaled systems are hydrodynamically equivalent. If however magnetic fields are significant in the

astrophysical system (as is often the case with plasmas) then the equations of ideal or even resistive magnetohydrodynamics (MHD) should form the basis of scaling. This will result in a greater number of scaled quantities than the purely hydrodynamic model (see section 1.3).

Moreover, in order to construct a true representation of an astrophysical system a consideration of the various initial and boundary conditions must be taken. These too must be conserved under the transformation of scaling. There are some exceptions however. If a system is turbulent and the timescale of interest happens sufficiently late in the evolution that memory of initial conditions is erased, then they become less important. Likewise if the interest region is far from the boundaries these conditions might be neglected. In general though questions like these should be carefully addressed.

Clearly there can be a significant number of constraints for laboratory plasmas to scale perfectly. As the complexity of the modelled system increases this task tends from being extremely difficult, to almost impossible. Thus it is an unrealistic goal to produce a replica of a supernova, whereby all the initial and boundary conditions are recreated and the physical properties scale exactly. Not only would this require an unprecedented level of control over the experimental conditions, but it would prerequisite a great deal of knowledge about the supernovae itself – the system which we are trying to model due to our initially limited understanding.

Fortunately the usefulness of the scaling tool goes beyond the perfect case where parameters are matched exactly. Most scaling parameters are dimensionless (although some are not, see Appendix A of [14] for example) and so if they happen to be significantly far from unity, both in laboratory and astrophysical systems, the numbers can afford not to be identical. In some cases they can even be several orders of magnitude apart and remain representative of one another. This is because dimensionless parameters far greater or smaller than unity usually describe properties unimportant to the overall solution, and so can be cast as "ignorable physics" [15]. It is when parameters are close to unity that they must be the same, and this is when scaling becomes most difficult.

As a final remark on the formalism of scaling it is noted that there are three sub-categories of invariance that can be established by scaling laws. These are discussed in detail by recent papers [14,16] under the regime of radiation hydrodynamics in optically

thick and thin materials. There the advantages and disadvantages of each are illustrated in the context of several laboratory astrophysics laser plasma experiments.

To summarise, the three kinds of invariance are “weak invariance”, “strict invariance” (also occasionally termed “absolute invariance”) and “global invariance”. Weakly invariant systems scale such that the equations governing their overall dynamics remain applicable under the transformation of dimensions and state variables from one system to the other. However no restriction is made to the microscopic processes that underlie the large-scale phenomena – for example the explicit mechanisms of radiative cooling. Under strict invariance these processes are included in the scaling by additionally constraining the equations of state (EOS) of the systems to be equal. So there are fewer free parameters in this approach. Global invariance similarly ensures that the physical microscopic processes are preserved, however it does this by only preserving the forms of the EOS, allowing differences of rates, constants of proportionalities, external fields, etc to be absorbed by the scaling. This means it is less restrictive than strict invariance, and can also have more free parameters than weak invariance due to the unfixed parameters of the EOS.

In terms of the suitability of these scaling categories, weak invariance is an attractive choice for situations where knowledge of the microscopic processes is poor, since an approximation of the EOS is not made. Alternatively it should be used if the microscopic processes of the laboratory plasma are known to be different to the astrophysics (e.g. Bremstruhlung rather than cooling via emission lines) but do not change the overall dynamics. Global invariance on the other hand is incredibly useful when these subtleties do not have to be avoided, because it provides a firm founding for self-similarity whilst giving freedom unavailable under strict invariance. Ionisation, chemical species and various other attributes can vary – the laboratory and astrophysical plasmas need not be the same under global invariance. This relieves the pressures of designing experiments where some material may be difficult to use for technological reasons. For instance in laser experiments it is much easier to monitor radiative shocks in xenon gas than hydrogen gas, which an astronomical system would be predominantly composed of. Likewise z pinch machines such as MAGPIE or the Z Machine of Sandia’s National Laboratory can utilise studies of plasma streams created by the ablation of solid (metallic) bodies. In this way global invariance is deemed better suited to “the real problem of laboratory astrophysics rescaling” as it demonstrates self similar behaviour,

whilst providing physical justification that the unconserved details do not modify the system dynamics [16].

1.3 Scaling invariants

In this section scaling invariants are demonstrated for several simple regimes which can provide good approximations for a variety of astrophysical plasmas. The framework for these scaling laws was developed in a series of papers by Ryutov et al. for the hydrodynamic [17–19] and ideal MHD [20,21] regimes, and by Bouquet & Falize et al. for the radiative hydrodynamic regime [14,16]. Their works provide a detailed discussion of the validity criteria of each regime and application of the scaling laws to experiments. Studies of this kind remain an ongoing area of research, with regular publications, as the demand for similarity concepts extends into further regimes with the invention of an ever increasing range of HEDP experiments and facilities.

1.3.1 Hydrodynamic invariants

The simplest way to model the motion of a plasma fluid is using hydrodynamics. This description assumes a negligible heat flow and viscosity for the medium, which, expressed quantitatively, means large Peclet (Pe) and Reynolds (Re) numbers:

$$\mathrm{Pe} = \frac{\text{heat convection}}{\text{heat conduction}} \gg 1$$

$$\mathrm{Re} = \frac{\text{inertial forces}}{\text{viscous forces}} \gg 1.$$

In addition the effects of fields and radiative cooling must be unimportant, and the particles of the fluid must be localised, either by collisionality, such that

$$\lambda_{\mathrm{mfp}} < \mathrm{L},$$

where λ_{mfp} is the mean free path, and L is the characteristic length scale; or by a sufficiently small ion Lamor radius r_{Li}, such that

$$r_{\mathrm{Li}} < \mathrm{L}.$$

The thermodynamic properties of the hydrodynamic fluid are also assumed to behave as a polytropic gas, with pressure and density given by the adiabatic relation

$$p \propto \rho^{\gamma}, \tag{1.1}$$

where the adiabatic index is

$$\gamma = \frac{C_p}{C_V} \tag{1.2}$$

for an isentropic ideal gas. When these criteria are met three differential equations govern the global dynamics. Namely, the conservation of mass

$$\frac{\partial \rho}{\partial t} + \nabla \cdot \rho \mathbf{v} = 0, \tag{1.3}$$

the equation of motion

$$\rho\left(\frac{\partial \mathbf{v}}{\partial t} + (\mathbf{v} \cdot \nabla)\mathbf{v}\right) + \nabla p = 0, \tag{1.4}$$

and the energy equation

$$\frac{\partial p}{\partial t} + \gamma p \nabla \cdot \mathbf{v} + \mathbf{v} \cdot \nabla p = 0. \tag{1.5}$$

If two systems are to scale under these hydrodynamic conditions then the equations must be left unchanged by the transformation of state variables

$$\mathbf{T}: (\mathbf{x}, t, \mathbf{v}, p, \rho) \rightarrow (\mathbf{x}', t', \mathbf{v}', p', \rho'),$$

where the above symbols represent quantities of space, time, velocity, pressure and density in the laboratory and astrophysical plasmas (dashed and undashed respectively). To derive the constraints of this scaling the ratios of the state variables are written for convenience in the form

$$X = a^{\delta_X} X', \tag{1.6}$$

with $X = x, t, v, p, \rho$ (hence a^{δ_X} is the scaling factor). Substituting this into the continuity equation 1.3 then gives

$$a^{\delta_\rho - \delta_t} \frac{\partial \rho'}{\partial t'} + a^{\delta_\rho + \delta_v - \delta_x} \frac{\partial}{\partial \mathbf{x}'} \cdot \rho' \mathbf{v}' = 0$$

$$\frac{\partial \rho'}{\partial t'} + a^{\delta_v + \delta_t - \delta_x} \nabla' \cdot \rho' \mathbf{v}' = 0,$$

and so

$$\therefore \delta_v + \delta_t - \delta_x = 0, \tag{1.7}$$

for the equation to hold under transformation. Thus

$$\frac{v}{v'} = \left(\frac{x}{x'}\right) \Big/ \left(\frac{t}{t'}\right),$$

and the first invariant is defined as

$$\frac{x}{vt} \equiv \frac{x'}{v't'}. \tag{1.8}$$

This dimensionless quantity is well-known as the Strouhal number and is best written in terms of the characteristic length and frequency of the fluid (more specifically the frequency of oscillating flow mechanisms such as vortex shedding, see [22]), giving

$$St = \frac{L\nu}{v}. \tag{1.9}$$

The next hydrodynamic invariant is found by again substituting 1.6, this time into the equation of motion (1.4). This gives

$$a^{\delta_\rho}\rho'\left(a^{\delta_v-\delta_t}\frac{\partial \mathbf{v}'}{\partial t'} + a^{2\delta_v-\delta_x}\right) + a^{\delta_p-\delta_x}\nabla' p' = 0,$$

which can be rearranged and using the previous result of 1.7 leads to

$$\delta_\rho - \delta_p + 2\delta_v = 0, \tag{1.10}$$

i.e.

$$\frac{p}{p'} = \left(\frac{\rho}{\rho'}\right)\Big/\left(\frac{v}{v'}\right)^2.$$

Hence the Euler number is also defined:

$$\frac{p}{\rho v^2} \equiv \frac{p'}{\rho' v'^2} = \frac{1}{Eu^2}. \tag{1.11}$$

One might expect to find a third invariant by applying the same procedure to the energy equation (1.5), however in this case the Strouhal is again recovered. Thus the scaling of the hydrodynamic equations merely requires the Strouhal and Euler numbers to be the same in each system and identical dynamics will apply. This is known as the "Euler similarity". It is noted that if the adiabatic index is also equivalent for the systems then the (sonic) Mach number can be used in place of the Euler number for the comparison, since

$$Eu = M_s\sqrt{\gamma}, \tag{1.12}$$

where the Mach number M_s is the ratio of flow velocity to sound speed in the plasma

$$M_s = \frac{v}{c_s}. \tag{1.13}$$

1.3.2 Ideal MHD invariants

For systems where magnetic fields are significant to the overall dynamics the equations of ideal MHD become a more suitable choice. The stipulations here are that the medium should have negligible resistivity and negligible Ohmic dissipation. The latter being ensured by a large magnetic Reynolds number

$$\mathrm{Re_M} = \frac{\text{magnetic advection}}{\text{magnetic diffusion}} \gg 1.$$

The hydrodynamic equations for mass continuity and energy remain unchanged, with the equation of motion now including a term for the magnetic field

$$\rho\left(\frac{\partial \mathbf{v}}{\partial t} + \mathbf{v}\cdot\nabla\mathbf{v}\right) + \nabla p = -\frac{1}{4\pi}\mathbf{B}\times\nabla\times\mathbf{B}. \tag{1.14}$$

Making substitutions as before, with equation 1.6 now being extended to include a ratio of the fields, one finds

$$a^{\delta_\rho}\rho'\left(a^{\delta_v-\delta_t}\frac{\partial \mathbf{v}'}{\partial t'} + a^{2\delta_v-\delta_x}\mathbf{v}'\cdot\nabla'\mathbf{v}'\right) + a^{\delta_p-\delta_x}\nabla' p' = -\frac{a^{2\delta_B-\delta_x}}{4\pi}\mathbf{B}'\times\nabla'\times\mathbf{B}'$$

$$a^{\delta_\rho+2\delta_v}\rho'\left(\frac{\partial \mathbf{v}'}{\partial t'} + \mathbf{v}'\cdot\nabla'\mathbf{v}'\right) + a^{\delta_p}\nabla' p' = -\frac{a^{2\delta_B}}{4\pi}\mathbf{B}'\times\nabla'\times\mathbf{B}'.$$

This again leads to the condition of 1.10 and additionally

$$2\delta_B - \delta_p = 0. \tag{1.15}$$

Thus the further invariant

$$\frac{B}{\sqrt{p}} \equiv \frac{B'}{\sqrt{p'}} \tag{1.16}$$

must be satisfied for ideal MHD, which is often used in the form of the beta parameter (ratio of thermal to magnetic pressure)

$$\beta_{th} = \frac{8\pi p}{B^2} \tag{1.17}$$

for the validation of self-similar behaviour under this regime (provided the Euler similarity is simultaneously satisfied).

1.3.3 Radiative hydrodynamic invariants

Radiative hydrodynamics can be considered in cases of systems in which the effect of radiative cooling is important, both for optically thin and thick plasmas. Here only the

results of the simpler optically thin case will be summarised, but both can be found in [14]. The essential difference is that a consideration of opacity must also be made for optically thick plasmas.

The cooling function Λ is introduced to give a measure of the radiative energy loss per unit volume and time. This parameter is expected to be both a function of density and temperature, but alternatively could be expressed as a function of density and pressure via the generic EOS

$$p(\rho, T) = C_{EOS}\rho^{\lambda}T^{\mu}, \tag{1.18}$$

Where C_{EOS} is a constant depending on the plasma properties (average ionisation Z, average mass number A etc), and where λ and μ are exponents. The cooling function is therefore assumed to have the form

$$\Lambda(\rho, p) = \Lambda_0\rho^{\varepsilon}p^{\varsigma}, \tag{1.19}$$

where again Λ_0 is a constant depending on the plasma properties and where ε and ς are exponents. This then appears in the energy equation (with the mass continuity and equation of motion untouched from their hydrodynamic versions)

$$\left(\frac{\partial}{\partial t} + \mathbf{v}\cdot\nabla\right)p - \gamma\frac{p}{\rho}\left(\frac{\partial}{\partial t} + \mathbf{v}\cdot\nabla\right)\rho = -(\gamma-1)\Lambda. \tag{1.20}$$

Substituting in the usual way gives

$$\left(\frac{\partial}{\partial t'} + \mathbf{v}'\cdot\nabla'\right)p' - \gamma\frac{p'}{\rho'}\left(\frac{\partial}{\partial t'} + \mathbf{v}'\cdot\nabla'\right)\rho' = -a^{\delta_\Lambda+\delta_t-\delta_p}(\gamma-1)\Lambda'.$$

and so the invariance is found for

$$\delta_\Lambda + \delta_t - \delta_p = 0. \tag{1.21}$$

Consequently in partnership with the Euler similarity,

$$\frac{\Lambda t}{p} \equiv \frac{\Lambda' t'}{p'} \tag{1.22}$$

should hold for self-similar radiative hydrodynamic plasmas.

1.3.4 Further Regimes

Beyond the simplistic domain of ideal MHD are systems whose viscosity η and resistivity $1/\sigma$ play an important role in the dynamics. This leads to an equation of motion

$$\rho\left(\frac{\partial \mathbf{v}}{\partial t} + \mathbf{v}\cdot\nabla\mathbf{v}\right) + \nabla p + \frac{\mathbf{B}\times\nabla\times\mathbf{B}}{4\pi} - \eta\nabla^2\mathbf{v} = 0, \tag{1.23}$$

as well as Faraday's law in the form of

$$\frac{\partial \mathbf{B}}{\partial t} - \nabla\times(\mathbf{v}\times\mathbf{B}) - \frac{c^2}{4\pi\sigma}\nabla^2\mathbf{B} = 0. \tag{1.24}$$

Scaling these [15] results in a requirement for the Reynolds number

$$Re = \frac{\rho v L}{\eta} \tag{1.25}$$

and magnetic Reynolds number

$$Re_M = \frac{4\pi\sigma v L}{c^2} \tag{1.26}$$

to be invariant, although they are now freed from their ideal MHD restrictions of being much greater than unity.

1.3.5 Applicability to systems with shocks

Many astrophysical systems of interest include regions of shocks. These can be caused by many occurrences such as collisions or pressure waves moving through media. They are characterised by a sudden transition in fluid properties (density, pressure, etc) with an abrupt change of flow velocity across the front. Fortunately such situations do not pose a difficulty for scaling, since the hydrodynamic laws do not depend on having a flow which is continuous. This can be demonstrated by the boundary conditions evaluated at the shock interface S. These are [23]

$$[\rho v_\perp]_S = 0, \tag{1.27}$$

$$[p + \rho v_\perp{}^2]_S = 0, \tag{1.28}$$

and

$$\left[v_\perp\left(\frac{\gamma p}{\gamma - 1} + \frac{\rho v^2}{2}\right)\right]_S = 0. \tag{1.29}$$

Clearly the introduction of scaling factors from the transformation of variables $X \rightarrow X'$ does not have any effect, since they can be factored out leaving the boundary conditions invariant. Therefore laboratory studies of shock based systems can be applied to astrophysical observations.

1.3.6 Strict and Global Invariance

The scaling laws demonstrated here have only been of the weak form of invariance as discussed in section 1.2. This is because they are based on the large scale variables of systems (density, pressure, etc) and ignore microscopic plasma properties. As an example of the other forms of invariance consider the equations of radiative hydrodynamics in section 1.3.3. To make them strictly invariant, equations 1.18 and 1.19 would also have to be equal for both astrophysical and laboratory plasmas, providing more stringent experimental conditions. On the other hand only their forms would have to be equal under global invariance and so $X = x, t, v, p, \rho, T, C_{EOS}, \Lambda, \Lambda_0$ in equation 1.6 becomes the full list of scaling ratios considered – see [14] for a more thorough analysis.

1.4 Outline of the thesis and the author's contribution

The work presented in this thesis constitutes the development of a wire array based experimental platform for the production and study of reverse shock structure. It uses the collision of a steady stream of supersonic and magnetised plasma with a stationary, planar obstacle to create a well-defined and highly diagnosable, 1D interaction geometry. This, coupled with a comprehensive suite of diagnostic instruments, allows for the direct measurement of the plasma properties key to interpreting and understanding the physical mechanisms underlying the structure and evolution of the shocks; as well as enabling their potential applicability to various astrophysical regimes and scenarios. The structure of this body of work breaks down in the following manner.

An introduction is given in Chapter 2 to the basic principles and concepts of shock physics, providing a review of the necessary theoretical background and equations for describing shocks in a variety of media and plasma conditions; including a statement of the jump conditions for shocks in the simple 1D hydrodynamic case, and an account of how these might be expected to change when a more complicated mix of physical behaviours (i.e. radiative effects and magnetic fields) are present. This then leads on to the presentation of the z pinch based platform, and in particular that of the inverse wire array, as a means for studying the scenarios of strong 1D shocks.

In Chapter 3 a description is given of the MAGPIE generator, which facilitated the experiments, and an overview is included of the diagnostic setup which accompanies this. Details are given on the principles of the relevant diagnostic techniques and a derivation of the measurements which can be made from these.

Experimental work concerning the design and adaptation of a wire array setup towards producing a plasma flow suitable for shock studies is presented in Chapter 4. Wire arrays are most typically known for their use in a z pinch configuration for research in fields such as inertial confinement fusion (ICF) and studies of EOS. The setup comprises of a cylindrical array of parallel wires, which on the application of a high amplitude, fast current pulse (typically MA's over 100's of ns) causes an implosion of the array via the axially directed $\mathbf{J} \times \mathbf{B}$ force felt by the wires; and the resulting high temperatures and densities created on the axis are usually of interest. During the early stages of this implosion process however the cores of the wires remain stationary while their outer material forms a plasma corona which is ablated towards the axis. This steady and predictable stream of supersonic plasma flow can be prolonged in time by simply increasing the initial mass of the wires, and as such this was identified as an ideal tool for use in shock experiments.

Moving away from the converging geometry of the z pinch, an inverse wire array was selected for these experiments as this produces a much more accessible flow, better suited for the placement of shock targets and the ability to perform diagnostic measurements. The inverse array geometry, which has been studied in detail previously on MAGPIE [6,7], incorporates a return path for the current, which runs in an opposing direction through a cylindrical cathode placed along the axis of the array, and inverts the $\mathbf{J} \times \mathbf{B}$ force such that the plasma is ablated radially outwards into the open external region. A further modification was made to the inverse array to adjust the trajectory of the plasma streams to achieve more planar flow, as this allows a more simplistic study of shock structures from the utilisation of a quasi 1D geometry. Instead of using a uniform wire spacing, the wires were distributed on the diameter of the array in a paired arrangement, with the angular spacing of the wires in each pair being marginally smaller than the average inter-wire separation. This increased pair proximity acts to magnetically focus the flow from the adjacent wires, and both a theoretical and empirical analysis was made to fine tune the angular separation to produce a sufficiently parallel and laminar flow from the wires.

Results are presented in Chapter 4 of the parameterisation of this flow, using measurements of velocity and temperature from Thomson scattering, magnetic field from locally placed inductive probes and a measurement of the plasma (electron) density from laser interferometry probing. An estimation of the plasma ionisation is also made on the basis of the rocket model [24], which approximates the density profile of the flow to very good accuracy at distances away from the surrounding corona of the array. The flow is found to be internally collisional and carries a strong (Tesla) level of frozen-in magnetic field. An assessment of the relevant Mach numbers for the flow show that these are sufficiently high to make the flow ideal for use in the study of strong magnetically-influenced shocks, and a summary is given of the relevant and scalable parameters which describe its fluid properties.

Chapter 5 presents data from experiments using the flow from the wire array platform in the study of magnetised reverse shocks and this forms the bulk of the experimental work of the thesis. The reverse shocks are created by the collision of the flow with a planar obstacle and data show that the structure includes a prominent and detached sub-feature (termed a "sub-shock"), which is first observed at a stand-off distance approximately equal to the inertial length of ions, and expands slowly upstream with time. This feature is unexpected for a normal thermal collision and accumulation of material at the obstacle; and yet it shows several shock-like discontinuities. However a measurement of the velocity and density discontinuities across the sub-shock appear far lower than are typical for the high Mach numbers of the flow, and the effects of heating also appear minimal. Calculations of the ion-ion mean free path of plasma moving into sub-shock show the interaction to be very weakly collisional at early times shortly after its formation, however this collisionality increases into a more collisional regime with time, as the feature becomes fully established. The sub-shock feature is believed to be supported by the accumulation of magnetic flux brought by the flow, which collects at the surface of the obstacle in a conducting layer and acts upon the magnetised electrons to build up a cross-shock electrostatic potential, which in turn decelerates the ions. An analysis of the field levels present in the interaction region however highlights and apparent shortfall in the magnetic pressure required to support the sub-shock; despite the field providing the only reasonable means of balancing the ram pressure of the oncoming flow.

An investigation in Chapter 6 addresses this inconsistency in the pressure balance by utilising an independent and non-evasive measurement of the spatial magnetic field

distribution in the shock structure, using a newly developed Faraday rotation diagnostic. Preliminary results are presented which suggest that an amplification of the field is achieved via the generation of current layers along the surface of the obstacle and through the front of the sub-shock, and that these may be at a sufficiently enhanced level to oppose the flow.

Chapter 7 concludes the thesis with a summary of the main experimental findings and a proposal for the continuation and extension of this project. It is noted that the intentions expressed here are genuine with further experimental campaigns planned for the near future. These include plans to make further developments to the Faraday rotation diagnostic to improve the sensitivity and resolution of the magnetic field measurements, as well as further measurements to be made with the Thomson scattering diagnostic to measure vertical drift velocities of ions in the search for evidence of current structures within the reverse shock interaction region. There are also plans for shock experiments utilizing a double inverse array setup, whereby the streams from two identical, adjacently placed wire arrays would be made to collide head-on. These opposing flows would carry anti-parallel magnetic field vectors and so would be fundamentally useful in the study of magnetic reconnection phenomena; such is applicable in astrophysical and space settings including solar flares and the Earth's magnetosphere.

All of the experimental work presented in this thesis was carried out at the MAGPIE pulsed power facility at Imperial College London. The author took a lead role in the design and management of these experiments, however this work would not be made possible without the support of the MAGPIE experimental team – a group of post-doctoral and PhD student researchers who contribute to the operation and running of every experiment. As part of this team the author has been involved in the vast majority of experimental campaigns carried out at the facility throughout the period September 2010 – December 2013. This has included the development and preparation of diagnostics and experimental hardware, the evaluation of data and the general upkeep and maintenance of the laboratory, including that of the pulsed power systems.

Many of the diagnostic capabilities of MAGPIE are also a product of the collaboration with the CERBERUS laser team, also of Imperial College London, who work closely with the MAGPIE team on the development of several of the laser systems – namely those used for Thomson scattering and Faraday rotation measurements. The author was an active member of this liaison and was involved in the frequent care, development and operation of these systems.

Analysis of the data was for the most part carried out by the author, however in the following cases special credit must be given to other members of the team. The analysis of measurements made using the Faraday diagnostic described in Chapter 6 was carried out by George Swadling, and the figures relating to this data are attributed to him (image credit is noted in place). Analysis of the spectral fitting to Thomson scattering data was carried out using software produced by Matthew Bennett and Swadling. Interferometry data was analysed by the author, using software and techniques produced by Swadling, which are described in the publication [25].

The author would also like to make acknowledgement to our collaborators David Burgess (Queen Mary London University, UK) and Paul Drake (University of Michigan, US) for their intellectual advice and input which has been invaluable in arriving at our present understanding and interpretations of the experimental data.

The work reported in this thesis has been presented at numerous international conferences, which to date include the 2014 and 2012 High Energy Density Laboratory Astrophysics (HEDLA) conferences, in Bordeaux (France) and Tallahassee (FL, US) respectively, the 2013 American Physics Society meeting of the Division of Plasma Physics (APS DPP) in Denver (CO, US), and the 2013 International Conference on High Energy Density Physics (ICHED) in Saint Malo (France). This work has also been published in the scientific journal Physics of Plasmas [26] and a future publication is in progress to report on the results from measurements with the Faraday rotation diagnostic.

Chapter 2:

The physics of shocks

Shock waves are a common occurrence in plasma physics as they are an inevitable consequence of the high energy and high velocity interactions instigated by the presence of extreme physical conditions. In their most basic sense, shocks are pressure disturbances, which travel through a medium at supersonic velocity, bringing about abrupt changes to that medium's properties or state. In a simple and hydrodynamically behaving fluid these changes are predictable and well understood. They can be described by a set of discontinuity equations which set calculable limits for the changes in state variables across the shock front; where the full extent of these limits can be expected to be achieved in cases of sufficiently high impact velocities that the transition is classified as a "strong shock". With the practical consideration of shocks in real life plasma systems however, the task of making accurate predictions of their transitions becomes much more complicated, as these systems introduce a whole host of additional physics beyond the hydrodynamic case, and as a result yield non-trivial solutions. This chapter summarises the hydrodynamic description of shock waves (as presented in [23]), as well as outlining further theoretical considerations which have to be made towards shock models in alternative regimes – namely those where radiation [27–30] and magnetism [31,32] play an important role in the plasma dynamics. This is then proceeded by a discussion of the requirements for studying astrophysically relevant shock systems in the laboratory, and a presentation is made of the z pinch based platform, and in particular that of the inverse wire array, as an experimental means of studying the scenarios of strong, radiative or magnetically-influenced shocks.

2.1 Shock waves

A shock is characterised by an abrupt change in the state properties of a medium. This arises when there is a sharp increase in the pressure at an interface, either by collision or some other means, and this in turn causes a jump in both the temperature and density across that interface. Shocks travel as waves, with the front of the wave accumulating and heating material as it propagates, and so carrying thermal and kinetic energy with it. The speed with which this disturbance travels is supersonic relative to the upstream, unshocked matter, however relative to the downstream material it is subsonic, due to an increase in the sound speed that accompanies the post-shock heating and compression. This allows the shocked material to communicate information regarding changes in the driving energy source to the shock front. In the laboratory frame several configurations of shock are possible – the upstream material might be initially stationary, with the shock front moving supersonically through it, or inversely the upstream material could be supersonic and colliding with a stationary or decelerated obstacle. In all cases however these reduce to the same picture in the frame of reference of the stationary shock front.

Fig. 2.1 illustrates this for a 1D shock. Here the relevant variables for describing the state of the hydrodynamic system are the flow velocity v, density ρ, temperature T, pressure p and internal energy ε; where the subscripts u and d refer to the upstream and downstream values of these quantities respectively. Despite discontinuities in these variables across the shock, the system must always obey the Euler equations of the conservation of mass, momentum and energy (see Chapter 1, equations 1.3 – 1.5). Each of these laws takes the form

$$\frac{\partial \mathrm{Q}}{\partial \mathrm{t}} + \boldsymbol{\nabla} \cdot \mathbf{F} = 0, \tag{2.1}$$

where Q and **F** are the density and flux of the conserved quantities respectively. Since the change in the density term across the shock

$$\int_{\mathrm{x_u}}^{\mathrm{x_d}} \frac{\partial}{\partial \mathrm{t}} \mathrm{Q}\, \mathrm{dx} \to 0, \tag{2.2}$$

for an abrupt transition ($\mathrm{x_u} - \mathrm{x_d} \to 0$), in a 1D case this gives

$$\frac{\partial}{\partial \mathrm{x}} \mathrm{F_x} = 0. \tag{2.3}$$

Thus the Euler equations can be evaluated across a shock as

$$\rho_u v_u = \rho_d v_d, \tag{2.4}$$

$$\rho_u {v_u}^2 + p_u = \rho_d {v_d}^2 + p_d, \qquad \text{and} \tag{2.5}$$

$$\left[\rho_u v_u \left(\varepsilon_u + \frac{{v_u}^2}{2}\right) + p_u v_u\right] = \left[\rho_d v_d \left(\varepsilon_d + \frac{{v_d}^2}{2}\right) + p_d v_d\right], \tag{2.6}$$

where these are referred to as the Rankine-Hugoniot "jump conditions" of the shock.

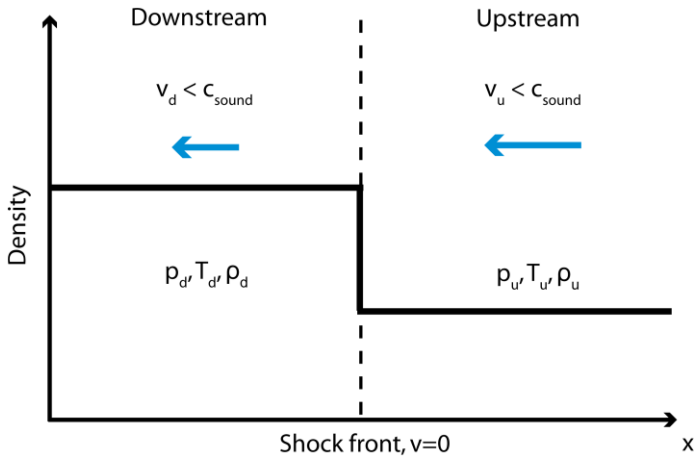


FIG. 2.1 Diagram of an idealised steady-state shock wave, shown in the frame of reference moving with the shock front.

Potentially these allow predictions of the post-shock variables based on measurements of the upstream variables and the two velocities (which may be found in the laboratory frame and then simply translated into the shock frame for use in the above equations). In their current form however they possess a free parameter, namely that of the internal energy. This however is often accounted for by assuming that the fluid is a polytropic gas with

$$\rho\varepsilon = \frac{p}{\gamma - 1}, \tag{2.7}$$

and an assumption of the adiabatic index γ can be made based on the composite medium of the fluid (e.g. $\gamma \sim 5/3$ for a monatomic ideal gas, or $\gamma \sim 4/3$ for an ionising plasma). Care has to be made however, as the shock transition may also affect this parameter, and in such cases γ should be treated as a subscripted variable too. By substituting this form and rearranging one can find an expression for the ratio of the upstream and post-shock densities

$$\frac{\rho_d}{\rho_u} = \frac{p_d(\gamma+1) + p_u(\gamma-1)}{p_u(\gamma+1) + p_d(\gamma-1)}, \tag{2.8}$$

or, allowing for a change in the adiabatic index across the shock

$$\frac{\rho_d}{\rho_u} = \left(\frac{p_d(\gamma_d+1) + p_u(\gamma_d-1)}{p_u(\gamma_u+1) + p_d(\gamma_u-1)}\right)\frac{(\gamma_u-1)}{(\gamma_d-1)}. \tag{2.9}$$

It is clear that this ratio has a limit, which is reached when $p_d \gg p_u$, and reduces the above to

$$\frac{\rho_d}{\rho_u} = \frac{(\gamma+1)}{(\gamma-1)}, \qquad \text{or} \tag{2.10}$$

$$\frac{\rho_d}{\rho_u} = \frac{(\gamma_d+1)}{(\gamma_d-1)}. \tag{2.11}$$

This is known as the "strong shock limit" and can be alternatively demonstrated, in terms of the sonic Mach number of the shock ($M_S = v_u/c_{Su}$), as being a consequence of a high shock velocity. The Mach number for a polytropic gas is

$$M_S = v\sqrt{\frac{\rho}{\gamma p}}, \tag{2.12}$$

and so substituting this into the jump conditions yields

$$\frac{\rho_d}{\rho_u} = \frac{{M_S}^2(\gamma+1)}{{M_S}^2(\gamma-1)+2}. \tag{2.13}$$

Thus when the Mach number is sufficiently high, equation 2.10 is again produced, and for the monatomic gas of $\gamma \sim 5/3$ yields the famous result of a factor of 4 density increase across the shock transition.

As well as the density jump, the temperature increase of the shocked material can also be of interest, as it is a more easily measurable property than the pressure. This variable can be introduced to the jump conditions via the use of the ideal gas law for a plasma in thermal equilibrium (ions and electrons described by a single temperature)

$$p = (Z+1)\frac{\rho k_B T}{m_i}, \tag{2.14}$$

where, in comparison to a neutral gas, the additional factor here of (Z+1) comes from the added pressure of the electron gas; with Z denoting the average ionisation of the plasma. Substituting this into the equation set 2.4 – 2.7, it can be shown [23] that the expression for the downstream temperature in the strong shock scenario is

$$k_B T_d = \frac{2m_i}{(Z_d + 1)} \frac{(\gamma_d - 1)}{(\gamma_d + 1)^2} . {v_u}^2, \tag{2.15}$$

which notably scales quadratically with the shock velocity.

The simple shock structure described thus far is that of an idealised, thermal 1D shock. It is accurate as far as the shock being modelled has a planar interface, the fluid has a reasonably low viscosity, and there are no strong magnetic fields or radiative effects present in the system. Each of these further complications introduces perturbations to the system which require separate evaluation. In the case of systems where there is a finite transverse velocity to the shock interface for example, the shock is referred to as "oblique", and the jump conditions should be derived using a conservation of the material flux brought by the normal velocity component as indicated in equations 1.27 – 1.29. On the other hand, when viscosity plays a role in the system, the interface between the upstream and downstream regions can no longer be considered infinitesimal and the change in parameters becomes more gradual as it is spread over a certain transitional thickness; where the jump conditions then compare the system state at locations suitably far from the shock front.

More challenging to account for are the effects of radiation and magnetism as they result in additional mechanisms of energy transfer and pressure balance, and so require terms for these in the momentum and energy conservation. Furthermore, they can create new means of interaction amongst the plasma fluid leading to a change in dynamics. Heated post-shock material which radiates strongly can transmit information and energy beyond the supersonic speeds of the shock wave, and so can act to pre-heat the material ahead of shock front, resulting in a radiative precursor whose properties depend on the way that matter couples with the radiation. Magnetic fields conversely can initiate alternative mechanisms of particle location – and thus can themselves bring about a pressure change capable of generating unique varieties of shock. The following sections are devoted to discussing situations relevant to each of these regimes.

2.2 Radiative shocks

2.2.1 Introducing radiation to shocks

If radiation is present in such a way that it emits a significant fraction of the mechanical energy of the shock, then it is described as a radiative shock. The criterion for a radiative shock can be posed in either of two ways. Which of these are satisfied

determines the degree to which radiative effects have to be included in the equations governing their evolution.

The first, and slightly weaker, condition for a radiative shock is that the radiation energy flux emanating from the post-shock region should be comparable to the material energy flux into the region. The radiative flux can be estimated as that of a blackbody, and hence

$$F_{radiation} = \sigma T_d{}^4, \tag{2.16}$$

with the material flux taken as

$$F_{material} = \rho_u v_u c_V T_d, \tag{2.17}$$

where c_V is the heat capacity at constant volume. It is clear from these temperature scalings that as the shock temperature increases the more likely it is that this condition will be reached. The same can also be said of the shock velocity, which as shown by equation 2.15 is the driving factor behind the temperature.

The second condition which could be posed would be for the radiation pressure to match the material (ram) pressure of the flow, mathematically given as

$$\begin{gathered} p_{radiation} \geq p_{ram} \\ \frac{\sigma T^4}{c} \geq \rho_u v_u{}^2 \ \text{[radiation dominated]}. \end{gathered} \tag{2.18}$$

This puts the shock into the radiation-dominated regime.

Again using the relation of equation 2.15, it is possible to plot the incident flow density at which each of these criteria are met, as a function of either shock temperature or velocity. Fig. 2.2 illustrates this for two materials typical of laboratory shock experiments. The regions to the right of each line in the diagram are the parameter ranges for which radiation flux (solid line) and radiation pressure (dashed line) must be included in the Euler equations of the system. There appears to be approximately an order of magnitude in shock velocity between the thresholds of each, with velocities of often hundreds of km/s needed to reach the radiation-dominated regime for these particular chemical species. However, for many systems these calculations may still be an underestimation of the velocities required. This is because they implicitly assume optically thick systems, where the radiation and matter are allowed to couple sufficiently that their temperatures equilibrate.

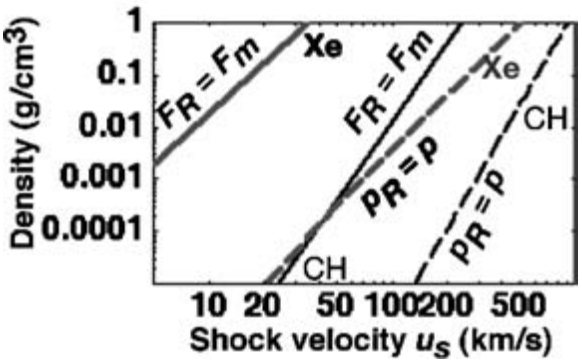


FIG. 2.2 Regimes of radiative effects as a function of flow density and shock velocity in xenon and CH gases. Reproduced from [27]. A similar plot showing the temperature dependence can be found at [23], p.286.

In optically thinner systems this assumption cannot be made since the large mean free path of radiation results in an equilibrating distance that is greater than the characteristic length scale L of the shock. In this case it is more accurate to replace equation 2.16 with that of a cooling function Λ (multiplied by L). This alternative parameter gives the power radiated per unit volume, and can be written in terms of the state variables of the shocked matter as

$$\Lambda = \Lambda_0 \rho_d^{\varepsilon} T_d^{\zeta}. \tag{2.19}$$

This results in a power output lower than the thick case and so higher temperatures / velocities are required to match the material flux or indeed pressure. Thus the optical thickness of the medium in which a shock is taking place can have a huge influence on how the shock develops and the regime it falls into. This can then decide the types of shock features produced.

2.2.2 Features of radiative shocks

- The Radiative Precursor (Optically Thick Case)

In an optically thick system the matter can couple with the radiation, and so in this case the radiation emitted from the shocked region can have a notable effect on the approaching upstream flow. If the radiative flux is significant, and if the opacity is large enough, then photons emerging from the shock front can ionise the unshocked material. This causes a pre-heating and density increase of the flow before it has reached the true shock position, and is known as a "precursor" formation (see Fig. 2.3a).

To estimate when a precursor will be seen in an optically thick plasma, one can take as an approximate criterion that the number of ionising photons emitted from the shock front should match the number of incident particles [27]. The density of photons from a black body is

$$n_\gamma = 1.202 \cdot 16\pi \left(\frac{k_B T}{hc}\right)^3, \tag{2.20}$$

and so the threshold can be written as

$$1.202 \cdot 16\pi \varepsilon_u \varepsilon_d \alpha \left(\frac{k_B T_d}{hc}\right)^3 \geq \frac{\rho_u v_u}{m_i}, \tag{2.21}$$

or alternatively in terms of the shock velocity (substituting equation 2.15) as

$$v_u{}^5 \geq \left(hc \cdot (Z_d + 1)\frac{(\gamma+1)^2}{2(\gamma-1)}\right)^3 \frac{\rho_u}{1.202 \cdot 16\pi \varepsilon_d \varepsilon_u \alpha m_i}, \tag{2.22}$$

where ε_d and ε_u are the down- and up-stream emissivity and α is the ionising fraction.

This is only a crude estimate, and more sophisticated methods, including the treatment of diffusion and transport regimes of radiative transfer are discussed in [23,29]. However the above threshold may serve as a useful means of anticipating in which shocked systems a precursor is likely to occur.

- *The Cooling Layer (Optically Thin Case)*

In the case of optically thin radiative shocks, the shock front, with its immediate post-shock temperature and density, is described by the ideal Rankine-Hugoniot jump relations. Behind this front is a region where the thermal energy of the shock is radiated according to an appropriate cooling function of the form 2.19. This causes the density to increase throughout the layer while the temperature decreases, reaching final values of ρ_f and T_f before a steady downstream state follows (see Fig. 2.3b).

In the optically thin limit T_f is determined by energy sources independent of the shock, and is likely similar to the pre-shock value T_i. If the downstream state has some non-negligible opacity however, then it is governed by the balance of absorbed flux across the boundary between cooling layer and steady downstream. The exact shape of the cooling layer depends on many factors, including its opacity and the relationship between this and the state variables; although the complete picture is arguably not yet fully understood. Theoretical discussions are made in [23,27].

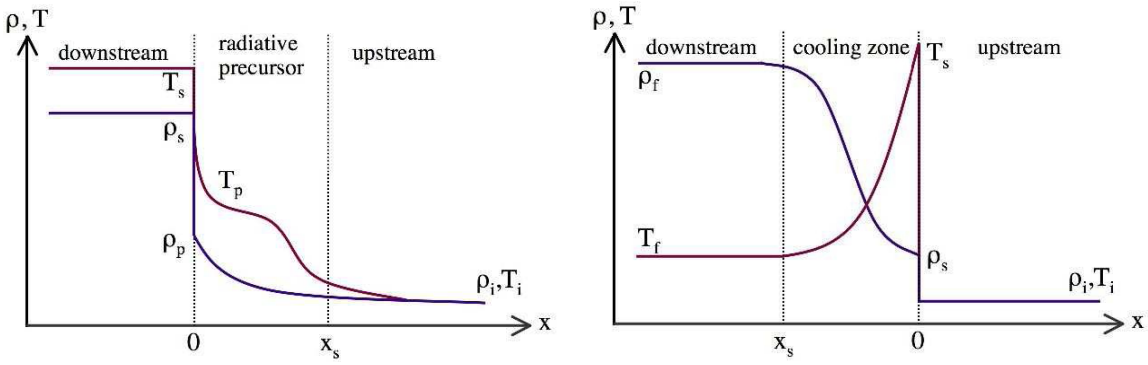


FIG. 2.3 The schematic structure of radiative shock features in (a) (*left*) an optically thick system, and (b) (*right*) an optically thin system. Subscripts i, p, s and f stand for 'initial' (upstream), precursor, shock and final (downstream) values respectively. Plots reproduced from [30].

2.3 Magneto-hydrodynamic shocks

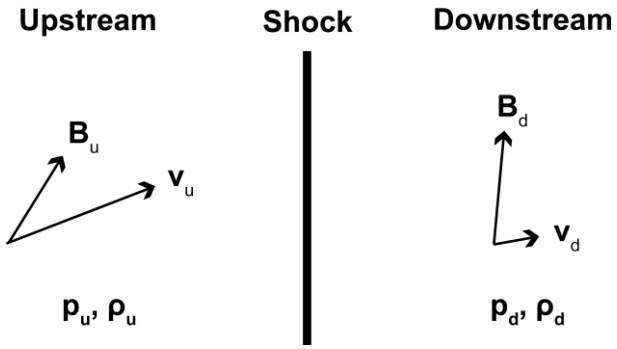


FIG. 2.4 Schematic of a MHD shock. Adapted from [31].

The general scenario for a shock in a magnetised plasma is illustrated in Fig. 2.4. In the same manner that a shock in a purely thermal system requires a conservation of the fluxes of the hydrodynamic equations, a shock in a magnetised system requires a conservation of the fluxes of the MHD equations. The first jump condition of equation 2.4 remains unchanged from the hydrodynamic case, as the mass flux equation is unaffected by the presence of field in the system. The second jump condition meanwhile, derived from the ideal MHD momentum equation 1.14 (and again remaining in the frame of reference of the shock), becomes [31]

$$\left[\rho_u v_{\perp u}{}^2 + p_u + \frac{B_u{}^2}{8\pi}\right] = \left[\rho_d v_{\perp d}{}^2 + p_d + \frac{B_u{}^2}{8\pi}\right], \tag{2.23}$$

with an additional constraint from the parallel momentum balance of

$$\left[\rho_u v_{\perp u}\mathbf{v}_{\parallel u} - \frac{B_{\perp u}}{4\pi}\mathbf{B}_{\parallel u}\right] = \left[\rho_d v_{\perp d}\mathbf{v}_{\parallel d} - \frac{B_{\perp d}}{4\pi}\mathbf{B}_{\parallel d}\right], \tag{2.24}$$

where $\perp$ and $\parallel$ represent vectors perpendicular and parallel to the shock front. Simultaneously the energy conservation gives

$$\left[\rho v_\perp\left(\frac{v^2}{2} + \frac{\gamma}{\gamma-1}\frac{p}{\rho}\right) + v_\perp\frac{B^2}{4\pi} - \mathbf{v}\cdot\mathbf{B}\frac{B_\perp}{4\pi}\right] = \text{constant}, \tag{2.25}$$

where the electromagnetic energy flux ($\mathbf{E}\times\mathbf{B}/4\pi$) has been calculated using the ideal Ohm's Law

$$\mathbf{E} = -\mathbf{v}\times\mathbf{B}. \tag{2.26}$$

Further boundary conditions also come from Maxwell's equation

$$\boldsymbol{\nabla}\cdot\mathbf{B} = 0, \tag{2.27}$$

yielding

$$[B_{\perp u}] = [B_{\perp d}], \tag{2.28}$$

and Faraday's Law

$$\boldsymbol{\nabla}\times\mathbf{E} = -\frac{\partial\mathbf{B}}{\partial t}, \tag{2.29}$$

with the assumption (under the same argument as equation 2.2) that

$$\frac{\partial\mathbf{B}}{\partial t} = 0, \tag{2.30}$$

where these combine to give

$$[v_{\perp u}\mathbf{B}_{\parallel u} - B_{\perp u}\mathbf{v}_{\parallel u}] = [v_{\perp d}\mathbf{B}_{\parallel d} - B_{\perp d}\mathbf{v}_{\parallel d}], \tag{2.31}$$

which completes the Rankine-Hugoniot relations under this regime.

These relations can be simplified further to describe MHD shocks in a planar / 1D system by setting $v_\parallel = 0$; $v_\perp = v$. Thus the elimination of this term from equations 2.24 and 2.31 gives

$$\left[\left(1 - \frac{{B_{\perp u}}^2}{4\pi\rho_u {v_u}^2}\right)v_u\mathbf{B}_{\parallel u}\right] = \left[\left(1 - \frac{{B_{\perp d}}^2}{4\pi\rho_d {v_d}^2}\right)v_d\mathbf{B}_{\parallel d}\right]. \tag{2.32}$$

This has two special cases and these are known as “parallel” or “perpendicular” shocks, depending on the orientation of the magnetic field relative to the normal of the shock interface.

For the parallel shock $\mathbf{B}_{\parallel u} = 0$, and so from equation 2.32, $\mathbf{B}_{\parallel d}$ must also equal zero. Thus in accordance with equation 2.28, the direction and magnitude of the original field are left unchanged by the parallel shock. There remains however both the usual heating and compression of the fluid across the interface, and so the parallel shock reduces to an equivalence with the hydrodynamic case.

For the case of the perpendicular shock $\mathbf{B}_{\perp u} = 0$, and so equation 2.31 becomes

$$v_u B_{\parallel u} = v_d B_{\parallel d}, \tag{2.33}$$

indicating that the field remains parallel to the shock front downstream. Here the magnetic field displays the same correlation to the up- and downstream velocities as the mass does in the flux conservation equation 2.4. Therefore in the perpendicular shock the field is subjected to the same compression ratio as the material flux, and it can be shown [31] that this has the same strong shock limit (equation 2.10 / 2.11) as the hydrodynamic system; provided that in addition to a high ratio of flow speed to sound speed, the ratio to the Alfvénic velocity (velocity of restorative magnetic tension waves along field lines) is also high. These criteria can be expressed in terms of the sonic and Alfvénic Mach numbers as $M_S \gg 1$ and $M_A \gg 1$.

Returning to the general (non-planar) set of MHD jump conditions, it is apparent that these equations describe discontinuities in the plasma parameters at a boundary, but they do not explicitly necessitate a shock at the interface. A discontinuity is only deemed a shock when there is a flow across the surface (i.e. $v_\perp \neq 0$) which is accompanied by dissipation and compression. In all cases where a discontinuity is not deemed a shock, further classification is made based on the orientation of the field relative to the boundary (i.e. $v_\perp = 0$, $B_\perp \neq 0 \Rightarrow$ “contact discontinuity”, $v_\perp = 0$, $B_\perp = 0 \Rightarrow$ “tangential discontinuity”, and any case where $v_\perp \neq 0$ with no compression / dissipation this is called a “rotational discontinuity”, due to a change in the direction of the field and / or flow velocity). Shocks are then distinguished on the basis of whether they are threaded by the field ($B_\perp \neq 0$) or not, where shocks with a non-zero perpendicular field component are called “oblique shocks” (not to be confused with the hydrodynamic case where this nomenclature refers to the presence of a flow velocity component parallel to the shock interface.)

Oblique shocks exist in two varieties and these can each be achieved if the upstream flow velocity is greater than the relevant magnetosonic velocity of the particular MHD wave that it is associated with. Therefore fast mode shocks occur when the flow velocity is in excess of the fast MHD wave speed

$$v_{fast}{}^2 = \frac{1}{2}\left(c_S{}^2 + v_A{}^2 + \sqrt{(c_S{}^2 + v_A{}^2)^2 - 4c_S{}^2 v_A{}^2 \sin^2\theta_B}\right), \tag{2.34}$$

while slow mode shocks occur when the flow velocity exceeds the slow MHD wave speed

$$v_{slow}{}^2 = \frac{1}{2}\left(c_S{}^2 + v_A{}^2 - \sqrt{(c_S{}^2 + v_A{}^2)^2 - 4c_S{}^2 v_A{}^2 \sin^2\theta_B}\right), \tag{2.35}$$

where θ_B is the angle between the upstream field and the shock interface. These two shocks differ in that the magnitude of the field increases across the interface for a fast shock, but decreases for a slow shock. Since the normal component of the field is bound by equation 2.28 to remain unchanged, this has the consequence that fast shocks bend away from the normal downstream, whereas slow shocks bend towards it (Fig. 2.5). It is apparent therefore that in the case of the planar perpendicular shock described previously, where there is no bending due to the absence of a parallel velocity component, this variety of shock is classified as a fast shock due to its downstream compression of the field.

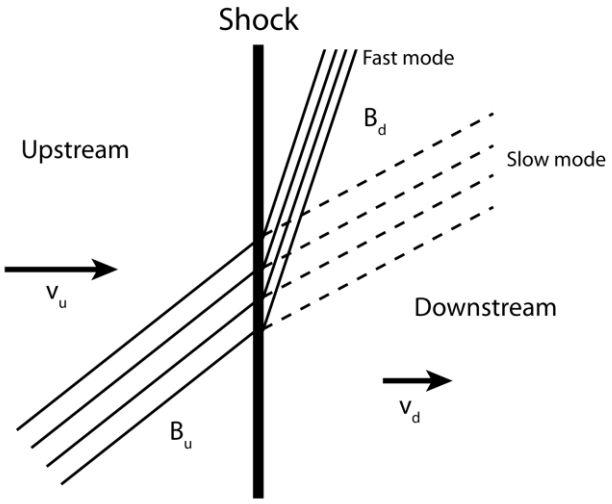


FIG. 2.5 Comparison of the magnetic field lines for fast and slow mode shocks. The field lines bend away from the shock normal for the fast mode, causing an increase in magnetic flux density. The opposite is true for the slow mode shock. Diagram adapted from [31].

The ideal MHD model presented thus far describes a set of six jump relations with six variables $(\rho, p, v_{\perp}, v_{\parallel}, B_{\perp}, B_{\parallel})$. This means that the downstream state can be found in terms of the upstream state, and so the system is effectively solvable. However as soon as further complexities are brought into the system there become free parameters and a greater level of information (either from supplementary theoretical relations or by measurement) is required to find unique solutions. For example one such common requirement is the inclusion of the "two-fluid description" of the plasma to account for differences in the behaviours of electrons and heavy ions. At long enough equilibration time these fluids act separately necessitating their own independently defined temperatures and pressures, and due to the differences in their inertia they respond disparately to the presence of fields in the plasma. The effects of viscosity, resistivity and thermal conduction are also frequently incorporated into the MHD description, and the expanded equations for the shock relations including these terms are examined in [32].

Another consideration to be made in systems with MHD shocks is that of the mechanisms responsible for mediating the localising pressure force and dissipating the initial kinetic energy brought from the upstream flow. Traditionally fluid shocks are initiated by an increase in thermal pressure at the shock interface, arising from an increase in particle collisions at the boundary. However in MHD fluids shocks can also arise due to collisionless (i.e. electromagnetic) localisation, or even a mixture of these and collisional processes. The most obvious form of collisionless localisation is that of the reflection and/or induced gyrational motion of charges when they intercept a magnetic field perpendicularly to field direction. For this reason charges can be more easily trapped in a perpendicular shock than a parallel one; which is why the equations for the parallel shock reduce to the hydrodynamic case – the particles there require collisions to solely provide the pressure jump as they are not subjected to any simultaneous magnetic pressure increase from the $\mathbf{v} \times \mathbf{B}$ force. Collisionless interactions can also be induced however by electric potentials built up by the separation of charges in the shocks (e.g. by Hall currents) which then act to decelerate the motion of further oncoming charges.

In terms of the dissipation of energy, where in regular fluids this is also achieved solely through collisions, MHD fluids can make changes to the particle distribution functions (and hence temperatures) by causing changes to particle motions through perturbations of the fields. These are often seeded by instabilities which produce turbulence in the

plasma (and its field), and so changes in the velocities of particles can be achieved even if there are no collisions.

An example of the structure of a perpendicular shock in a purely collisionless plasma is shown in Fig. 2.6. The data is from a measurement of the bow shock formed by the interaction of the solar wind with the Earth's magnetic field, as made by a spacecraft moving through the shock front, and shows features which are typical of a strong, collisionless shock. The plots of electron density and velocity show that whilst the material is compressed into the downstream region, the magnetic field increases, and hence is a fast mode shock. There are three main features to the shock which are indicated – these are the "foot", the "ramp" and the "overshoot". The foot is also commonly referred to as a "magnetic precursor" and is created by the reflection of ions

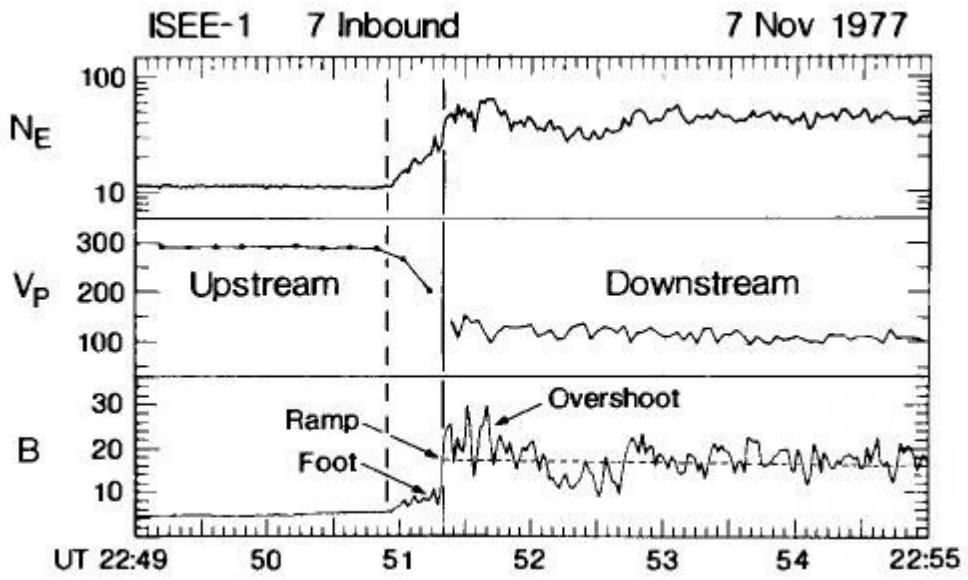


FIG. 2.6 Measurements taken by a spacecraft passing through the Earth's bow shock. The plots show the electron density (n_e), plasma velocity (v_p) and magnetic field (B) through the bow shock. The x-axis shows the time of the measurements, and corresponds to a linear spatial scale due to the fixed speed of the probe. Diagram reproduced from [33].

at the shock surface, which can be subsequently dragged back into the shock by their induced gyration. Following this, the ramp then indicates the main rise / compression of both the field and fluid medium, where its non-zero thickness is owed to an effective viscosity in the plasma arising from collisionless field interactions; and the overshoot corresponds to high energy ions which are reflected beyond this. The presence of both

the foot and the overshoot in the shock structure depend strongly on whether the shock reaches a critical Mach number, which varies as a function of the field angle, as shown by the plots in [31] p.149. However in plasmas where there is a mixture of both collisional and collisionless effects, the presence of features such as these depends on the relative dominance of those effects.

Clearly there are many factors determining the type of shock produced in a MHD system – the orientation of the field and flow velocity, the strength of the shock (as gauged by the various Mach numbers), the degree of collisional versus non-collisional effects, and of course all the usual factors regarding its material and fluid composition and thermal properties. Consequently the structure of magnetised shocks can be extremely difficult to predict, and as such experimental and computational simulations remain an active area of research in establishing the structures produced in various scenarios of MHD.

2.4 Shocks in astrophysics and the laboratory

Shocks are often observed amongst a wide variety of astrophysical systems. These can include the high velocity (supersonic and often super-Alfvénic) ejections of young or unstable stars and supernovae, propagating through the interstellar medium, to the obstructions of solar winds by planetary bodies (see Fig. 2.7).



FIG. 2.7 (a) (*left*) An arc-shaped nebula near the star R Hydrae is the first bow shock ever seen around a pulsating red giant. The bow shock arises as material streaming off the star slams into the interstellar medium. (b) (*right*) Bow shock around the very young star, LL Ori, in the Great Nebula. This star emits a vigorous stellar wind, which collides with slow-moving gas evaporating away from the centre of the nebula (located lower left of image). The surface where the two winds collide is the crescent-shaped bow shock. [Image credit: NASA/ESA, 2007]

Radiative cooling and magnetic fields can both play a significant role in the energy transfer and pressure mechanisms of these shocks and their likelihood in doing so is measured via the dimensionless parameters of these systems. In the case of radiation one considers the cooling parameter, which gives the ratio of the system's cooling time to its characteristic hydrodynamic time

$$\chi = \frac{t_{cooling}}{t_{hydro}} = \frac{p}{\Lambda} \cdot \frac{v}{L}, \tag{2.36}$$

where L and v are the characteristic length and flow velocity of the system. Similarly in cases where one wishes to evaluate the importance of the magnetic effects, one considers the Beta parameter of the system (equation 1.17).

A wide variety of regimes are applicable, both in terms of the field strengths, radiative fluxes, and optical properties discussed in section 2.2. In addition flows into shock structures can show a range of collisionality and collisional processes. In many cases plasma Beta are found in the region of $\beta_{th} \sim 20$ [23]. This factor gives the ratio of thermal to magnetic pressures and indicates that thermal pressures are generally responsible in causing the collisions of astrophysical shocks. Large magnetic fields can however feature – for example as was shown in Fig. 2.6, the fields of planetary bodies can play a dominant role in the structure of bow shocks caused by the interaction with stellar wind, far from the planetary surface [10–12,33].

Understanding the dynamics of these astrophysical phenomena can be a significant challenge from a purely theoretical or computational point of view, as they combine the physics of magnetohydrodynamics and radiation in a non-trivial manner. Hence it is useful to have laboratory based experiments as a complimentary means of simulating them and the effects that key physical parameters have on them. Under the appropriate reference frame the astrophysical scenarios can be equated to static obstructions in fast plasma flows ($M_S > 5, M_A > 2$). This means that it is possible to make relatively simple models of these objects in the laboratory by placing fixed targets in the paths of high velocity plasma streams created by modern day HEDP facilities.

The majority of facilities which carry out experiments such as these employ high powered lasers, focussed down to small length scales with short, intense pulse shapes. These are directed onto ablator targets, which when impacted by the laser beam produce a plume of plasma ejecta which expands away from the ablator surface and towards an external obstacle / target (see for example [2,34,35]). The experiments of this thesis differ however, in that they use a steady stream of supersonic plasma generated by the

pulsed power driven ablation of a wire array. Unlike the laser based configuration, this setup has the unique advantage that it generates a sizeable magnetic field (originating from the current pulse) which is embedded into the plasma and propagates with the flow. This therefore makes these plasmas particular suitable for studying phenomena of magnetised shocks, as they do not require any externally applied fields to achieve this. The following section outlines the applicability of the pulsed power, wire array setup, and in particular the inverse wire array, as a platform for studying magnetised shocks.

2.5 Wire arrays as a platform for magnetised shock experiments

HEDP pulsed power machines such as the MAGPIE facility were originally commissioned for the study of the radiative collapse of fibre z pinch loads, which was of interest as a potential means of creating controlled fusion energy [5]. In the modern era however the ability of these facilities to access high energy regimes has seen their purpose adapted for the study of a wide range of plasma physics processes and phenomena, with an increasing focus placed on laboratory astrophysics applications; and of particular interest in this area are the physics of shocks.

The MAGPIE generator operates by delivering a 1MA current pulse to its load over the duration of a $\sim 300-500$ns timescale. This high energy density causes the load to undergo a rapid resistive heating, producing a plasma medium which is then subjected to its own self-accelerating $\mathbf{J}\times\mathbf{B}$ force, whose direction is determined entirely by the geometry of the load circuit. One such load geometry which has been used recently to

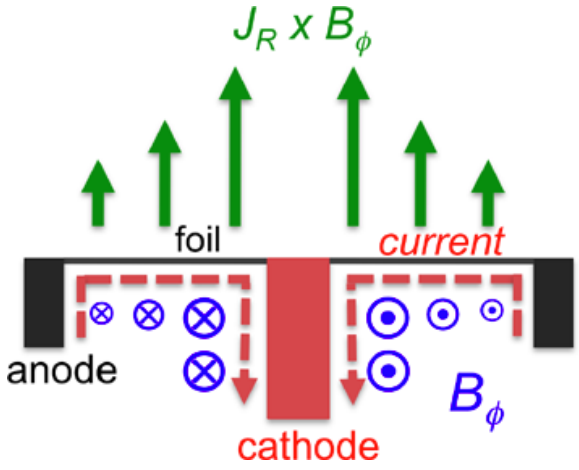


FIG. 2.8 Schematic of the radial foil load, showing the current path through the foil, the toroidal field and the force acting on the plasma produced by the foil. Diagram reproduced from [39].

produce and study plasma shocks is that of the "radial foil" [36,37], as shown in Fig. 2.8. In this setup the negative and positive terminals of the generator, which consist of a central cylindrical cathode post and a surrounding concentric anode ring, are connected at their end via a thin (10μm) circular disk of conducting metallic foil. The current electrons, originating from the cathode, pass radially through the foil to the anode, whilst creating a plasma layer across the foil surface. The $\mathbf{J} \times \mathbf{B}$ force here has a vertical direction, with an enhanced magnitude at the centre of the foil due to the higher current density. This acts to launch the plasma from the surface, producing a cylindrical jet, and has been shown to have scalable similarity to real astrophysical jet structures, such as those emitted by young stellar objects [38,39]. In the interest of shock studies these jets have been collided with both ambient gases in the region above the jet [40–42], as well as head-on with similar or identical plasma jets in a double foil setup [43]. These examples produce interesting results, however due to the 3D geometry of the jets, with their radially and axially varying density profiles, the resultant shock structures can be difficult to measure and therefore interpret in terms of their basic fluid and particle processes.

Wire arrays offer an alternative means of studying plasma shocks, with the advantage of a more simple density and flow structure due to their axial symmetry. Typical wire arrays consist of a cylindrical arrangement of fine (ϕ~10μm) metallic wires which are

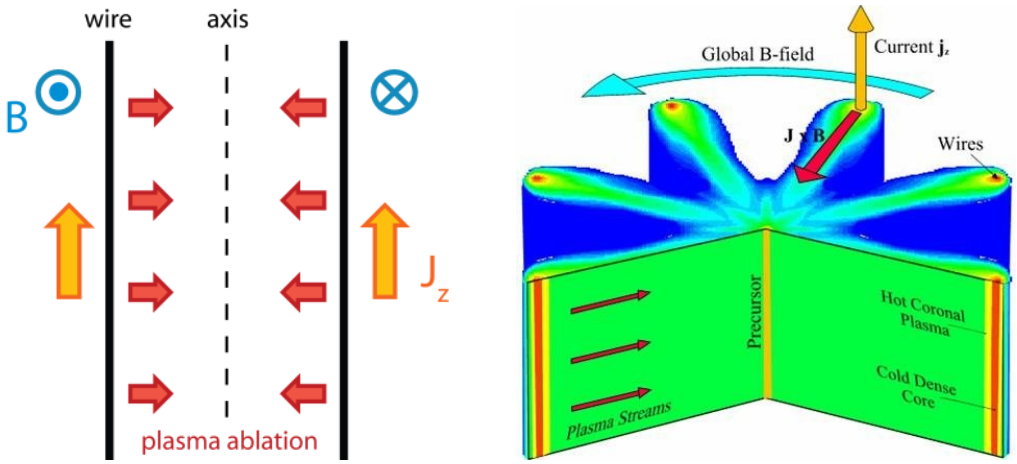


FIG. 2.9 The cylindrical wire array z pinch, showing the current applied to the array and the axial implosion of ablated plasma, which is directed by the **J×B** force of the global field. (a) (*left*) A side-on cross-section of a wire array. (b)* (*right*) A 3D simulation of the plasma flow during the ablation stage of the implosion. *[Image property: MAGPIE group.]

placed concentrically, and with equal spacing about a $\sim 0.5-1\text{cm}$ radius, with the current terminals connected at either end (Fig. 2.9). The $\mathbf{J}\times\mathbf{B}$ force of the array drives its implosion onto the central axis on a timescale approximately equal to the rise-time of the current pulse. Typically during the first $75\%-80\%$ of this process the wire cores of the array remain stationary while resistively heated material is ablated from the wire surface to form a surrounding coronal plasma. This corona is diverted towards the axis by the pinch force with an approximately constant supersonic ($M_S\sim 5$) velocity, giving rise to a stream of plasma flow which is found to be accurately approximated by a phenomenological model based on a rocket-type equation [24]. Here the momentum influx into the flow

$$\frac{dp}{dt} = v\frac{dm}{dt} \tag{2.37}$$

(per unit length of the wires) is equated to the accelerating magnetic force $\left(\mathbf{F} = I\cdot\hat{\mathbf{I}}\times\mathbf{B}\right)$ as calculated at the wire positions by Ampère's law:

$$IB_\theta = -\frac{\mu_0 I^2}{4\pi R} \tag{2.38}$$

(where R is the radial position of the wires). The mass distribution of plasma inside the flow can be estimated from this using

$$\rho = \frac{1}{dA}\frac{dm}{dt}dt, \tag{2.39}$$

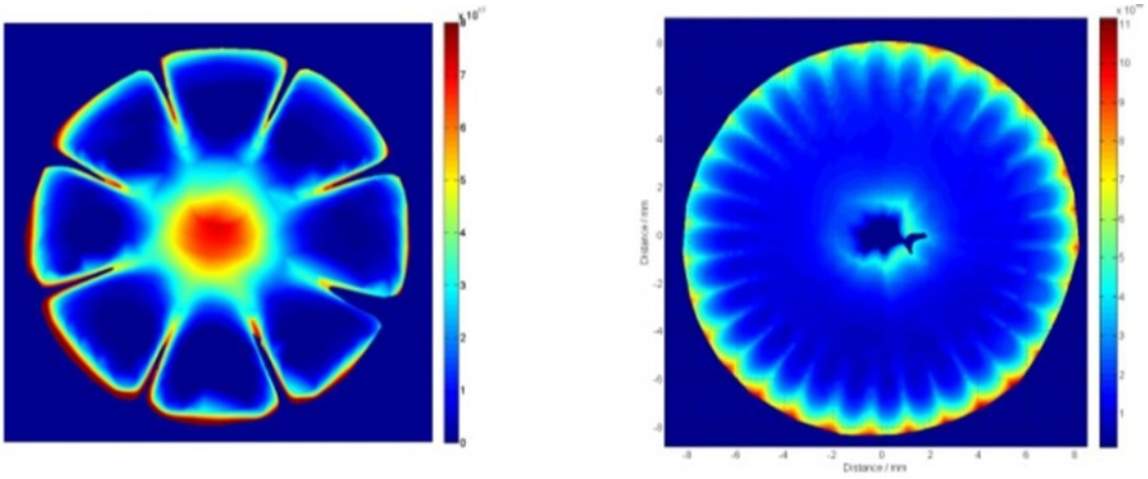


FIG. 2.10 End-on electron density maps of the ablation phase for cylindrical 8 wire (*left*) and 32 wire (*right*) arrays. For a higher wire number the flow is seen to behave more collectively and give a more uniform flux through the array. [Image credit: G. Swadling [46], MAGPIE group].

where

$$dA = 2\pi rvdt. \tag{2.40}$$

Taking into account the time delay required for the material to reach some radial position r, the mass density at any point in the flow can be written as

$$\rho(r,t) = \frac{\mu_0}{8\pi^2 Rrv^2}\left[I\left(t - \frac{R-r}{v}\right)\right]^2. \tag{2.41}$$

This phase of the array dynamics ends when a considerable amount of the wire material (~50% of the initial mass) has been ablated. At this time the wire cores tend to break and the remaining mass follows in a trailing implosion. This secondary implosion phase can be avoided however by "over-massing" the wires such that they have a significant enough abundance of material not to reach breakage during the experimental (i.e. current-pulse) timescale. Thus the arrangement can be utilized by placing static target objects in the path of the flow. As mentioned already, performing experiments in this manner has the benefit that the wire array has an axis of symmetry, and therefore by using a shock target which runs along the length of the array, the interaction can be viewed from a 1D perspective in the vertical ("end-on") direction. Additionally they also have the advantage that the number of wires around the array circumference can be chosen to select the type of shock interaction simulated. For example, a low wire number can produce collimated plasma streams from each of the wires (Fig. 2.10), and would be applicable to simulating jet-like collisions. Increased wire number flows however behave collectively and so a more uniform shock front can be produced; better suiting accretion phenomena for example.

Preliminary shock experiments have previously been fielded on MAGPIE in this way, using a nested wire array setup [44]. This consisted of plasma flow from an outer ablating array incident on the wires of a concentric, non-ablating (i.e. isolated from the current source) inner array. However, limited conclusions could be draw from the investigation, due to the inherent difficulty of making diagnostic measurements in a converging geometry such as this. On this basis the inverse wire array has been identified as a preferable means of utilizing the current driven plasma flow, in a more open and accessible setup. The inverse (or "exploding") wire array has been explored in detail in previous experiments on MAGPIE [6,7]. It differs from the standard arrangement in that a cathode rod is located on the axis, providing an opposing current direction to the surrounding wires, which themselves connect to the cathode at one end

and provide the return path to the anode (Fig. 2.11). This has the effect of reversing the global field of the array, such that the plasma streams are directed radially outward from the array. During the ablation phase, the plasma flux from the inverse array is found to be analogous to that of the standard array [6]. Thus there is the same benefit of being able to provide a reliable and predictable density of plasma flow for shock experiments. However since the targets can be placed externally the interaction region is open for probing with a wider selection of the diagnostic tools on MAGPIE.

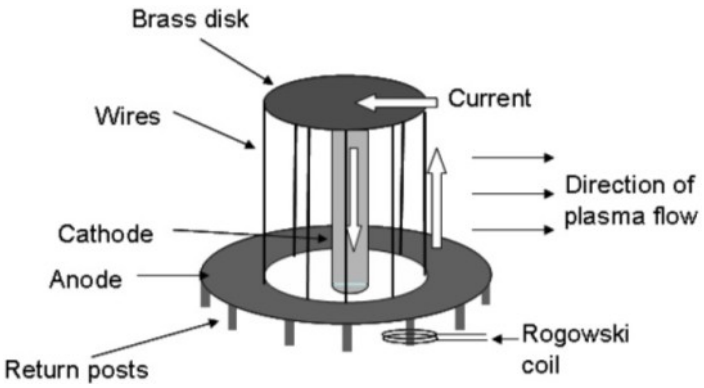


FIG. 2.11 Schematic of the inverse (exploding) wire array. Reproduced from [6].

It is this premise which forms the basis of the current PhD project, where a newly adapted configuration of the inverse wire array was used to study the effect of an advected magnetic field inside the plasma flow on the structure of shocks made by the collision of the flow with a planar foil obstacle. A scenario of this type is known as a "reverse shock", owing to the post-collision reflection of the compressed downstream material, which moves back away from the obstacle surface and into the oncoming flow. At first instance this could be considered as only a very specific category of shock, however the relevance of this situation is wide reaching since in essence any laminar shock geometry can be equated to that of a reverse shock under the correct frame of reference. Hence by learning about the fundamental properties of shocks (or in this case magnetically-perturbed shocks) in this setup, an insight can be made of the physics of a variety of astrophysical phenomena. It is noted that whilst the effect of radiative effects on the shocks was not considered in this work, this could later be investigated by varying the wire material. The experiments used only aluminium wires, where radiation is expected to be small for such a low-Z element. However with increased Z number, radiation via line emission rapidly increases and could therefore have a measurable effect on the observed structures.

The experimental setup for the inverse wire array, reverse shock experiments is presented over the next two chapters. Chapter 3 gives an overview of the MAGPIE generator, chamber and diagnostic setup, and chapter 4 describes the setup used for the shock experiments, including data from experiments to characterise its plasma flow properties.

Chapter 3:

The MAGPIE generator and plasma diagnostics

This chapter provides an overview of the experimental facility where the work of the thesis was carried out. This includes a description of the pulsed power generator MAGPIE, its experimental chamber and the layout and function of its diagnostic components, including derivations of the measurements which each of these tools can provide.

3.1 The pulsed power generator

The Mega Ampere Generator for Plasma Implosion Experiments, known more concisely as MAGPIE, is a pulsed power generator based at Imperial College. It is capable of producing a 1.4MA, 240ns rise-time current pulse, of terawatt power, which it delivers to its load section to create extreme physical states of matter. Its original commission was for the study of the radiative collapse of fibre z pinch loads [5], made from low-z, cryogenic materials such as hydrogen and deuterium, and at the time were of interest as a potential means for creating controlled fusion energy. Today its high impedance output means that it finds use as a current driver for a wide range of applications including wire array [25,45,46] and HEDP laboratory astrophysics experiments [38,41,42,47,48]. The paper of [5] describes the working principles of the generator hardware and is summarised in this section.

A cartoon of the generator is shown in Fig. 3.1. It consists of four Marx bank modules (labelled #1 in the diagram), which each hold an array of $N = 24$ individual $C = 0.7\mu F$

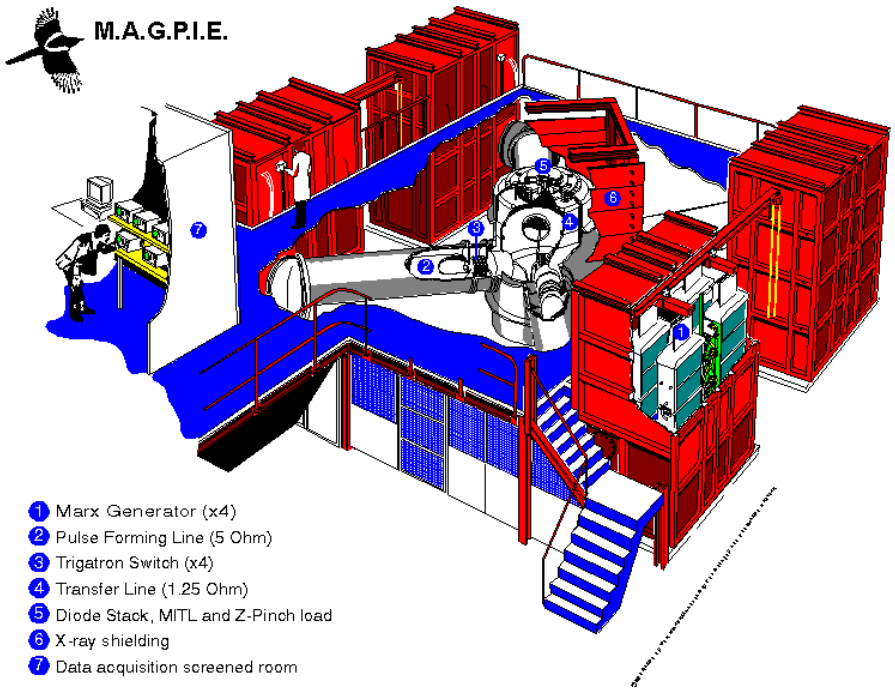


FIG. 3.1 A drawing of the MAGPIE pulse power generator [Image credit: The MAGPIE group].

capacitors connected in parallel. These capacitors are charged in DC to alternating voltages of $V_{charge} = \pm 65V$ over the course of a $\sim 2-3$ minute period, before suddenly connecting them in series via the initiated dielectric breakdown of the connecting gas-filled spark gap switches (as shown by the circuit diagram in Fig. 3.2). Thus the voltages of the capacitors are stacked to achieve a high voltage (HV) signal

$$V_{Marx} = NV_{charge} \tag{3.1}$$

$(= 1.56MV)$ from a low voltage supply, with the total energy of each bank output at

$$E_{Marx} = \frac{1}{2} NCV_{charge}{}^2, \tag{3.2}$$

and a total capacitance of the bank

$$\frac{1}{C_{Marx}} = \sum_N \frac{1}{C_N} = \frac{N}{C}. \tag{3.3}$$

The output from the Marx banks is fed into the pulse forming lines (PFLs, label #2) which act to channel and compress the HV signal in time. The PFLs are large coaxial transmission lines, filled with deionised water, which due to this medium's high resistivity ($10^4 \Omega m$) are able to withstand a large potential difference. During their

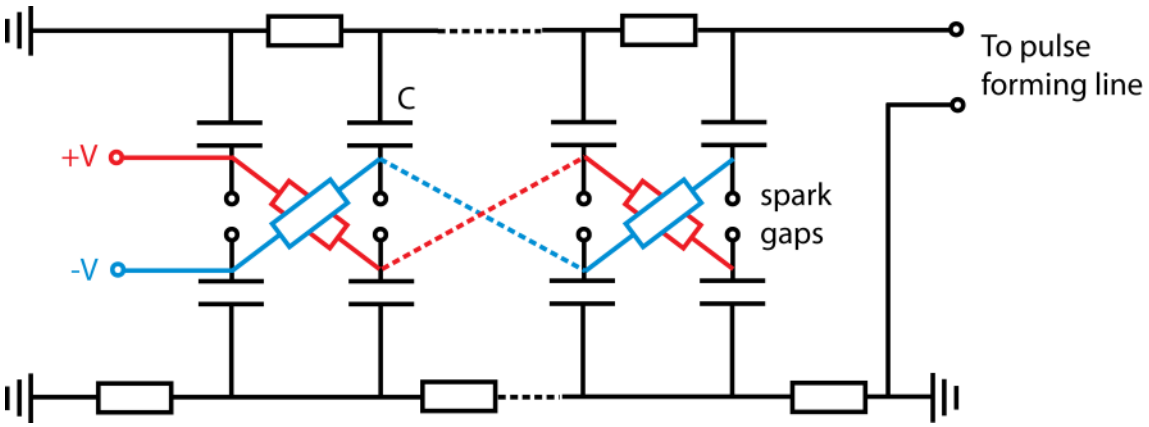


FIG. 3.2 Circuit diagram of the Marx bank capacitors.

charging the PFLs are isolated from the subsequent stage of the generator via further spark gaps (referred to as trigatrons, label #3) and therefore act as large capacitors for the intermediate storage of charge. The PFLs are charged on a timescale of

$$t_{charge} = \pi \sqrt{\frac{L_{Marx} C_{PFL} C_{Marx}}{C_{PFL} + C_{Marx}}}, \tag{3.4}$$

to a voltage

$$V_{PFL} = \frac{2 C_{Marx} V_{Marx}}{C_{PFL} + C_{Marx}} \tag{3.5}$$

where the Marx inductance L_{Marx} is 5μH, and from equation 3.3 $C_{Marx} = 29\text{nF}$. The capacitance of the PFL is

$$C_{PFL} = \frac{\tau}{Z_0} \cdot \lambda \tag{3.6}$$

where τ is the single transit time of the line (100ns), $Z_0 = 5\Omega$ is its characteristic impedance, and its length is $\lambda = 3.3\text{m}$. Hence $C_{PFL} = 66\text{nF}$, $V_{PFL} = 0.95\text{MV}$ and $t_{charge} = 1\mu\text{s}$.

In order for the PFL to deliver the maximum transmission of its stored energy into the next stage, the vertical transmission line (VTL, label #4), it has to be impedance matched with this. The impedance matching has the effect of dropping the voltage of the signal by a factor of two as the PFLs are discharged into the VTL over a timescale of twice their single transit time. This is the result of two square waves, with equal magnitude ($V_{PFL}/2$) and speed, travelling in opposite directions from the switch end of the PFL upon short circuit connection with the VTL. The forward travelling wave

empties half of the PFL charge into the VTL, while the other depletes the charge in twice the time; by first propagating back along the line, before reflecting back off the other end due to the impedance mismatch with the Marx bank. Thus upon fully charging the PFLs and firing their trigatron switches, the initial 1μs discharge of the Marx banks is shortened to a $2\tau = 200$ns pulse into the VTL.

The constant, square-wave voltage of the pulse has the effect of driving a linearly rising current into the VTL, since

$$\frac{dI}{dt} = \frac{V}{L}. \tag{3.7}$$

However, the geometry of the VTL and remaining circuitry mean that this linearly rising current is more accurately described by a $\sin^2$ shaped pulse by the time it reaches the load, with a slightly longer rise time of 250ns. Mathematically therefore the driving current for MAGPIE experiments is given to good approximation by

$$I(t) = I_0 \cdot \sin^2\left(\frac{\pi t}{500\text{ns}}\right). \tag{3.8}$$

The four PFLs are arranged in parallel about the VTL and their switches are ideally fired in synchronisation so that their currents sum in phase thereafter. There is however some operational jitter in the firing system, typically of order 10ns, and this can reduce the peak amplitude of the current supplied to the experiment on a shot-to-shot basis. The superposition of the four PFL contributions sets the upper limit for the peak of the current pulse at $I_0 \leq 1.4$MA; with the assumed pulse shape of equation 3.8 becoming less accurate the further out of synchronisation the trigatron switches are fired.

The VTL, which like the PFLs is a coaxial line of deionised water, delivers the total power of the discharge up through the central column and to the load chamber via a feed-through section known as a magnetically insulated transmission line, or MITL (#5). This section of the generator is shown as a cross-section in Fig. 3.3. The MITL performs the function of focusing the current flux of the pulse from the 1.5m diameter of the VTL to the ~1cm scale of the experimental load. The outer surface of the MITL is contained within the vacuum of the experiment chamber and has a smooth, curved profile to minimise the emission of electrons, and therefore, the possibility associated with this of causing a short circuit before the load is reached. Towards the load section where the inner cathode is at its closest to the anode (~1.5cm), and the electric field is consequently highest, the MITL is at its narrowest. This has the effect of significantly

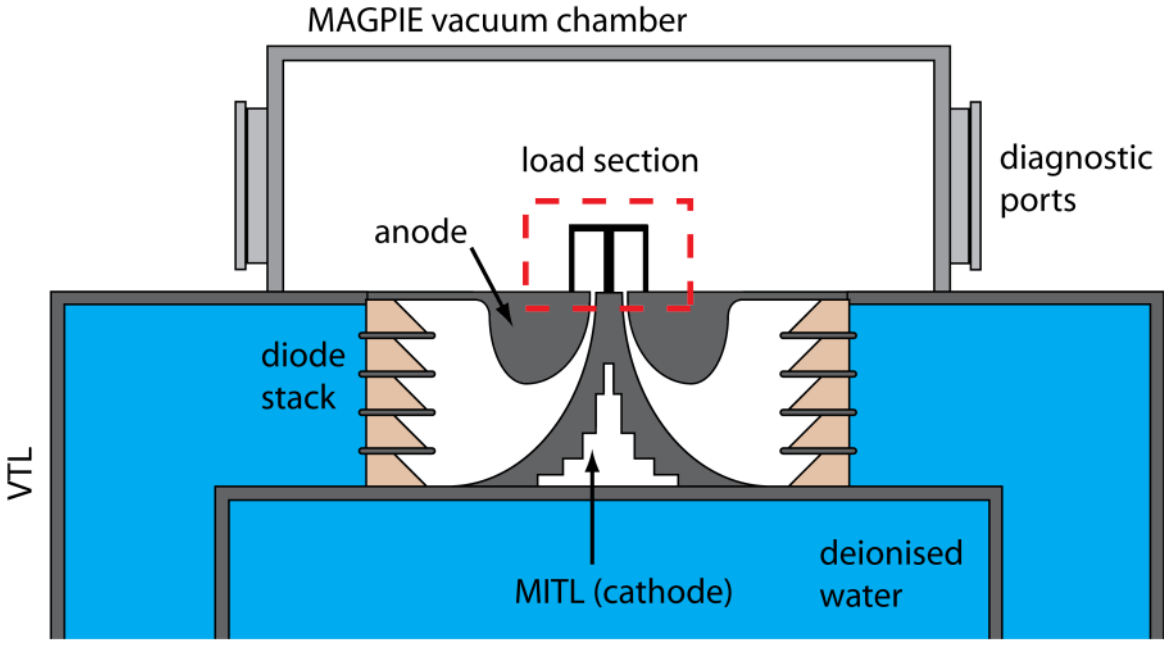


FIG. 3.3 The interface of the VTL and MITL generator sections and their connection to the chamber load.

increasing the magnetic field surrounding the cathode so that the tight gyro-radius of the field emitted electrons acts to suppress the dielectric breakdown of the vacuum between the terminals. Hence the inductance of the MITL forces the current to take the path through the load apparatus, and provided the chamber is held under a good vacuum ($< 3 \times 10^{-4}$mbar), breakdown is avoided until beyond the timescale of the experiment; which typically is after the peak current time (~250ns) when the load has been spent leaving an open circuit in the chamber.

Other considerations have been made in the design of the MITL section to ensure that current is successfully delivered to the load. Along the water-vacuum interface at the end of the VTL the anode and cathode terminals are insulated by a series of concentric plastic (Perspex) spacers separated by stainless steel grading rings, which comprise the diode stack. On the vacuum side of the stack the spacers are cut with a 45° surface to provide a magnetic-flashover inhibition; whereby the $\mathbf{E} \times \mathbf{B}$ drift of electrons emitted from the insulator directs them away from the surface to prevent an avalanche process, as this could lead to surface tracking causing leakage currents and breakdown. The grading rings meanwhile ensure a uniform electric field across the height of the stack via capacitive voltage division. Finally the surfaces of the diode stack and MITL are shielded by the geometry of the anode and cathode bodies, to minimise the unwanted

photo-electric emission of surfaces caused by the high energy UV and x-ray radiation produced by plasmas in the experimental chamber. The anode ensures that there is no direct line-of-sight to the diode stack and only a restricted view of the cathode surface from the load.

3.2 The MAGPIE experiment chamber

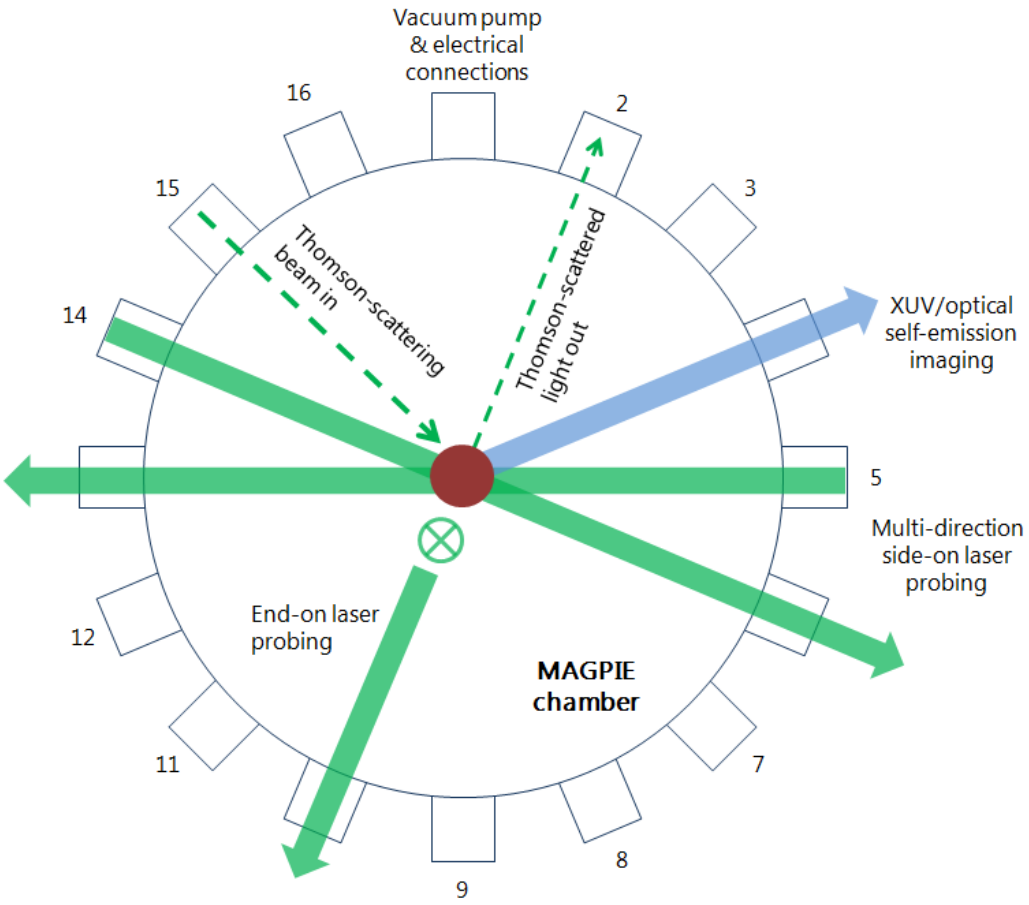


FIG. 3.4 Overview of the MAGPIE chamber and its diagnostic layout.

Fig. 3.4 shows a schematic of the MAGPIE chamber from an end-on view with an example of its typical diagnostic layout. The load hardware for experiments is located in the centre of the chamber which is kept under high vacuum ($\sim 2 \times 10^{-4}$mbar) during the course of the experiments to prevent electrical breakdown of the apparatus, as well as to avoid any ambient interaction with the plasma. The chamber has 16 ports spaced evenly about the circumference of the chamber, which are used for diagnostic measurements of the plasmas, as well as for housing connections to the vacuum pumps and current monitoring probes which record the generator output through the MITL and load sections. The chamber also has a central view port located vertically above the load

hardware to allow measurements from an end-on perspective. End-on measurements which require both an input and output path (i.e. laser probing beam-lines) are achieved by mounting a 45° mirror beneath the load such that the beam can be directed through one of the horizontal ports.

The diagnostic assembly on MAGPIE consists of a high intensity, narrowly focussed laser beam used for spatially resolved Thomson scattering measurements, several collimated beams for shadowgraphy and interferometry based imaging (including one dual-wavelength channel allowing time-separated imaging), XUV and optical multi-frame cameras for recording time-gated self-emission images, and local inductive probes for magnetic field measurements. Thanks to the large number of available ports and the symmetry of the chamber, as well as the design of the loads, many of these diagnostics can be fielded in combination during a single experiment; potentially allowing a comprehensive knowledge of a wide range of plasma conditions. The working principles of the diagnostic suite are described in the following sections.

3.3 Current diagnostics

The current through the load section is measured by the use of Rogowski groove probes which are mounted on current return posts between the anode and experimental load. These record the voltage generated by the time-varying magnetic field of the current pulse which is then integrated to recover I(t). Probes of a similar nature are also located at several positions in the MITL section (referred to as MITL B-dots) to monitor the current there and these operate under the same working principle.

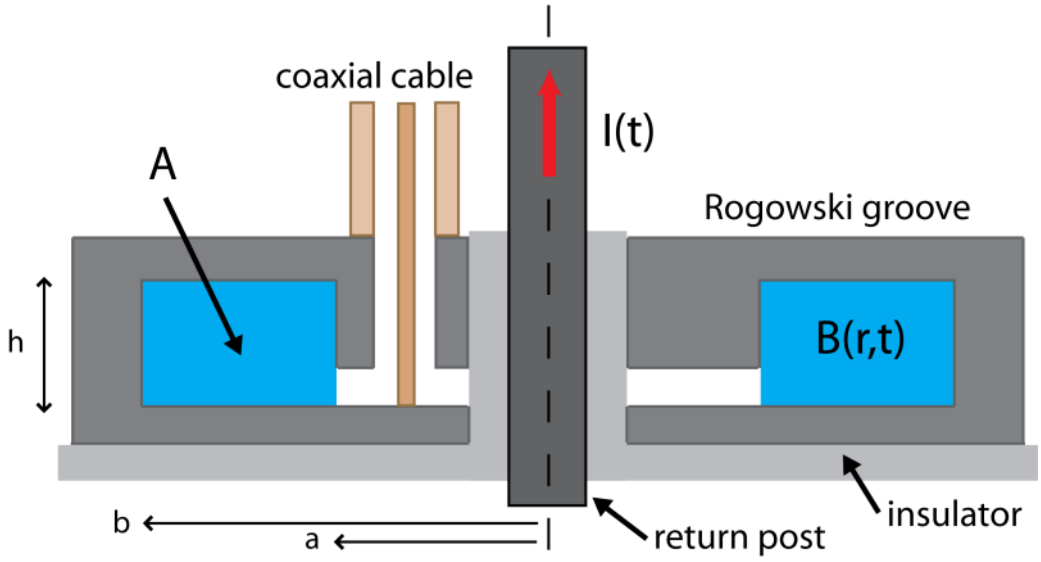


FIG. 3.5 Cross-section of the Rogowski groove which monitors the current through the load.

The Rogowski groove consists of a circular cavity with square cross-section which is shown schematically in Fig. 3.5. The groove is centred on the current carrying return posts such that the poloidal field lines of this link a flux to the cavity equal to

$$\Phi = \int \mathbf{B} \cdot d\mathbf{A}. \tag{3.9}$$

The top and bottom faces of the groove are connected to the terminals of a coaxial cable, as shown in the illustration, and this registers a voltage

$$V_{rog} = -\frac{d\Phi}{dt}, \tag{3.10}$$

which on an element by element basis is given by

$$dV_{rog} = -dA\frac{dB}{dt} = -h \cdot dr\frac{dB}{dt}, \tag{3.11}$$

where h is the height of the cavity and r is the radial position from the axis. Since the field given by Ampere's law is

$$B(t) = \frac{\mu_0 I(t)}{2\pi r}, \tag{3.12}$$

performing the integration of equation 3.11 leaves

$$V_{rog} = \frac{\mu_0 h}{2\pi}\ln\left(\frac{b}{a}\right)\frac{dI}{dt}, \tag{3.13}$$

where a and b are the inner and outer radii of the cavity respectively.

Experimental setups used on MAGPIE usually incorporate multiple return posts (typically 4, 8 or 16) which are symmetrically distributed about the load such that an even split of the current is expected to pass through each post. Thus on integrating the signal it is multiplied by the appropriate factor to give the total current. A pair of Rogowski grooves is used for the experiments and these are mounted on separate posts and in reverse polarity to one another. This allows the symmetry of the current distribution to be checked, and on combining the signals allows any offset from capacitive coupling to be removed.

3.4 Laser probing

3.4.1 Thomson scattering

Thomson scattering is a valuable technique for making direct measurements of the physical conditions of laboratory plasmas. It utilizes the elastic scattering of light by

charged particles, where the spectrum of scattered light from a population of charged particles can be used to extract the state variables of the system. Depending on the regime of the scattering interaction these variables can include plasma density, average particle velocities and ionisation, as well as species temperatures. The methods for making these measurements are summarised in what follows.

When an electromagnetic wave is incident on a charged particle, the electric and magnetic fields of the wave set that particle in an oscillatory motion via the Lorentz force

$$\mathbf{F} = q(\mathbf{E} + \mathbf{v} \times \mathbf{B}). \tag{3.14}$$

The subsequent acceleration of the charge causes the particle to re-emit the energy it has gained from the wave as further radiation at the same frequency, and so is equivalent to the light being scattered by the particle. If the scattering particle is moving with velocity $\mathbf{v}$ within the plasma then in its own frame of reference the incident wave appears Doppler shifted, and hence in the laboratory frame the re-emitted wave also displays a shift. For an incident wavevector

$$\mathbf{k}_{in} = \frac{\omega_0}{c}\hat{\mathbf{z}} \tag{3.15}$$

the angular frequency of the wave as observed by the electron is

$$\omega' = \omega_0 - \mathbf{k}_{in} \cdot \mathbf{v}, \tag{3.16}$$

and the frequency that it re-emits in the lab frame is

$$\omega_{out} = \omega' + \mathbf{k}_{out} \cdot \mathbf{v} = \omega_0 + (\mathbf{k}_{out} - \mathbf{k}_{in}) \cdot \mathbf{v}, \tag{3.17}$$

where $\mathbf{k}_{out}$ is the wavevector of the re-emitted light. (Note that since the radiation has a

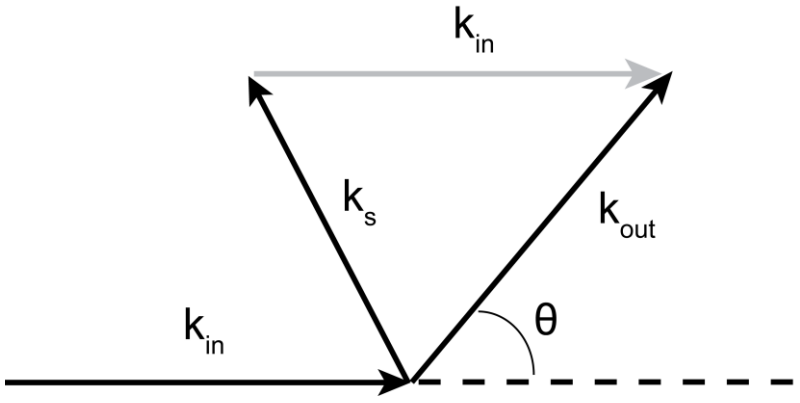


FIG. 3.6 Geometrical relation of the Thomson scattering vectors.

finite probability of being scattered in any direction, $\hat{\mathbf{k}}_{out}$ in a practical sense defines the direction of chosen observation.) The total Doppler shift is therefore

$$\Delta\omega = \omega_0 - \omega_{out} = \mathbf{k}_s \cdot \mathbf{v}, \tag{3.18}$$

where the scattering vector is defined as

$$\mathbf{k}_s = \mathbf{k}_{out} - \mathbf{k}_{in}. \tag{3.19}$$

This geometrical relationship is illustrated in Fig. 3.6, and it can be readily shown that for small Doppler shifts ($v \ll c; |k_{in}| \approx |k_{out}|$)

$$|\mathbf{k}_s| = \frac{2\omega_0}{c}\sin\left(\frac{\theta}{2}\right), \tag{3.20}$$

where θ is the angle between the incident and observation vectors. Hence by recording the Doppler shift of the scattered light it is possible to measure the velocity component of the charged particles along the direction of the scattering vector, where this is

$$v_{\parallel} = c\frac{\Delta\omega}{2\omega_0}\mathrm{cosec}\left(\frac{\theta}{2}\right). \tag{3.21}$$

A plasma consists of both ions and electrons and both of these have the ability to scatter light. However since the mass of the ions is so much greater, their Lorentz acceleration can be neglected, and so in considering the interaction of light with the system only the contribution of scattering by the electrons need be included. Despite this, the motion of the electrons can under certain conditions become correlated with the motion of the ions. For scales greater than the Debye sphere the electrons act to shield the charge of the ions and so move around with them. Therefore if the wavelength of the light travelling through the plasma is greater than the Debye length

$$\lambda_D = \sqrt{\frac{k_B T}{4\pi n_e e^2}}, \tag{3.22}$$

then the light is scattered by those shielding electrons. The superposition of the light scattered from a volume of the plasma produces a combined spectrum, and so electrons correlated to the ions cause a coherent interference due to this collective behaviour. In this case the shape of the scattered spectrum reflects the properties of both the ions and electrons. Conversely, if the light wavelength is smaller than the Debye length then it is not sensitive to this coherence and the spectrum only displays properties of the electron fluid. The scattered spectrum can therefore be expressed in terms of two components as

$$S(\mathbf{k}_s, \omega) = S_e(\mathbf{k}_s, \omega) + S_i(\mathbf{k}_s, \omega), \tag{3.23}$$

where S_e is the electron component, which only depends on the electron fluid, and S_i is the ion component, which exhibits the combined effects. There are therefore two main regimes of Thomson scattering, where either one of these becomes the dominant term. In order to distinguish which regime is relevant under a certain set of conditions the parameter

$$\alpha = \frac{1}{k_s \lambda_D} \approx \frac{\lambda_0}{4\pi\lambda_D} \cdot \operatorname{cosec}\left(\frac{\theta}{2}\right) \tag{3.24}$$

is defined. Here $\alpha \ll 1; (\lambda_0 \ll \lambda_D)$ corresponds to the "incoherent" or "non-collective", electron component dominated regime, and $\alpha \gg 1; (\lambda_0 \gg \lambda_D)$ is the "coherent" / "collective", ion component dominated regime. Evidently this depends on both the incident wavelength of light (determined by the laser used to probe the medium), as well as the angle of chosen observation with respect to the probing direction, and so from an experimental point of view the choice of these parameters can be made accordingly to access the preferred regime.

The exact form of the spectrum of equation 3.23 can be intricate. However under the assumption of a weakly coupled, collisionless plasma in thermal equilibrium, and in the absence of any strong external magnetic field, the spectrum can be described to good approximation by a form proposed in the 1960 theoretical paper of Salpeter [49]. This describes the two components as

$$S_e(\mathbf{k}_s, \omega) = n_e \sqrt{\frac{m_e}{2\pi {k_s}^2 k_B T_e}}\, \Gamma_\alpha(X) \tag{3.25}$$

and

$$S_i(\mathbf{k}_s, \omega) = Z n_e \left(\frac{\alpha^2}{1+\alpha^2}\right)^2 \sqrt{\frac{m_i}{2\pi {k_s}^2 k_B T_i}}\, \Gamma_\beta(Y), \tag{3.26}$$

where the intermediary functions are defined as

$$\Gamma_\xi(x) = \frac{\exp(-x^2)}{\left[1 + \xi^2\left(1 - f(x)\right)\right]^2 + \pi\xi^4 x^2 \exp(-2x^2)}, \tag{3.27}$$

$$f(x) = 2x \cdot \exp(-x^2) \int_0^x \exp(y^2)\mathrm{d}y, \tag{3.28}$$

$$X = (\omega - \omega_0)\sqrt{\frac{m_e}{2\pi {k_s}^2 k_B T_e}}, \tag{3.29}$$

$$Y = (\omega - \omega_0)\sqrt{\frac{m_i}{2\pi {k_s}^2 k_B T_i}}, \tag{3.30}$$

and

$$\beta = \frac{ZT_e}{T_i}\left(\frac{\alpha^2}{1+\alpha^2}\right). \tag{3.31}$$

These spectrums, whose shapes are shown schematically in Fig. 3.7, can then also be integrated over the frequency range (i.e. by calculating the area underneath each component) to yield the "form factors"

$$S_e(\mathbf{k}_s) = \frac{1}{1+\alpha^2} \tag{3.32}$$

$$S_i(\mathbf{k}_s) = \frac{Z\alpha^4}{(1+\alpha^2)[1+\alpha^2+Z(T_e/T_i)\alpha^2]}. \tag{3.33}$$

Thus when the spectral component S_e is observed the parameters n_e and T_e can be measured by fitting the theoretical spectrum to the measured spectrum. Likewise when the ion component S_i is observed the parameters n_e, T_e, T_i and Z can be measured from

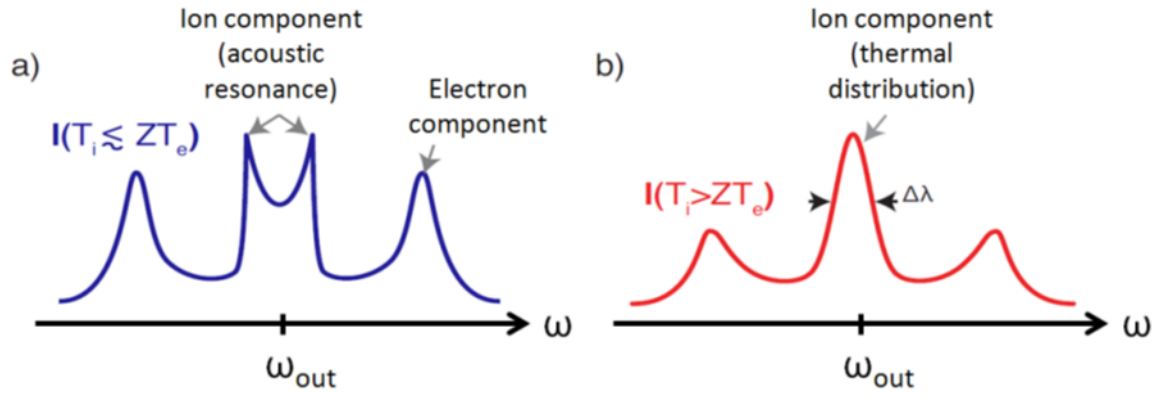


FIG. 3.7 Schematic diagram of the ion and electron components of the theoretical Thomson scattered spectrum, as described by the form given in [49]. The spectral shape is shown for (a) $T_i < ZT_e$, and (b) $T_i < ZT_e$ (in both cases $\alpha > 1$). Note: the spectral forms here are not to scale; the relative contributions of the components can be found from an analysis of the form factors $S_{e/i}(\mathbf{k}_s)$. Figure reproduced from [43].

the fitting. In addition, these spectral functions are always symmetric in their shape and centred upon the Doppler shifted wavelength of the average particle velocity, which can be measured regardless of the regime via equation 3.21.

The Thomson scattering system on MAGPIE utilizes an 8ns-FWHM, 3J, 532nm laser to provide the incident light source. This is narrowly focussed and passed through the experimental chamber with an effectively uniform spot size of $200-300\mu m$ over a range $\pm 13mm$ either side of its focal position; which is a sufficiently large enough range to cover the length of any plasma of interest. The laser beam is passed into the chamber though one of the ports and scattering is observed at multiple positions along the beam. In doing so the direction of the $\mathbf{k}_{out}$ wavevector is defined by the position of the chosen viewing port which due to the symmetry of the chamber is restricted to any angle at $\pm 22.5°$ ($360°/16$ ports) multiples to $\mathbf{k}_{in}$.

The scattered light is collected via a lens which focuses the light from each position into one of an array of optical fibres. The array is 2.34mm in length, and composed of either 7 or 14 fibres (two setups exist, with 200μm and 100μm fibre diameters respectively), which sets the total number of scattering points. The spacing of the scattering positions along $\hat{\mathbf{k}}_{in}$ is then set by the magnification of the collection system (i.e. the positioning and focal length of the lens); where the optical alignment of the system is performed pre-experiment by the use of a vertically suspended, movable ($\phi = 100\mu m$) pin (mounted on a three-way, Cartesian fine-adjustment translation stage) to scatter the beam onto the fibres.

The array of fibres is fed into an imaging spectrograph (ANDOR Shamrock 500) through a vertical diffraction grating of 2400 lines/mm. The signal is recorded using a 4ns time-gated ICCD camera (ANDOR iStar) which displays the position of each fibre vertically across its CCD, with the spectra of those fibres plotted horizontally, owning to the diffraction along this axis from the grating. The overall spectral resolution achieved depends on the diameter of the fibres used, and is 0.25Å for 100μm, or 0.5Å for 200μm*. This results in a "Gaussian blurring" response of the spectrograph to the input spectra, which must be accounted for when fitting each of the fibre signals with its predicted

* It is noted however that despite the resolution improvement accompanying the use of 100μm fibres, there is a simultaneous reduction in the total amount of scattered light collected per fibre, and so this configuration yields a lower signal to dark-field noise which should be considered in situations where a low density plasma is expected; as this might give rise to a weak scattered signal, below the detection threshold.

theoretical form. This is achieved by convolving the theoretical spectra with a Gaussian function, where the convolution procedure is expressed mathematically as

$$S * G(\lambda) = \int_{-\infty}^{\infty} S(\tau) \cdot G(\lambda - \tau)\, d\tau, \tag{3.34}$$

and the appropriate (normalised) Gaussian function has the form

$$G(\lambda) = \frac{1}{\sqrt{2\pi}\Delta\lambda} \cdot \exp\left(-\frac{\lambda^2}{2(\Delta\lambda)^2}\right), \tag{3.35}$$

where $\Delta\lambda$ is the spectral resolution. Thus the convolved spectrum retains the original form factor (due to the normalisation) but has a more smoothed profile due to the weighting introduced at each wavelength-position by the exponential drop-off of the Gaussian function.

The spectrometer is triggered via the backscatter of the laser pulse through the optical delivery system, which is monitored by a photodiode. This triggering mechanism minimises the need for a longer camera exposure due to any timing jitter of the system, since the time of flight of the optical system has a fixed duration, and so guarantees that the spectrometer is always in synchronisation with the scattered signal. Thus the scattered signal is maximised against the noise introduced by self-emission of the plasma, which is time-integrated over the exposure time.

In total apparatus for two Thomson scattering collection systems exists, and so these are generally fielded in unison to simultaneously observe the light scattered from identical positions along the probe beam, but from opposite directions. This allows a 2D velocity vector of the plasma flow to be constructed at each position from measurements of the velocity components along their orthogonal $\mathbf{k}_s$ scattering vectors.

3.4.2 Laser backlit imaging – shadowgraphy

The laser imaging system on MAGPIE uses a pulsed 500mJ, 0.4ns, Nd:YAG laser, which produces beams at the 2nd (532nm, green) and 3rd (355nm, UV) harmonics of the laser crystal. These can each be split into multiple beam-lines to produce backlit images of the experiments. The optical setup for a single shadowgraphy imaging beam-line is shown in Fig. 3.8. A collimated beam passes through the plasma sample and an optical telescope system is used to image a plane through the plasma onto a CCD detector; where the detector used in the setup is a Canon 350D SLR camera.

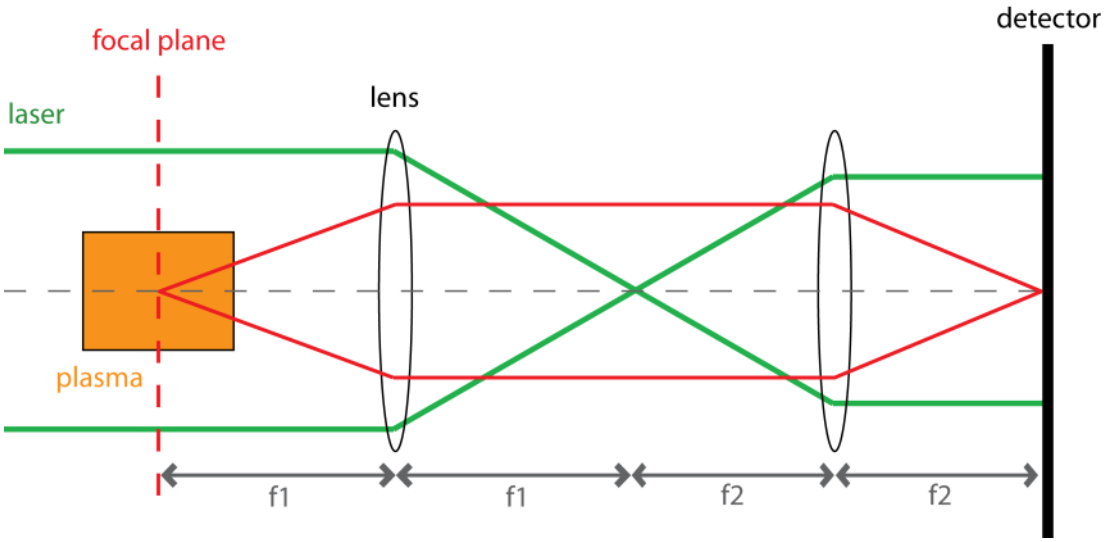


FIG. 3.8 Optical setup for the shadowgraphy (laser-backlit) imaging system.

The intensity of the backlit image is sensitive to the distribution of the second spatial derivative of the refractive index of the plasma normal to the line of sight of the beam, and is a much more complicated dependence than that of the interferometry diagnostic (which is introduced later in section 3.4.3). For this reason shadowgraphy images are generally used as a qualitative snapshot of the plasma dynamics, whereas quantitative measurements of the electron density distribution, which can be shown to be proportional to the plasma's refractive index (section 3.4.3), are reserved for the latter diagnostic.

Fig. 3.9 demonstrates the principle of shadowgraphy imaging. As the laser beam propagates through the plasma along its original path in the z-direction, lateral gradients in the refractive index $\left(\frac{dN}{dy}\right)$ cause the deflection of the light rays. For a single path l through the plasma, the contribution from each minute element dl, with its own refractive index N(l), can be summed to give a total angular deviation

$$\theta_y = \frac{d}{dy}\int N(l)dl. \tag{3.36}$$

If the lateral refractive index gradient of the plasma varies (i.e. $\frac{d^2N}{dy^2} \neq 0$), then the angular perturbation of the light will change with height in the image. For regions where the gradient is decreasing (i.e. the second derivative is negative) the plasma acts as a focusing lens and the image appears brighter. Conversely, an increasing gradient causes the light to diverge, appearing darker in the image.

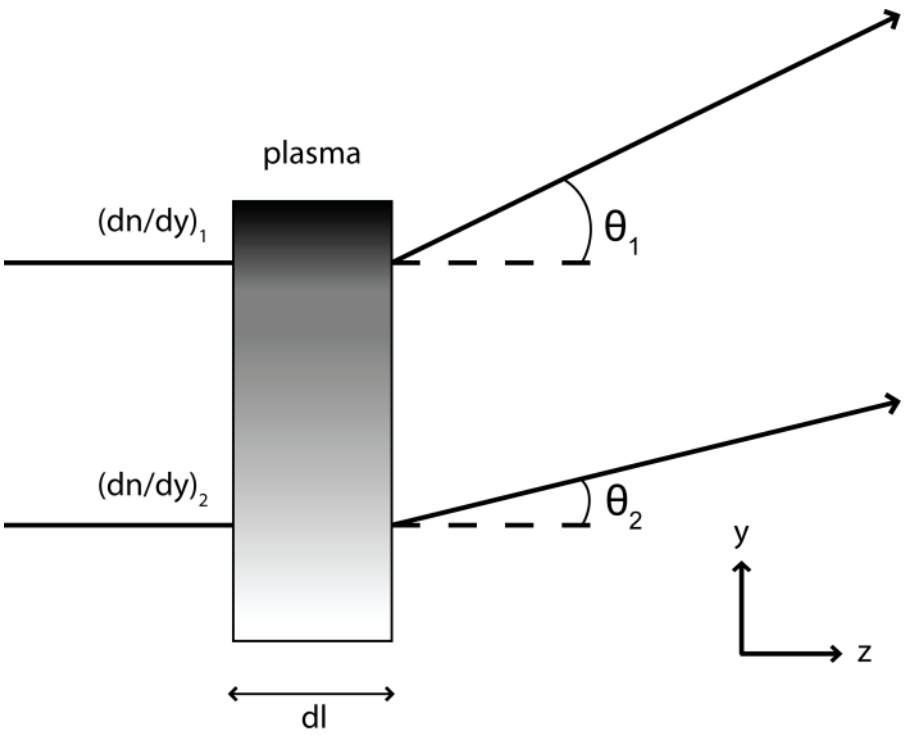


FIG. 3.9 Gradients in the refractive index lateral to the direction of propagation of a light beam cause it to deflect. Changing gradients therefore cause a convergence or divergence of the rays resulting in bright and dark regions in the shadowgraph image.

In principle there is a limit to plasma density through which the laser can probe. The laser light can only propagate through the plasma provided its frequency ω is greater than the plasma frequency

$$\omega_{pe} = \sqrt{\frac{4\pi n_e e^2}{m_e}}, \tag{3.37}$$

which translates to a critical electron density of

$$n_c = \frac{\omega^2 m_e}{4\pi e^2}. \tag{3.38}$$

For 532nm light this equates to $4 \times 10^{21}\,e/cm^3$ and for 355nm $9 \times 10^{21}\,e/cm^3$. Typical plasma densities from the ablation of wire arrays or the ejections from radial foils tend to be in the range $10^{17} - 10^{19}\,e/cm^3$ [6,36,50], with densities approaching that of the critical density only usually obtained in the stagnation column of z pinch implosions or inside the heated wire cores. Thus the density gradients of the plasmas in experiments set a much more relevant limit on the probing capability of the system, as these can deflect the light path beyond the acceptance angle of the imaging optics, causing the plasma to appear opaque.

Another consideration to make with the imaging system is the signal-to-noise ratio owing to the bright, white-light self-emission of the plasma. Whilst the intensity of the laser is much greater than that of the self-emission, the contribution of the latter is enhanced by the time-integrated nature of the measurement. Since the SLR camera cannot be triggered on a nanosecond timescale, the shutter is held open for the duration of the experiment whilst the laser is pulsed at the desired time index. Therefore the ratio is maximised by selecting a high beam intensity; the limit of which is set by the specification of the lenses and the intensity at which the air at the focal point of the optical system begins to undergo breakdown (which can be avoided if necessary using a vacuum tube). Once the intensity of the beam is selected, neutral density (n.d.) filters are used down-line of the experimental chamber to readjust the brightness to an appropriate range for the camera, whilst maintaining this reduced relative noise level.

As an additional precaution an aperture can be added at the focal point of the beam, acting as a spatial filter for light originating from outside the focal plane identified in Fig. 3.8. This method vastly decreases the contribution of stray light however this is at the detriment of further restricting the acceptance angle and hence spatial resolution of the images (noting that for a telescope system angular resolution is inversely proportional to the acceptance / aperture size).

3.4.3 Interferometry

The laser probing system uses a Mach-Zehnder interferometer setup to make measurements of the spatial electron density distribution of the plasmas. This measurement is performed on the basis of a comparison of the interference patterns created between two laser beams, before and during the experiment. One of these beams passes through the experimental chamber whilst the other by-passes it. The addition of plasma in the path of the chamber beam during the experiment changes the optical length of that path, due to the refractive index of the plasma medium. This introduces a phase offset to the chamber beam, and so a change in the position of the interference fringes, on combination with the fixed-phase reference beam, can be used to calculate the (line-integrated) refractive properties of the plasma; and therefore the electron density along that line which can be deduced from its known dependence on those properties.

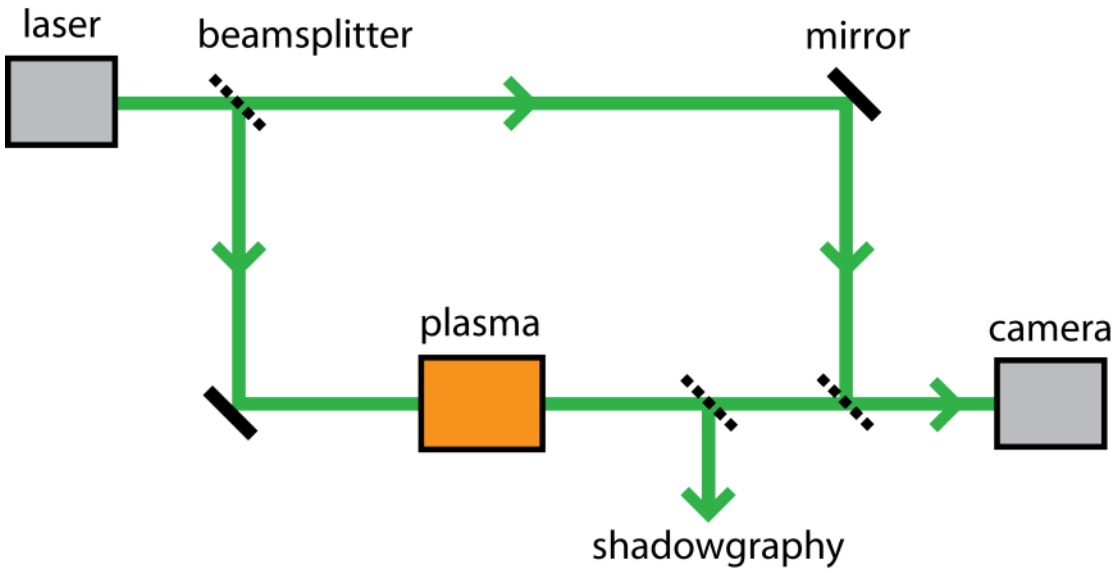


FIG. 3.10 Schematic of the Mach-Zehnder interferometer.

A schematic of the laser interferometer is shown in Fig. 3.10. The laser system provides a collimated beam which is passed through a beamsplitter, dividing the laser into two components. One of these passes through the chamber and the other along a separate leg, with the recombination later made at a second beamsplitter before reaching the detector plane at the imaging camera. As shown in Fig. 3.11, due to a slight angular misalignment of the beams at the second beamsplitter, their wavefronts intersect, causing fringes of alternating constructive and destructive interference across the plane of the image, where each fringe represents a contour of constant phase. For the pre-experiment (also commonly termed a “pre-shot”, “background” or “reference”) image the distribution of these fringes tends to be fairly straightforward, forming approximately evenly spaced bands. With the addition of the sometimes complicated 3D structure of the plasma however, these can become significantly and non-uniformly shifted, and with the superposition of the shadowgraphy effect care has to be taken in correctly identifying the corresponding fringes in order to calculate the correct spatial phase shifts. Consequently it can be helpful to image a large area through the chamber, including some line of sight containing little to no plasma. This allows a “zero phase difference” reference point to be indentified and the fringes in both the pre-shot and experiment image to be counted and matched accordingly.

The spatial distribution of phase difference between the two images can be written in terms of the line-integrated refractive index as

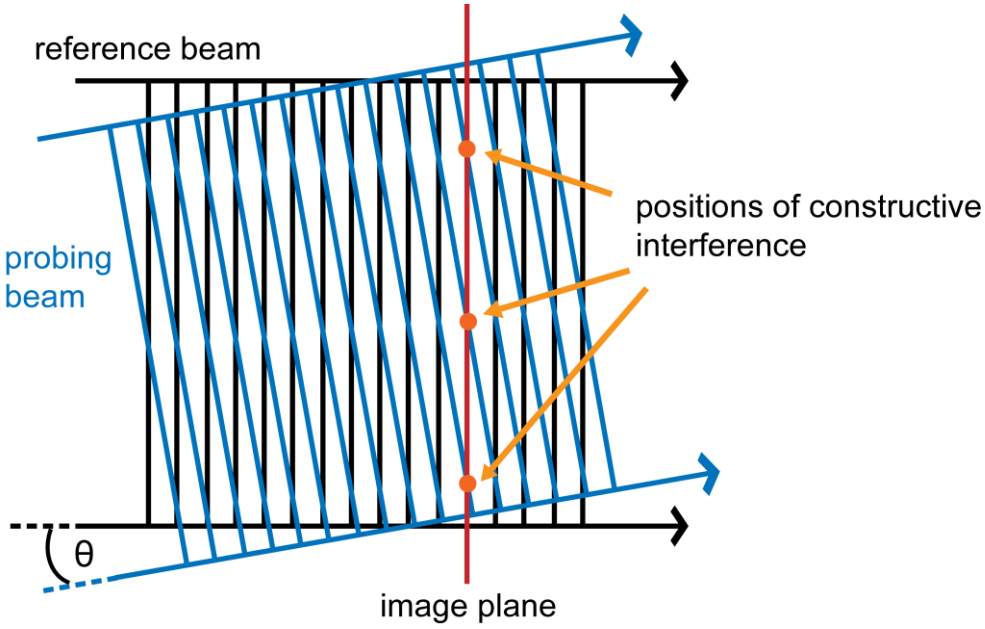


FIG. 3.11 The misalignment of the probing and reference fringes causes their wavefronts to intersect, producing an interference pattern at the detector image plane.

$$\Delta\phi(x,y) = \int (k_{plasma} - k_0)dl = \int (N-1)\frac{\omega}{c}dl. \tag{3.39}$$

This is usually expressed as a multiple of the wave-cycle, such that the number of fringe shifts at each point in the image is

$$N_f = \frac{\Delta\phi}{2\pi}. \tag{3.40}$$

For the refractive index in equation 3.39 it is accurate to assume that the plasmas created on MAGPIE are not strongly magnetised, and so the effects of the B field on the propagation of light can be neglected. The derivation for this case is given in [51] and is included here for completeness.

Taking Maxwell's equations as a starting point, Faraday's and Ampere's laws in their differential forms are

$$\nabla \times \mathbf{E} = -\frac{1}{c}\frac{\partial \mathbf{B}}{\partial t} \tag{3.41}$$

$$\nabla \times \mathbf{B} = \frac{1}{c}\left(4\pi\mathbf{j} + \frac{\partial \mathbf{E}}{\partial t}\right). \tag{3.42}$$

Using the vector triple product relation

$$\mathbf{A} \times (\mathbf{B} \times \mathbf{C}) = (\mathbf{A}\cdot\mathbf{C})\mathbf{B} - (\mathbf{A}\cdot\mathbf{B})\mathbf{C}, \tag{3.43}$$

the curl of equation 3.41 can be written as

$$\nabla^2\mathbf{E} - \nabla(\nabla\cdot\mathbf{E}) = \frac{1}{c}\left(\nabla\times\frac{\partial\mathbf{B}}{\partial t}\right). \tag{3.44}$$

Meanwhile the time derivative of equation 3.42 is

$$\nabla\times\frac{\partial\mathbf{B}}{\partial t} = \frac{1}{c}\left(4\pi\frac{\partial\mathbf{j}}{\partial t} + \frac{\partial^2\mathbf{E}}{\partial t^2}\right). \tag{3.45}$$

If the light waves are assumed to be travelling through the plasma in the z-direction, with a transverse electric field, then they can be described by the form

$$\mathbf{E} = E_x\exp\big(i(kz-\omega t)\big)\hat{\mathbf{x}}, \tag{3.46}$$

and the divergence in the second term of equation 3.44 goes to zero. Therefore using equations 3.44 and 3.45 to then eliminate $\left(\nabla\times\frac{\partial\mathbf{B}}{\partial t}\right)$, and substituting the light wave electric field

$$-k^2\mathbf{E} = \frac{1}{c^2}\left(4\pi\frac{\partial\mathbf{j}}{\partial t} - \omega^2\mathbf{E}\right). \tag{3.47}$$

Making the further assumptions that the current $\mathbf{j}$ is provided entirely by the motion of the electrons, and that the plasma is cold (such that the oscillations of the electrons in the electric field are unimpeded by thermal collisions), this gives

$$\begin{aligned}\mathbf{j} &= -n_e e\mathbf{v_e}\\ \Rightarrow \frac{\partial\mathbf{j}}{\partial t} &= -n_e e\frac{\partial\mathbf{v_e}}{\partial t}\end{aligned} \tag{3.48}$$

and the equation of motion

$$m_e\frac{\partial\mathbf{v_e}}{\partial t} = -e\mathbf{E}. \tag{3.49}$$

Combining these results and cancelling through by the electric field the dispersion relation is found:

$$\omega^2 = \frac{4\pi n_e e^2}{m_e} + c^2k^2 = {\omega_p}^2 + c^2k^2. \tag{3.50}$$

The phase speed of the light wave can be calculated from this as

$$v_\phi = \frac{\omega}{k} = c\left(1-\frac{{\omega_p}^2}{\omega^2}\right)^{-1/2}, \tag{3.51}$$

which it is noted is greater than c in plasmas. The refractive index is then the ratio of the speed of light to this

$$N = \frac{c}{v_\phi} = \left(1 - \frac{{\omega_p}^2}{\omega^2}\right)^{1/2}, \tag{3.52}$$

or in terms of the critical electron density

$$N = \left(1 - \frac{n_e}{n_c}\right)^{1/2}. \tag{3.53}$$

For $n_e \ll n_c$, which was shown in section 3.4.2 to apply for the 532nm and 355nm frequencies, the above expression can be Taylor expanded to give

$$N \approx 1 - \frac{n_e}{2n_c}. \tag{3.54}$$

Thus substituting back into equation 3.40

$$N_f = -\frac{1}{2\lambda n_c}\int n_e dl, \tag{3.55}$$

and so the number of fringe shifts at each point in the interferometry image is proportional to the line-integrated electron density, allowing a measurement of this often important plasma parameter.

Several geometric considerations must be made when designing the interferometer to ensure high quality interference images are produced. Due to the extremely short 0.4ns pulse of the laser it is important that the path lengths of the two legs of the interferometer are comparable in order for the beams to overlap in time as well as space. The pulse time equates to a distance of 12cm, however for a reasonable synchronisation in the intensities, which ensures a good contrast in the interference, the path lengths should be equal to within ~1cm. Further differences in intensity can arise from either a preferential reflection/transmission percentage at the beamsplitter or from significant absorption/scattering by the plasma medium. If after achieving equivalent path lengths the beams are still found to differ significantly, the intensity of either beam can be suitably reduced with the insertion of n.d. filter. In addition to these considerations the beams should be accurately collimated before recombination. The diameters of the two beams do not have to be equal; however the light rays of the beam should be parallel for a horizontal interference pattern to be formed. If this is not achieved then an elliptical pattern arises which can result in a much more complicated identification procedure for the shifted fringes.

As depicted in Fig. 3.10 the probing beam-line can be used simultaneously for both the shadowgraphy and interferometer systems. The only requirements of this are that the components for both camera-lens systems are placed at the correct focal lengths to image the desired plane of the experiment (as specified in Fig. 3.8), as well as the reference beam being correctly n.d.-filtered to compensate for the loss in chamber signal. Additionally each line may incorporate the dual wavelengths of the laser. This can be particularly useful for allowing images to be taken from the same perspective, but at separate times in the evolution; without the need for repeating the experiment. The separate wavelength pulses are emitted from laser cavity in unison, however by using achromatic mirrors to separate and add an additional path length to either channel before the chamber is reached, a relative temporal delay can be introduced. It is noted that from the speed of light in vacuum each 30cm difference in path corresponds to an additional 1ns delay. The separate frequencies each require a unique detector (again due to the open-shutter camera measurement), and this is achieved with further achromatic lenses at the end of the beam-line. Clearly the optical components required for an interferometry-shadowgraphy, dual-wavelength system are numerous, and for this reason it is beneficial to incorporate long focal length lenses into the system. Typically f=1m lenses are used on MAGPIE.

3.4.4 Faraday rotation

The Faraday rotation diagnostic is one of the most recent additions to the MAGPIE diagnostic suite. Its installation has taken place during the lifetime of this thesis and its development is an ongoing work. Data presented in chapter 6 of the thesis represents the first measurements this has yielded.

The diagnostic is introduced here, first with a description of the property of birefringence in plasmas, and how this is related to the magnetic field present in the plasma. When a medium is described as being birefringent, it means that there are unequal indices of refraction for the separate electric field components of light which pass through that medium. In what follows it is shown that light passing through a magnetised plasma has separate indices for left and right handed circular polarisations. Linearly polarised light, which in a vacuum can be thought of as a superposition of two phase-synchronised, equal amplitude, oppositely rotating circularly polarised waves, therefore undergoes a rotation in its plane of polarisation as it passes through a plasma, due to the speed differential introduced to the two components. It is this principle which is made use of, by measuring the rotation angle of a linearly polarised light source after

it is passed through a known thickness of plasma. The magnetic field strength inside the plasma can then be deduced from the theoretical dependence.

The refractive index of a cold plasma can be shown to depend only on the electron density and the magnetic field present [52]. This is expressed in the Appleton-Hartree formula for the refractive index via the dimensionless parameters

$$X = \omega_{pe}{}^2/\omega^2 \tag{3.56}$$

and

$$Y = \omega_{ce}/\omega, \tag{3.57}$$

where ω is the wave-frequency of the EM-radiation. The full formula for waves propagating with a $\mathbf{k}$ vector at an angle of θ to the magnetic field is

$$N^2 = 1 - \frac{X(1-X)}{1 - X - \frac{Y^2}{2}\sin^2\theta \pm \left[\left(\frac{Y^2}{2}\sin^2\theta\right)^2 + (1-X)^2Y^2\cos^2\theta\right]^{1/2}}. \tag{3.58}$$

In general $Y \ll 1$; which is why for most plasmas density measurements can be made using the interferometry techniques described in section 3.4.3, without having to worry about the small perturbation to the refractive index that the magnetic field causes. It is therefore reasonable to approximate the Appleton-Hartree formula to first order terms in Y, giving

$$N_{\pm}{}^2 = 1 - X \pm XY\cos\theta. \tag{3.59}$$

This shows that except for the special case $\theta \approx \pi/2$ (in which case the next order term in Y should be considered) the largest correction to the refractive index is dependent only on the component of the field parallel to $\mathbf{k}$. The presence of the $\pm$ sign here indicates that there are two dispersion relation solutions, and hence there are two characteristic modes which can travel through the plasma at differing speeds. The '+' solution here is referred to as the "ordinary" mode and the '−' solution the "extraordinary" mode. These modes are rotating waves of opposite helicity, whose superposition combines to give the full $\mathbf{E}$ vector of the overall EM-wave, which is itself circularly polarised. This is demonstrated as follows. If a coordinate system is defined such that

$$\mathbf{k} = k\hat{\mathbf{z}}, \tag{3.60}$$

$$\mathbf{B} = B\cos\theta\hat{\mathbf{z}} \tag{3.61}$$

(since only the parallel component contributes) and

$$\mathbf{E} = E_x\hat{\mathbf{x}} + E_y\hat{\mathbf{y}}, \tag{3.62}$$

then solving the wave equation [51] gives the electric components

$$(\omega^2 - c^2k^2 - A)E_x + iA\frac{\omega_{ce}}{\omega}E_y = 0 \tag{3.63}$$

$$(\omega^2 - c^2k^2 - A)E_y - iA\frac{\omega_{ce}}{\omega}E_x = 0, \tag{3.64}$$

where

$$A = \frac{{\omega_{pe}}^2}{1 - ({\omega_{ce}}^2/\omega)}. \tag{3.65}$$

Thus, dividing these reveals

$$\frac{E_x}{E_y} = \pm i, \tag{3.66}$$

which indeed defines a circular polarisation. Consequently, if a linearly polarized light source enters a plasma in the presence of a magnetic field its plane of polarisation will begin to rotate due to the growing phase difference between the modes. This effect is known as Faraday rotation. The relative polarization of the beam at any position along the propagation is given using the average refractive index, such that

$$\alpha = (N_+ - N_-)\frac{\omega}{2c}z = \left[\frac{XY\cos\theta}{(1-X)^{1/2}}\right]\frac{\omega}{2c}z, \tag{3.67}$$

which shows that the Faraday rotation is directly proportional to both the distance travelled and the parallel magnetic field component (recalling $Y \propto \omega_{ce} = eB/m_ec$). If in addition $X \ll 1$, which is a reasonable assumption under the conditions of interest for this thesis $(\omega_{pe}\sim10^{13}\text{Hz}, \omega\sim10^{15}\text{Hz})$, then

$$\alpha \approx \frac{{\omega_{pe}}^2\omega_{ce}\cos\theta}{2\omega^2 c}z, \tag{3.68}$$

and so the rotation is also proportional to the electron density (since $n_e\sim{\omega_{pe}}^2$). Taking into account non-uniformities in both the plasma density and the field through the use of an integral, this gives

$$\alpha = \frac{2\pi e^3}{\omega^2 c^2 {m_e}^2} \int n_e \mathbf{B} \cdot d\mathbf{l}. \tag{3.69}$$

Thus a measurement of the Faraday rotation, together with an electron density measurement from interferometry, and an assumption of the field geometry, yields a value of the average field strength in the plasma. For values lying in the appropriate ranges for the experiments of this thesis (a magnetic field of $1-10$T, with $n_e \sim 3-6\times 10^{17}\,e/cm^3$, and a 10mm probing thickness parallel to the field) this formula predicts rotation in the range $\alpha \sim 0.2-3°$.

It is noted here that in the special case of $\mathbf{B}\perp\mathbf{k}$, which was omitted in the above, the modes allowed by the plasma are a planar-polarisation ordinary mode, and an elliptically polarised extraordinary mode; the superposition of which is an elliptically polarised wave, resulting in a more complex B dependence. Since the field direction in the reverse shock experiments can be reasonably assumed to be in the poloidal direction of the wire array – parallel to the obstacle surface (see chapters $4-6$), the probing direction can be chosen in this direction such that it is away from perpendicular, so that only the parallel component contributes to the rotation angle.

Moving now to a discussion of the practical setup of the Faraday rotation diagnostic, the system on MAGPIE utilises a newly installed 1053nm, 5J (currently operating at 3J), 1ns pulse length laser to provide a linearly polarised light source, which is passed through the experimental chamber in a collimated beam. Images for this system are recorded on an ATIK 383l Monochrome camera with a linear polarising filter, placed within the imaging path at a known angle to the beam. For a laser of initial intensity I_0 passing through the filter at an angle of θ to its polarisation axis, the intensity of transmission is

$$I = I_0 \cos^2\theta. \tag{3.70}$$

This enables the Faraday rotation angle to be measured at each point on the image by comparing the intensity of the signal prior to and during the experiment.

As demonstrated in the previous section, the expected rotation angle for the appropriate experimental conditions is small ($\alpha \leq 3°$). It is therefore tempting to choose $\theta = \pi/4$ for the filter, so that the intensity is most sensitive to the angular displacement. However, in order to make full use of the dynamic range of the camera (which can be normalised to the brightest level of the expected transmission using sufficient levels of n.d. filter) an angle close to extinction should be used. Rather than setting full extinction, a small offset φ is chosen to this, such that $\theta = \pi/2 \pm \varphi$; giving an asymmetric response to the

intensity function which enables the opposing rotation directions (corresponding to parallel and anti-parallel magnetic field components) to be distinguished. For these experiments an offset of $\varphi = 4°$ was selected as this was deemed to be above the upper limited for the expected Faraday rotation; meaning that the opposing field directions are characterised by either a darkening or lightening of the beam, since they either take the beam closer to or further from the extinction point.

A dual channel system is used for the diagnostic with identical imaging systems but inverted polarising filters in each. This allows the origin of any brightness changes in the images to be confirmed as a Faraday rotation only if a brightening on one channel coincides with a darkening (of comparable angular displacement) in the other. If the total extraneous losses are summarised by a single term c, then the intensity of the two channels is given by

$$I_{C1}(x,y) = I_0(x,y)\cos^2\left(\frac{\pi}{2} + \phi + \alpha\right) - c \tag{3.71}$$

$$I_{C2}(x,y) = I_0(x,y)\cos^2\left(\frac{\pi}{2} - \phi + \alpha\right) - c. \tag{3.72}$$

Thus by combining the two channels any changes to the beam intensity resulting from effects such as absorption or losses of the beam due to density gradients can be subtracted from the calculation. Normalising the images relative to the background images

$$I_{B1}(x,y) = I_0(x,y)\cos^2\left(\frac{\pi}{2} + \phi\right) \tag{3.73}$$

$$I_{B2}(x,y) = I_0(x,y)\cos^2\left(\frac{\pi}{2} - \phi\right) \tag{3.74}$$

also removes any spatial dependence on the original beam profile. Hence

$$\frac{I_{C1}}{I_{B1}} - \frac{I_{C2}}{I_{B2}} = \frac{\cos^2\left(\frac{\pi}{2} + \phi + \alpha\right) - {}^{c}/_{I_0}}{\cos^2\left(\frac{\pi}{2} + \phi\right)} - \frac{\cos^2\left(\frac{\pi}{2} - \phi + \alpha\right) - {}^{c}/_{I_0}}{\cos^2\left(\frac{\pi}{2} - \phi\right)}, \tag{3.75}$$

which due to the symmetry of the $\cos^2$ function in the denominators becomes

$$\frac{I_{C1}}{I_{B1}} - \frac{I_{C2}}{I_{B2}} = \frac{\cos^2\left(\frac{\pi}{2} + \phi + \alpha\right) - \cos^2\left(\frac{\pi}{2} - \phi + \alpha\right)}{\cos^2\left(\frac{\pi}{2} + \phi\right)} \equiv 2\cot\phi \cdot \sin 2\alpha. \tag{3.76}$$

The Faraday rotation angle can therefore be calculated from the difference of the normalised images, giving

$$\alpha = \frac{1}{2}\sin^{-1}\left(\frac{1}{2}\left(\frac{I_{C1}}{I_{B1}} - \frac{I_{C2}}{I_{B2}}\right)\tan\phi\right). \tag{3.77}$$

A third channel is also used in the same system as an interferometer to provide line integrated electron density data, and so from α and an average value in n_e, as desired an average for $B_{\parallel}$ can be found.

3.5 XUV and optical self-emission imaging

Self-emission imaging provides a useful means for tracking the dynamics of plasma experiments. Since these systems intrinsically do not rely upon pulsed laser backlighting, they provide a much better means for capturing multiple time-separated images throughout the course of a single experiment. The use of time-gated micro-channel plate detectors (MCPs), triggered by an applied voltage signal, means that the exposure time and interval of these multi-frame systems is easily programmable. Thus the evolution of experiments can be efficiently established, and the timing parameters of the laser diagnostics appropriately chosen to make quantitative measurements of the plasma properties at times of interest. The MAGPIE suite utilizes self-emission cameras in both the XUV (extreme ultra-violet) and optical spectrums and these systems are described in the following sections.

3.5.1 XUV self-emission pinhole imaging

The XUV self-emission camera uses a simple pinhole setup for its imaging system. The radiation emitted from the plasma passes through a pinhole aperture of diameter D, placed at a distance p from the load. This creates an inverted 2D image on the far-side of the pinhole, where the distance q of the detector image plane from the pinhole can be freely chosen to set the magnification

$$M = \frac{q}{p} \tag{3.78}$$

of the system. The resolution limit of the system is set by both geometrical and diffraction considerations. The geometrical limit is illustrated in Fig. 3.12 and arises due to the light cone reaching the detector plane from a single point in the plasma. The light cones from two point-source origins, separated by a distance x, overlap on the detector if the relation

$$\frac{x}{p+q} < \frac{D}{q} \tag{3.79}$$

holds. Hence the geometrical resolution limit is given by

$$\delta_{geo} = D\left(\frac{p}{q} + 1\right) = D\left(\frac{1}{M} + 1\right). \tag{3.80}$$

The diffraction limit on the other hand is set by the Rayleigh Criterion

$$\delta_{diff} = 1.22\frac{\lambda p}{D}, \tag{3.81}$$

which describes the overlap of the Airy disks from separated point sources. The limiting resolution of the pinhole camera is therefore set by the combination of the physical parameters q, p and D, and the minimum energy (maximum wavelength) of the radiation. Typical distances used in the setup are $p = 0.5m$, $q = 0.3m$ $(M = 0.6)$ and $D = 100\mu m$; with the threshold energy of the detector at ~7eV (λ~170nm) [53]. This places the above resolution limits at $\delta_{geo} = 270\mu m$ and $\delta_{diff} = 1mm$, and so at the lower end of the energy spectrum the image is diffraction limited. For energies $> 30eV$ ($\lambda < 40nm$) however, the geometrical resolution becomes the limiting factor. In general the emission from the plasma is strong across a significant breath of the XUV spectrum and the entirety of this radiation is allowed to reach the detector plane. It is possible however to select certain bands of the energy spectrum by placing absorption filters over the pinhole. This is particularly useful for identifying regions of specific temperature, for example hot spots in the plasmas where there is a local increase in the emission of hard radiation. The system possesses a cut-off temperature / energy of $> 100eV$ however,

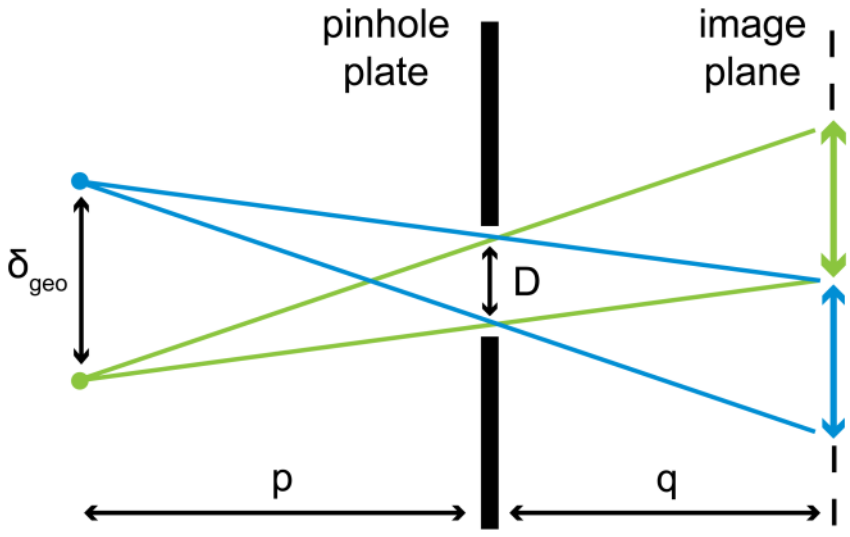


FIG. 3.12 The resolution of the pinhole camera is geometrically limited by the light cone produced from a single point source which can pass through the aperture. The minimum resolvable distance is the separation at which the light cones from different origins overlap.

since the MCP detector is not sensitive at wavelengths shorter than ~10nm. It is noted that a pinhole system can be used to image more energetic photons than this by using a photographic x-ray film rather than a MCP detector [54]; although this then provides a single image, time-integrated over the entire duration of the experiment. For this reason only imaging with MCPs was used for the work presented in this thesis. In addition to the resolution limits described here, the length parameters of the pinhole system also contribute to the intensity of radiation reaching the detector. This scales as $\sim D^2/(p+q)^2$ and is in general chosen empirically, with the aforementioned scales providing a reasonable signal-to-noise ratio at the detector.

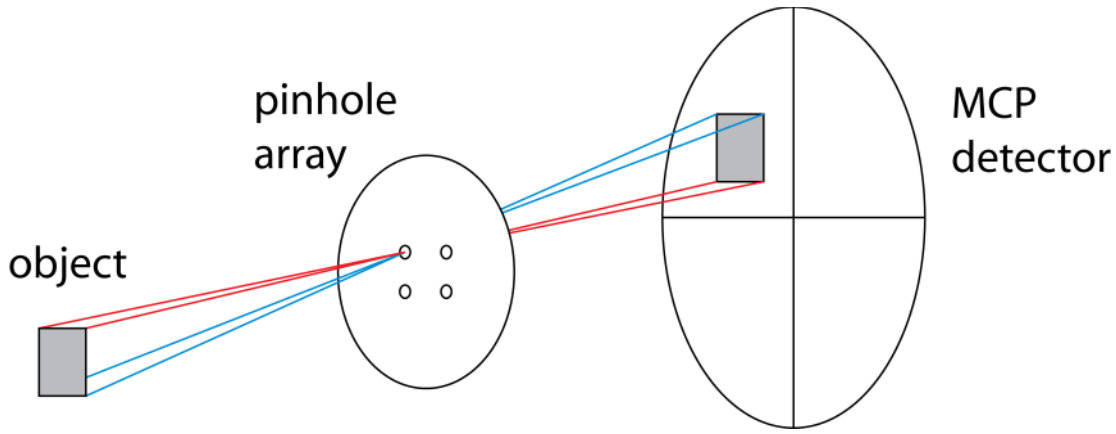


FIG. 3.13 The pinhole camera images onto four independently time-gated quadrants of an MCP detector.

As mentioned in the introduction, the self-emission diagnostics provide a means of recording the time evolution of the experiments. The XUV camera setup achieves multiple image frames by utilizing a rectangular array of pinholes with an accompanying MCP for each (Fig. 3.13). The MCPs are triggered by a single 6kV electrical pulse, which is sent to each detector separately through cables of differing lengths. This sets the inter-frame timing Δt due to the relative signal propagation time of the cables, which under the present inventory can be set at either 10 or 30ns. There is however some loss of sensitivity for the later frames in the sequence due to the attenuation of the signal along the length of the cable. For the URM43 coax used this is specified at a loss of ~20% gating voltage between the first and last frames at a 30ns inter-frame [53]. The exposure of each frame is determined by the width of the triggering pulse which is equal to ~3ns.

The MCP detectors in this system consist of a gold photocathode backed with a phosphor screen, with an intermediate array of microscopic (10μm diameter, 20μm spacing) photo-multiplying tubes (PMTs). The emission of electrons at the cathode due to incident photons is amplified by the PMTs, proportional to the applied trigger voltage. This then leads to the illumination of the phosphor screen which is captured using a high resolution digital SLR camera (Canon 350D, as per the laser diagnostic system). The MCP has a resolution of 70μm [53], and so suitably outperforms the geometric and diffraction resolution limits, preventing any associated reduction in image quality.

3.5.2 Optical self-emission fast-frame imaging

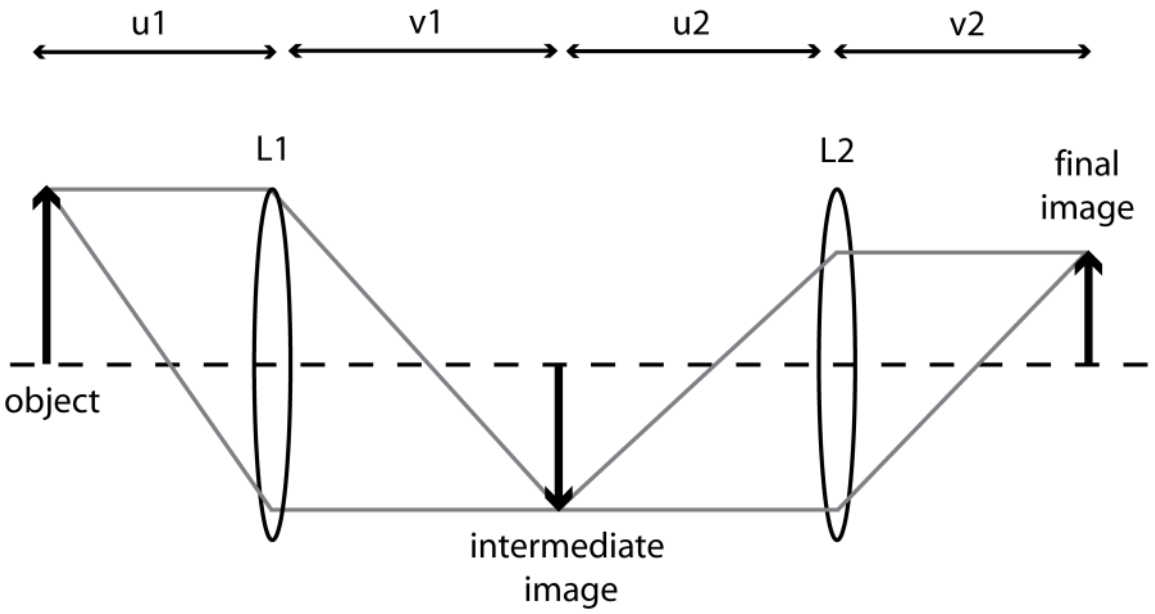


FIG. 3.14 Double image (telescope) setup for the optical emission camera; the object (u) and image (v) distances of the two lenses L1 and L2 are marked.

The diagnostic for optical self-emission imaging uses a more conventional lens system, by creating focussed images of a plane through the plasma using a telescope configuration. The optical components of this are illustrated in Fig. 3.14. The lenses are positioned such that the image of the first lens forms the object of the second, with the object and image positions for each individual lens described by the relation

$$\frac{1}{f} = \frac{1}{u} + \frac{1}{v}, \tag{3.82}$$

where f is the focal length of the lens, u and v are the object and image distances respectively, and $u > f$. The magnification of each lens component is then the ratio of

these distances, as in equation 3.78, with the overall magnification of the telescope then given by their product

$$M = M_1 \cdot M_2. \tag{3.83}$$

Since the plasmas produce a white light source, emitting brightly across the frequency range, the system employs achromatic doublet lenses. These are each composed of a pair of conjoined lenses of differing refractive index, which act to minimise the chromatic aberration. The achromatic lenses used specify the difference in the focal positions of red and blue components of the spectrum to < 1mm per lens [55].

The diffraction related resolution limit of the optical self-emission camera is much lower than for the XUV system due to the much larger aperture size (2"~5cm) of the collecting lens. For typical distances of the first lens ($\sim 1-2$mm) this places $\delta_{diff} \sim 10-20\mu$m. Consequently the optical system is generally sensor resolution limited. The camera images onto CCD detectors of 649×558px (W × H), of a physical size 12×10mm, giving a pixel size of ~18μm. The sensor resolution is then found by dividing this pixel size by the magnification of the setup, which for the experiments of this thesis was in the range $0.3-0.6$; and hence gives $\delta_{sensor} \sim 30-60\mu$m.

The optical camera contains 12 CCDs in total which are triggered independently, in a sequence determined by the user through a programmable pulse shape generated by computer software; thus providing a greater number of snapshots of the plasma behaviour than with the XUV camera, and with a greater level of flexibility in their timing. The minimum exposure time however for each image frame in the sequence is 5ns, and so this introduces an additional resolution limit on images due to the motion of the plasma. At typical MAGPIE wire ablation speeds (10^7 cm/s) this can correspond to as great as 500μm of displacement and therefore is likely the greatest source of error in the spatial measurements produced by this diagnostic.

3.6 Local magnetic field probes

Miniature inductive probes allow a measure of the local magnetic field in experiments. This is particularly useful for determining the amount of magnetic flux, which after originating from the MAGPIE driving current, is advected by flow of plasma and is therefore made present in the subsequent plasma interactions. The probes consist of a semi-rigid coaxial cable, where at the end the inner conductor has been exposed and turned to form a single loop of area A, and then connected to form a short circuit with

the outer conductor. In the presence of a changing magnetic flux, where the spatial gradient of the field is sufficiently small that the field can be represented by a single value across the area of the loop, the associated voltage measured by the probe is

$$V = \mathbf{A} \cdot \frac{d\mathbf{B}}{dt}. \tag{3.84}$$

The outer surface of the probe is shielded to suppress any electrostatic pickup by a thin layer of conducting (silver) paint; however it is likely that some level will always be present. For this reason the probes are always used in pairs; placed in overlapping positions but with connections to their respective oscilloscope channels made in opposite polarity. Thus the probes measure inverse magnetic signals, but any electrostatic noise offset φ is identically superimposed. Hence

$$\begin{aligned} V_{probe1} &= \varphi + \mathbf{A} \cdot \frac{d\mathbf{B}}{dt} \\ V_{probe2} &= \varphi - \mathbf{A} \cdot \frac{d\mathbf{B}}{dt} \\ V_{probe1} - V_{probe2} &= 2\mathbf{A} \cdot \frac{d\mathbf{B}}{dt}, \end{aligned} \tag{3.85}$$

and the magnetic field signal B(t) can be obtained by integrating and rearranging the difference in the two probe signals.

Chapter 4:

Characterisation of the plasma flow from an inverse wire array z pinch

4.1 Overview

The inverse wire array provides an ideal candidate for producing a source of steady plasma flow suitable for shock experiments. Like a standard (imploding) wire array z pinch [56,57], the inverse array is formed of a cylindrical arrangement of fine metallic wires; additionally however it possesses a central cathode rod which runs along the axis of the array. This cathode acts as a return path for the current applied to the array, and its opposing current direction inverts the direction of the global $\mathbf{J} \times \mathbf{B}$ force at the position of the wires, causing an outward (exploding) flow of the ablated plasma. This geometry has the advantage that it creates a plasma which is open for diagnostic access, whilst maintaining the same predictable and calculable flow rate as described by the simple model of the rocket equation [24].

Inverse wire array z pinches were used as a source of 1D, magnetised plasma flow for use in the reverse shock experiments of this thesis. This chapter describes the wire array setup and steps that were taken in its design to ensure that a relatively planar flow was provided by the array to its external region; so that this flow could later be used in combination with a planar obstacle to produce a 1D perpendicular reverse shock (chapters 5 & 6). Data here is presented on the characterisation of the flow parameters, including the spatial and temporal electron density profile of the ablated plasma, as well as the first ever direct measurements of plasma flow velocity and temperature (ZT_e) from inverse wire arrays using Thomson scattering. Local magnetic field probe

measurements also demonstrate the advection of magnetic field in the plasma from these arrays. The properties of the flow are summarised at the end of the chapter, and several dimensionless flow parameters are calculated which categorise the physical regime(s) most relevant at these plasma conditions.

4.2 The inverse wire array setup

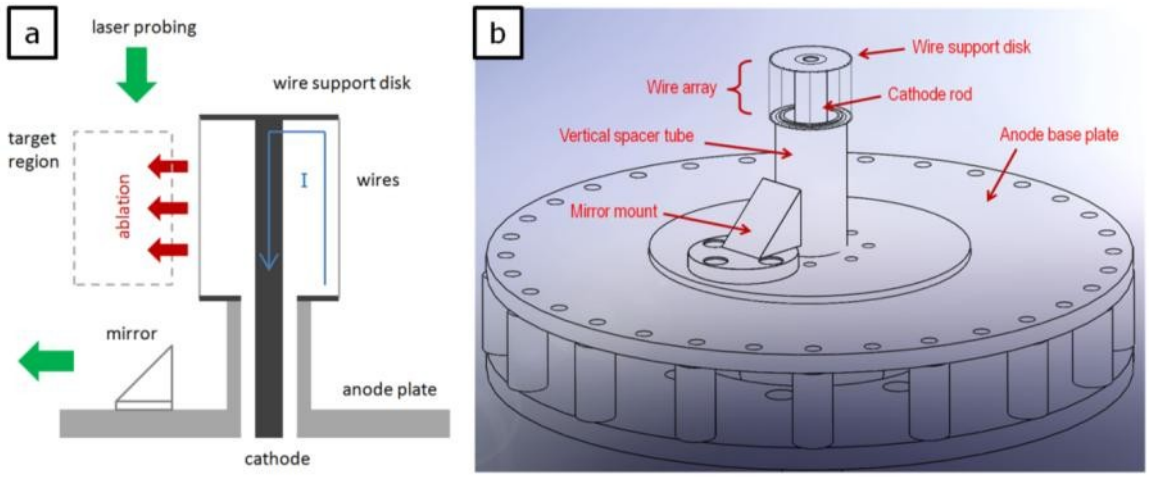


FIG. 4.1 (a) A schematic diagram of the inverse wire array with (end-on) laser probing of the shock-target interaction region. The current path is indicated. (b) A 3D design drawing of the array hardware.

The array design used in this work is similar to the setup described in [6,7] and is illustrated schematically in Fig. 4.1a, along with a scale, 3D drawing of the hardware assembly in Fig. 4.1b. The array consists of 16, 40μm-diameter, aluminium wires, which are 15mm in length, and positioned concentrically about the array axis on a diameter of 20mm. There is a central cathode with an 8mm diameter which runs along the axis and is connected to the wires at the top of the array via a thin (100μm) conducting disk. At the bottom of the wire array there is a second disk which connects the wires to the anode base plate via a thin-walled vertical tube. The purpose of the tube is to vertically position the array above the base plate such that there is enough room to place a mirror beneath the plasma flow, as illustrated in the two diagrams, allowing end-on (z-direction in cylindrical coordinates) laser probing of the target-interaction region. The array wires are located by vertically aligned grooves in the two disks and provide the connecting current path from the anode base plate to the axial cathode.

In the inverse wire array geometry the $\mathbf{J} \times \mathbf{B}$ force of the applied current acts only in the horizontal $(r - \theta)$ plane, such that the ablation of plasma from the resistively heated

wires is directed radially outward from the array in this plane. For the purpose of shock experiments a uniform and planar flow is desired in order that reverse shocks can be studied in as 1D and simplistic environment as possible. The use of an ablation stream from a single wire of the array was deemed unsuitable for these criteria, as a single stream possesses a transversely varying density profile [25], which would require the use of Abel-inversion techniques [58] to unfold the 2D structure of the stream from the integrated density measurements of laser probing in side-on directions. It was therefore decided that a collective flow from multiple wire contributions, as demonstrated for standard wire arrays [25], would be most appropriate for flow uniformity.

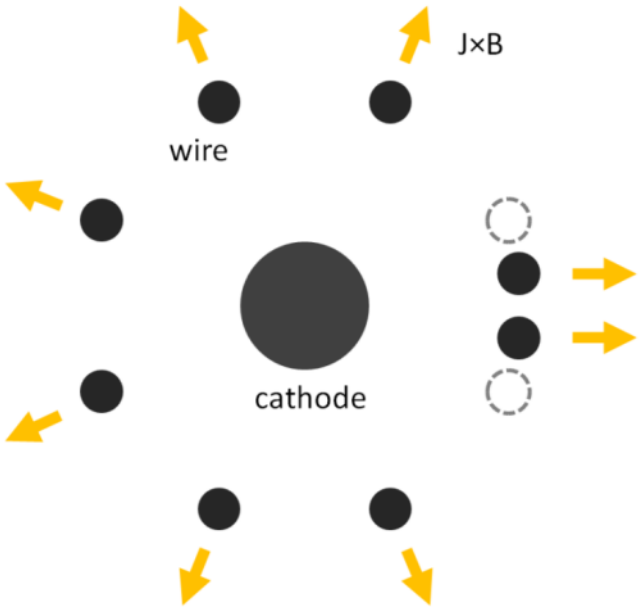


FIG. 4.2 By perturbing the wire positions of an array away from their standard, evenly-spaced configuration, the mutual magnetic attraction of a pair of wires can be used to manipulate the flow direction. At the correct angular displacement parallel streams can be achieved.

A standard cylindrical, evenly-spaced wire arrangement was also rejected on the requirement of a 1D flow. In such an array the plasma flow is purely radial, possessing a curved wave front at the collisional interface with an external shock target; causing higher dimensional structure in the resulting shocks. A perturbed arrangement of paired wires was therefore used (as illustrated in Fig. 4.2), whereby the increased proximity of adjacent wires in each pair increases the pair's mutual magnetic attraction, producing a parallel flow of plasma along the direction of their radial centreline. The correct angular positioning of wires for this was estimated by calculating the global field at the wire positions and ensuring that the component of field along the perpendicular

bisector of the pair tends to zero, such that the $\mathbf{J} \times \mathbf{B}$ force here acts only in the intended flow direction (Fig. 4.3). All wires in the array were grouped in pairs in this way, with the flow from a single pair providing the plasma stream for an individual flow-target interaction. This array geometry not only guarantees an equal and therefore predictable current division amongst the wires, but also creates several identical flow regions around the array. This is a benefit for shock experiments since multiple shock interaction regions can be created within a single experiment – both maximising the number of diagnostic measurements that can be made, and allowing simultaneous comparison of plasma conditions with and without a shock target present.

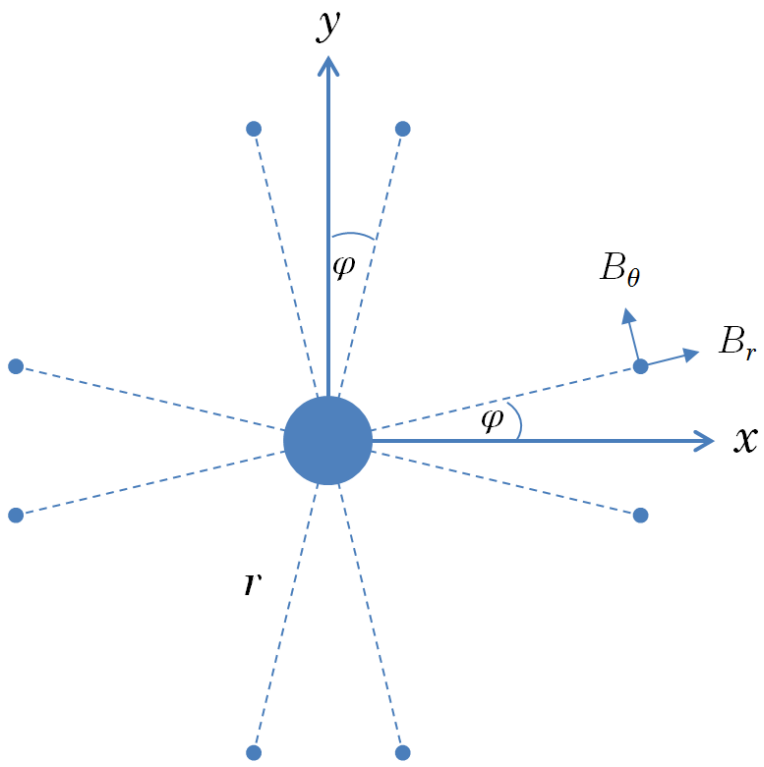


FIG. 4.3 The global field components acting at the position of a single wire in an 8 wire inverse array. All wires are at a distance r from the central cathode, with a half opening angle of φ for the pairs. The axes x and y are introduced for convenience to calculate the angle necessary for the flow from the pairs to be directed along these directions.

In the evaluation of the components of magnetic field acting at the wire positions, as a function of the angular separation of the wire pairs, an assumption was made that the current passing through the wires could be treated as being localised at their point positions. Fig. 4.3 illustrates the components of magnetic field acting on a single wire in the example of an 8 wire array. For convenience the radial and azimuthal components

B_r and B_θ of the field are resolved in terms of more appropriate components along the x- and y-directions as shown. The half-angle φ of the pairs is chosen such that, in the case of the left and right pairs in the diagram, the component $B_x = 0$ at the wire positions. Likewise $B_y = 0$ at the positions of the wires in the top and bottom pairs. This condition can be expressed as

$$-B_\theta \cos\varphi = B_r \sin\varphi. \tag{4.1}$$

The field components at the position of the α^{th} wire of an (infinite length) cylindrical array of wires (without a cathode) are given in [59] as

$$B_\theta = (N-1)\frac{\mu_0 I}{4\pi N R} \tag{4.2}$$

and

$$B_r = \frac{\mu_0 I}{4\pi N R}\sum_{\beta=1,\beta\neq\alpha}^{N}\frac{\sin(\theta_\alpha - \theta_\beta)}{1-\cos(\theta_\alpha - \theta_\beta)}, \tag{4.3}$$

where all wires are at a radius R from the axis, N is the total number of wires and $\theta_{\alpha/\beta}$ are the angular positions of the wires. When the field contribution of the central cathode of the inverse array is included in the setup the angular component of the field is reversed, giving

$$B_\theta = (1-N)\frac{\mu_0 I}{4\pi N R}. \tag{4.4}$$

The radial component however remains unaffected by this addition, since the purely poloidal field of the cathode is orthogonal to this direction.

An array with $N = 16$ was used for the experiments, giving 8 pairs. This wire number was chosen to fit with the symmetry and diagnostic arrangement of the MAGPIE chamber, and does not change the condition of equation 4.1. When substituting the appropriate values for B_θ, B_r and N into equation 4.1 it is found that

$$17\tan\varphi = \sum_{i=0}^{7}\frac{\sin(2\varphi - {}^{\pi}/_{4}\,i)}{1-\cos(2\varphi - {}^{\pi}/_{4}\,i)}, \tag{4.5}$$

which solved numerically predicts a half angle $\varphi \sim 9°$ to produce parallel ablation from the pairs of adjacent wires (compared to a uniformly spaced wire array which has $\varphi = 11.25°$). Experimentally however this was found to be an overestimate of the angular perturbation required, due to the assumption that the wires have definite and

point-like positions. On application of MAGPIE current it has been observed that the wires heat to form a dense core surrounded by extended coronal plasma and it is from this corona that the ablated plasma is ejected [24]. Consequently a half angle of $\varphi = 10°$ was used for the shock experiments, as this was found to give a sufficiently parallel flow into the external region.

Aluminium was chosen as the wire material in these arrays due to its ease of use and well studied behaviour as a z pinch subject [24,25,57,60,61]. Its low mass places it in an ideal density range for the laser probing diagnostics and its low proton number minimises the effects of radiative cooling, which increase through line emission further up the periodic table. This enables the structure of shocks to be studied in the absence of complications arising from the radiative cooling (see chapter 2, section 2.2), although it is noted that this is an interesting and non-trivial dependence on shock structure and could be investigated in future work via the comparison of different wire materials.

The thickness (40μm) of the aluminium wires was selected such that the array would be 'over-massed' in comparison with a typical pinch experiment [50]. In other words the ablation phase (which lasts until $dm/m_0 \sim 50\%$ of the total initial wire mass has been ablated) was extended to be beyond the typical (~300ns) timescale of the experiments; thus preventing the onset of wire breakage and the subsequent explosion phase [6,24] which would provide an unwanted turbulence in the plasma flow. Whilst for reasons of simplicity a smooth flow was desired for the shock experiments of this thesis, it remains an interesting possibility for future studies to utilise the explosion phase, as this could produce more structured and clumplike interactions which may exhibit diverse astrophysical applications.

The following section describes the overall structure of the unobstructed plasma flow from a single wire pair in the inverse wire array. These measurements are presented for comparison to the structures and flow properties presented in the following chapter when an obstacle is introduced.

4.3 Structure of the plasma flow from a pair of ablating wires

Fig 4.4 shows a timeline of the optical emission from the plasma flow generated by a pair of ablating wires in the inverse array. The flow is viewed end-on (along the z-axis) with the array at the top edge of the images and the flow directed radially outwards (downwards in the images). In the first frame, shortly after the start of the applied

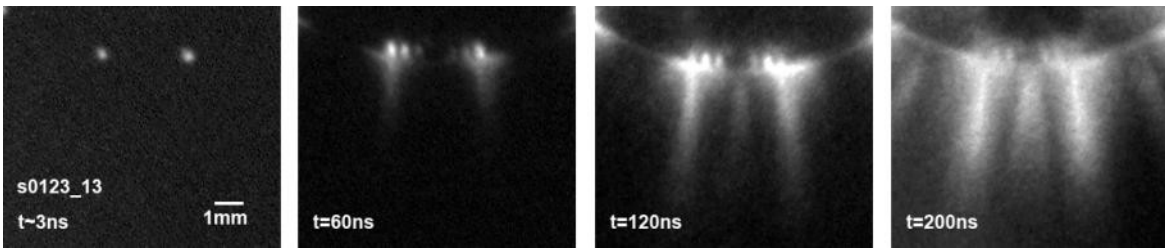


FIG. 4.4 An optical emission timeline showing the evolution of plasma flow from a single pair of ablating wires in the inverse array. Frame times are given relative to the start of current.

current, the wires are observed to emit due to their resistive heating. Soon after, in the second of these images, a coronal plasma is formed around the wire positions and accelerated due to the $\mathbf{J} \times \mathbf{B}$ force to form parallel streams propagating outwards. Later in time, from approximately $t = 100\text{ns}$, emission emerges from a central region inbetween the streams (third image). This region appears to have a triangular cross-section, and is bound by oblique shock fronts on either side, which are formed by the collision of material from the adjacent ablation streams. Similar oblique shocks have been seen in the interaction of aluminium ablation streams in standard wire arrays [25], where this collective downstream flow has been found to exhibit a more uniform density distribution than the individual wire ablation streams. The oblique shocks are a consistent and stable feature in the flow structure and following their formation are observed to survive in dynamic equilibrium for the duration of the experimental timescale; during which the intensity of self-emission from both the coronal and shocked plasma regions increases in time (forth image) due to the increasing mass injection as the peak current amplitude is approached (recalling that $dm/dt \propto I^2$; I_{max} at $t \approx 250\text{ns}$).

The flow structure from the ablation of a wire pair is shown in an end-on interferogram in Fig 4.5, along with a schematic diagram detailing the main features and trajectory of the flow. The shift of the initially horizontal fringes in the interferogram (measured as the number of fringe shifts N_f in multiples of the fringe thickness) provides a measure of the line-integrated electron density at each region in the image. Due to the uniformity of the structure along the length (z) axis of the array this can be approximated as a measure of the electron density itself, since $N_f \propto \int n_e \cdot dl \approx n_e L$. (Here $L = 15\text{mm}$, since this is the depth of the array in the images.) It is seen in the data that the areas of greatest shift and hence plasma density are in the coronal plasma, as well as in the central collective region of the flow (bound between the oblique shock lines). This second region has a high density since it receives a mass contribution from each of the adjacent

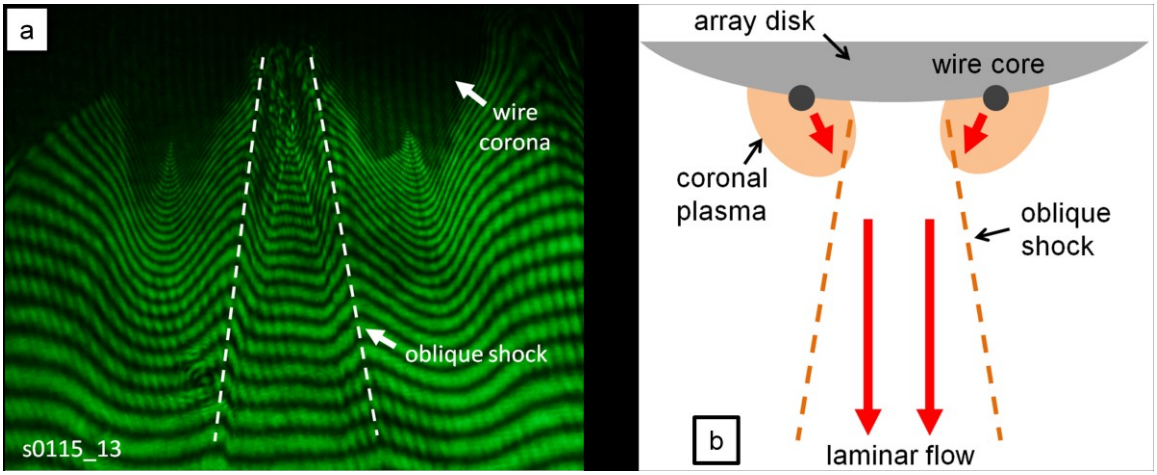


FIG. 4.5 (a) An end-on (r-θ plane) interferogram showing the flow structure created by a pair of wires of the inverse array. As per Fig. 4.4, the array is located at the top edge of the image with the flow propagating downwards (radially outwards from the array) in the image. The areas of highest density gradient in the image (i.e. the coronal plasma close to the wire cores) are opaque to the probing laser beam and so do not show fringes. Note: the initial fringe pattern, as recorded by the pre-shot image, consisted of horizontal fringes. (b) A schematic diagram of the flow trajectory in this structure.

ablation streams. The density inside the central region however appears to decrease away from the array, and it is expected that rather than being due to a radial divergence in the flow, this decrease is due to the time history of the ablation; specifically, there is an increasing rate of mass injection with time into the flow, and so the flow further away from the wires corresponds to mass injected at an earlier, lower ablation rate time. It is seen that the downstream flow inside the oblique shock-bound region is indeed to good approximation laminar and appears, as verified from Thomson scattering data presented later in the text in section 4.5, to propagate with a trajectory parallel to the centreline of the wire pair; thus sufficiently achieving the intension of a 1D flow for reverse shock experiments.

4.4 Density profile of the flow

Fig. 4.6 shows interferometry data from a side-on perspective of the array. The data was taken at $t = 223ns$ after current start and is shown alongside the pre-experiment (background) fringe distribution (Figs. 4.6b and 4.6a respectively). Again the key features are marked in these images including the original wire pair position and the opaque coronal plasma which surrounds them. An areal (i.e. line-integrated) density map was calculated from the relative shift in the position of the fringes between the two

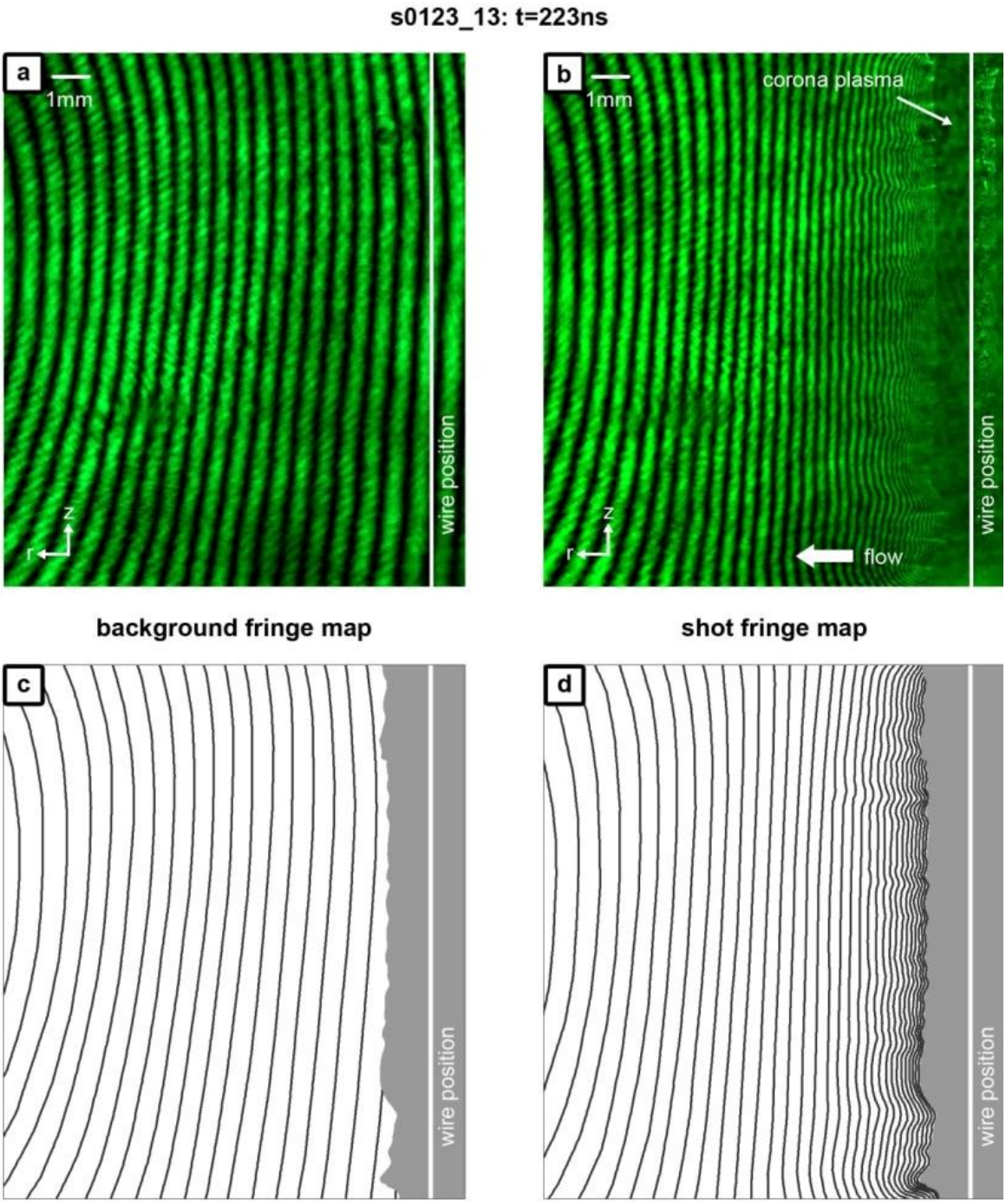


FIG. 4.6 A side-on (r-z plane) interferogram of ablation flow from the inverse wire array. The raw interferometry images from (a) before ("background") and (b) during ("shot") the experiment are shown. (c) and (d) show the traced fringe distributions of these which were used for the areal electron density calculation (see Fig. 4.7). Each black line in the traced image marks a local minimum of the interference pattern; the areas of the image which were opaque to the probing laser (e.g. the coronal plasma) are masked from the calculation and coloured here in grey. In all images the flow is towards the left, with the array on the right.

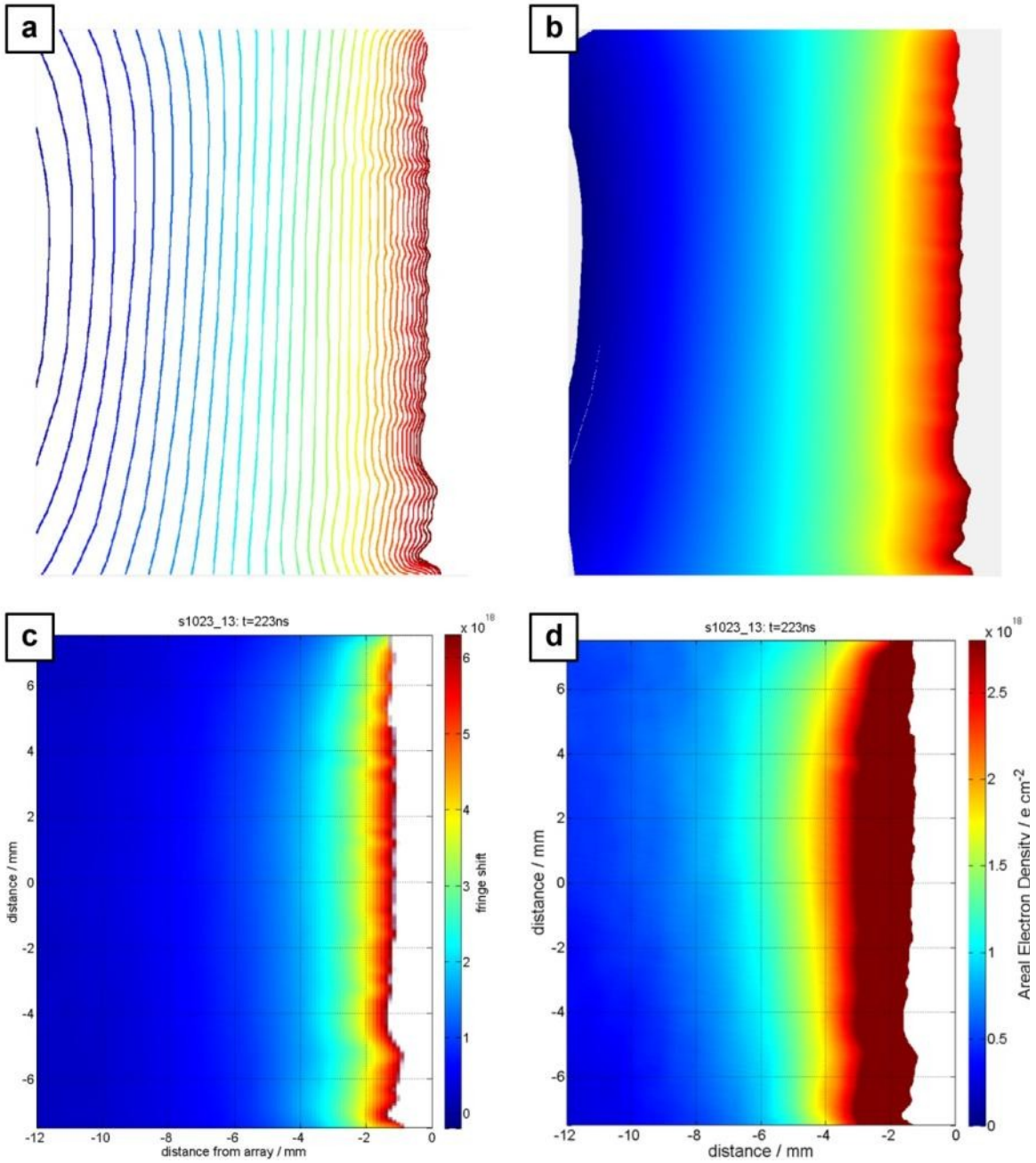


FIG. 4.7 The images here show the steps in the areal density calculation process using the interferometry data in Fig. 4.6. (a) The fringes are each assigned a sequential (integer) numbering as depicted graphically here by their colouring. (b) Pixels in the area between each fringe minima are then assigned intermediate number values based on a linear interpolation. (c) These steps are completed for both the background and shot images and a subtraction of the positional values is performed to provide a map of the spatial fringe shift. (d) From the fringe shift the line-integrated electron density is calculated; in doing so it is often necessary to apply a systematic (integer) offset to the fringe shift values to account for differences in the numbering of the corresponding fringes between the background and shot images. The appropriate offset is evaluated by ensuring that the shift equates to zero at regions far from the plasma locality, where the electron density should be negligible.

images. This process required tracing the fringe distributions so that they could be processed by the interferometry analysis software MAGIC [25] (developed at Imperial College by G. Swadling). The traced fringe profiles are shown in Figs. 4.6c and 4.6d, with the areas of the image which were opaque to the probing laser masked from the calculation and shown here in grey. The original wire position is also marked on these images for reference. The analysis process used by MAGIC is illustrated in Fig. 4.7 and described in detail in the above publication reference. The resulting areal density map from the fringe shift calculation is displayed in Fig. 4.7d.

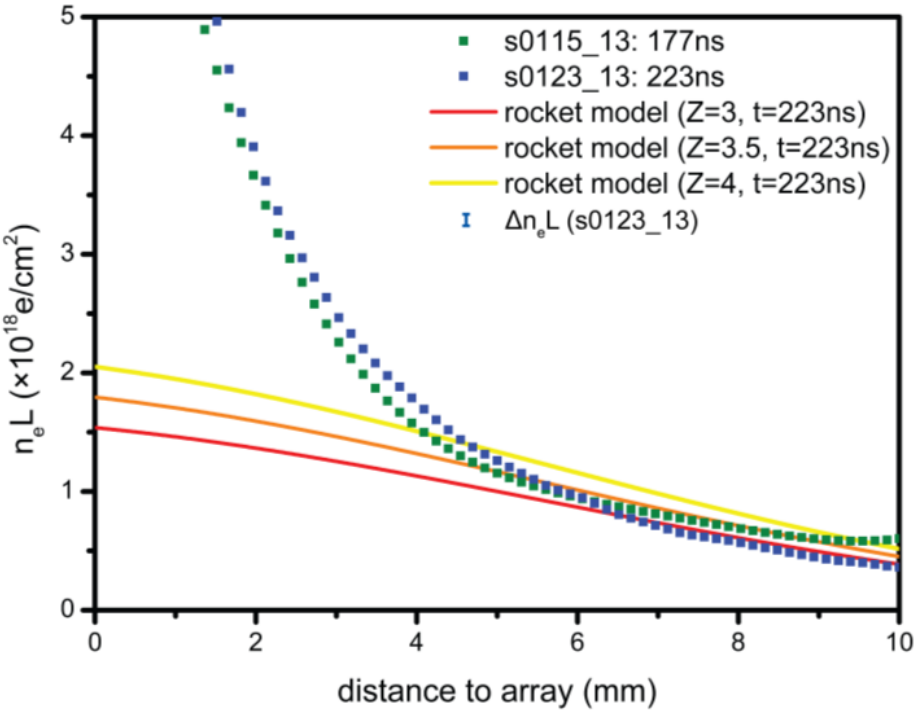


FIG. 4.8 Vertically averaged, radial profiles of the areal electron density in the flow from a wire pair, taken from the side-on interferometry data. The profile at t=223ns (s0123_13) corresponds to the data shown in Fig. 4.7d. Predictions of $n_eL(r)$ from the rocket model of wire array ablation are plotted at various possible ionisation levels for aluminium. An experimental profile from another experiment (s01115_13), performed at a slightly earlier time, is also shown for comparison.

The interferometry data shows the decreasing density of the flow away from the wires. A plot of the n_eL profile along the radial axis, vertically averaged over a 2mm interval in z ($-0.1\text{mm} \rightarrow +0.1\text{mm}$ on Fig. 4.7d), is shown in Fig. 4.8 (blue dots). The profile is qualitatively similar to that previously presented for inverse wire arrays with an equal wire spacing [6], with some differences due to the larger diameter of the array in these experiments, as well as the paired configuration of the wires. In both cases there is a

steep spatial gradient in the region close to the wires, corresponding to the region in which the plasma is accelerated. This region is more extended however for the present setup, occupying $r \lesssim 4\text{mm}$ as opposed to $r < 2\text{mm}$ for the equally-spaced wire inverse arrays. At greater radii the profile flattens off providing an approximately linear profile for $r \gtrsim 5\text{mm}$.

The error in these measurements is estimated from the thickness of the interference fringes in Fig.4.6 as a fraction of the local fringe shift, which translates to an error in areal density via equation 3.55. Evidently this is fractionally more significant for the measurements at greater radii to the wire array, where the fringe thickness is larger, and the plasma density and hence fringe shift is smaller. For radial positions of $r = 4, 6\ \&\ 8\text{mm}$ the error in $n_e L$ was estimated at $\pm 6.0 \times 10^{16}, 5.5 \times 10^{16}$ and $4.3 \times 10^{16}\ \text{e/cm}^2$ respectively. The average of these values is illustrated on the graph of Fig. 4.8.

From a record of the spatial profile such as this it should be possible to attain the temporal profile at a given position by applying a "time-of-flight" shift. Since the velocity of the flow from wire arrays is to good approximation constant [24,61], for the linear portion of the profile it should be possible to apply a simple transformation of

$$\rho(t)|_{r_0} = \rho(r_0 - v[t - t_0])|_{t_0}. \tag{4.6}$$

It must be noted however that due to the shot-to-shot fluctuation in the current applied to the array by the pulsed power generator, an accurate estimation of the temporal density profile requires at least one measurement of the spatial density profile for each experiment (as the plasma mass scales quadratically with current). This is demonstrated in Fig. 4.8 where $n_e L$ data is plotted from another experiment (green dots) with an equivalent array setup. Comparison of the profiles shows them to be reproducible in their shape, however despite being at an earlier experimental time of $t = 177\text{ns}$ the profile for s0115_13 displays a higher electron density due to a larger driving current in this experiment. As a typical range, for the position of $r = 10\text{cm}$ (which was later used as the location for obstacles in shock target experiments – see chapters 5 & 6), the areal density has been found to generally reach $3 \rightarrow 6 \times 10^{17}\ \text{e/cm}^2$ for timescales of interest, corresponding to a number density of $3 \rightarrow 6 \times 10^{17}\ \text{e/cm}^3$ for the $L = 10\text{mm}$ side-view thickness of the plasma flow.

The areal density profile results can be compared to a prediction of the radial distribution using the rocket model described in [24]. This assumes a momentum

balance of the material ejected from the array with the magnetic force acting at the position of the wires, such that the rate of mass introduced to the flow per unit length of the array (in S.I. units) is

$$\frac{dm}{dt} = \frac{\mu_0 I^2}{4\pi R v}, \tag{4.7}$$

where v is the (assumed constant) velocity of the ablation. Since the flow from a single wire pair corresponds to $1/8^{th}$ of this mass, the areal mass density as a function of time and position, viewing the pair side-on, is

$$\rho L = \frac{\mu_0}{32\pi R v^2} I(t - {}^{r}/_{v})^2; \tag{4.8}$$

and henceforth the electron density is

$$n_e L = \frac{\mu_0 Z}{32\pi R v^2 m_i} I(t - {}^{r}/_{v})^2. \tag{4.9}$$

This is plotted in Fig. 4.8 for a sample of typical ionisations achieved in aluminium plasmas in past experiments and simulations on MAGPIE. Since the model omits the acceleration process it does not reproduce the steep gradients close to the array, however there is a reasonable fit to the data for $v = 1 \times 10^7$ cm/s, Z~3 – consistent with that found for equally spaced wire inverse arrays [6].

4.5 Velocity and temperature properties of the flow

Direct measurements of the flow properties in the central, collective-flow region were made using the optical Thomson scattering diagnostic described in section 3.4.1. The diagram in Fig. 4.9 shows the setup for these measurements. The probing laser beam was propagated along the radial axis in the $r - \theta$ plane. The beam path passed between a pair of wires (along the centreline of the pair), through a 2mm diameter hole in the central cathode and again between the centre of another pair of wires on the far-side of the array. Due to the long focal length of the optics used in this setup, the beam width remained approximately equal to the focal spot size (200μm) across the range of interest. Scattered light was collected from several spatial positions within the flow at ~0.55mm separations along the beam's propagation, and observed at opposite ±90° directions within the same horizontal plane. The light was focussed into individual optical fibres of 200μm diameter and delivered to a 0.5m ANDOR SHAMROCK imaging spectrometer, coupled with an ANDOR ICCD camera providing a gating time of 4ns. The

spectral resolution, determined by the size of the optical fibres and 2400g/mm grating was 0.45Å. A typical fibre spectrum is shown in Fig. 4.10.

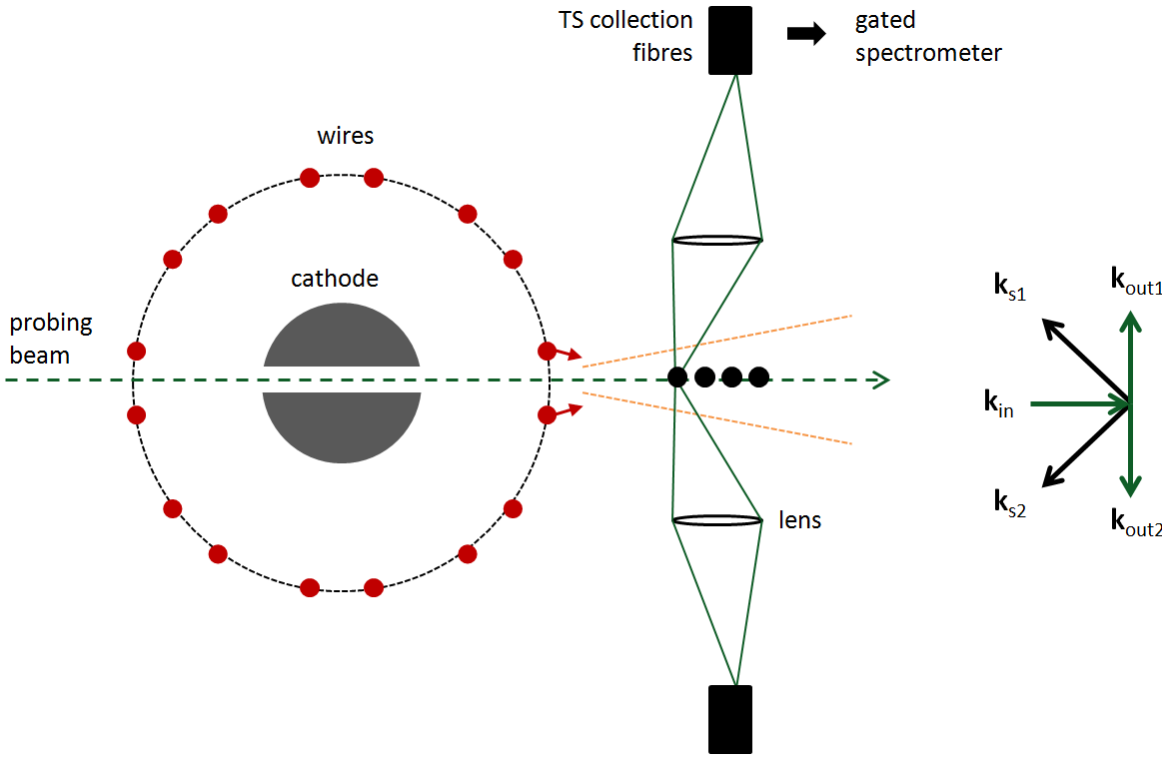


FIG. 4.9 Experimental setup for Thomson Scattering measurements of the plasma flow. The probing beam and scattering collection geometry are depicted.

Comparison of the central wavelength of the scattered signal to the original laser frequency (equal to that of the superimposed stray light) allows the velocity of the plasma ions to be measured from their Doppler shift; where the shift gives the velocity in the direction of the scattering wavevector $\mathbf{k}_s$ (the resultant wavevector of the output and input vector difference, $\mathbf{k}_{out} - \mathbf{k}_{in}$). The full velocity vector in the $r - \theta$ plane can be reconstructed from the components of the two orthogonal wavevectors $\mathbf{k}_{s1}$ and $\mathbf{k}_{s2}$ (as shown in Fig. 4.9); where the subscript numbering corresponds to each of the two directions of collected light. Data shows that to very good approximation the plasma is directed along the radial centreline of the wire pair, with very little transverse motion. The parallel component of velocity $v_{\parallel}$ is measured to be in the region of $(110 \pm 10)\,\mathrm{km/s}$ at early times ($80\mathrm{ns} < t < 200\mathrm{ns}$), slowing to $(90 \pm 5)\,\mathrm{km/s}$ later on (t~250ns). In comparison the perpendicular component is negligible, remaining at $v_{\perp} \lesssim 3\,\mathrm{km/s}$ throughout.

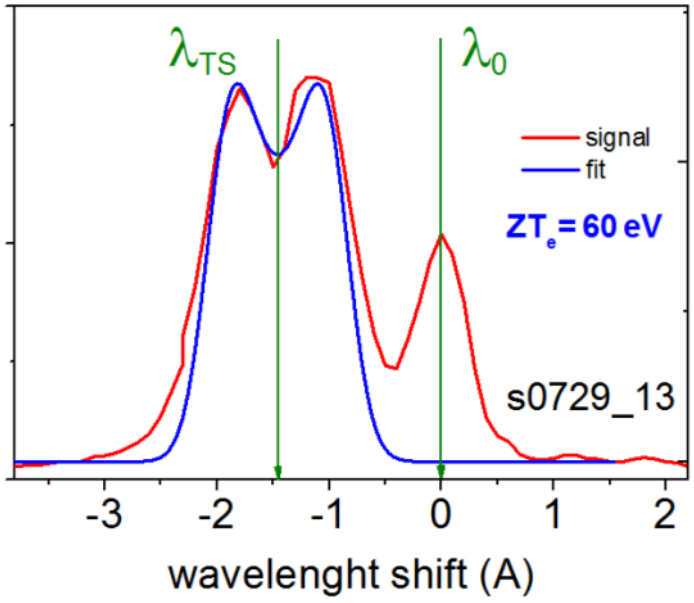


FIG. 4.10 A typical fibre spectrum obtained from the Thomson scattering system, showing the ion feature of the spectrum. λ_{TS} is the Doppler-shifted central wavelength and λ_0 is that of superimposed stray light at the original wavelength. A fitted theoretical spectrum is over-plot to find the temperature and ionisation parameters of the plasma.

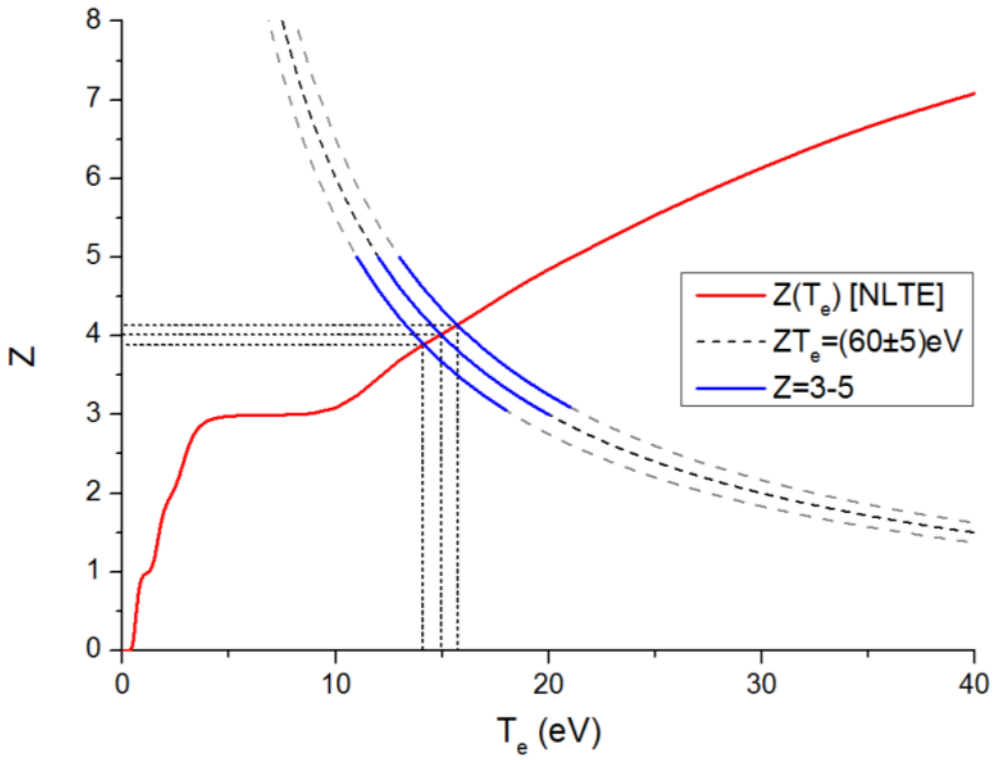


FIG. 4.11 Plot of $Z(T_e)^*$ at NLTE (red) against the measured constraints of the ZT_e product from Thomson scattering. The range $Z=3\rightarrow5$ for typical MAGPIE plasmas is marked in blue. [*Calculation performed by N. Niasse, MAGPIE Group.]

The shape of the Thomson scattered spectra shown in Fig. 4.10 displays the well-separated "ion-acoustic" peaks of the ion component of the spectrum, which indicate that the ionisation-electron temperature product ZT_e is much greater than the ion temperature T_i. The theoretical form of the scattered spectrum is described in detail in chapter 3, section 3.4.1, and when fitted to the data yields $ZT_e = (60 \pm 5)\text{eV}$. Using the previous estimate of Z~3 from the rocket model (section 4.4) this equates to an electron temperature of $T_e \sim 20\text{eV}$, however a more sophisticated estimate can be gained from a calculation of Z as a function of T_e for a plasma in non-local thermal equilibrium (NLTE). This was calculated using an effective temperature model in collisional radiative equilibrium, based on a modification of the Saha equation [62]. The result is plotted for the relevant plasma parameters in Fig. 4.11 against the measured constraints, with the limits of the typical range $Z = 3 \rightarrow 5$ for plasmas generated on MAGPIE indicated. From this analysis the average ionisation is estimated at $Z = 4.0 \pm 0.2$, with $T_e = (15 \pm 1)\text{eV}$.

Combining these estimates with the measured electron density from the interferometry measurements it appears that the Thomson scattering diagnostic operates in an intermediate scattering regime (i.e. α not far from unity); with a calculated alpha parameter of $\alpha = 1.3 \rightarrow 1.5$ at the position of the furthest fibre from the wire array ($r = 1\text{cm}$; $n_e \sim 5 \times 10^{17}\,\text{e/cm}^3$), and $\alpha = 1.9 \rightarrow 2.2$ for the nearest fibre to the array ($r = 0.6\text{cm}$; $n_e \sim 1.1 \times 10^{18}\,\text{e/cm}^3$). This places the diagnostic marginally towards collective, rather than non-collective scattering; however, only the ion component was observed in the data, as even with an alpha parameter marginally greater than 1, the electron component possess a much lower signal-to-noise ratio, with lower intensity peaks which are spread over a wider wavelength interval.

4.6 Magnetic measurements of the flow

The plasma flow from the inverse wire array is expected to possess a frozen-in magnetic field, the advection of the magnetic field having been observed previously in standard wire arrays [63–65], although not measured for inverse arrays prior to these experiments. The magnetic field in the plasma flow was measured using pairs of identical, overlapped, inductive probes with a loop area of $2.7\text{mm}^2 (= 1.55 \times 1.75\text{mm}^2)$, which were wound in opposite directions and centred at a position of $r = 8.5\text{mm}$ from the array. The probes were shielded by a thin layer of conductive paint to suppress possible electrostatic noise from variations of the plasma potential. The signals from each probe were recorded separately and typical results are shown in Fig. 4.12.

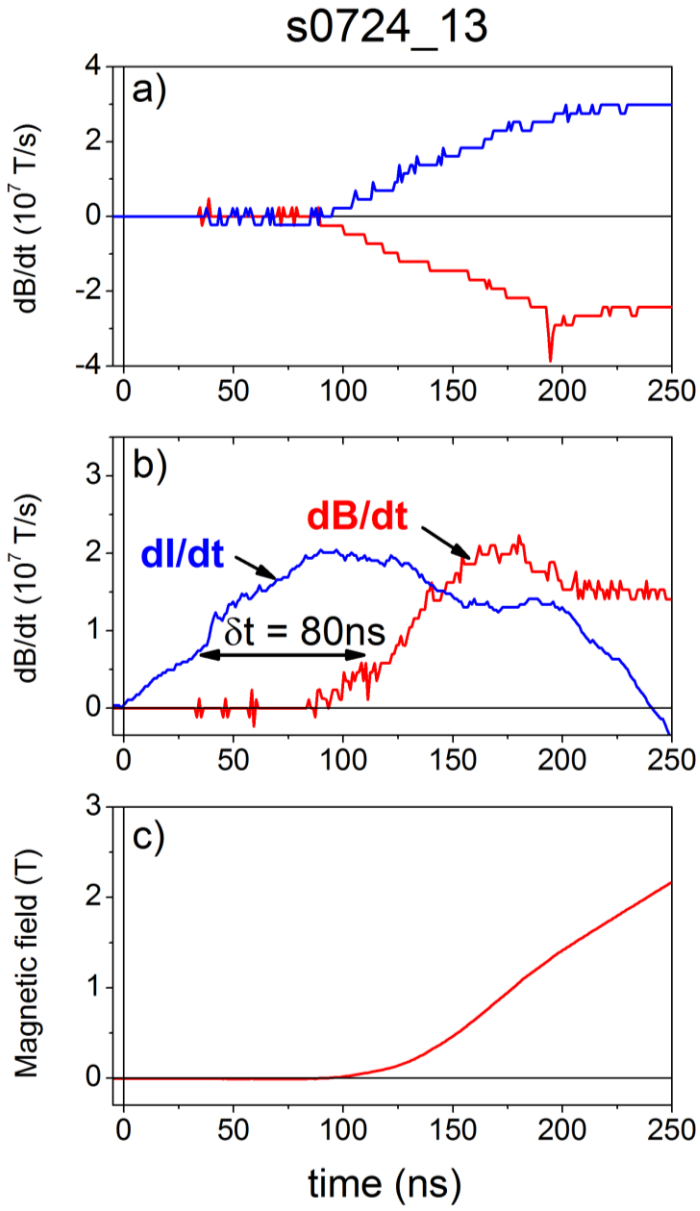


FIG. 4.12 The magnetic field measured by inductive probes positioned at a distance of 8.5mm from the wires. (a) Signals from two co-located, oppositely wound probes, (b) comparison of the combine signals, alongside dI/dt of the current (a.u.) driving the ablation plasma flow, and (c) the magnetic field obtained by integrating the signals shown in (b).

Fig. 4.12a shows the raw dB/dt signals from a probe pair. It is seen that they have approximately equal amplitude but are of opposite polarity, which demonstrates that the signals are produced by the magnetic field and a possible contribution from a capacitive coupling to the plasma potential is negligible. The probe signals start at t~80ns, when the plasma moving with v_{flow}~10^7 cm/s reaches the probes. The combined pair signal is plotted alongside the derivative of the generator driving current (dI/dt as measured by Rogowski coils) in Fig. 4.12b. It is evident that the probe signal repeats

this shape, albeit with the time of flight offset of the flow, and is therefore consistent with the advection of the magnetic field by the plasma flow. Integration of the dB/dt signals yields the magnetic field evolution (Fig. 4.12c), showing that the field strength at this position reaches 1T at t~175ns and 2T by t~250ns. Hence, as the material flux of the flow increases with time due to the increasing mass injection from wire ablation, so too does the magnetic flux increase due to their advective coupling.

4.7 Parameterisation of the flow

From the detailed measurements listed in this chapter it is possible to summarise the properties of the inverse wire array plasma flow in terms of a number of characteristic parameters, which assess both its suitability for use in shock experiments and its applicability towards the study of different physical regimes. The values calculated below are summarised in Table 4.1 at the end of the section and are compared for reference to the ranges expected for various astrophysical objects in Table 4.2.

The primary criteria for designing an experiment where the plasma is to be used in shock experiments with stationary obstacles is that the flow must be supersonic, and possess a Mach number of several ($M_S^2 \gg 1 \Rightarrow M_S \gtrsim 3$) for the study of strong shock scenarios. The ion sound speed is calculated from the measured plasma parameters as

$$c_S = \sqrt{\frac{\gamma Z k_B T_e}{m_i}} \simeq (1.9 \pm 0.1) \times 10^6 \text{cm/s}, \tag{4.10}$$

where the units in this calculation are expressed in cgs, except for the temperature which is in eV. The sonic Mach number is then simply the ratio of the flow velocity to this, giving $M_S = 5.8 \pm 0.6$ for the flow velocity measured by Thomson scattering at $180\text{ns} < t < 200\text{ns}$, reducing to $M_S = 4.8 \pm 0.6$ for $t = 250\text{ns}$; where the assumption has been made that the plasma is described by a monatomic adiabatic index of $\gamma = 5/3$.

If the inclusion of strong MHD shock effects is also desired then so should the plasma be moving greater than the Alfvén and / or magnetosonic velocity (see section 2.3), depending on the orientation of the flow relative to the field direction. These velocities correspond to the propagation of MHD waves in the plasma, caused by the transverse and longitudinal oscillation of ions respectively. Whereas the Alfvén waves travel along the field lines due to a restoring force in the magnetic tension, the acoustic waves travel perpendicularly to the field lines and are therefore perhaps the most relevant for

consideration in the current geometry setup (flow propagating with a perpendicular field direction). The Alfvén and magnetosonic speeds are

$$v_A = \frac{B}{\sqrt{4\pi n_i m_i}} \tag{4.11}$$

and

$$v_{MS} = \sqrt{{c_S}^2 + {v_A}^2} \tag{4.12}$$

respectively. Due to the time variance of the magnetic field strength (and to a lesser degree the flow density) this gives magnetic Mach numbers of $M_A = 10.2 \pm 3.6$ and $M_{MS} = 5.1 \pm 0.7$ at t~180ns, evolving to $M_A = 7.2 \pm 2.6$ and $M_{MS} = 4.5 \pm 0.8$ by t~250ns; thus despite the decreasing Mach values, the flow does indeed satisfy the strong shock and magnetic-shock requirements on the duration of typical MAGPIE experimental timescales.

As demonstrated by the measurements from local magnetic field probes, the plasma shows strong advective properties. This is reflected by the magnetic Reynolds number of the flow, which gives the ratio of the magnetic advection to diffusion in the flow, and for a plasma with $Z \geq 3$ [20] can be estimated as

$$Re_M = 0.8 M_S \sqrt{\frac{Z+1}{Z^2 A}} L(\text{cm}), \tag{4.13}$$

where A is the atomic mass number for the plasma material (i.e. $A = 27$ in the case of aluminium). For the measured parameters of the plasma ($M_S = 5.8 \rightarrow 4.8, Z = 4, T_e = 15\text{eV}$), and using $L = 1\text{cm}$ as a characteristic spatial scale for the flow, this yields $Re_M \approx 110$ at t~180ns, reducing to $Re_M \approx 90$ at t~250ns. Whilst it is noted that this is significantly lower than the majority of astrophysical objects (which are quoted in [15] to generally exceed $Re_M \sim 10^{10}$) it is still far greater than unity and therefore ensures that the shock studies remain applicable as laboratory astrophysics experiments.

The mechanism of particle localisation is also a fundamental factor in flow and shock categorisation. Primarily shocks can be grouped into either collisional or collisionless regimes, where the distinction is made on comparison of the collisional mean free path of the ions to the scale lengths of the system; such as the shock transition thickness or any internal structure lengths within the shock. Prior to an observation of a specific shock structure therefore it is impossible to comment on what the collisionality of that shock might be. On a more general level however it is possible from the measurements

already made to gauge the internal collisionality of the flow. The NRL Plasma Formulary [66] gives formulas for the collisional rates between particles of different species. These are expressed in terms of test particles moving at a known velocity in a population of separate background particles. In the frame of reference of the velocity of the test particles is equivalent to the thermal velocity $\left(v_{th} = \sqrt{2k_B T_i / m_i}\right)$ of the ions. Under the approximation of "slow" moving ions, where the test and background particles are of the same species and ionisation, the collisional rate is given by

$$\nu^{i\backslash i} = 6 \times 10^{-8} \mathrm{Hz} \cdot \frac{n_i Z^4 \lambda_{ii}}{\sqrt{2A} T^{3/2}}, \tag{4.14}$$

where units are in cgs (except T in eV) and λ_{ii} is the coulomb logarithm

$$\lambda_{ii} = \ln(\Lambda) = 23 - \ln\left(\sqrt{2n_i} \cdot \frac{Z^3}{T^{3/2}}\right). \tag{4.15}$$

Substituting the measured values into these equations yields an average collisional time of 0.07ns, corresponding to a mean free path for the thermal ion-ion collisions of 7×10^{-5}cm $\approx 1\mu$m. Comparing this to the overall length scale of the flow structure (~1cm) the plasma can therefore be described as being an internally collisional system.

Returning to the magnetic properties of the plasma, the beta parameter β gives the relative strength of the collisional and magnetic pressures of the flow, and can be calculated both internally, from the thermal collisional pressure, as well as from the perspective of an external stationary body, as is applicable in shock experiments. The thermal beta for the inverse wire array flow is given by

$$\beta_{th} = \frac{8\pi n_i k_B T}{B^2} = 4 \times 10^{-11} \cdot \frac{n_i T(\mathrm{eV})}{B^2}, \tag{4.16}$$

which for the plasma flow here $\cong 0.5 \rightarrow 0.1$ (0.5 at t = 180ns, reducing as the field size increases, to 0.1 at t = 250ns). This shows that there is an approximate balance of the internal pressures early in time, with the magnetic pressure becoming more significant towards the later stages. From the outside, laboratory frame perspective, the collisional force felt by a solid, stationary body interacting with the plasma is given by the ram pressure (ρv^2) of the flow. The corresponding beta is therefore

$$\beta_{ram} = \frac{8\pi\rho v^2}{B^2}, \tag{4.17}$$

which suggests that the collisional pressure dominates the field by a factor of ~100 at t = 180ns, reducing to ~10 by t = 250ns.

Another important parameter in describing the behaviour of the flow is the Reynolds number. This assesses the relative importance of inertial and viscous forces in the plasma fluid, and is a property often of interest when comparing experiments to observation; particularly since the validity of scaling between these systems via the Euler equations requires the viscous effects to be an unimportant factor in the overall system dynamics. The Reynolds number is given by

$$\mathrm{Re} = \frac{\mathrm{Lv}}{\nu}, \tag{4.18}$$

where the numerator is the product of the length scale and velocity of the flow and ν is the kinematic viscosity of the flow. This viscosity is best approximated for a plasma in the collisional limit (i.e. with a dynamically insignificant magnetic field – as was shown by the ram pressure beta parameter) by

$$\nu = 2 \times 10^{19}\,\mathrm{cm^2/s} \cdot \frac{\mathrm{T}^{5/2}}{\Lambda\sqrt{\mathrm{A}}\mathrm{Z}^4\mathrm{n_i}}, \tag{4.19}$$

which results in a Reynolds number of $\mathrm{Re}\sim 10^6$ for the measured parameters. Hence the inverse array flow is deemed to be highly inertial.

The values calculated here reflect different aspects of the fluid and magnetic properties of the flow, and should therefore form a key consideration when scaling the results of any experiments performed in the current setup for astrophysical studies. The following chapters present one such example of HEDP experiment, where the plasma flow described here is used in combination with a planar obstructing body in the study of the resulting magnetised reverse shock structure; the results of which may later prove insightful as a laboratory astrophysics simulation.

	t = 180ns	**t = 250ns**
Sonic Mach number, $\mathrm{M_S}$	5.8 ± 0.6	4.8 ± 0.6
Alfvénic Mach number, $\mathrm{M_A}$	10.2 ± 3.6	7.2 ± 2.6
Magnetosonic Mach number, $\mathrm{M_{MS}}$	5.1 ± 0.7	4.5 ± 0.8
Magnetic Reynolds number, $\mathrm{Re_M}$	110	90
Reynolds number, Re	10^6	
Internal collisional time	0.1ns	

Thermal mean free path	10^{-4}cm	
Thermal beta, β_{th}	0.5	0.1
Dynamic beta, β_{ram}	100	10

TABLE 4.1 Summary of properties of the flow produced by a pair of wires (at a distance of r = 10mm) in the inverse wire array setup.

	YSO jet	**SNR**	**Solar-planetary**
Sonic Mach number, M_S	$\gg 5$	5	$5-10$
Alfvénic Mach number, M_A		10^2	$4-8$
Magnetosonic Mach number, M_{MS}		5	
Magnetic Reynolds number, Re_M	$> 10^{15}$	10^{17}	10^{12}
Reynolds number, Re	$> 10^8$	10^8	$10^{16}-10^{17}$
Internal collisional time		10^{10}s	10^6s
Thermal mean free path	10^9cm	10^{18}cm	
Thermal beta, β_{th}	$0.01-100$	10^3	1
Dynamic beta, β_{ram}		10^5	

TABLE 4.2 For comparison to Table 4.1 of the laboratory experiment; summary of the properties of plasma flows in various astrophysical environments including: jets from young stellar objects (YSO) [1], shocked ejecta of young supernova remnants (SNR) (at 13yrs) [17], and solar-planetary environments (relevant to the heliospheric plasma at the position of the Earth's orbit) [67,68].

Chapter 5:

The structure of reverse shocks formed in the collision of a magnetised, supersonic plasma flow with a planar foil obstacle

5.1 Introduction

This chapter presents data from experiments designed to study magnetised reverse shocks, formed using the platform described in chapter 4 which provides a high energy density, supersonic and magnetically-advective plasma flow from the ablation of an inverse wire array z pinch. This chapter focuses on the formation and structure of reverse shocks created by the collision of this flow with a planar obstacle; in particular the development of a sub-structure feature, observed upstream of the main obstacle-surface stagnation shock, which is referred to here as a "sub-shock". The sub-shock displays significantly lower density and velocity discontinuities than expected for the high Mach number flow and appears as a very narrow transition, of the same order of magnitude as the calculated collisional length of the oncoming ions. Notably, the sub-shock is first detected at a detached position, ahead of the main obstacle-surface by a distance of order c/ω_{pi}, and subsequently expands further upstream until a later equilibrium is achieved with the ram pressure of the oncoming flow. Data presented here from Thomson scattering, laser interferometry and local magnetic field probes suggests that the sub-shock is formed due to the pile-up of magnetic flux which cannot penetrate the (conducting) obstacle surface. It is believed that the increased field acts on the magnetised electrons of the flow to create an electrostatic, cross-shock potential

which decelerates the flow. Issues with an apparent deficiency in the magnetic pressure supporting the sub-shock are explored later in chapter 6, along with an investigation of the possible mechanisms of field generation due to current loops in the downstream region.

5.2 Setup for the reverse shock experiments

The inverse wire array setup used to provide a steady-stream of laminar and 1D, magnetised, supersonic plasma flow for these shock experiments is described in chapter 4, along with a detailed parameterisation of the flow. In summary the plasma flow is produced by the ablation of $N = 16$, thin, metallic (Al) wires, 15mm in length, which are driven by a $1.4\text{MA}, 250\text{ns}$ rise-time current pulse $\left(I \approx 1.4\text{MA} \cdot \sin^2(\pi t/500\text{ns})\right)$. The wires are arranged to form an inverse wire array z pinch, where the current is applied through the wires and then returns through a central (cathode) electrode, which is positioned coaxially with the array. In this inverse array setup the J×B force drives the ablated plasma with its frozen-in magnetic field ($Re_M \sim 100, B \sim 1-2\text{T}$) radially outward into an external region, initially free from magnetic field. The wires are paired, with the angular spacing of the wires in each pair being marginally smaller than the average inter-wire separation (20° separation for the pair instead of $360°/N = 22.5°$). This increased pair proximity acts to magnetically focus the flow from the adjacent wires, such that a planar, rather than radially divergent, flow is produced. The interaction from the paired wires creates two standing oblique shocks, between which the flow is essentially one-dimensional, and it is inside this flow that stationary obstacles are placed for the reverse shock experiments.

The obstacle targets chosen for these experiments were planar, aluminium (i.e. conducting) foils of varying dimensions. Typically $10 \times 10\text{mm}^2$ square foils were used with 15μm thickness, however experiments were also carried out with foils 5 or 10mm wide, 5, 10 or 15mm tall, and $10-40$μm thick; where a compromise was sought between the lower density cut-off limit associated with probing over longer distances and the presence of increased edge-turbulence and shock-front curvature for narrower obstacle bodies. These targets were installed perpendicular to the plasma flow and suspended from the rear-side on metal (brass) mounts (see Fig. 5.1), which were connected to ground potential through a high inductance return path. A line-of-sight through the mount (parallel with the foil surface) allowed a fine alignment of the foil to be made relative to the array wires and laser probing directions; ensuring that the foil was placed perpendicular to the flow and at the desired distance from the wires. The positional and

angular adjustment of the foil was made through the use of a multi-directional translation stage attached to the mount holder.

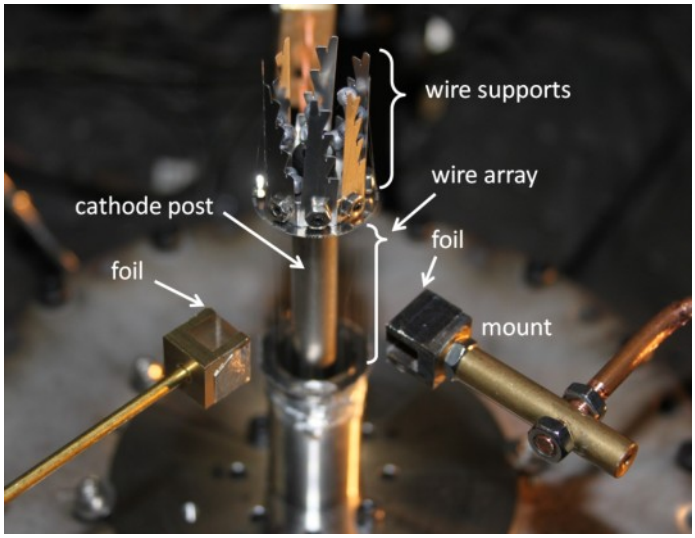


FIG. 5.1 A photo of two planar aluminium foil shock targets, mounted on support posts and positioned externally to an inverse wire array. The foils are each aligned parallel to a pair of wires of the array to intercept the plasma ablated from these during the experiment.

Generally an array-foil distance of 10mm was set, with a full range of $7-13$mm trialled during different experiments. This proximity was selected as it was deemed suitably far from the steep density gradients close to the wires (<4mm), whilst remaining within a reasonable density range for the effective performance of the laser probing diagnostics. For a 10mm wide foil, at a 10mm distance from the array, the plasma flow from a single wire pair falls comfortably onto the bounds of the foil surface. The first arrival of plasma at the foil surface is from t~100ns after the start of driving current (v_{flow}~10^7 cm/s), with a rising mass density of the flow thereafter (due to the rising current pulse shape which scales with the mass injection into the flow as $dm/dt \propto I^2$). Typical values of the electron density in the undisturbed plasma at this position for experimental timescales of interest ($150-300$ns) are generally in the range $3-6\times10^{17}$ e/cm^3, with some shot-to-shot variance due to fluctuations in the current delivered by the MAGPIE generator.

The collision of the plasma flow with the foil obstacle leads to the accumulation of material in the interaction region in front of the foil, with the formation of a reverse shock wave propagating in the incoming plasma. The azimuthal symmetry of the setup, which has eight nominally identical plasma flows, allows several plasma streams to be used simultaneously to create multiple obstacle interaction regions, maximising the

amount of information that can be collected by the different diagnostics (see Fig. 5.2). The symmetry also allows direct comparison to the parameters and behaviour of the undisturbed plasma flow which can be measured in the same experiment.

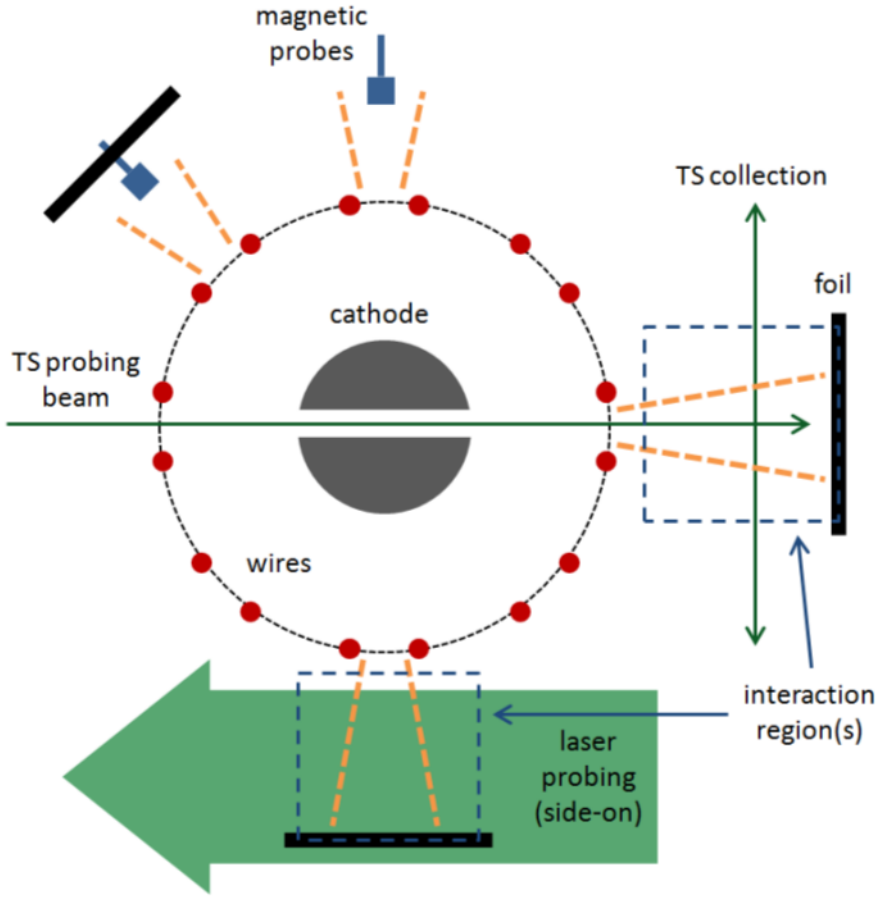


FIG. 5.2 An example of the diagnostic setup for the reverse shock experiments, demonstrating the use of the array symmetry to create multiple flow-obstacle interaction regions to collect simultaneous data from different diagnostics. Measurements can also be made for the undisturbed plasma flow. Note: end-on (vertical) laser probing of the interaction region was also performed – often simultaneous with Thomson scattering (TS) measurements (see section 5.4).

A number of diagnostics were used both in combination and inter-changeably to study the interaction of the flow with the obstacle. Gated multi-frame cameras were used to obtain time-resolved images from the self-emission of the interaction region and follow the temporal evolution of shocks. An optical, time-gated camera (12 frames with 5ns exposure and variable inter-frame separation) imaged the interaction from the end-on direction, while an XUV camera (photon energy > 30eV, 4 frames gated at 2ns with 10ns or 30ns inter-frame separation) recorded side-on images. Laser probing (355nm and 532nm, 0.3ns pulse-length) of the interaction region was performed, often

simultaneously, in side-on and end-on directions using interferometry and shadow channels. Thomson scattering (532nm, 5ns – FWHM, 3J, ~200μm spot size) at spatially resolved positions throughout the region was used to measure profiles of plasma velocity and temperature across the shocks. The local magnetic field in the plasma flow was also measured using pairs of inductive probes. More details on all these diagnostic systems and their analysis techniques can be found in chapter 3 and the references given therein. The following section describes an overview of the structures observed in the flow-obstacle interaction region.

5.3 Overview of the flow-obstacle interaction

5.3.1 Timeline of the reverse shock

This section begins a presentation of the experimental results, describing an overview of the structure which develops during the interaction between the plasma flow and the planar foil obstacle. Fig. 5.3 shows a timeline of events in the formation of the reverse shock structure, compiled from images of optical self-emission, which were taken from multiple experiments with the fast-frame camera. The images are taken from an end-on perspective, perpendicular to the surface of a $10 \times 10\text{mm}^2$ foil.

As described previously (section 4.3) the first 100ns after current start see the beginning of wire ablation and the formation of an oblique shock bound region containing a laminar plasma flow. Once the flow has reached the obstacle the first feature observed to form in the interaction is a thin layer of emission at the foil surface. This becomes observable from t~70ns after the start of current and expands upstream with an approximately constant velocity of $3 \times 10^5\,\text{cm/s}$ thereafter – starting from zero at $t = 70\text{ns}$ and reaching ~0.5mm by $t = 230\text{ns}$. The delay between the start of driving current and the appearance of this stagnated plasma gives a flow velocity of $\sim 1.5 \times 10^7\,\text{cm/s}$ from the time-of-flight needed to reach the obstacle. This is ~50% higher than the ablation velocities measured in the undisturbed flow with Thomson scattering for later experimental times (see section 4.5); although is in agreement with the initial material "blow-off" speed which is recorded for both standard and inverse wire arrays [6,24]. It is also however noted that some contribution of this emission may be from ablation of the foil surface, due to photo-ionisation by high energy (x-ray) radiation from the array; however, without a measurement of the radiation intensity (for example using photo-conducting diode (PCD) diagnostics [69]) it is difficult to estimate how significant this contribution may be.

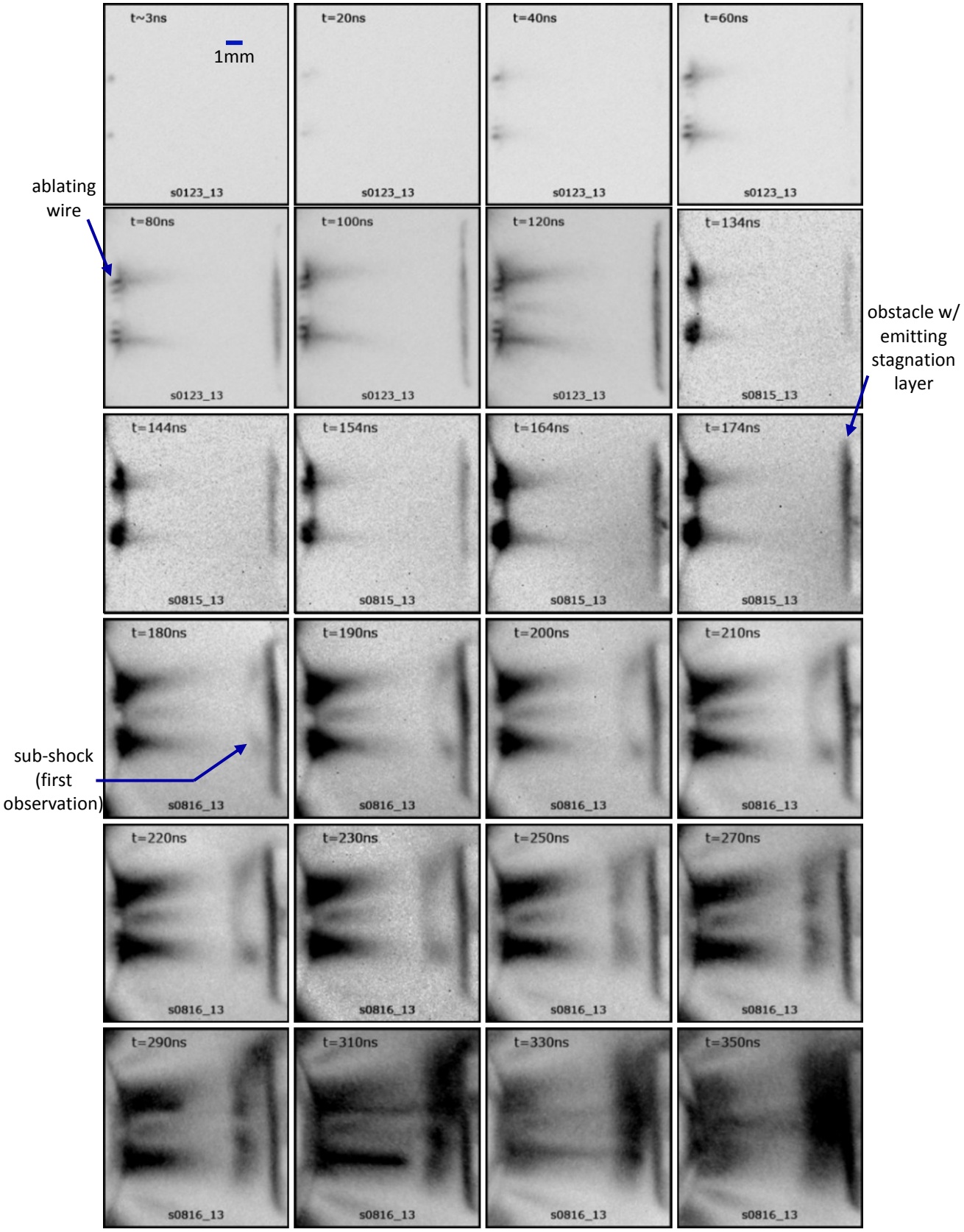


FIG. 5.3 An optical, self-emission timeline of the flow-obstacle interaction, recorded from an end-on perspective over multiple experiments. The images are inverted, such that the dark areas correspond to the greatest emission. In all images the flow is from the wire pair located on the left hand side, towards the planar obstacle at the right.

A second prominent feature in the flow-obstacle interaction region is seen to form in the images at a slightly later time. A detached, bow shock-like structure, which is referred to hereafter as a "sub-shock", is formed upstream of the foil at a distance of ~2mm, and is detectable from t~180ns in the optical images. This region of enhanced emission moves further upstream with a speed of $\sim 1.5 \times 10^6\,\mathrm{cm/s}$ ($\sim 10-15\%$ of the upstream flow velocity), reaching a position of ~3mm from the foil at $t = 250\mathrm{ns}$.

It is observed in the image timeline ($t = 180-200\mathrm{ns}$) that the sub-shock forms both inside the central, oblique shock bound (1D) flow region and in the adjacent single-wire plasma streams. For the single-wire streams the sub-shock is formed closer to the foil surface, which gives the overall combined feature a curved interface. Later however these side parts of the sub-shock expand away from the foil faster than for the central region until they reach an equidistant position, and the feature stabilises with a planar wave-front for the transition, at about $t = 260-270\mathrm{ns}$. From this time onwards the sub-shock-front remains approximately stationary in the flow.

The timeline of these events is seen also in Fig. 5.4, from a side-on perspective, imaged from self-emission in the XUV. Here the bright stagnated plasma is again seen in front of the foil surface, with the higher resolution of the XUV imaging system showing a notable wave-like outline to the shock front of this feature. The sub-shock front is also seen to form, becoming visible to this diagnostic at the slightly earlier time of $t = 140-150\mathrm{ns}$, and at a closer distance of 1.4mm from the foil. Images taken shortly after its appearance ($t = 150-170\mathrm{ns}$) repeatably show a bubble-like structure in the region between the transition fronts of these two main features. This may be an indication that the sub-shock is initiated by an instability which propagates upstream from the stagnated layer. It would be useful to increase the magnification (and hence resolution) of the imaging system and reduce the inter-frame time to investigate this structure in greater detail, however these modifications are currently left for future experiments. In particular it would be interesting to image the fine-structure in the region behind the sub-shock, and also ascertain if the sub-shock does indeed form in place, upstream of the stagnated plasma, or if it is launched from the layer during its formation.

Following its initial observation the upstream propagation of the sub-shock is observed in the XUV images, again showing that the feature moves steadily ahead of the foil until it reaches a stationary position at around $t = 250\mathrm{ns}$. The shape of the sub-shock front from this side-on perspective however shows a distinct vertical curvature, and is asymmetric between its top and bottom edges. The top edge of the sub-shock front sits

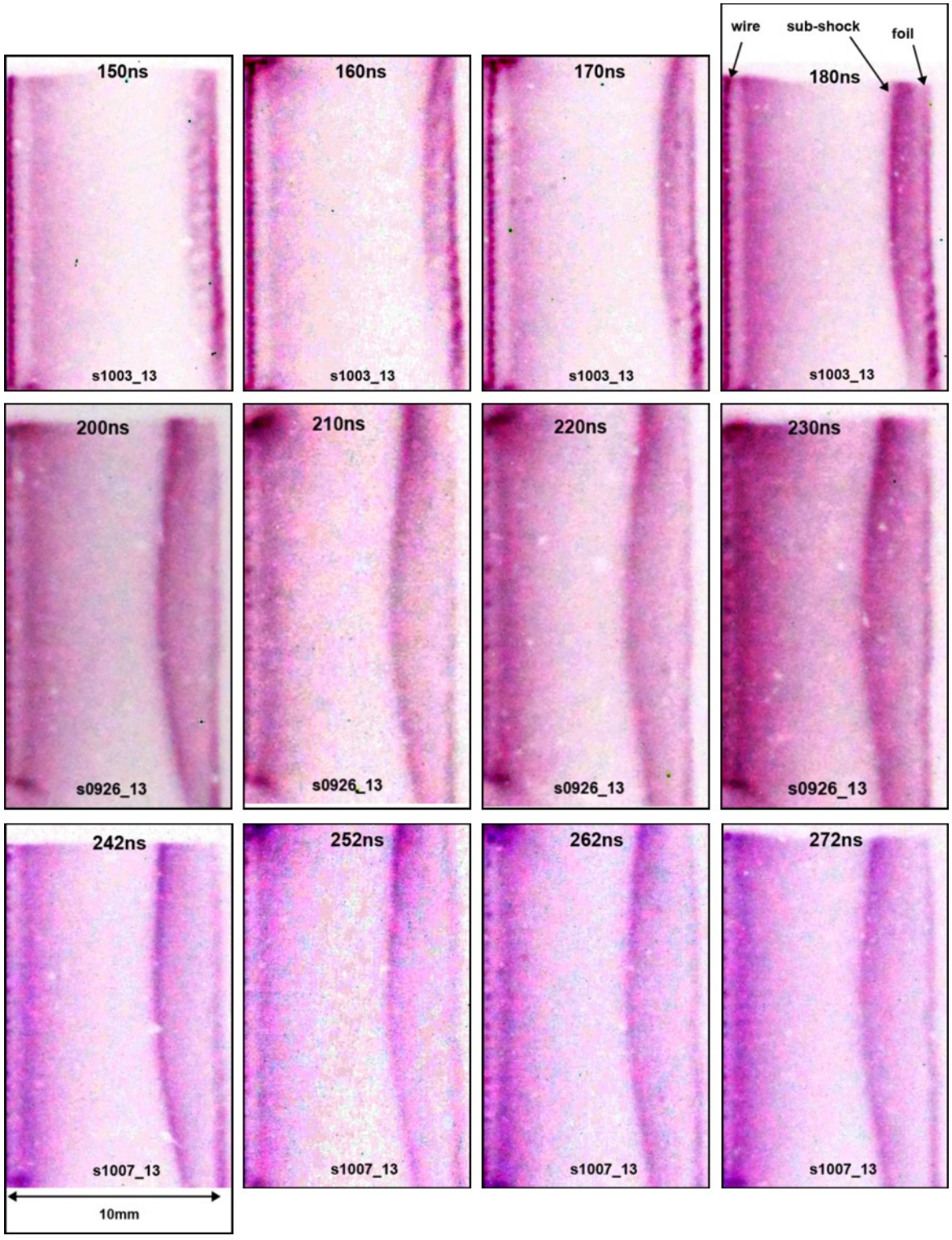


FIG. 5.4 A (false-colour) XUV self-emission timeline of the flow-obstacle interaction, recorded from a side-on perspective over multiple experiments. The flow is from the ablating wire array, positioned vertically on the left hand side of the image, towards the planar obstacle on the right hand side (also vertically aligned in the images). The distinct, curved sub-shock stands off from the obstacle (with its emitting surface stagnation layer) at an increasing distance with time.

slightly further upstream than the lower part, and shows a greater intensity of emission. This indicates that there is a greater driving force behind the sub-shock at the higher vertical position, and so has to move further upstream than the lower part to achieve a pressure balance with the oncoming flow. (Note that the ram pressure increases upstream in the flow due to the spatial density profile of the flow which is always falling away from the array.)

In one experiment images were taken with a 2μm polycarbonate filter placed over two out of four of the pinhole apertures of the XUV camera imaging system (see section 3.5.1 for details of the setup) in order to gain an estimate of the energy of the observed emission. This filter acts as a soft radiation filter and is specified with a transmission curve allowing light only with photon energies of $h\nu \approx 200 - 300\text{eV}$ and $\gtrsim 600\text{eV}$ [36] to pass. It was found that all emission above the background noise level of the MCP was blocked from the filtered frames, whilst the unfiltered frames recorded a consistent intensity with previous experiments. This therefore indicates that all plasma in the array-obstacle region is "cool", with $k_B T \ll 200\text{eV}$.

A more detailed and quantitative analysis of the shock structure is now given from laser probing images of the interaction region.

5.3.2 Structures observed with laser probing

Fig 5.5 shows a typical interferogram of the full array-foil interaction region, obtained from side-on laser probing in 532nm. The image in Fig. 5.5a is taken at $t = 250\text{ns}$ after current start when all the observed features are well defined. The original positions of the array wires and foil surface are marked and the scales of various key features illustrated. The interference fringes here are shifted relative to their pre-shot distribution, which is shown for comparison in Fig. 5.5b. The accompanying image in Fig. 5.5c plots the areal density map unfolded from the fringe shift calculation.

The image shows that there is a narrow, opaque region directly in front of the foil surface, corresponding to an area of high density plasma. This is the same layer of accumulated plasma which was observed from its bright emission in the optical and XUV, and shows a thickness consistent with the previous measurements of ~400μm. It is noted that the apparent opacity of the layer here is likely not due to the region exceeding the critical density cut-off of the probing system, but rather due to high density gradients here perturbing the laser beyond the acceptance angle of the imaging optics. The cut-off electron density n_c for a $\lambda = 532\text{nm}$ system is $4 \times 10^{21}\,\text{e/cm}^3$ – several

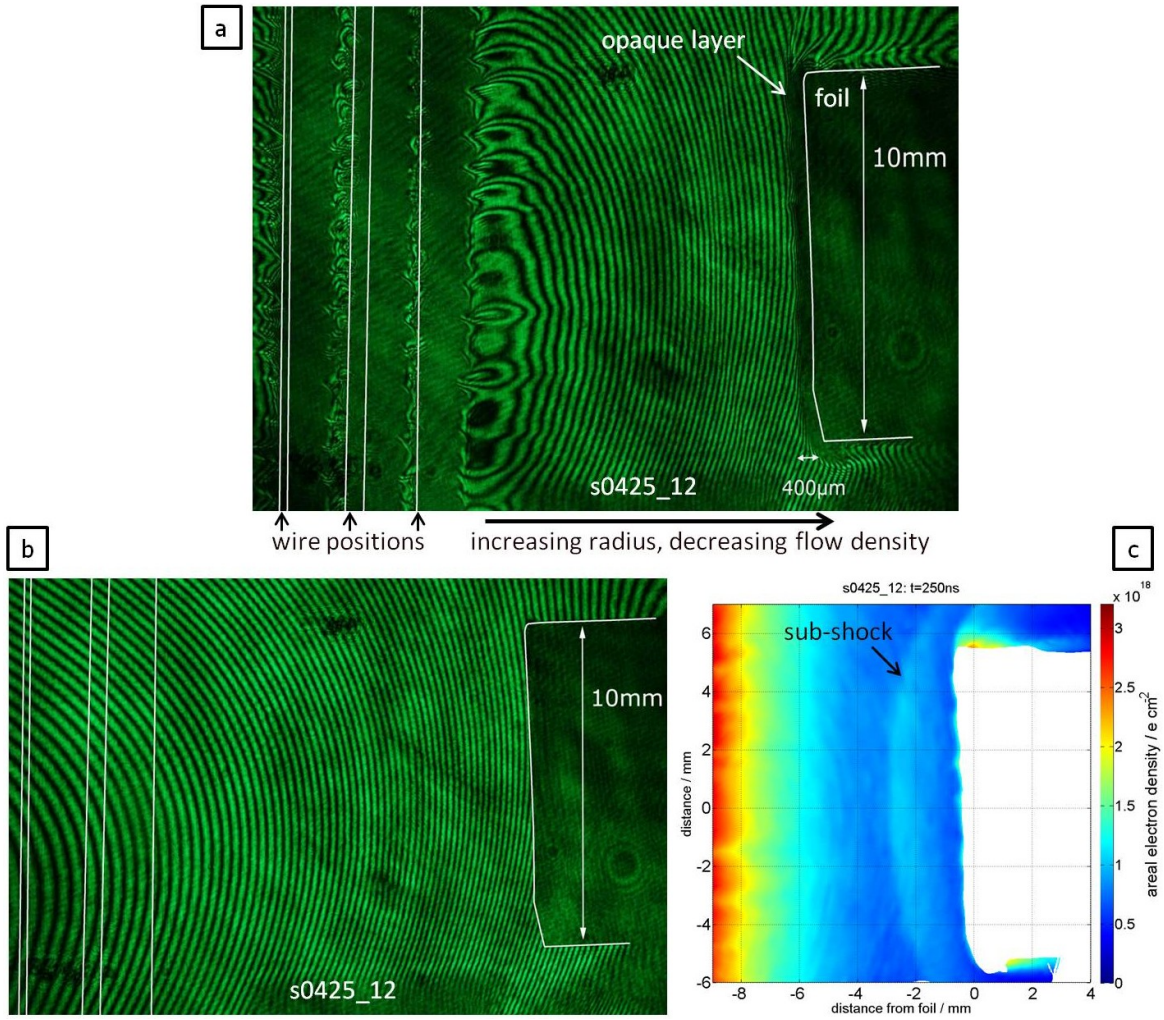


FIG. 5.5 (a) Side-on (532nm) laser interferometry data showing the full array-foil reverse shock interaction region at t=250ns, accompanied by (b) the pre-shot interference pattern for comparison, and (c) the areal density map from the fringe shift calculation.

orders of magnitude larger than the expected density range of $10^{17} - 10^{19}\,\mathrm{e/cm^3}$ (predicted from the assumption that the density should be approximately a factor of $\sim 4\times$ the upstream flow for a strong shock). Indeed it is possible to verify this estimate from a calculation of the average density inside the reverse shock layer, owing to the material flux into the region at the time of the image. Using the Rocket model described in [24], the total mass per unit length δm(t) ablated from a cylindrical wire array can be found (in S.I. units) from the integral

$$\delta m(t) = \frac{\mu_0}{4\pi v R_0}\int_0^t I^2 dt', \qquad (5.1)$$

where v is the (constant) plasma flow velocity (10^7 cm/s), R_0 is the radial size of the array (1cm) and the current form $I(t) = I_{max} \cdot \sin^2(\pi t/500ns)$ can be substituted. Due to the symmetry of the array the mass from a pair of wires in a 16 wire array should therefore be $1/8^{th}$ of this. Operating under the assumption that this mass then accumulates entirely inside the $400\mu m \times 10mm$ area A of the opaque layer seen in the images, and adjusting the limit of the integral to allow for the time of flight for the material to reach the foil surface, this gives an average density inside the layer of

$$\rho_{av} = \frac{\mu_0 I_{max}}{32\pi v R_0 A}\int_0^{t-r/v} \sin^4\left(\frac{\pi t'}{500ns}\right) dt'$$

$$= \frac{\mu_0 I_{max}}{32\pi v R_0 A}\left[\frac{3t'}{8} + \frac{125ns \cdot \sin\left(\frac{\pi t'}{125ns}\right)}{8\pi} - \frac{125ns \cdot \sin\left(\frac{\pi t'}{250ns}\right)}{\pi}\right]_0^{t-r/v}. \quad (5.2)$$

In the experiment (s0425_12) which the image data was taken from, only 75% of the maximum current capability was achieved[2], giving $I_{max} \simeq 1MA$. At the time of the image ($t = 250ns$) this gives an average mass density inside the layer of $\rho_{av} = 5 \times 10^{-2}\,kg/m^3$. Taking the mass of aluminium ions to be $m_i(Al) = 27m_p$, and assuming Z~4, this equates to an average electron density of $n_e \sim 4 \times 10^{18}\,e/cm^3$, which falls within the predicted range. Comparing this to the flow density immediately upstream of the stagnation layer of $n_e \sim 7 \times 10^{17}\,e/cm^3$, and neglecting possible changes in ionisation, this gives a compression ratio of $n_d/n_u \sim 6$, which corresponds via equation 2.10 to an adiabatic index of $\gamma = 1.4$.

An alternative estimate of the compression can also be found from a comparison of the upstream and reverse shock flow speeds, which should provide a more reliable calculation as it does not rely upon the assumption of a rocket model flow. Due to conservation of material across the shock transition, the velocity ratio should reflect the reciprocal of the up- and downstream density ratio. Taking an average expansion velocity of the shock layer as its 400μm thickness, divided by the $(250 - 70)ns = 180ns$ accumulation time of the stagnated material ($= 2.2 \times 10^5$ cm/s), this yields a far greater compression ratio for the layer of $n_d/n_u \sim 50$ (i.e. a downstream density of $n_e \sim 3.5 \times 10^{19}\,e/cm^3$) and a corresponding adiabatic index of $\gamma = 1.04$, characteristic of an ionising plasma [23]. At present no further verification of the reverse shock properties exist,

[2] This was due to a single Marx bank firing out of sync, delivering its current after the experimental timescale.

however future investigation of this feature would be of significant interest, as it may provide some insight into the radiative perturbations caused to the structure of this strong, reverse shock. At present a mono-chromatic x-ray back-lighting diagnostic, based on the principle of Bragg reflection from a spherically-bent, quartz crystal, is being developed for use on MAGPIE [70]. It is noted that this may provide an ideal opportunity to study the high density / density-gradient conditions observed here, for which a larger transmission would be expected using the higher probing energy.

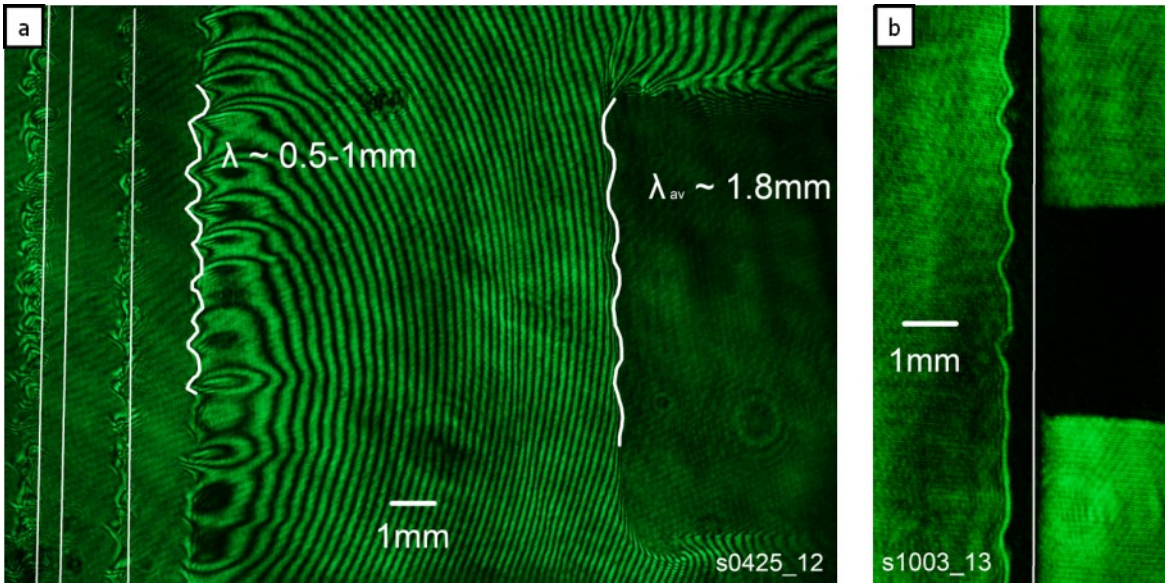


FIG. 5.6 (a) Highlighted in the interferometry data from Fig. 5.6 are: (*right*) modulations in the stagnation layer shock front, and (*left*) fluctuations in the wire ablation. The average wavelength for each feature is estimated. (b) High magnification image of the reverse shock front modulations from a different experiment. The position of the foil surface is marked in white.

Returning to the observed structure, the wave-like modulations in the shock front of the stagnated layer, which were observed in the XUV images (Fig 5.4), are again observed in the laser-probing data. They are highlighted on an annotated version of the same interferogram in Fig 5.6a and shown at high magnification in a shadowgram from a different experiment in Fig 5.6b. At present it is unclear what the source of these modulations is. One possibility is that the variance could be associated with axial non-uniformity in upstream flow. Axial modulations in the ablation rate along the length of the wires are an established characteristic of both standard [24,50,57] and inverse arrays [6,7], and are indicated in the interferometry data here (Fig 5.6a). There does not however seem to be an obvious correlation between the natural frequencies of the two features, with a factor of $2-3$ difference between their measured average wavelengths.

It can also be argued that the fluctuations in ablation should have negligible effect on the flow at the distance of the shock target, due to merging of the streams in the close proximity of the wires – as was observed for inverse arrays in [6,7]. The axial density profile does indeed seem to be fairly uniform for $r > 4\text{mm}$ from the wires, as demonstrated for example in the data of Fig. 4.8. An alternative suggestion for the source of the modulations could be the development of an instability in the shock front. With the presence of a high density reverse shock layer moving into the lower density upstream flow a Rayleigh-Taylor type instability might be considered a likely candidate; however others including current driven MHD instabilities or thermal instabilities (due to rapid cooling behind the shock) also remain feasible.

The detached, upstream sub-shock feature is again observed in the laser-probing data. This feature, which can be identified by the trained eye in the raw interferometry image, is best revealed in the areal density map of Fig. 5.5c as a bow-like increase in plasma density, $\sim 2.5 - 3\text{mm}$ ahead of the foil. In comparison to the previously described reverse shock at the foil surface, the sub-shock shows a considerably lower density jump relative to the plasma flow directly upstream; with an areal density increase of only a factor of ~ 2 across the transition. It is possible however that the data may disguise the true extent of the compression, due to curvature of the sub-shock front in the orthogonal $(r - \theta)$ plane smoothing out the perceived profile. As was shown by the end-on optical emission images in Fig. 5.3, the sub-shock front shows significant curvature in this plane at times shortly after formation and only reaches an approximately planar shape by $t \approx 260 - 270\text{ns}$. Thus the side-on interferometry data obtained before this time will contain at least some degree of smoothing. Despite this, a measure of the thickness of the sub-shock transition can be made from side-on shadowgraphy-Schlieren images of the region.

Fig. 5.7 shows a shadowgram which was taken at a slightly earlier time ($t = 225\text{ns}$) with an aperture surrounding the focal point of the imaging system. The aperture acts as a spatial filter for any laser light which has been perturbed from its normal optical path by high density gradients within the plasma, and the image therefore shows a "light-field Schlieren" effect; whereby steep transitions in density such as shock fronts appear as darkened regions. The darkening at the sub-shock in this image appears as a very narrow layer, whose thickness is of order the 100μm resolution of the imaging system, and therefore acts as an upper limit for the sub-shock thickness.

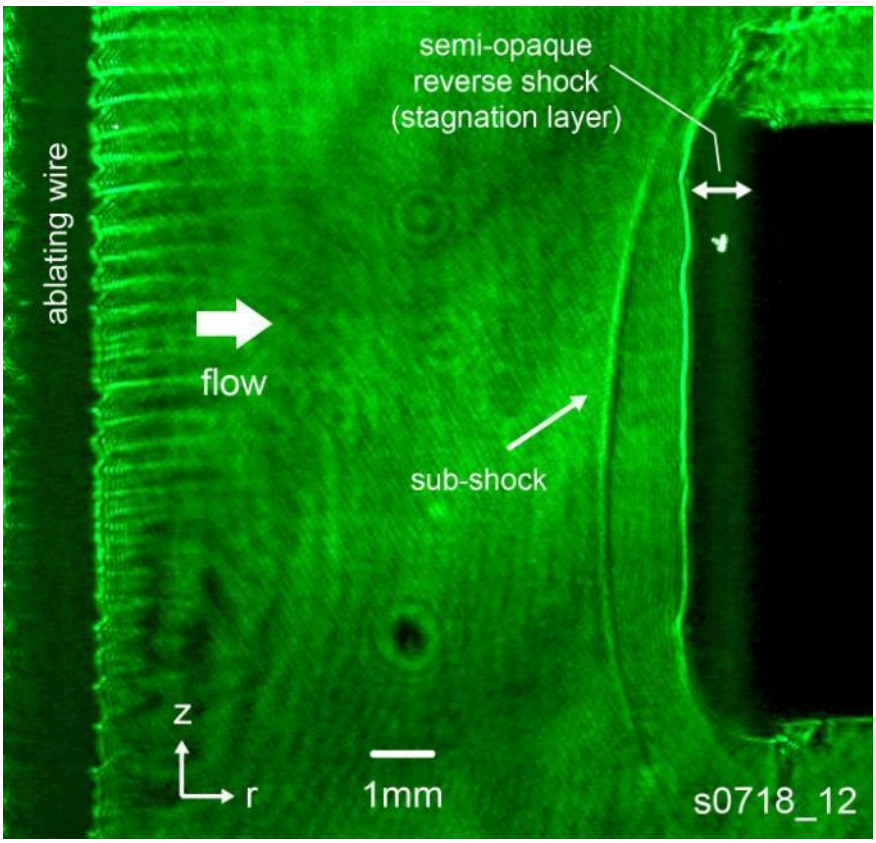


FIG. 5.7 Side-on shadowography / light-frame Schlieren image of the reverse shock region showing the narrow transition thickness of the sub-shock (curved arc shape). The ablating wire is shown on the left of the image with the foil obstacle and its attached stagnation layer (appearing semi-opaque) on the right.

The plasma-foil interaction was also imaged with the laser probing system from the end-on (z) direction. Fig. 5.8 shows an example of interferometry data taken from this perspective at t = 225ns. At this experimental time the sub-shock front is beginning to become planar. The fringes, which were distributed approximately parallel with the foil surface in the pre-shot image, show a compression – corresponding to an increase in electron density at the sub-shock position, followed by a downstream rarefaction indicating a subsequent density drop-off before again compressing heavily directly ahead of the opaque, stagnated plasma layer. Unsurprisingly the sub-shock appears even more extended in the areal density map calculated from this image. This is due to the greater extent of vertical curvature shown by the feature. Whereas the sub-shock flattens in the r – θ plane for mid-late times, the vertical curvature remains throughout the experimental timescale, as was demonstrated in the side-on XUV images. Thus for times $\gtrsim$ 230ns (optical emission time-line, Fig. 5.3) side-on interferometry measurements can be expected to yield a more representative average electron density

profile of the sub-shock than the end-on interferometry, due to the less significant curvature in the orthogonal plane (that is, provided only a simple estimation of $N_f \propto n_e L$ is being used). A full consideration of the geometry using Abel-inversion techniques [58] would provide a more accurate calculation, and would require simultaneous data from each perspective. Even in the simple case however, interferometry from the end-on perspective remains useful for determining the appropriate thickness length L of the structures observed in the side-on images.

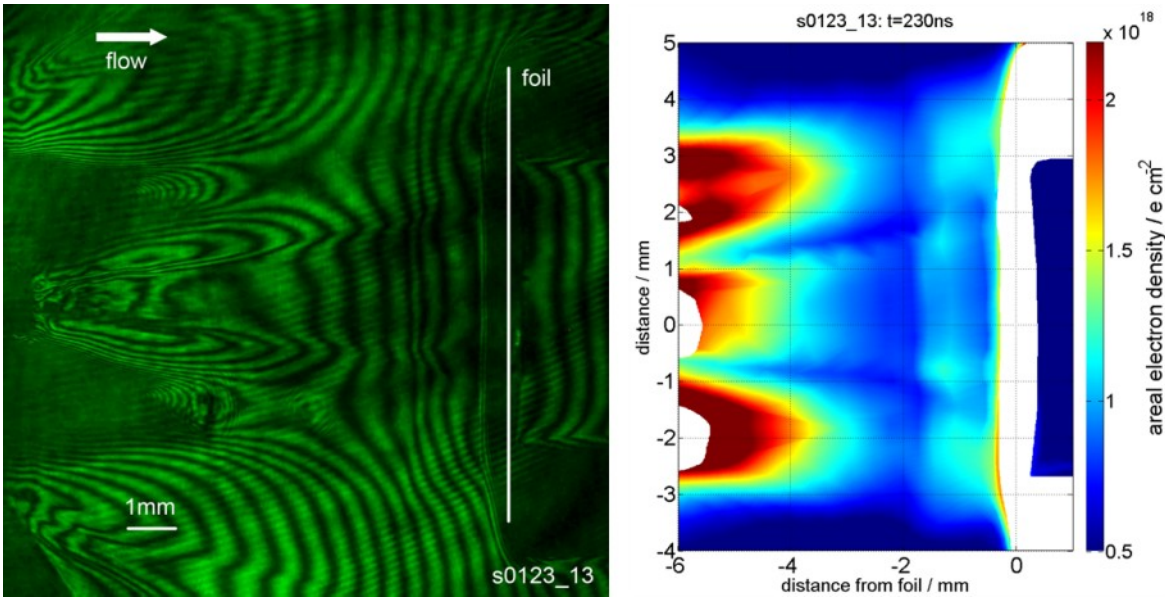


FIG. 5.8 End-on perspective interferometry data taken at t=225ns, showing the raw data (left) and calculated electron density map (right).

5.4 Spatial profiles of the plasma properties through the reverse shocks

5.4.1 Diagnostic setup for experiments with simultaneous Thomson scattering and laser interferometry

Several experiments were performed with simultaneous Thomson scattering (TS) and interferometry diagnostics to allow a comparison of the velocity and electron density profiles through the flow-obstacle interaction region. TS measurements were made with both the input beam and collection fibres in the same (horizontal) $r - \theta$ plane, allowing the plasma velocity vectors within this plane to be constructed at each of several scattering positions along the probing beam path. Laser probing for the interferometry system was carried out from the end-on direction; due to the limited number of

remaining MAGPIE chamber ports, and also because this enabled the exact scattering positions of the TS system to be recorded onto the interferometry images during the pre-shot alignment process. This process (which is described in [61,65]) was achieved by mounting a 100μm diameter, vertically suspended needle to a fine-adjustment, $x-y-z$ translation stage, in order that it could be inserted and accurately manoeuvred in the space between the array and foil shock target. The pin was positioned into the region of interest and the input beam aligned to the needle. The light scattered from the needle was then focussed onto the first fibre in the array of collection fibres and a pre-shot (un-Doppler shifted) spectrum recorded on the spectrometer. The needle was sequentially translated to each of the positions at which the scattered light was received by the remaining fibres and their linear separation noted. Pre-shot images of the scattered light from the needle were also taken with the end-on interferometer camera, allowing the positions of the TS measurements to be mapped onto the images of the $r-\theta$ plane.

Several alternate scattering geometries were used for the TS diagnostic, which are illustrated in Fig. 5.9. Early experiments were carried out in the geometry shown in Fig. 5.9a, where the focussed probing laser beam was passed between the wires of the array and through the central region of the flow-obstacle interaction at an angle to foil surface. The scattered signal could then be collected from the two opposite directions parallel to the foil surface.

This setup was found to have the disadvantage that unwanted stray light was collected by the spectrometer fibres from the reflection of the TS beam incident on the foil surface. Attempts were made to reduce the scattered light, both by using a smaller, 5mm width foil, with the beam avoiding the foil surface as shown in Fig. 5.9b, and later by introducing a small (~1mm diameter) exit hole in the foil. The presence of this hole was not found to have any noticeable effect on the reverse shock structure, either in the interferometry data or on the measured velocity profiles.

A later modification to the geometry was also made to avoid out-of-plane defocusing associated with an incident beam that was not perpendicular to the collection fibre bundle. In the modified setup, shown in Fig. 5.9c, the input beam was passed directly through a 2mm hole in the central cathode post of the array, and along the centreline of the interaction region, perpendicular to the scattering directions, exiting again through a 1mm hole in the foil. In several experiments the foil was placed on the opposite side of the array, with the laser beam first passing through this hole in the foil from behind, before then continuing through the wire array / cathode as before. This geometry, with

the addition of several baffle plates was found to keep stray light levels at a minimum, although the presence of stray light was never entirely eradicated.

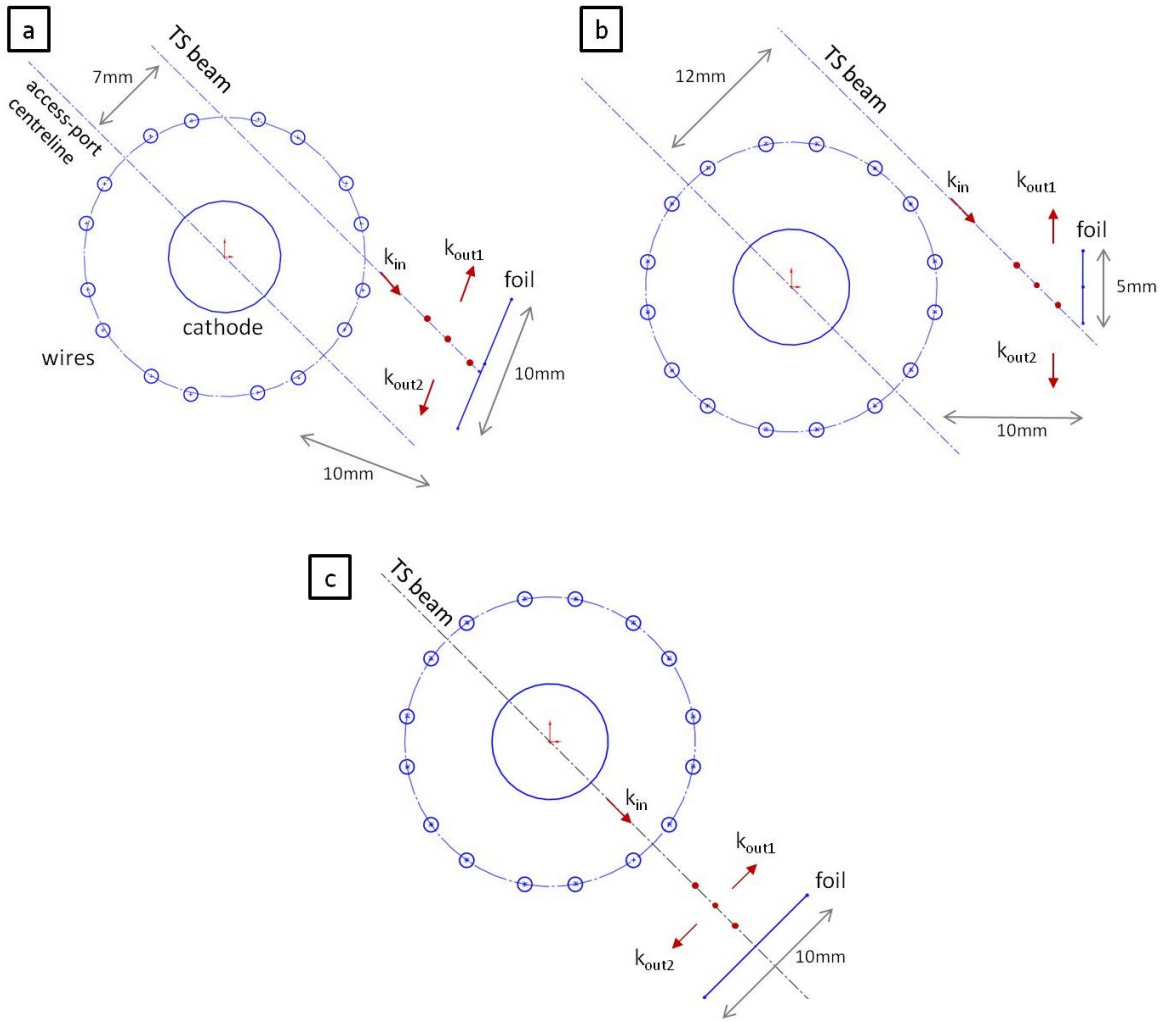


FIG. 5.9 Scale drawings of the probing and scattering geometry used for Thomson scattering experiments of the reverse shock interaction, shown from an end-on perspective. The trajectory of the probing TS beam relative to the array wires and foil is illustrated, as well as the direction of the input and output (scattered) wavevectors and several scattering positions. In early experiments, using the setups shown in (a) and (b), the probing beam was horizontally offset from the centreline of the MAGPIE chamber access port (indicated) to avoid hitting the central cathode of the array; and the beam entered the interaction region at an angle to the foil surface. In a later modification (c) issues arising from this of reflective stray light and of out-of-plane defocusing of the scattering positions at the observation ports were tackled by passing the beam directly through the centre of the array via small (~1mm) holes in the central cathode post and foil surface.

5.4.2 Comparison of plasma density and velocity profiles through the sub-shock

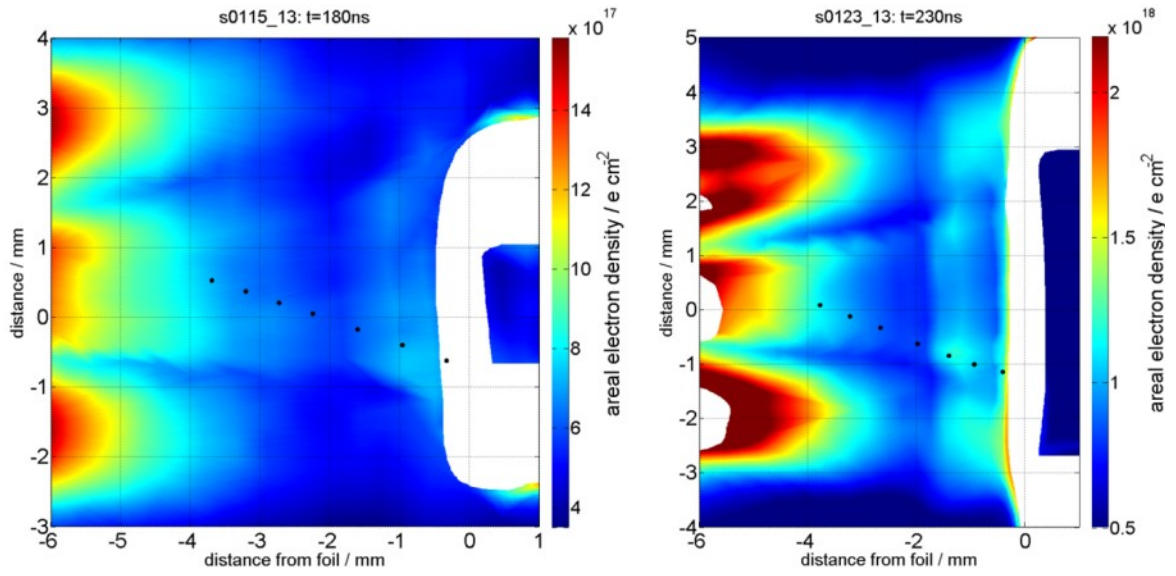


FIG. 5.10 End-on areal electron density maps from two experiments with simultaneous interferometry and TS measurements. The positions of the TS collection along the laser beam-line are marked in black.

Here data is presented from experiments using the geometric setup shown in Fig. 5.9a. Areal electron density maps from the end-on laser probing are given in Fig. 5.10, with the spatial positions of the TS measurements marked. The two interferograms were taken at t = 180ns and t = 225ns after current start, with $5 \times 5\text{mm}^2$ and $10 \times 5\text{mm}^2$ foils respectively. The first of these times corresponds to shortly after the first observation of the sub-shock feature, and the second to when all the main features of the interaction are well established. In these experiments Thomson scattered light was collected from only a single direction parallel to the foil surface – the direction labelled $\mathbf{k}_{\text{out1}}$ in Fig. 5.9a. This direction was chosen as it was the least prone to stray light reflected from the foil surface[3]. The anti-parallel direction was not used in these early iterations of the interferometry-TS experiments as the access port was occupied by the imaging optics for the end-on laser system. Therefore velocity measurements from the scattered signal were made only in the direction of the $\mathbf{k}_{\text{s1}} = \mathbf{k}_{\text{out1}} - \mathbf{k}_{\text{in}}$ vector, with the full velocity vector assumed to be purely in the radial direction of the array (i.e. 1D flow onto the

[3] Note: in the second of these experiments a hole was placed in the foil surface to attempt to reduce stray light.

foil). This was later found in experiments using a dual direction TS setup to be an accurate assumption (as discussed in sections 4.5 and 5.4.3).

Fig. 5.11 shows the spectrometer CCD read-outs for the 7 collection fibres in each of these experiments. The fibre array is aligned vertically (along the y-axis) to the CCD with the 2400l/mm grating orientated such that the spectrum from each fibre is refracted horizontally, plotting the constituent wavelengths of each signal linearly along the x-axis (centred on the un-shifted laser wavelength of ~532nm). The fibres run sequentially from the upstream-most scattering position at the top of the CCD image (fibre 1) to the position closest to the foil surface at the bottom of the image (fibre 7).

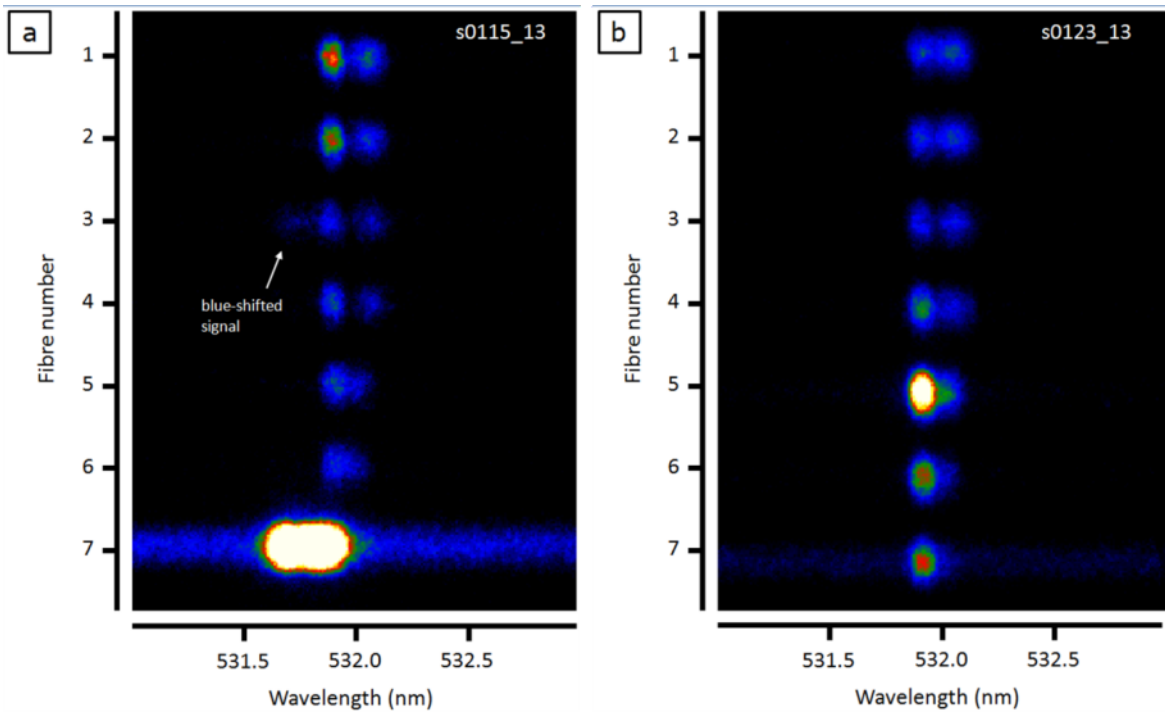


FIG. 5.11 Images of the Thomson scattering spectrometer CCD, showing the spectral peaks for each of the fibre positions in Fig. 5.10.

A significant amount of stray light is superimposed on the spectra, showing up at the original wavelength of the laser, and appears slightly more intense than the TS signal. The TS signal is seen at predominately red-shifted positions (to the right of the stray light) indicating in this geometry that the plasma flow is moving with an anti-parallel/negative component in the $\mathbf{k}_{s1}$-direction, and therefore (assuming radial trajectory) towards the foil target. In both experiments the first four fibres are positioned upstream of the sub-shock front, and show an approximately constant shift, and hence flow velocity. Immediately downstream of this feature, at the fifth fibre

position, the plasma is seen to move with a noticeably slower velocity, however the TS signal here is still red-shifted showing that the flow has not completely stopped and continues towards the foil surface, with a decelerated flow speed across the remaining fibres. The final scattering position shows a noticeably higher intensity of background / broadband radiation, indicating that the plasma close to the foil surface / inside the stagnation layer is hotter and more brightly emitting. In the case of the first CCD image (Fig. 5.11a) the intensity of the stray and scattered light is also much higher which may be attributed to a higher density in the plasma. The final TS position in this experiment is both closer to the foil surface, at a distance of only ~0.3mm (inside the stagnated plasma layer), and is also adjacent to the position where the beam is incident with the foil (since no escape hole was used in this experiment). The signal, which appears blue-shifted, shows the reverse propagation of the ions, which may be due in part to both the reverse shocked material as well as the laser-heated ablation of the foil. A second blue-shifted signal is also seen at the third fibre in this experiment, ahead of the sub-shock. The presence of both forwards and rearwards motion here indicates that some portion of the ions might be reflected by the sub-shock front, particularly since their velocity seems to be roughly equal in magnitude. The absence of blue-shifted ions at the later time however indicates that this may only be a transient phenomenon associated with the formation of the sub-shock. Assuming that the ions are travelling upstream with an approximately constant velocity their origin can be traced back to either the sub-shock front at $t \approx 175$ns, or the stagnated layer at $t \approx 165$ns.

To gain a quantitative measure of the flow velocity at each of the TS positions Gaussian profiles were fitted to the data, with the central wavelength of each peak compared to the pre-shot wavelength, thus giving the Doppler shift. This was done by means of a least-squares-fit to the portion of the spectrum least affected by the unwanted stray light signal, and is therefore most accurate for the upstream positions whose peaks were shifted furthest from the original wavelength. Fig 5.12 shows the fitted spectra for the data at $t = 180$ns. The velocity profiles calculated from the Doppler shift measurements are presented in Fig. 5.13a and b, for $t = 180$ns and $t = 225$ns respectively, and plotted against their perpendicular distance x(mm) from the foil. They show that the post-sub-shock flow velocity falls to about 60% of the upstream value and thereafter continues to decrease reaching ~30% at the boundary with the dense plasma in front of the foil surface. The rearwards propagating ions are also measured to be travelling with equal speed to the upstream ions, supporting the hypothesis of an elastic reflection either from the sub-shock front or closer to the foil.

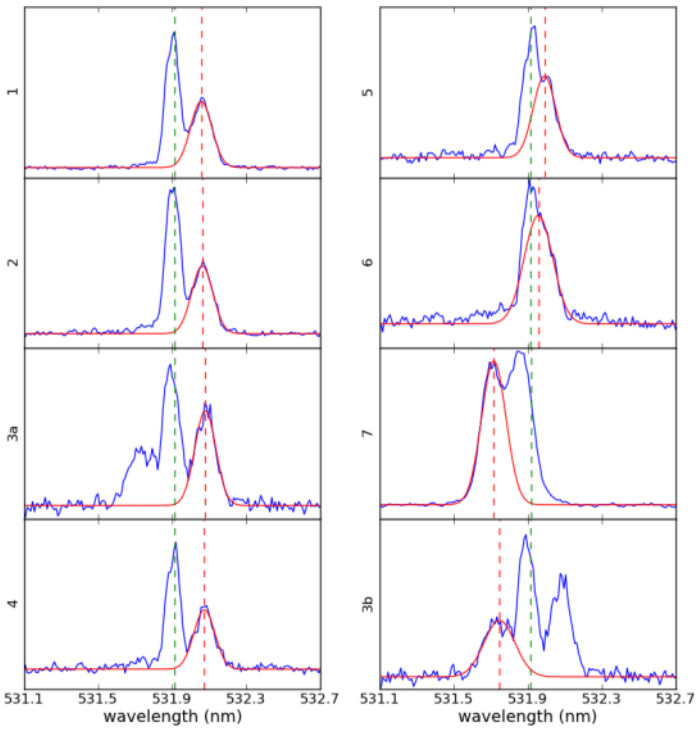


FIG. 5.12 Gaussian fits to the spectrometer data in Fig. 5.11a for t=180ns (s0115_13). Data is averaged over several rows of pixels on the CCD output for each of the 7 fibres. The blue lines in the image show the raw signal, with the Gaussian profiles over-plotted in red, and the red and green vertical dashed lines indicating the shifted and un-shifted (pre-shot) central wavelengths respectively. Fibre 3 is fitted for both the red-shifted and blue-shifted ion motion peaks (labelled 3a and 3b). [Image credit: M. Bennett, MAGPIE GROUP].

Electron density profiles from the end-on interferometry are also plotted in Fig. 5.13 in graphs (c) and (d) (green lines), again with x(mm) denoted here as the perpendicular distance to the foil. The areal electron density was measured from a line-out taken along the fibre positions. The values of n_e were then calculated from the areal density assuming a form

$$\int n_e \cdot dl \approx n_e L_s + n_{eb} L_b, \tag{5.3}$$

where L_s is the vertical thickness of the foil-interaction region (5mm), L_b is the thickness of the background plasma flow above and below this (15mm array – 5mm interaction = 10mm) and n_{eb} is the electron density inside the background plasma. This background density was found from simultaneous side-on laser probing of an undisturbed plasma flow on the far-side of the array, and its profile is over-plotted (as $n_{eb}L$) in Fig. 5.13d for comparison.

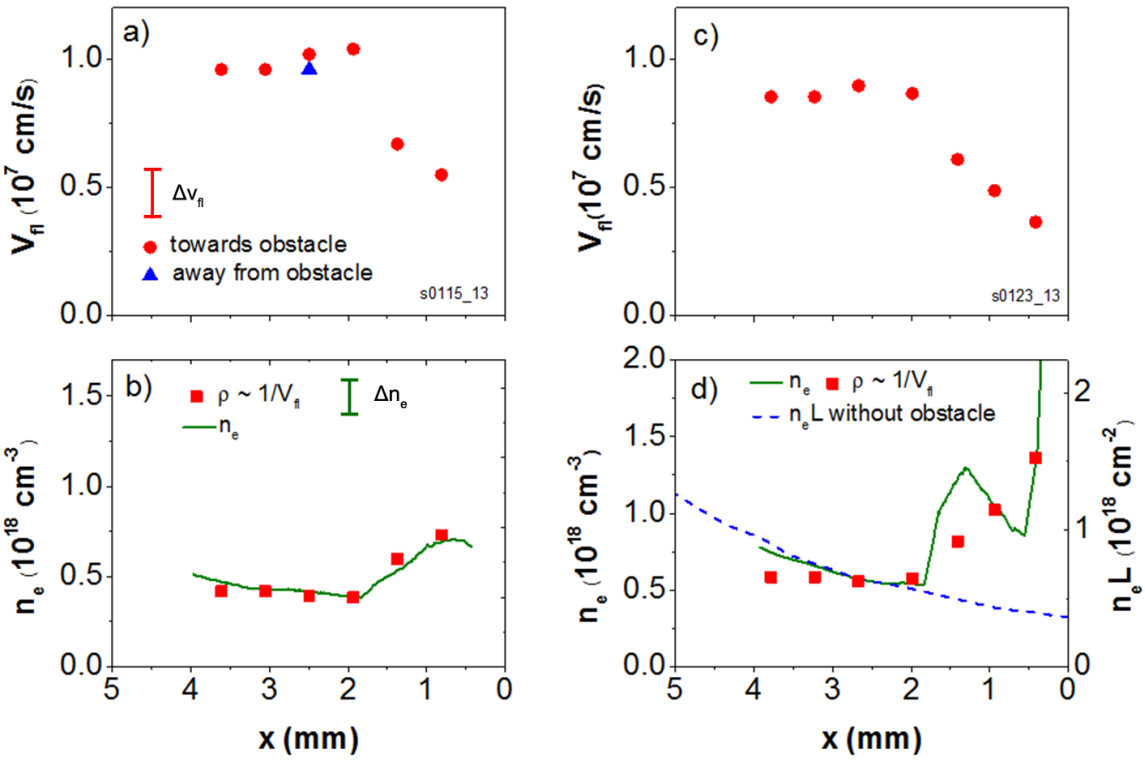


FIG. 5.13 Plots of the plasma flow velocity profiles measured from TS at (a) t=180ns and (c) 225ns, as well as, (b) and (d), profiles of electron density (interferometry) and relative mass density calculated from the velocity profiles at these times.

The electron density profiles seem to indicate that there is only a small increase in n_e at the sub-shock, of not more than a factor of ~2 in comparison to the upstream density, and the data shows a steepening of the transition profile with time. However reference must again be made to the potential underestimation of the density increase here due to the r – z plane curvature of the sub-shock. Thus the density immediately after the sub-shock may be slightly higher than represented here and the transition likely narrower. In contrast the TS provides local measurements of the flow velocity and is therefore a better indicator of the flow behaviour at the sub-shock.

It is instructive to compare the measured electron density profiles with mass density distributions which can be estimated using the measured velocities. Since the sub-shock position is moving relatively slowly in comparison with the flow speed (~10% of v_{flow}) one can use conservation of mass about this position to say that the mass density should scale as $\rho(x) \sim 1/v_{flow}(x)$, under the approximation of a time-independent density in the upstream flow. Density profiles calculated in this way are shown in red in Fig. 5.13c and d, and plotted on an arbitrary y-scale which is normalised to overlap with the upstream

electron density profile. For the temporally increasing density of the flow the estimated values represent an upper limit for the mass density profile. This is because each data point after the sub-shock corresponds to an earlier experimental time (as given by the time-of-flight from the sub-shock) when the density was lower and the velocity greater. Nevertheless, comparison of the electron and mass density profiles shows a divergence in the flow immediately downstream of the sub-shock at t = 225ns, which indicates an increase in the average plasma ionisation at the sub-shock at this fully-formed stage in its evolution. The convergence of profiles further downstream however may indicate the plasmas subsequent cooling and re-ionisation.

5.4.3 Spectral fitting to the Thomson scattered signal

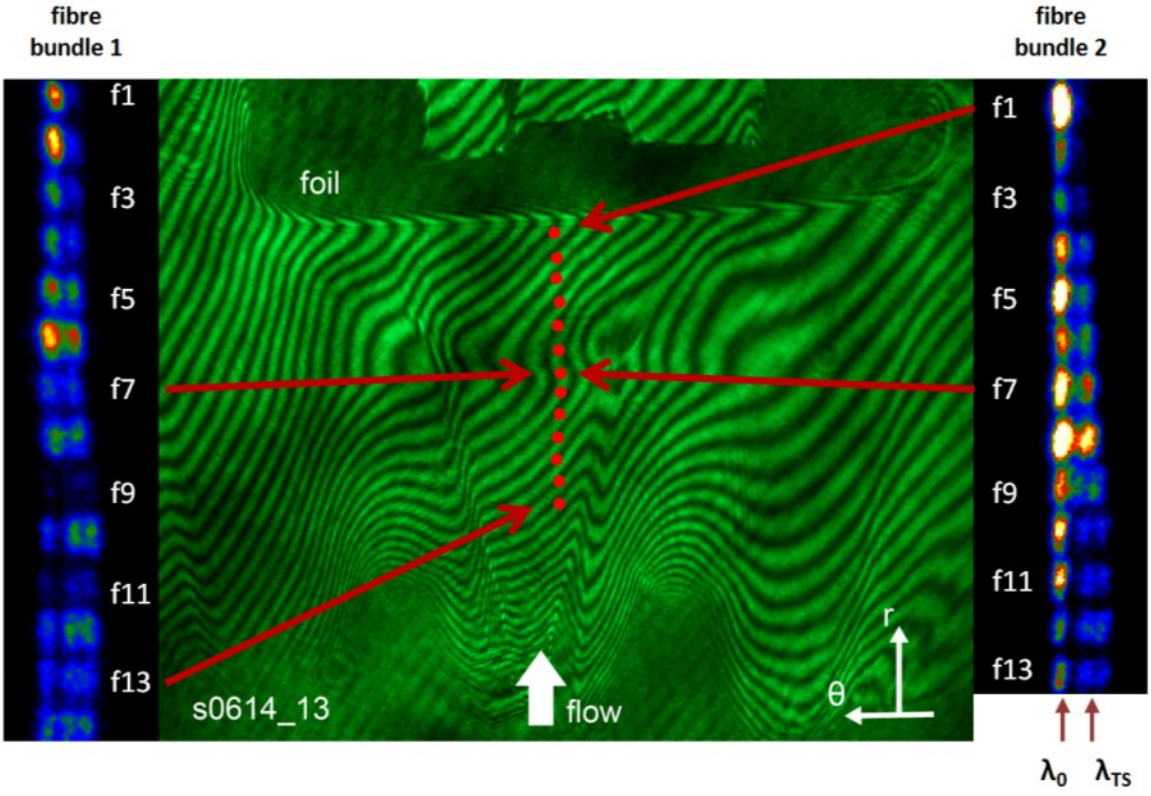


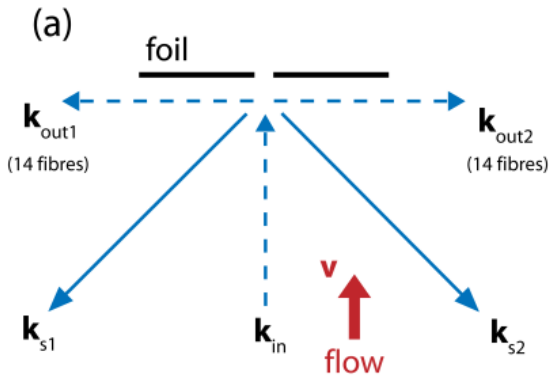
FIG. 5.14 End-on interferogram with accompanying TS positions and spectrometer CCD images of the scattered spectra for the two fibre bundles. This TS data was obtained with the high-res (14-fibre per bundle) setup, and shows the resolved double peak structure of the scattered spectra in the upstream flow. (Note: no signal was obtained for fibre 14 of the second bundle, due to vertical misalignment with the CCD).

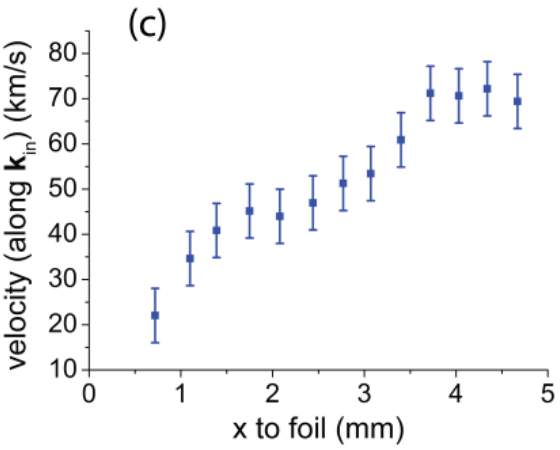
Several TS-interferometry experiments were carried out using the modified geometry setup shown in Fig. 5.9c, in combination with a fibre collection system of higher spatial resolution, which allowed a greater spectral resolution at the spectrometer. Instead of

using $7 \times 200\mu m$ fibres, giving 0.45Å spectral resolution, the collection optics were replaced with an equal length array of $14 \times 100\mu m$ fibres, resulting in a 0.25Å spectral resolution. Collection fibres were also used at each of the opposite directions parallel to the foil surface (with the interferometry optics using an alternate port) allowing the full $r - \theta$ plane velocity to be measured.

The end-on interferogram from an experiment at $t = 250ns$ is presented in Fig. 5.14, with TS positions marked in red, and is accompanied by the spectrometer-CCD read-outs for each of the two fibre arrays. The fibre collection volumes in these images are displayed from the position closest to the foil (just upstream of the stagnation layer), at the top of the CCD, down to the position furthest upstream, ~4.5mm from the foil. The position of the sub-shock front lies at approximately fibre 9. As before, stray light remains at a significant level in the system and occupies the un-shifted laser wavelength (marked λ_0 in Fig. 5.14). The TS spectra appear red-shifted, indicating that the flow ahead of the stagnation layer is still moving towards the foil surface, with the symmetry between the two fibre arrays supporting the argument that the flow here behaves one dimensionally. A notable difference to previous data is the observation of closely-spaced double peaks in the TS spectra. These are particularly apparent for the upstream positions ahead of the sub-shock, but may also be present for the positions further downstream where the lower wavelength peak would be merged with the stray light signal. The double peak structure is indeed predicted for a TS spectra with $\alpha > 1$ (as was calculated in section 4.5). This ion acoustic resonance was likely unresolved in the 7 fibre setup due to its lower spectral resolution merging the features into a Gaussian-like distribution. The Doppler shift of each fibre is measured from the central wavelength between the resonances. Fig. 5.15 presents the velocity vector calculations from the Doppler shift measurements.

As concluded from the table of data in Fig. 5.15 the flow is to very good approximation one dimensional. The angle between the velocity vector and the radial axis ($\mathbf{k}_{in}$-direction) is $< 3°$ for all data points except those at the sub-shock and reverse shock positions where perturbations / turbulence due to the changing conditions are most likely to occur. The upstream flow velocity at this time appears to be reasonably constant, but with a speed of ~70 km/s which is slower in comparison to the earlier time measurements. The velocity after the sub-shock still shows a gradual decrease, reaching 75% upstream velocity immediately after the front, and 30% at the stagnation layer boundary, with signs of varying deceleration strength inbetween.





(b)

Fibre pair	x(mm) to foil	v_{s1} (km/s)	v_{s2} (km/s)	$\lvert v_{total} \rvert$ (km/s)	θ to normal (°)	v_{par} (km/s)	v_{perp} (km/s)
1	0.72	-19.8	-11.4	22.8	15.1	22.0	5.9
2	1.10	-25.4	-23.6	34.7	2.1	34.6	1.3
3	1.39	-29.3	-28.7	40.9	0.3	40.8	0.2
4	1.75	-32.2	-31.6	45.2	0.5	45.1	0.4
5	2.08	-32.6	-29.6	44.0	2.7	44.0	2.1
6	2.44	-32.7	-33.7	47.0	-0.8	47.0	-0.7
7	2.77	-35.5	-37.1	51.3	-1.3	51.3	-1.1
8	3.07	-33.8	-41.8	53.7	-6.0	53.4	-5.7
9	3.40	-47.3	-38.8	61.2	5.7	60.9	6.1
10	3.72	-51.6	-49.1	71.2	1.4	71.2	1.7
11	4.03	-48.8	-51.4	70.7	-1.7	70.6	-2.1
12	4.34	-49.2	-52.9	72.2	-2.1	72.2	-2.7
13	4.67	-48.8	-49.4	69.4	-0.3	69.4	-0.4
14	-	-44.8	-	-	-	-	-

FIG. 5.15 Velocity vector calculations using the 14 fibre TS data shown in Fig. 5.14. (a) The TS geometry: scattered light was collected in opposite directions by fibre pairs focussed on 14 collection volumes spaced along the input ($\mathbf{k}_{in}$) vector (as marked in the interferometry image), allowing the Doppler shift components to be measured along each of the orthogonal $\mathbf{k}_s$ directions. (b) Table of calculated Doppler shifts as a function of distance from the foil surface; showing velocity along each scattering direction, the total velocity magnitude, the angle of the velocity relative to $\mathbf{k}_{in}$, and the velocity components resolved parallel and perpendicular to $\mathbf{k}_{in}$. (c) A plot of flow velocity along $\mathbf{k}_{in}$ (normal to foil surface) as a function of distance from the foil surface.

Other parameters of the plasma can be estimated from fits of the TS signals to the theoretical form for the spectrum. The fits for two fibres, one up- and one downstream of the sub-shock, are shown in Fig. 5.16. The fits were performed "by-eye" and were found to show little dependence on T_i, with $ZT_e > T_i$ for both spectra. There was only a modest increase in ZT_e across the sub-shock by a factor of $\lesssim 2$, from (60 ± 5)eV to (110 ± 10)eV; as indicated by the increased width of the spectrum. Using the NLTE calculation, as shown in Fig. 4.11, this corresponds to $Z = 4.0 \pm 0.2$ and $T_e = (15 \pm 1)$eV upstream and $Z = 5.0 \pm 0.2$ and $T_e = (22 \pm 2)$eV downstream. Whilst T_i could not be accurately measured upstream, a fit to the central dip of the acoustic peak yielded a best estimate of $T_i = T_e \approx 25$eV downstream.

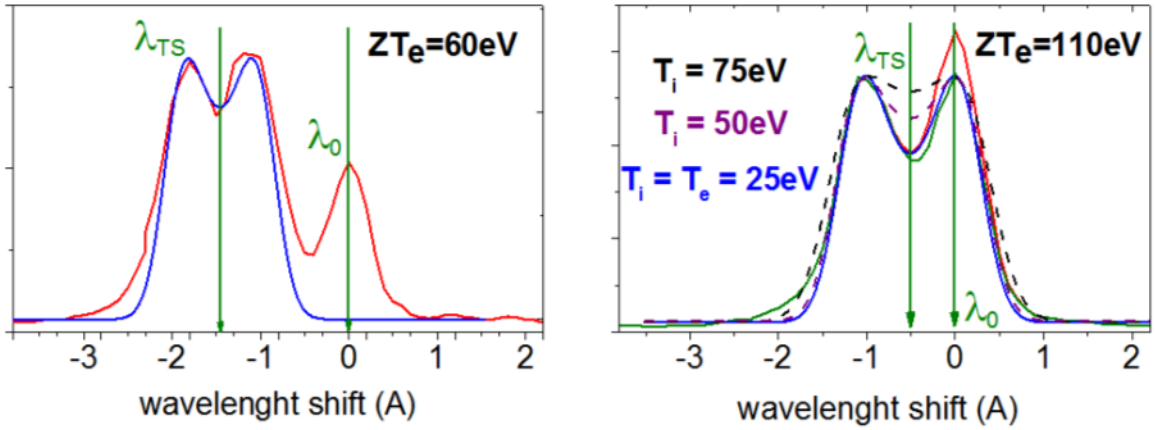


FIG. 5.16 The ion feature of the TS spectra measured in (left) the upstream flow and (right) after the sub-shock. The red profile shows the raw data signal, with various parameter fits made to this using the theoretical spectra form described in section 3.4.1.

5.4.4 Measurements of the magnetic field behind the sub-shock using inductive probes

The strength of the magnetic field advected by the plasma flow was monitored using the inductive probe-pair diagnostic previously described in sections 3.6. Measurements were made both when the foil obstacle was present and also when the flow was undisturbed. In each case the probes were placed at the same $8 - 8.5$mm distance from the wires; equivalent to the position at which the sub-shock front is first observed for an obstacle at a 10mm distance from the array wires. The probe pairs were held in place in the interaction region by vertically separated supports passing through 2mm diameter holes in the foil surface. The probe-obstacle arrangement is shown (pre-shot) in Fig. 5.17 from

a side-on perspective, obtained from the laser interferometer. Fig. 5.18 shows the combined dB/dt and integrated signals obtained from the probes both with and without the obstacle. Comparison of these shows identical behaviour until t~175ns, after which the signals diverge with the field appearing to grow more quickly with the obstacle present. A quantitative analysis of the field strength behind the sub-shock is not however possible from this data. This is because of the relatively large size of the probes, which is comparable to the distance between the sub-shock and the obstacle and therefore lacks the necessary spatial resolution for such measurements.

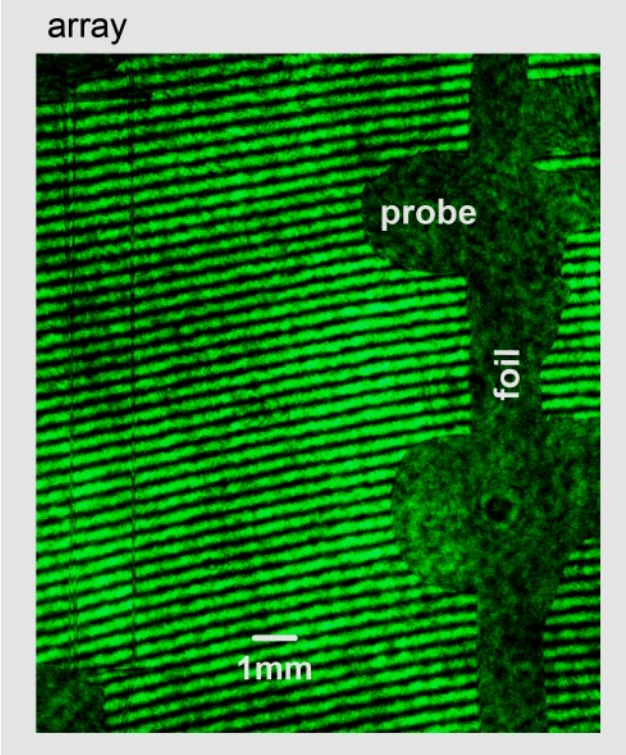


FIG. 5.17 A pre-experiment, side-on interferogram showing the magnetic field probe placed ahead of the foil for measurements of the post-sub-shock flux compression.

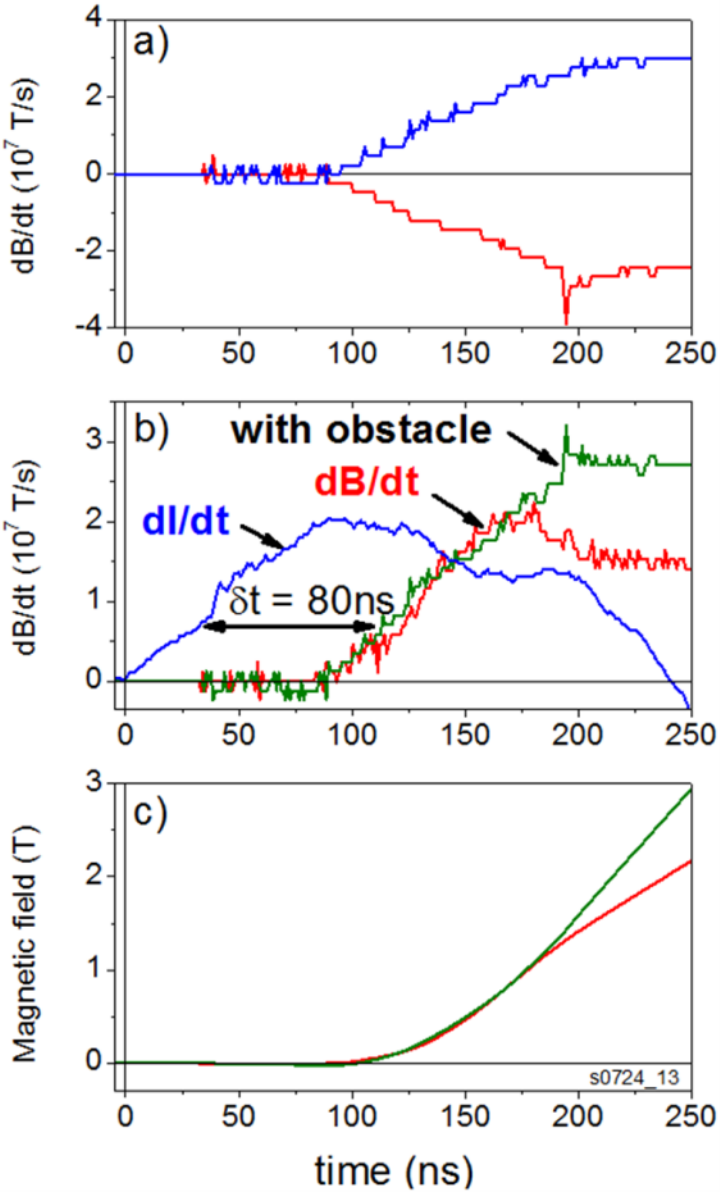


FIG. 5.18 The magnetic field measured by inductive probes centred at a distance of 8.5mm from the wires (1.5mm from foil). (a) Signals from two co-located, oppositely wound probes, (b) comparison of the signals with (green) and without (red) the obstacle located at 10mm from the wires. The blue trace shows dI/dt of the current (a.u.) driving the ablation plasma flow. (c) Magnetic field obtained by integrating the signals shown in (b).

5.5 Discussion: scale lengths relevant to the shock structure and pressure balance at the sub-shock

In summary, the results presented in this chapter have shown that the collision of a super-sonic and magnetised plasma flow with a planar foil obstacle leads to the formation of a reverse shock with an evolving sub-structure. The interaction is seen to develop a thin layer of high density, stagnated plasma at the obstacle surface. This layer expands from the surface with a much reduced velocity relative to the upstream plasma flow, and the density jump across the layer boundary, due to the accumulation of material inside, is consistent with that of a strong shock. A secondary shock-like feature is also observed to form later in time in the interaction: a detached sub-shock, upstream of the stagnation, and with much smaller jumps in both the flow velocity and plasma density. The transition is shown to be extremely narrow ($< 100\mu m$) and with little increase in either the plasma temperature or ionisation downstream. In light of the high Mach numbers upstream of the sub-shock ($M_S \sim 5-6$, $M_A \sim 7-10$, $M_{MS} \sim 4-5$) this evidence suggests that the sub-shock is unlikely to be of "standard" thermal / kinetic origin. Indeed, at early-times the factor of < 2 reduction in flow velocity across the sub-shock indicates that the flow downstream of the feature remains moving super-sonically, which is in contradiction with the classic definition for a perpendicular shock (chapter 2, section 2.1).

Further evidence towards this non-typical post-shock behaviour can be found by comparing the collisional scale length of the plasma with that of the sub-shock thickness. On an internal scale the plasma behaves collisionally (section 4.7), with a thermal ion-ion mean-free-path (m.f.p.) of order 10^{-4}cm$(= 1\mu m)$; i.e. well within the sub-shock thickness, as one would expect for particles which are able to undergo an abrupt transition in properties within such an interval. With the increased relative velocity between the particles on either side of the sub-shock however, Coulomb cross-sections are reduced and the collisional interaction length becomes longer. This is reflected in the predicted m.f.p. for an ion moving at the relative velocity between the upstream and downstream plasma flow, into plasma with a density equal to that of the post sub-shock region. Formulae for the collisional frequencies of charged particles of various species can be found in the NRL Plasma Formulary [66], and are shown here to predict a much longer collisional length for the interaction than the aforementioned internal (thermal) scale.

For a test particle α, of mass m_α, charge $e_\alpha = Z_\alpha e$, streaming with velocity v_α through a population of background particles β at density n_β, the collisional rate is given in cgs units (with T in eV) by

$$\nu^{\alpha\backslash\beta} = \left(1 + m_\alpha/m_\beta\right)\psi\left(x^{\alpha\backslash\beta}\right)\nu_0^{\alpha\backslash\beta}, \tag{5.4}$$

where

$$\nu_0^{\alpha\backslash\beta} = \frac{4\pi {e_\alpha}^2 {e_\beta}^2 \lambda_{\alpha\beta} n_\beta}{{m_\alpha}^2 {v_\alpha}^3}, \tag{5.5}$$

$$x^{\alpha\backslash\beta} = \frac{m_\beta {v_\alpha}^2}{2k_B T_\beta}, \tag{5.6}$$

$$\psi(x) = \frac{2}{\sqrt{\pi}}\int_0^x \sqrt{z} e^{-z} dz, \tag{5.7}$$

and $\lambda_{\alpha\beta}$ is the coulomb logarithm. Since the test and background particles here share the same intrinsic properties (they are both are Al ions at approximately equal ionisation and temperature) these expressions reduce to

$$\nu^{i\backslash i} = 2\psi(x){\nu_0}^{i\backslash i}, \tag{5.8}$$

$$\nu_0^{i\backslash i} = \frac{4\pi Z^4 e^4 \lambda_{ii} n_\beta}{{m_i}^2 {v_\alpha}^3}, \tag{5.9}$$

$$x^{i\backslash i} = \frac{m_i {v_\alpha}^2}{2k_B T}. \tag{5.10}$$

The coulomb logarithm for mixed ion-ion collisions is

$$\lambda_{\alpha\beta} = 23 - \ln\left[\frac{Z_\alpha Z_\beta\left(A_\alpha + A_\beta\right)}{A_\alpha T_\beta + A_\beta T_\alpha}\left(\frac{n_\alpha {Z_\alpha}^2}{T_\alpha} + \frac{n_\beta {Z_\beta}^2}{T_\beta}\right)^{1/2}\right], \tag{5.11}$$

(where A here is the atomic mass number) which again simplifies due to the shared test and background particle conditions to

$$\lambda_{ii} = 23 - \ln\left[\frac{Z^3}{T^{3/2}}\left(n_\alpha + n_\beta\right)^{1/2}\right]. \tag{5.12}$$

For the measured early-time parameters $(t = 180\text{ns})\ T_i \approx T_e = 15\text{eV}, Z = 4, n_\alpha = 1.7 \times 10^{17}\text{cm}^{-3}$, and using the relative velocity between the up- and downstream particles of $v_\alpha = 4 \times 10^6\,\text{cm/s}$, one finds a corresponding ion-ion mean free path in the laboratory

frame of $1 \times 10^{-2}\text{cm} = 100\mu\text{m}$. This length is only slightly above but of the same order of magnitude as the thickness of the sub-shock, and so, at the time surrounding the formation of this feature, places the interaction in a very weakly collisional regime. Even allowing for a modest level of heating and ionisation across the sub-shock $(Z_\beta = 5, T_{i\beta} = 75\text{eV})$, along with the rising density of the flow $\left(n_\beta = 3 \times 10^{17}\text{cm}^{-3}\right)$, and using the unabridged set of equations, this m.f.p. reduces to just 50μm. At later time in the experiment however (at $t = 250\text{ns}$), when the upstream flow velocity is measured to decrease to $v_{flow} \approx 7 \times 10^6\,\text{cm/s}\,; v_\alpha = 3 \times 10^6\,\text{cm/s}$, the ion-ion collisional scale is found to drop by approximately an order of magnitude. This suggests that over the course of the experiment the sub-shock is evolving to a more fully collisional feature.

In terms of the formation of the sub-shock though, one should also consider the magnetic field in the system to evaluate the likelihood of a collisionless interaction mechanism allowing the initial deceleration of the flow. The Lamor radius describes the gyrational localisation of particles travelling perpendicular to magnetic field lines and acts as a minimum scale length for the transitions of collisionless magnetic shocks [31]. This parameter, which is equal to

$$r_L = \frac{v}{\omega_c}, \tag{5.13}$$

is given for ions by

$$r_{Li} = 1.04 \times 10^{-4}\text{cm} \cdot \frac{vA}{ZB}. \tag{5.14}$$

For a magnetic field of $1 - 2\text{T}$ (the size of the advected field as measured by the inductive probes) this gives a Lamor radius for ions of $0.3 - 0.8\text{cm}$, and is therefore unlikely to be significant enough to localise the ions within the sub-shock thickness at any stage of the experiment. In contrast however the electrons in the flow are much more susceptible to field levels present. Due to their lower mass their cyclotron frequency is much higher, and under the equivalent conditions they possess a Lamor radius of

$$r_{Le} = 2.38\text{cm} \cdot \frac{\sqrt{T_e}}{B} \approx 4 - 9\mu\text{m}. \tag{5.15}$$

This disparity between the magnetic force felt by the separate charge species may offer some insight into the formation of the sub-shock. When the two fluid bodies of the plasma are differentially affected it becomes possible for them to decouple on a scale of the order of the ion inertial length

$$\frac{c}{\omega_{pi}} = 2.28 \times 10^7 \text{cm} \cdot \frac{1}{Z}\sqrt{\frac{A}{n_i}}, \tag{5.16}$$

leaving the magnetic field to become frozen into the electron fluid rather than the bulk plasma. It is important to note however that without first stopping the field relative to the flow, neither of the fluids will experience any force associated with the field line crossing, since both will be moving in the same frame of reference as the advected field. Thus, the presence of an obstacle in the flow, whose conducting surface does not allow magnetic flux penetration, provides a means of accumulating the field such that it can act upon the flow.

With the pile-up of magnetic flux at the boundary of the obstacle a vertical current layer would be generated across its surface, driven by the $\mathbf{E} = -\mathbf{v} \times \mathbf{B}$ field of the oncoming charged particles. As the field accumulates and the magnetised electrons are subjected to an increasing level of gyrational localisation, the ions will continue to pass through to the stagnation layer with their greater level of inertia. As the thickness of the stagnation reverse shock then expands away from the obstacle surface due to the build up of material inside, and is itself able to support the induced current layer due to its charged constituents, the front/influence of accumulated magnetic field will move further outward into the upstream flow. If the distance between the electron shock front and the stagnated plasma is allowed to grow in this way to reach the size of the ion inertia length, then the development of a re-equilibrating electrostatic potential would be expected to counteract the dispersion. Such a potential could then indirectly decelerate the ions of the flow to create the observed sub-shock, with the measured reduction in the flow velocity $v_d/v_u \sim 0.5$ across the sub-shock corresponding to a decelerating potential of

$$\Delta\varphi = 0.75\frac{E_i}{eZ} \approx 300\text{V}. \tag{5.17}$$

This interpretation is indeed consistent with the reflection of ions that was observed in the Thomson scattering data at t = 180ns, with ion reflection being a typical behaviour of electrostatic potentials [71]. The reverse propagating ions were detected only in the upstream flow immediately ahead of the sub-shock, with an average velocity the same as that of the incoming flow, highlighting the elastic (and hence collisionless) nature of the reflection. The fact that these reflected ions were only observed at this early time suggests that the reflection is a transient phenomenon accompanying the formation of the potential, but further investigation is required here, in particular for $t < 180$ns.

For the plasma parameters measured in the experiments the calculated ion inertia length equates to ≈ 1mm, and is in reasonable agreement with the observed stand-off distance between the obstacle surface and the sub-shock feature at its earliest observation. The sub-shock is first seen in the XUV image data at x = 1.4mm from the foil surface, however it should be noted that it may have formed closer to the foil surface at an earlier time when the emission was too small to detect with this diagnostic.

Despite these agreements between the observations and the proposed magnetic field pile-up mechanism, an important and as of yet unexplained issue in this picture is the apparent imbalance of the opposing pressures in the system. Throughout the early to mid stages of the experiment the sub-shock front is observed to drift slowly and steadily upstream until it reaches a stationary equilibrium at t ≈ 260ns. In light of the fact that the sub-shock can not only exist as a detached feature from the obstacle surface, but also propagate against the flow, the post sub-shock pressure must primarily exceed, and later come into balance with, the ram pressure (ρv^2) of the flow. If however one calculates the plasma beta for the ram pressure of the flow

$$\beta_{ram} = \frac{8\pi\rho v^2}{B^2} \tag{5.18}$$

using the signal magnitude of the magnetic probes, it is found that this lies in great excess of unity ($\beta_{ram} \approx 30 - 200$); suggesting that without amplification an advected field of this size lacks the pressure necessary to impede the progress of the heavy ions. Even with the accumulation of all flux brought by the flow within the experimental timescale, the magnetic pressure still remains at an insufficient level to overcome the ram pressure. By approximating the post-sub-shock region as an area of height h and thickness x_{ss}, the total flux entering the region in time interval dt is given by

$$d\Phi = h v_{flow} B|_{ss}(t) dt, \tag{5.19}$$

where $B|_{ss}(t)$ is the (time-varying) magnetic flux density evaluated at the position of the sub-shock. Thus, under the assumption of an unvarying flow velocity, by a time t during the experiment the total flux accumulated is

$$\Phi = h v_{flow} \int_0^t B dt', \tag{5.20}$$

giving a spatially averaged flux density inside the layer of

$$B_{av} = \frac{v_{flow}}{x_{ss}} \int_0^t B dt'. \quad (5.21)$$

Integrating the magnetic field measurements presented in section 5.4.4 this yields B_{av}~3T at $t = 225$ns. An estimate of the ram pressure from the plasma parameters measured at the same time suggests that in order to achieve at least a balance of these pressures, a magnetic field larger than B_{av} by a factor of ~4 is needed.

In spite of this discrepancy, the magnetic field pressure remains the only viable means of supporting the sub-shock, given that the thermal pressure ($n_i k_B T$) is two orders of magnitude too small to achieve this alone. On this basis one might therefore look towards a field amplification process whereby an additionally generated magnetic field could make up for the apparent shortfall. One way this could come about would be if there was a current loop(s) operating in the post sub-shock region. It is indeed likely that following the proposed generation of a current layer at the obstacle surface this would have a tendency to form a closed loop via the formation of a return path elsewhere in the system. The asymmetrical shape of the sub-shock front could indeed be suggestive of such a phenomenon taking place there. Images of the sub-shock consistently show the highest edge to have a greater stand-off distance than the bottom, and with a different radius of curvature, which could be caused by the directional flow of an electron sheet through the feature. To test this hypothesis it is necessary to develop a higher resolution diagnostic than the magnetic field probes used in this section, which are not sensitive to the small scale fluctuations in field that a current loop structure might create. The following section describes experiments designed to explore the possibility of field enhancement and current loops in the post sub-shock region, as well as the implementation of a newly built Faraday rotation diagnostic, designed to make non-invasive, high spatial resolution measurements of local field strength in the experiments.

Chapter 6:

Investigation of the magnetic field in the reverse shock sub-structure

6.1 Introduction

The experiments presented in chapter 5 have shown the structure of a reverse shock formed by the perpendicular collision of a supersonic and magnetised plasma flow with a planar (foil) obstacle. Within the structure a prominent sub-shock feature has been observed, which is detached from the obstacle surface and positioned upstream in the flow. Diagnostic measurements made in the experiments provide convincing evidence that this sub-shock is produced by the pile-up of the advected magnetic field, which accumulates at the surface of the obstacle, decelerating the incoming electrons of the flow to create a cross-shock potential, which in turn indirectly decelerates the bulk ion mass. Despite the broad agreement of the results with this interpretation, attempts to measure the magnetic field brought by the flow, using local inductive probes placed at the sub-shock position, have shown an apparent discrepancy between the total magnetic flux passing into the region and that required to support the feature against the ram pressure of oncoming plasma. Calculations made using the integrated probe signal show an average field of the post sub-shock region approximately 4 times too small to balance these pressures. Nevertheless, the magnetic field in the system remains the only likely candidate for supporting the sub-shock, with the thermal pressure of the relatively cool plasma being negligible in comparison.

This chapter presents data from a series of subsequent experiments, designed to address the question of the apparent shortfall in magnetic field pressure of the reverse shock

interaction. At the forefront of this investigation is the development of a new Faraday rotation diagnostic on MAGPIE, intended to provide an independent and non-invasive measurement of the magnetic fields present in these experiments. If successful this diagnostic should provide a verification of the reliability of the field measurements made by the inductive probes in the upstream plasma flow, as well as demonstrating the levels and distribution of the compressed field present in the post sub-shock region. The results presented here are preliminary, but so far show a good agreement with the upstream advected field levels detected by the probes. The average post sub-shock field is also consistent with that estimated by the accumulation of the flux inside this region; however there are signs of a significantly enhanced field across the abrupt transition of the sub-shock front, suggestive of a current sheet inside this layer. Work to improve the sensitivity and spatial resolution of the diagnostic is ongoing, but remains a primary goal of future work and progress is due to be reported in an upcoming publication (Swadling et al., Rev. Sci. Instrum. 2014, accepted).

In addition to the Faraday rotation measurements, experiments were also carried out with modifications to the obstacle's material and geometry to explore their effects on the sub-shock structure. These modifications were made to test the assumption of current loops operating in the post sub-shock region, which might be disrupted by the changes, and if so, prevent the magnetic field enhancements deemed necessary to support the sub-shock. In switching the obstacle surface from aluminium to a plastic foil the sub-shock was found to be reproduced; implying that the conductive properties of the obstacle are non-critical, and that the surface current responsible for the flux pile-up is driven through the stagnated plasma layer in front of the obstacle. An experiment was later trialled with a break in the obstacle surface to cause a discontinuity in the stagnated layer. The effect of this was to create two separate sub-shocks on either side of the break, with a clear asymmetry in the shape of their edge bows. This result provides further indication that the sub-shock front does indeed contain a current layer, with the asymmetry demonstrating the directional nature of the current path(s) inside the layer. A further alteration that was made was to replace the obstacle with an array of fine wires. The aim of this was to provide an obstacle permeable to the flow, but which might trap the frozen-in flux due to the smaller magnetic Reynolds number that may be associated with the reduced length scale of the inter-wire separation. Results from the laser interferometry did not show the formation of a sub-shock; suggesting that either the array was insufficient in trapping a large enough portion of the advected magnetic flux to act effectively upon the magnetised electrons, or that without halting the ions at

the obstacle surface the electrons could not be effectively decoupled from the ion fluid. Further investigation is required to make a conclusion here.

6.2 Preliminary measurements of the magnetic field distribution in the reverse shock structure using a Faraday rotation technique

The results presented here comprise the first experimental test of the dual channel Faraday rotation diagnostic described in section 3.4.4. As a proof of principle for the diagnostic the reverse shock interaction was imaged in a setup using a $10 \times 25\text{mm}^2$

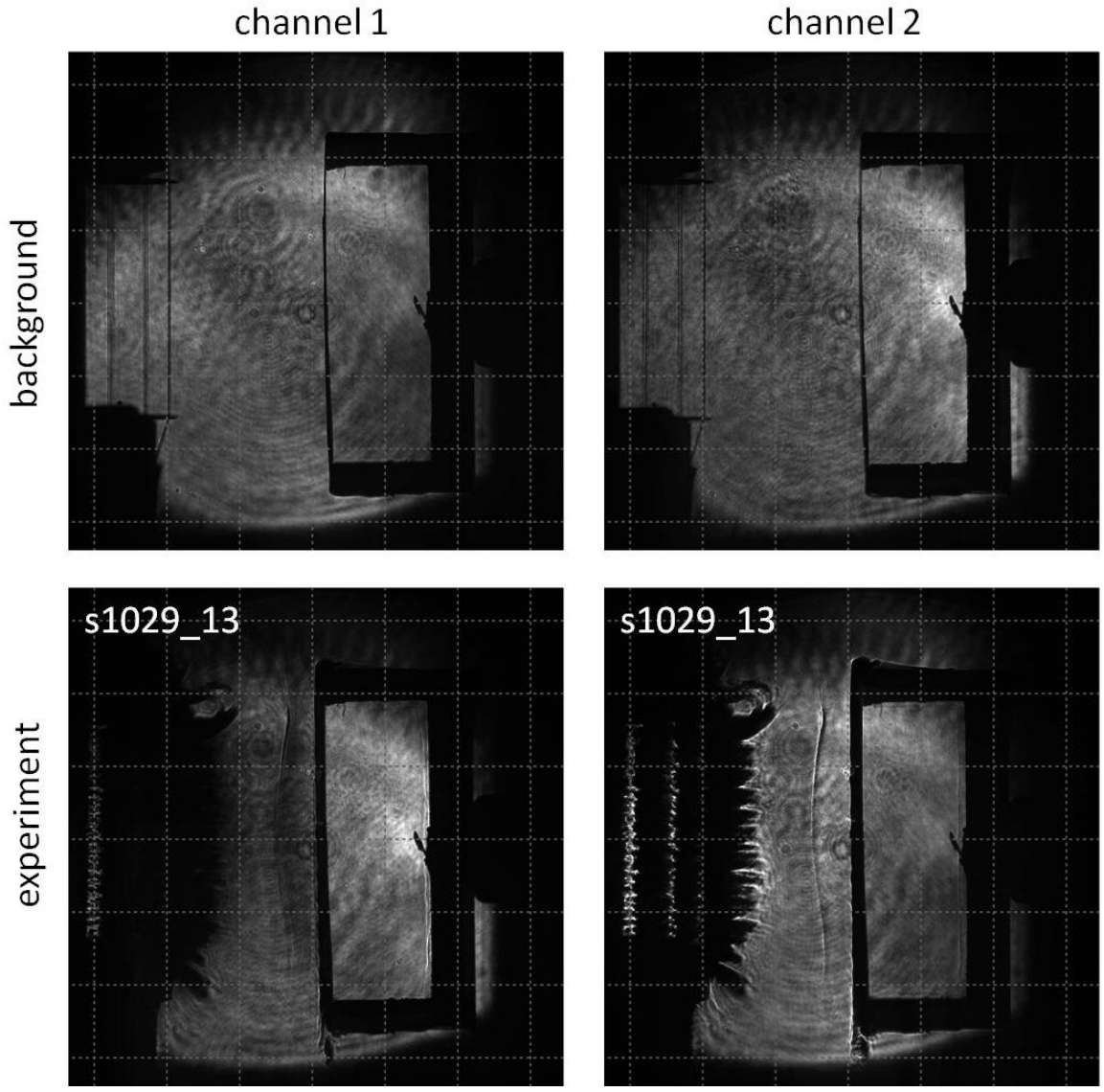


FIG. 6.1 Side-on intensity maps of a reverse shock experiment as measured by the two channels of the Faraday rotation diagnostic. Displayed here are the background images, experimental images (t=250ns) for each channel.

aluminium foil obstacle, positioned at a distance of 10mm from the wire array. Images with the diagnostic were taken at t = 250ns after current start to ensure that a fully developed sub-shock was observed.

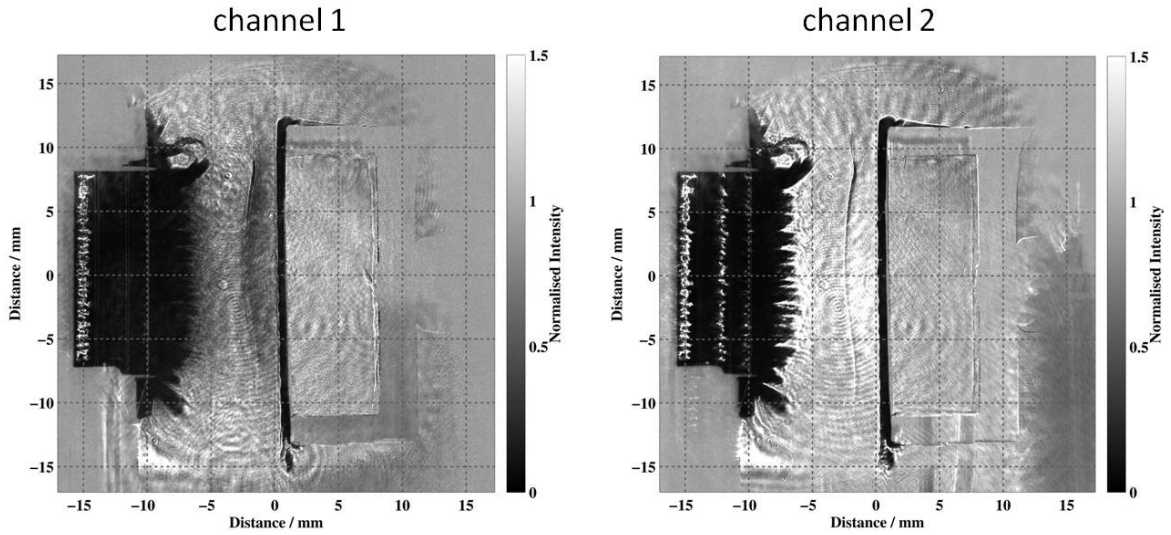


FIG. 6.2 Normalised (I_C/I_B) intensity images from each channel of the Faraday system. (Produced from the images in Fig. 6.1). [Image credit: G. Swadling, MAGPIE GROUP].

Fig. 6.1 shows the background and experimental images for the two channels, with the normalised intensity images for each channel in Fig 6.2. Comparison of the images shows a distinct change in the brightness of the post sub-shock region, with an opposing brightening and darkening observed between the channels, indicating the presence of the accumulated magnetic field here. Notably the fronts of both the sub-shock and stagnated layer show the most enhanced changes in brightness, which are most apparent in the second channel due to their large increase in intensity. Interestingly these images also illustrate the large fields present within the wire array and inside the ablated flow at small radii to this, where there is also substantial brightening and dimming taking place. (Note that some regions within the high density plasma here are opaque in both images due to their steep density gradients.)

Despite attempts to construct the two channels of the diagnostic with an equal magnification and field of view there is always likely to be some level of variance in the optical setup and positioning of the image on the camera CCD. Consequently secondary background images were taken for each of the channels with a superimposed mesh grid to assist in the accurate overlay of their images prior to subtraction. Fig. 6.3 shows an example of this from one of the cameras. Following the successful overlay, equation 3.77

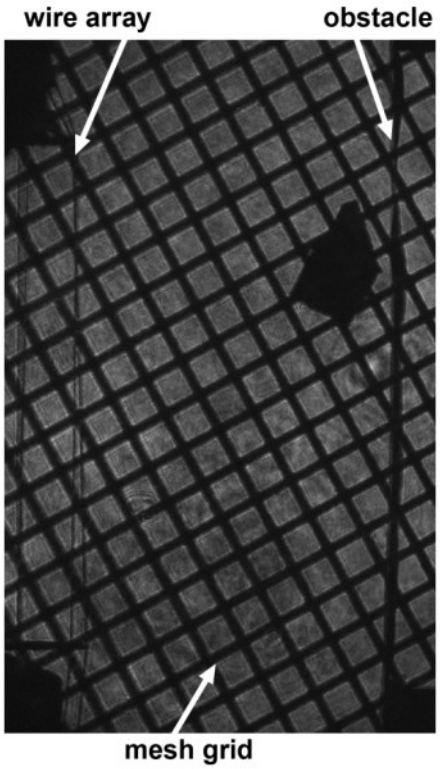


FIG. 6.3 Secondary background images are taken for each of the Faraday rotation camera channels to assist in the accurate synchronisation of the channels for the analysis procedure. A mesh grid is placed in the probing beam at a position ahead of the dual channel beam splitter, such that the overlaid pattern has a fixed position relative to the background image. Thus any translational or magnification adjustments can be made to the image data to account for small differences in the optical setups of the channels.

was used to produce a map of the rotation across the reverse shock interaction region, which is shown in Fig. 6.4.

The rotation map shows that there is an appreciable rotation angle across the area of the post-shock region, corresponding to a combination of the effects of increased electron density and magnetic field strength here (equation 3.69). There is also evidence for a smaller rotation of the probing beam in the plasma upstream of this. The fact that the rotation angle is of the same direction (defined as positive angular displacement in the figure) for the entirety of the space between the array and foil obstacle provides a good indication that the field embedded here originates from the poloidal field at the array wires, which is advected with the ablated plasma. Outside the region of interest, at the areas of the image corresponding to the obstacle's support hardware as well as to the rear of this, small rotations are also registered. Here the plasma density is assumed to

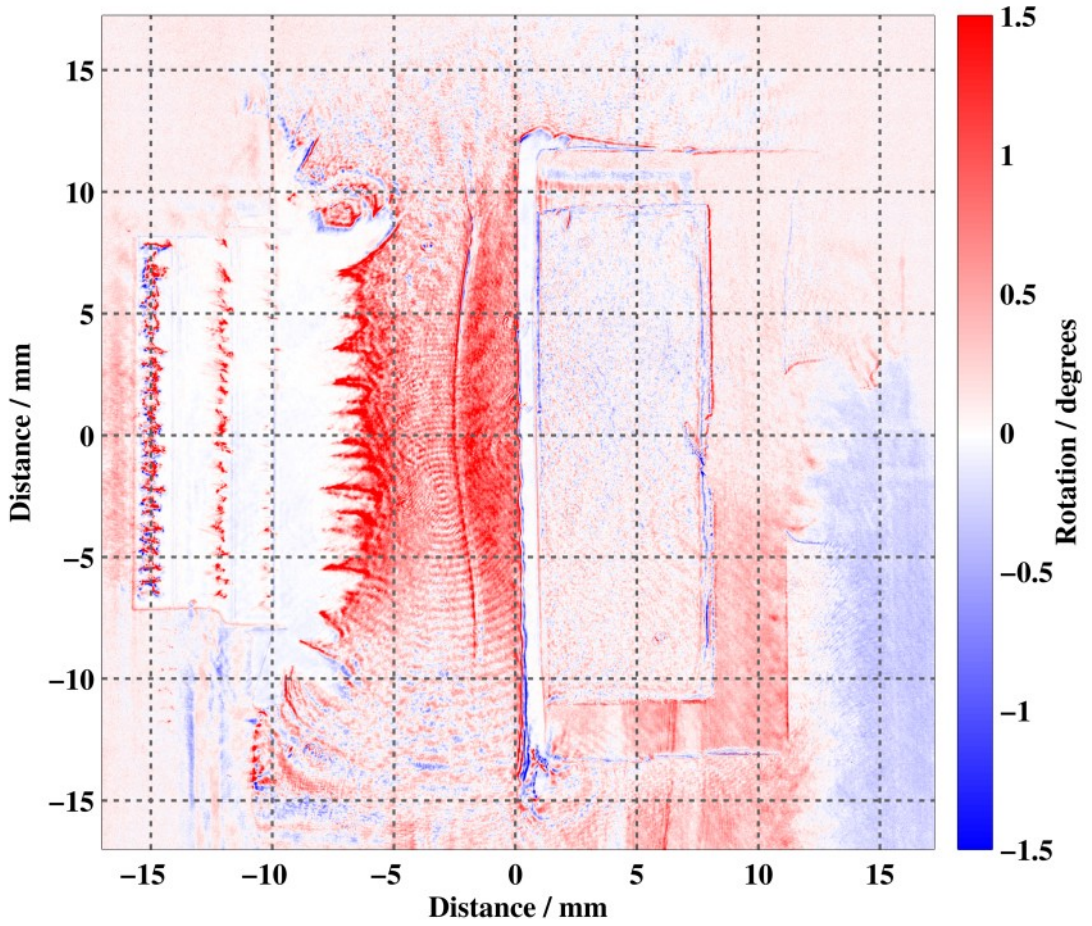


FIG. 6.4 Map showing the measured Faraday rotation angle as a function of position for the full area of the probing beam. The region of interest for the reverse shock experiment lies within the bounds -10<x<0mm and -10mm<y<10mm, however the area outside of this (where the plasma density and hence rotation of polarisation is expected to be negligible) demonstrates the level of noise fluctuations in this measurement. [Image credit: G. Swadling, MAGPIE GROUP].

be negligible and so Faraday rotations are not expected. These areas are therefore deemed artefacts arising from a combination of noise on the cameras and intensity fluctuations in the profile of the beam, limiting the overall sensitivity of the diagnostic. Indeed the effect of beam fluctuation is seen in the data-map in the form of circular fringes which are imprinted across a large part of the region of interest. Despite this interference the average level of rotation for both the upstream plasma, and in particular the post sub-shock region, appears stronger than the background level for the "zero-density" regions. The strong spatial correlation between the changes in rotation angle and the boundaries in the structure of the reverse shock indicates that a genuine Faraday Effect is observed.

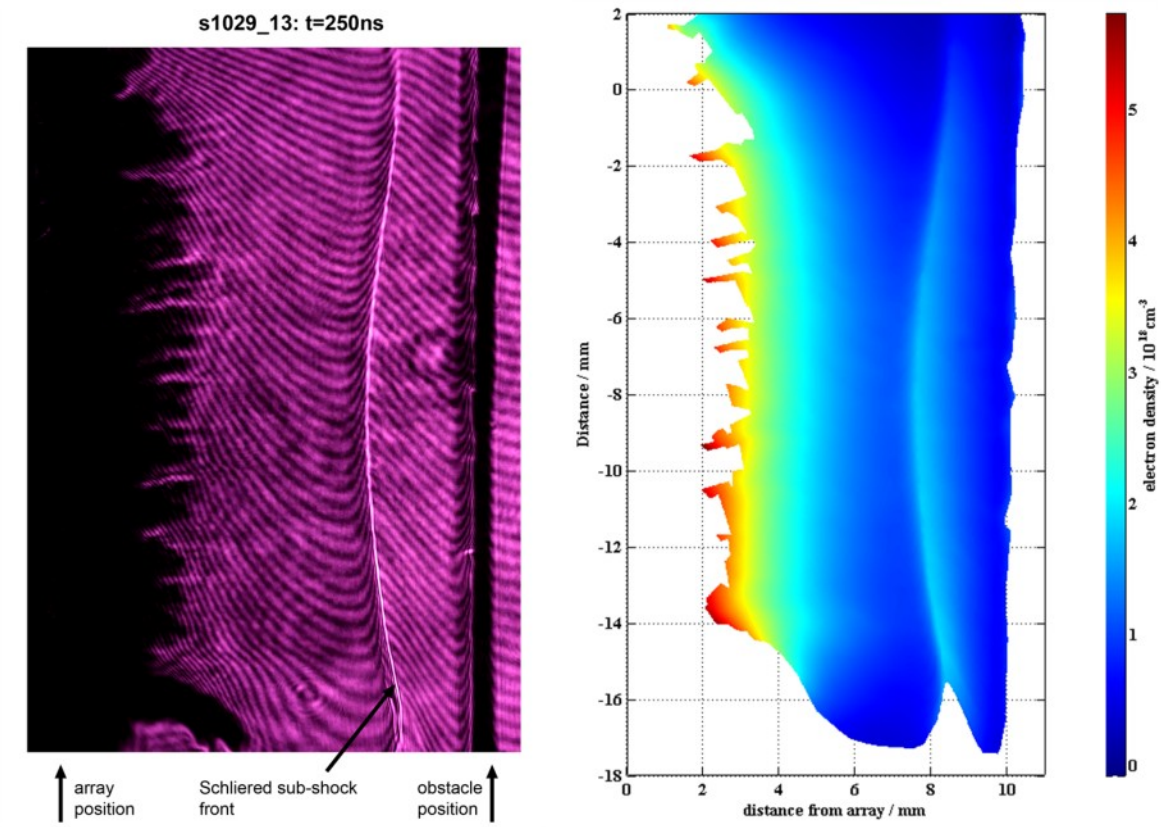


FIG. 6.5 Data from the Faraday rotation interferometry channel. (a) Raw interferogram of the reverse shock region. The fringes in the background image were to a good approximation horizontal and therefore the profile for each fringe closely resembles a 1D plot of the areal electron density along the x direction. Due to the longer wavelength of the I.R. beam the fringe shifts here are more sensitive to changes in electron density in comparison to the previous 355 / 532nm interferometer system; because of this the steepest density gradient part of the sub-shock front appears Schliered (bright white line) in this image. (b) Areal electron density plot.

1053nm laser interferometry data was collected from a separate channel on the same beam-line as the rotation measurements. This interferometer operates on the same principles as the 532 / 355nm laser system used in previous experiments, but has the added advantage of exhibiting more sensitive fringe shifts upon changes to the electron density, due to its longer wavelength (see equation 3.55), and hence gives higher precision measurements. The raw interferogram and accompanying areal density map are shown in Fig. 6.5. The synchronisation of this image with the previous channels was again achieved using a secondary background image with an overlay grid. In this instance however the process proved more difficult due to distortions in the image caused by spherical aberration in the interferometry optics. This aberration is illustrated in Fig. 6.6 and arises due to the use of lenses in the imaging system which are cut with a spherical surface, and so do not share a common focal point for parallel rays incident at the edge and central surfaces of the lens. These lenses have been used due to their much lower cost in comparison to aspheric lenses, however it may be possible to recover a more satisfactory image quality in future experiments, without the need to install more expensive optical components. If a longer telescope section is used for the camera, with a longer focal length lens, the effect should appear less significant. For the image analysis here however the interferometry data was corrected to match the rotation map via a rescaling of the interferometry image using Adobe Photoshop software. Here a satisfactory overlay of the images was achieved by ensuring that each of the hardware bodies (array and obstacle) coincided in background images across the

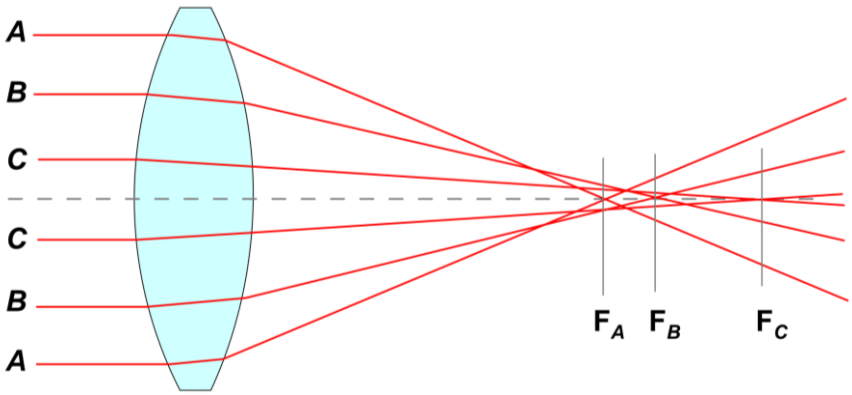


FIG. 6.6 Diagram illustrating the aberration caused by a spherical lens, which focuses parallel light rays to different lengths depending on their distance from the lens axis (horizontal blue line). These lenses are used in the Faraday rotation diagnostic setup due to their much lower price in comparison to high performance aspheric lenses. The effect can be minimised by either using long focal length lenses, or using a small area of the lens surface. Image reproduced from [72].

separate channels. The magnetic field map yielded after this process is displayed in Fig. 6.7, together with a line-profile taken along the axis of the reverse shock.

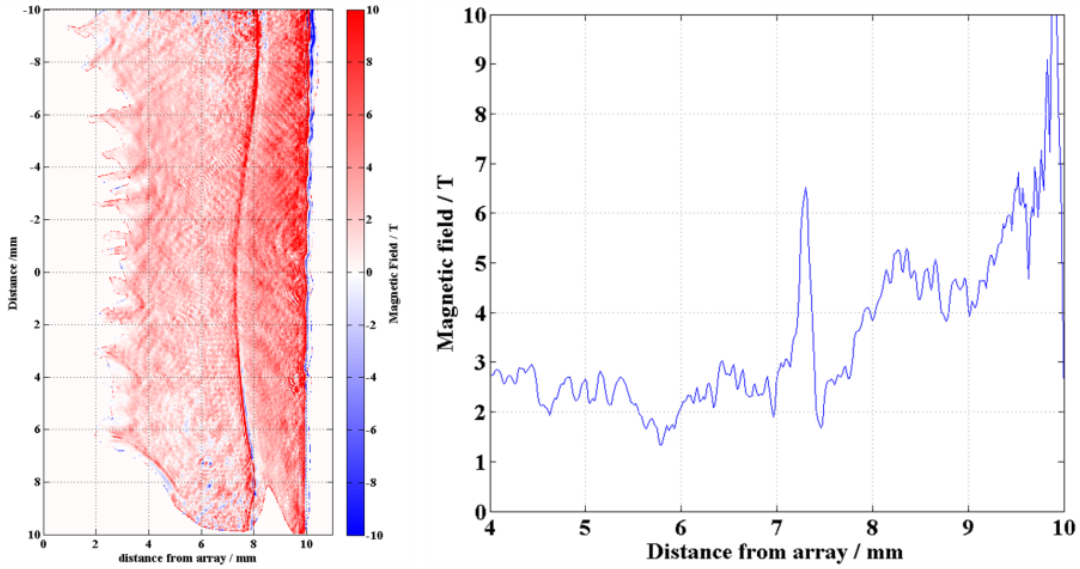


FIG. 6.7 (a) Map of the magnetic field as a function of position for the reverse shock region, together with (b) a line profile taken from this along y=0. [Image credit: G. Swadling, MAGPIE GROUP].

The data show an average field strength recorded upstream of the sub-shock in the $2-3$T range. At the front of the sub-shock the field then locally peaks, before settling at $\sim 4-5$T in the space ahead of the obstacle and then rising furthermore towards the surface stagnation layer (positioned at $x = 10$mm); although again no measurement could be made inside this layer due to the divergence of the probing beam as it passes through the steep density gradient region. These results are in reasonably good agreement with the measurements made with the magnetic field probes presented in section 5.4.5. The values upstream of the sub-shock are consistent, and although the post sub-shock field could not be accurately measured with that diagnostic (due to its inherent spatial resolution limitations) the estimate of the average field from the calculation of the integrated flux passing through the sub-shock front (section 5.5) also matches the level seen here with the Faraday rotation diagnostic. The observation of the narrow field jump at the sub-shock front is highly suggestive of a current sheet embedded within the feature, which might be responsible for causing this local enhancement. Whilst the peak magnitude of the magnetic field here does not appear to achieve the calculated level of ~12T that would be required hold-off the ram pressure of the oncoming flow, this may however be an underestimation, disguised by the resolution

limit of the diagnostic as well as the natural curvature of the feature in the orthogonal plane.

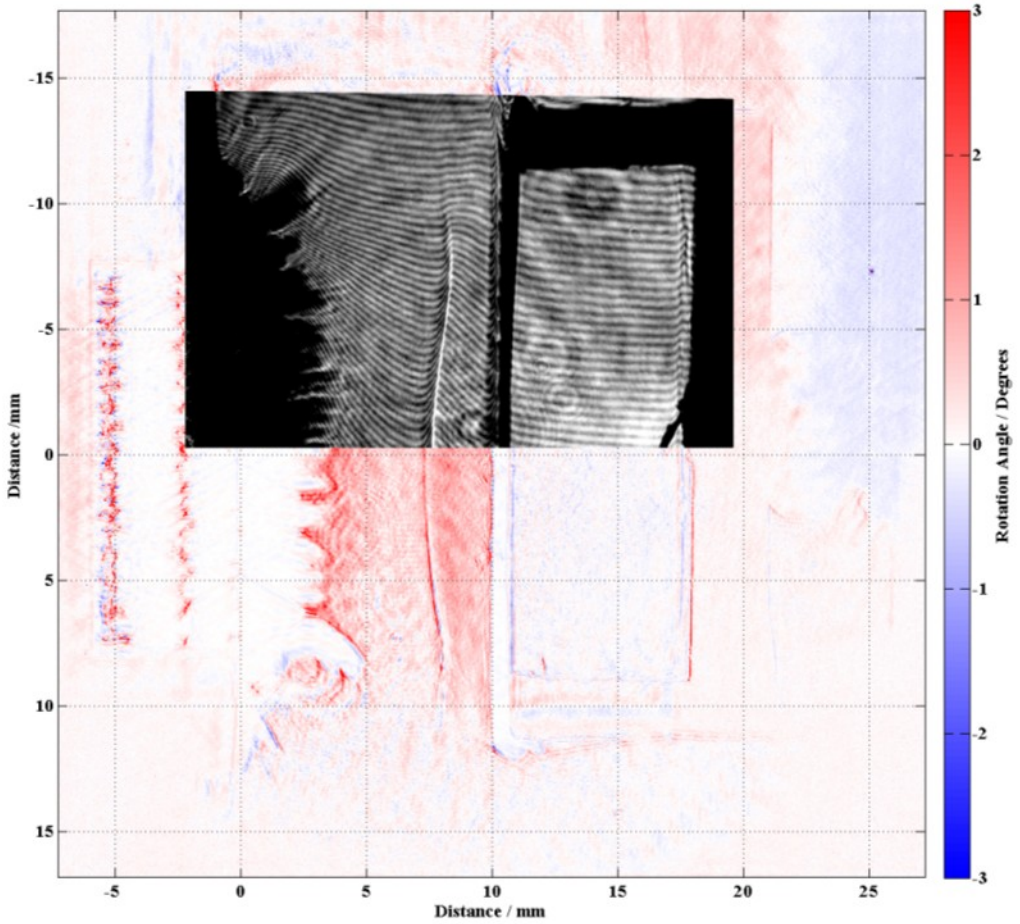


FIG. 6.8 Faraday rotation map with an overlaid section of the interferometry data showing the offset in the positions of highest rotation (magnetic field) and electron density for the sub-shock front. [Image credit: G. Swadling, MAGPIE GROUP]

A further interesting attribute of the sub-shock field peak becomes apparent when the interferometry data is overlaid with the field measurement. This is shown in Fig. 6.8. Here the field increase appears ahead of the point of highest density, which is seen as the Schliered bright line in the interferometry data. This separation may be suggestive of an inertial effect taking place between the point where the greatest force is felt on the particles and the distance over which the particles stop. However, whilst the images of the different channels were deemed to overlay in a convincing manner following the processing, at this time it cannot be ruled out that the offset observed here could be a facet of the interferometry camera's previously mentioned spherical aberration. Consequently confirmation of this result, as well as further justification of the

quantitative values of the reverse shock field profile quoted here will depend on repeat observations following improvements to the diagnostic setup. It is a primary goal of future work to continue to develop the Faraday rotation diagnostic to address this issue, and in doing so allow a more reliable measurement of the field distribution in these experiments. In particular work will be carried out to remove or limit the aberration, as well as improve the stability and uniformity of the beam profile to reduce the signal of the background noise. Progress in both the diagnostic development and future reverse shock experiments using this are due to be reported in future publications.

6.3 Experiments exploring the current structure of the sub-shock region

In interpreting the results of the reverse shock structure presented in chapter 5 it was argued that the observed sub-shock was formed due to the pile-up of the magnetic flux at the obstacle surface. It was assumed that the conducting properties of the obstacle were responsible for this pile-up, with the surface being non-penetrable to field lines, and so driving a current vertically through the surface to maintain the field here, which would then grow in time due to the ever increasing flux accumulation.

An experiment was designed to test the necessity in this model of having a conducting obstacle in creating the sub-shock. By replacing the aluminium foil obstacle with one of plastic it could be determined if the field was maintained by instead driving a current through the stagnated plasma, or if the field would instead diffuse through the surface

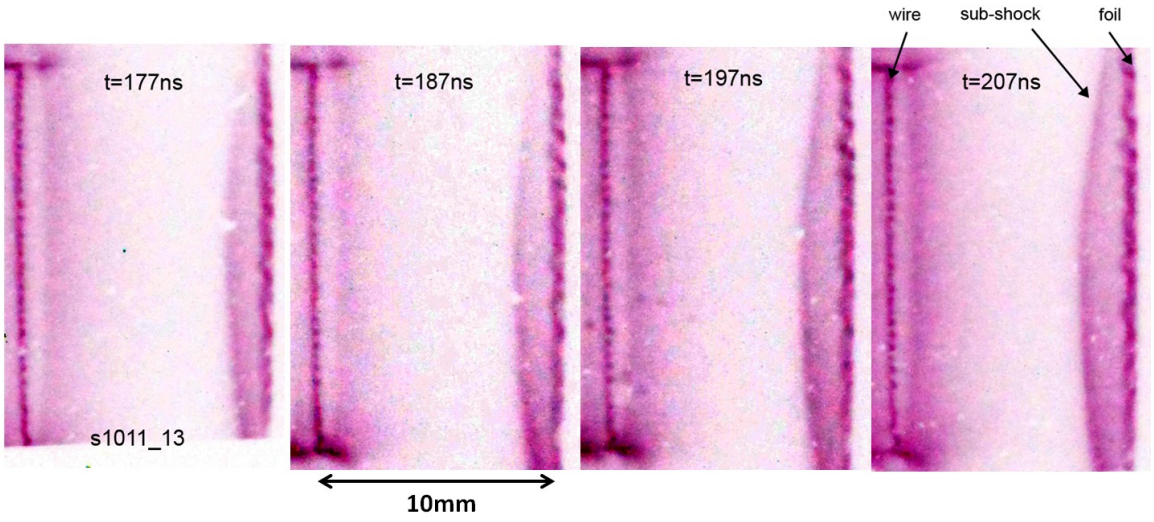


FIG. 6.9 Side-on XUV image time-line showing the development of the sub-shock in an experiment where a plastic foil obstacle has been used instead of the original aluminium foil.

preventing a pile-up. The experiment used a 10mm wide and 12.5μm thick, PVDC plastic foil, extending beyond the full height of the array. The foil was placed at ~10mm from the array wires and the reverse shock region was imaged side-on in the XUV (4-frame, 5ns exposure, 10ns inter-frame, time-gated self-emission). Fig. 6.9 shows the results.

In the first image, taken at t = 177ns after current start, the sub-shock is observed to be fully formed, with a maximum distance from the foil at the central part of the obstacle of 2.0mm. Over the next 30ns the sub-shock is observed to expand away from the surface, reaching 2.3mm at t = 207ns. Comparing this time-line with that of the aluminium obstacle shown in Fig. 5.4 it is apparent the dynamic behaviour of the sub-shock remains consistent, with little difference seen in either the shape or stand-off distance of the feature. Thus under the assumption that the pile-up mechanism is responsible for the sub-shock, it is reasonable to conclude that the magnetic field remains embedded in the plasma following stagnation and does not require a conducting obstacle to prevent diffusion through the surface. The stagnated plasma itself should provide suitable conductive properties to support a current layer, and as this layer grows so too should the influence of its magnetic field reach further upstream from the obstacle, as is observed in the upstream-wards motion of the sub-shock front.

It naturally follows from this interpretation that if a sustained current is driven at the obstacle surface then this will seek to form a closed circuit via return paths elsewhere in the system. The results of the Faraday rotation measurements in the previous section have already shown evidence of a second current sheet present at the surface of the sub-shock front. It is at present unclear how these sheets might be connected (both in terms of geometry and closing mechanism), however the sub-shock can be identified as the most likely candidate for such a return path.

To assess this hypothesis a second modified experiment was carried out to examine the effect of placing a horizontal break in the obstacle surface. This would effectively mean that there were two separate, vertically aligned obstacles in the flow, each generating their own surface current and return paths. Thus one would expect separate sub-shocks and current loops for each. In the experiment two $10 \times 10\text{mm}^2$ aluminium foils were used for the obstacles with a 6mm thick PTFE (insulating) spacer placed between the foil mounts; suitably far behind the foil surface so as not to interfere with the flow. Fig. 6.10 shows XUV and interferometry images of this arrangement at t = 200ns and t = 210ns respectively. In both images there appear separate and distinct sub-shocks

standing ahead of the two foils. The result in itself is not definitive; whilst matching the prediction, it is not clear whether the discontinuity between the sub-shocks is indeed due to individual current loops, or due to the lack of some other effect caused by the now absent material accumulation at the obstacle body. What is insightful here however is the shape of the sub-shock bows at the edges of the separate obstacles. There is a clear asymmetry in these bows, much like that in the overall shape of the single sub-shock seen in the original experiments. The fact however that this asymmetry is reproduced here, at a more central height of the wire array, shows that it is indeed a characteristic of the sub-shock itself, and not due to uneven flow pressures between the top and bottom parts of the array. Such an asymmetry as this is very indicative of a polar phenomenon (i.e. a current path) whose directional nature here is highlighted.

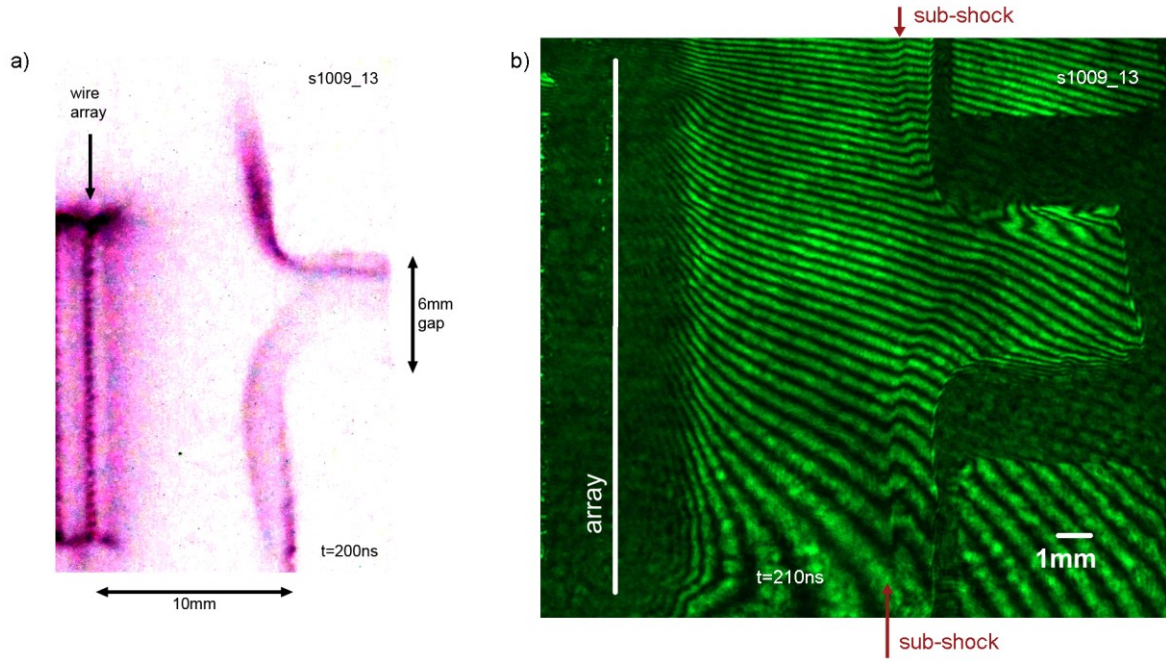
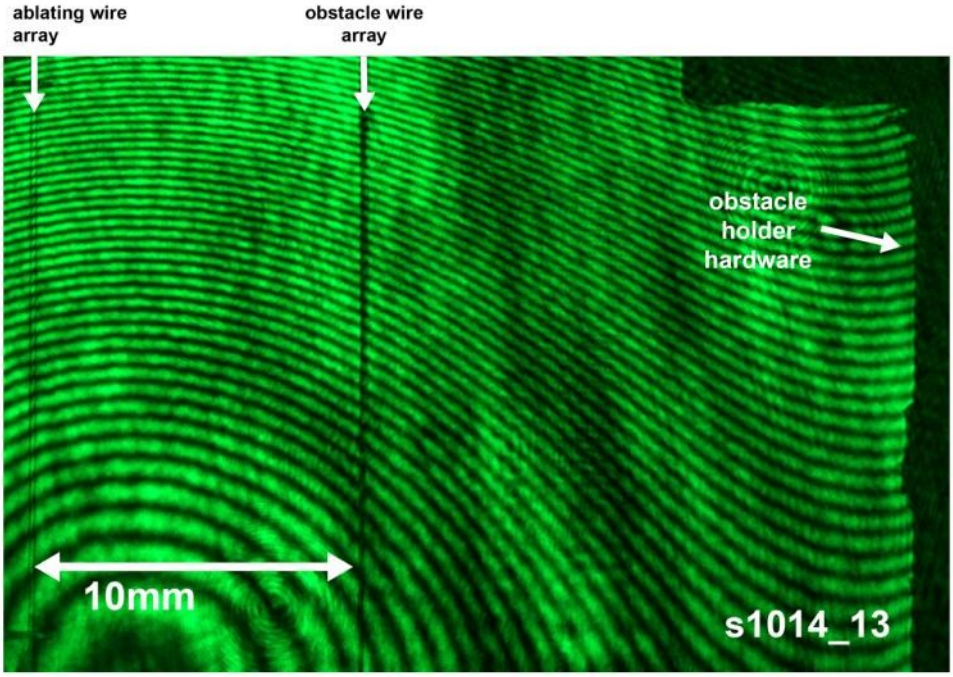
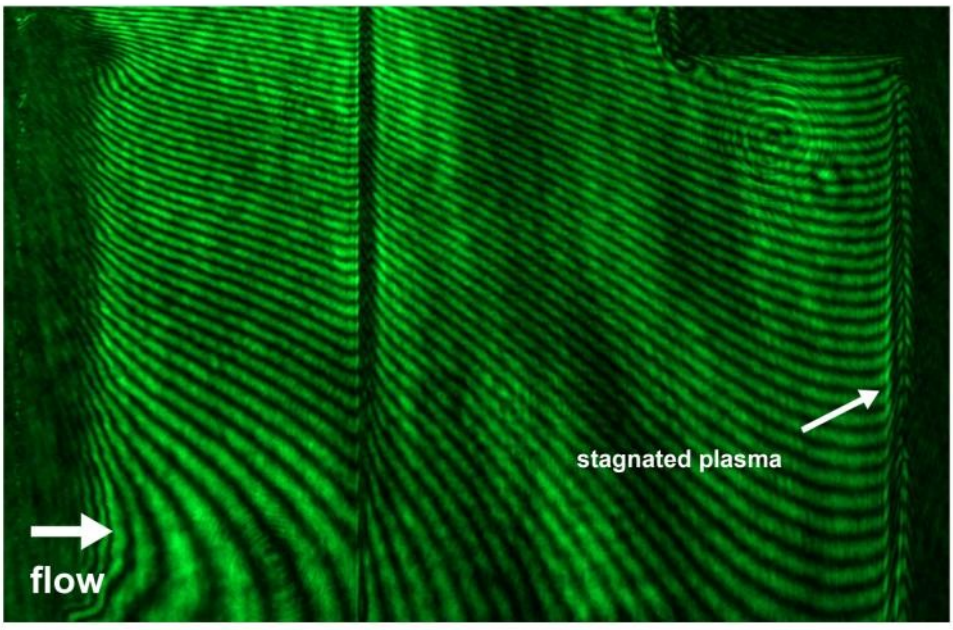


FIG. 6.10 (a) Side-on XUV image of an experiment where two separate, vertically aligned foil obstacles were used with a 6mm gap between the two, and (b) interferometry image from the same experiment. The shape of each of the sub-shocks generated in front of the foils display a clear asymmetry.

A final modified experiment was carried out to determine if the current loop(s) and resulting structure described here could be maintained by trapping only the magnetic field from the flow, whilst allowing the material flux to pass through the system. The obstacle was replaced by a vertical array of 10μm thick, conducting (copper) wires, with a ~0.7mm inter-wire separation. Since the magnetic Reynolds number of a system is proportional to its characteristic length scale (equation 4.13) it was considered that with



Background



t=200ns

FIG. 6.11 Side-on interferometry data from an experiment where the obstacle used is a linear array of 21×10μm copper wires with an inter-wire spacing of ~0.7mm. The flow is from the left, with the obstacle array in the centre of the image, and the hardware which supports this obstacle is shown on the right. In the experimental image (bottom) the flow is seen to permeate the obstacle and collides with the back wall (which is planar and parallel with the obstacle) forming a stagnation layer there.

the scale of the inter-wire gap being a factor of $10-20$ smaller than the 10mm source-obstacle distance, diffusion of the field might be sufficiently increased here to allow a magnetic pile-up by inducing a current through the wires; thus avoiding the need for a stagnated plasma conduction layer. Results from laser interferometry and the XUV camera (Fig.6.11 and 6.12 respectively) show that the wire obstacle does not however produce the same prominent sub-shock feature observed previously, and the plasma is seen to instead collect far behind the obstacle in a collision with the rear wall of the array suspension hardware. Despite this there is some evidence of fringe shifting and an increased emission, which could point to a slightly increased electron density and some heating in the region ahead of the obstacle. From the dataset available it is presently unclear whether this might merely be a result of photo-ionisation / heating of material from radiative emission of the (current-driven) wire array, or if these are indeed the signs of sub-shock formation with a reduced magnetic field accumulation. The reduction of the Reynolds number by the assumed factor still leaves $Re_M \sim 10$, with the majority of the field remaining attached to the passing flow. Future measurements with the Faraday rotation system might allow measurements to confirm the level of magnetic field trapped by this method. However a true comparison to the original scenario may prove difficult, since trapping a comparative level field may require $Re_M \sim 1/200$, entailing an inter-wire separation which would be no longer permeable to the flow.

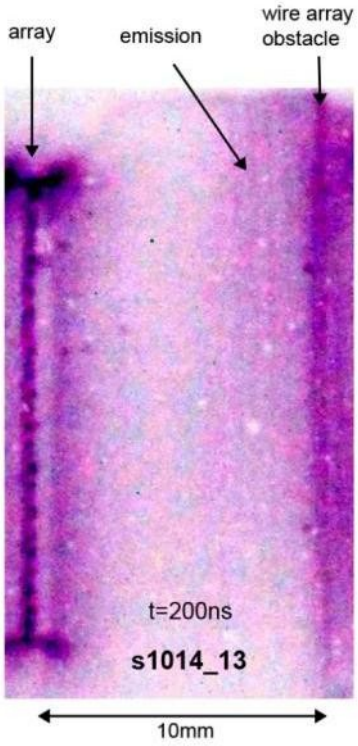


FIG. 6.12 Side-on XUV image taken in the same experiment as Fig. 6.11. The emission seen in front of the array may be the early signs of a sub-shock formation.

Chapter 7:

Conclusions & proposals for future study

7.1 Conclusions

This thesis has presented the design and results from a novel pulsed-power driven platform for creating a supersonic and quasi-1D plasma flow with an embedded and advected magnetic field. This flow has been used in a highly diagnosed, HEDP experiment to study the structure and properties of a perpendicular magnetised reverse shock, formed by the collision of the flow in a 1D geometry with a stationary planar foil obstacle.

The flow was measured to be highly advective, as reflected by its large magnetic Reynolds number (Re_M~100), and carries a Tesla-level, frozen-in magnetic field, embedded into the plasma during its generation by the large (mega-Ampere) current pulse responsible for driving the experiments. Whilst this advected field is considered strong on an internal scale, with a thermal Beta parameter in the region of $\sim 0.1 - 0.5$, it is comparatively insignificant to the dynamic material ram pressure of the system, owing to the high ejectile velocity ($v \sim 10^7\,cm/s; M_S \sim 5$) of the flow (material pressure scales as $\sim v^2$). Despite this, the high velocity entails a flow which is both super-Alfvénic and super-magnetosonic ($M_A \sim 4 - 8; M_{MS} \sim 3 - 5$) and the presence of the field is found to produce a significant effect on the structure of the reverse shocks produced.

In addition to the expected accumulation of stagnated plasma material in a thin, high density (strong shock) layer at the obstacle surface, a separate detached shock-like transition is also observed upstream of the obstacle, first seen in images of XUV self-emission at a distance $\sim c/\omega_{pi}$, and subsequently moving slowly further upstream.

Measurements of the reverse shock profile from Thomson scattering (ZT_e, v_{flow}) and interferometry (n_e), show that this "sub-shock" feature displays only small (factor of ~2) discontinuities in flow velocity and density, and only minor heating / ionisation in spite of the high Mach numbers of the flow. Qualitative measurements of the magnetic field in the post-sub-shock region, through the use of locally placed inductive probes, also show that there is an increased magnetic field strength behind the sub-shock front.

Following an analysis of these results the sub-shock is believed to be a consequence of the accumulation and compression of the magnetic flux at the obstacle surface; which acts on the magnetised electrons of the flow, decoupling the plasma fluids on the scale of the inertial length. In doing so it is expected that a cross-shock, electrostatic potential is generated, offering a means of indirectly decelerating the ions, whose Lamor radius / cyclotron period is shown to be too large to be directly affected by the accumulated magnetic field. Evidence for the presence of a potential such as this is observed in the Thomson scattering data in the form of an early-time reflection of ions at a position ahead of the sub-shock, shortly after its formation. These ions show an equal speed to the oncoming flow, but travel in the opposite, upstream direction, indicating an elastic interaction with the boundary. Their absence at other experimental times and other positions in the reverse shock provides vindication that they are a transient feature of the sub-shock formation and indeed do not originate from elsewhere in the shock structure.

A calculation of the total magnetic flux brought by the flow and accumulated at the obstacle surface was achieved from an integration of the upstream inductive probe signals. This shows that at the time of the sub-shock formation the magnetic pressure required to support the feature against the ram pressure of the oncoming flow is unlikely to be provided by field pile-up alone. Preliminary measurements using a newly fielded Faraday rotation diagnostic however offer some insight into the field distribution within the structure of the reverse shock. The results show an upstream field strength consistent with the inductive probe measurements, and an average field downstream of the sub-shock which matches that predicted by their integration. Interestingly though the data also shows local enhancements in the field structure both at the sub-shock front and along the surface of the obstacle. These seem indicative of current sheets operating inside those regions and with more detailed measurements following future improvements to the resolution of the diagnostic, may indeed be shown to address the issue of pressure balance.

7.2 Future work

7.2.1 Continued investigation of reverse shock structure

At present several questions still remain in our understanding of the observed sub-structure. Though it seems probable that the two field-enhancing current sheets observed in the Faraday rotation images might join in the regions above and below the sub-shock to compose a single current loop, the manner and mechanism by which such a connection might be initiated is presently unknown. It is expected that since magnetic flux accumulates at the surface of the obstacle this could give rise to a vertical current through the plasma there due to the $\mathbf{E} = -\mathbf{v} \times \mathbf{B}$ force felt by charges in the incoming flow. An equivalent driver for the sub-shock current however has not yet been identified. It is interesting also that the current sheet at the sub-shock front appears to be offset from the sharp density jump of the feature shown in the (1053nm) interferometry data, with the magnetic jump seeming to act as a precursor to the density jump – as demonstrated by the overlaid rotation / density maps of Fig. 6.8. Further investigation of these structures and the field distribution are planned, with improvements to the Faraday rotation diagnostic a work in progress. Efforts are being made to improve the quality and uniformity of the beam profile, which should help to reduce the level of background noise recorded in the intensity map data. There are also plans to contain large sections of the beam-line within positive-pressure or low-vacuum housings to reduce the amount of ambient dust in the system. This will therefore allow the diagnostic laser to operate at higher energy and hence boost the signal intensity, without introducing significant risk of damage to the optical components. In addition to these modifications work is also being carried out to reduce the effects of the spherical aberration identified in section 6.2 – either by extending the focal lengths used in the telescope sections of the interferometry channel, or by employing a higher grade, i.e. aspherically cut lens.

There are also plans to investigate the observed current structures using the Thomson scattering diagnostic. To date measurements have only be taken horizontal mid-plane of the flow-obstacle interaction region. Vertical probing along the height of the sub-shock however might allow components of velocity to be measured in the directions of the assumed particle drifts. Horizontal measurements above and below the mid-plane of the sub-shock may also offer some insight into the observed asymmetry (Figs. 5.4 and 6.10) of the sub-shock in the (z) axial direction as well as possible closure mechanisms of any current loops which may exist in the region.

The early-time behaviour of the sub-shock is another a topic of further interest. The earliest existing Thomson scattering data was obtained at t = 180ns (Fig. 5.11) and shows the blue-shifted reflection of ions ahead of the sub-shock position. This was not observed in any later-time measurement; however it is at present unclear for what duration after the emergence of the sub-shock that the ions are reflected. A temporal scan of the early-time velocity profile of the region would therefore be advantageous in both confirming the origin of the counter-streaming ions as an (elastic) reflection at the sub-shock front, as well as indentifying the possible formation time for an electrostatic cross-shock potential.

The early-time observation of "bubble-like" intermediate structures between the sub-shock and stagnation layer also merits future study. As proposed in section 5.3, a high magnification configuration of the XUV self-emission camera, with a reduced inter-frame separation time would be well suited for this purpose. Adaptations towards a higher magnification pinhole camera would most likely include moving the camera setup closer inside the MAGPIE chamber towards the load, in order to maximise the intensity of the emission signal which is likely to be weak during the time of interest (due to the relatively cooler plasma conditions at early-time). A key question surrounding the formation of the sub-shock is whether the feature is indeed first formed at its detached position and if this agrees well with the calculated value for c/ω_{pi}. In terms of the formation mechanism it would be insightful to ascertain whether the sub-shock front first appears as a smooth transition, as has so far been observed throughout its evolution, or if it is initiated through an instability or wave-like mechanism propagating ahead of the obstacle's stagnated shock layer – as might be indicated by the presence of the transient early-time intermediate structure.

The discussion of this thesis has predominantly concerned the sub-shock feature of the reverse shock, however the stagnation layer is also of potential interest, particularly since the effects of radiative cooling could be influential in this structure. The laser probing diagnostics of the current setup are ill-suited to the high-density gradients of the region, however developments to implement a monochromatic x-ray backlighting camera on MAGPIE are promising [70]. This diagnostic, which is illustrated in Fig. 7.1, makes use of the CERBERUS laser system to heat a silicon target with an intensely focussed ~7J, 527nm, 1ns pulse. The broadband emission from this then passes through the chamber where it intercepts a spherically-bent quartz crystal. This crystal acts to Bragg reflect only radiation at 1.865keV, corresponding to the target's Silicon He-α line.

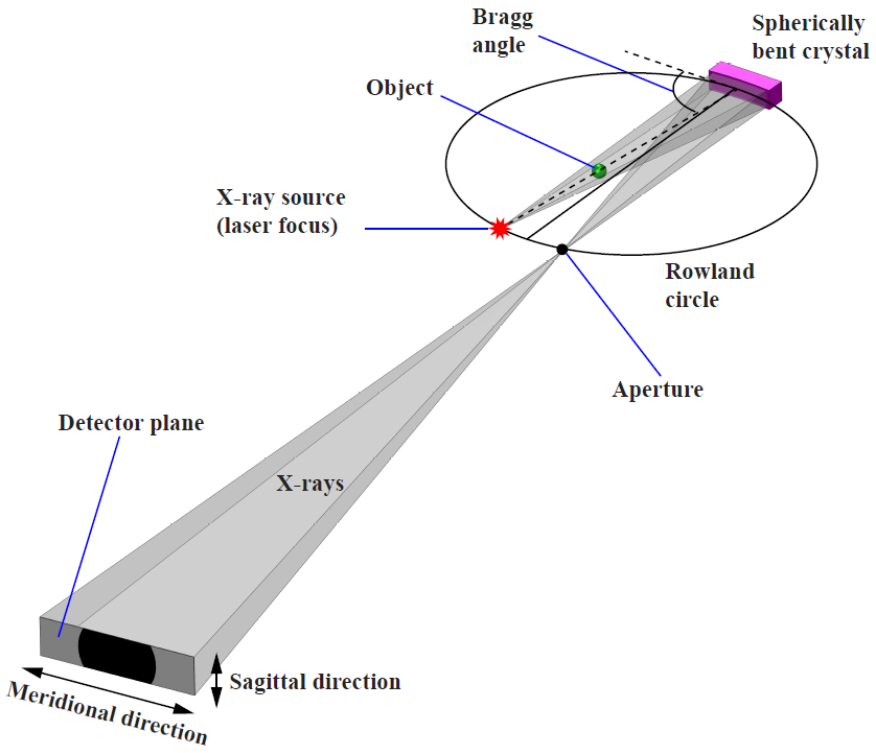


FIG. 7.1 Diagram of the monochromatic x-ray backlighter diagnostic. X-rays from the silicon target source (silicon-α line) pass through the experiment and are Bragg reflected from a quartz crystal, before being imaged through a pinhole camera. The camera detector measures the intensity of the spatially resolved x-ray signal transmitted through the plasma and can be used to create a (line-integrated) density map based on the material's absorption properties. [Image credit: G. Hall, MAGPIE GPROUP].

The angle of the crystal is carefully aligned to a pinhole aperture and the signal is imaged on a detector film-pack, where the recorded intensity can be used to estimate material density and ionisation of the load plasma on the basis of the absorption. In general a high density or high-z plasma material is desired for the load in order to place the absorption of these hard x-rays in a measureable range (note: higher z elements possess a greater number of available energy states and so show increased line-emission / absorption). Preliminary results from this diagnostic showing the obstacle stagnation layer using a tungsten ($z = 74; A = 184$) plasma are shown in Fig. 7.2.

It would be interesting in future experiments to study the effect that the wire material has on the structure of the reverse shocks. Aluminium is a low z element and as such is expected to show relatively little radiative cooling due to its limited line emission. Hence by moving to higher-z materials the perturbations of radiative shocks could be investigated in the present setup. In addition to the effects of cooling, alternative plasma materials also offer the chance to explore different regimes of collisionality. Due to the

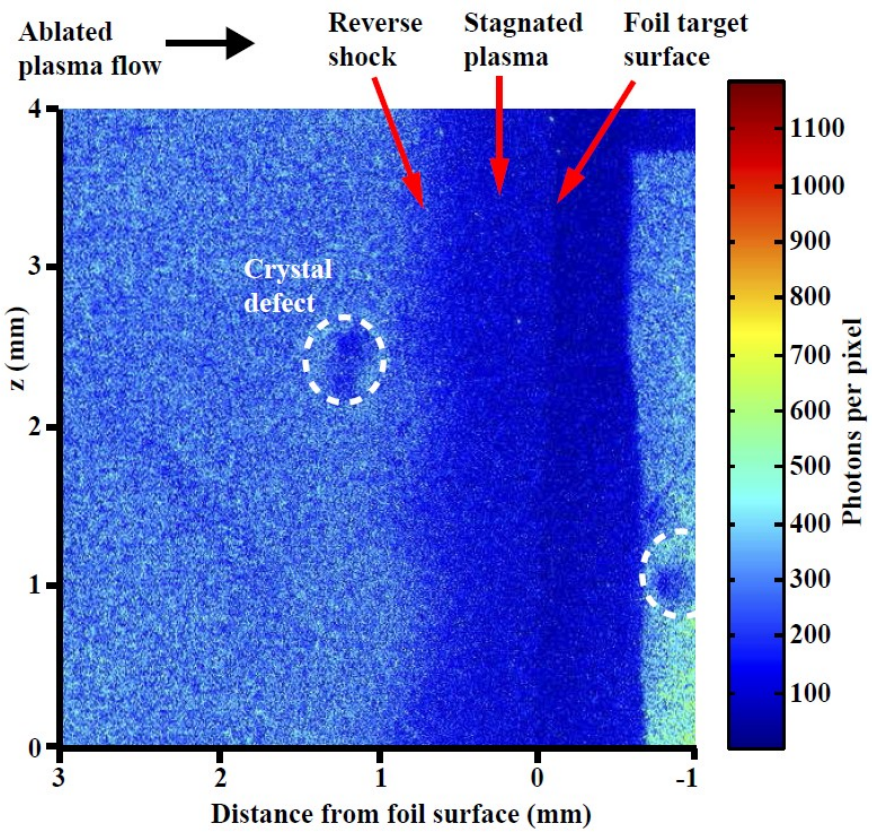


FIG. 7.2 Radiograph of the reverse shock stagnation layer formed with a tungsten plasma. Results show that the feature created with this plasma medium is in an ideal density range for absorption within the sensitivity range of the backlighter diagnostic. [Image credit: G. Hall, MAGPIE GPROUP].

higher atomic mass of high-z elements, a lower particle density can be expected in their plasma flows, since for a given driving current it is the material density which is conserved. Preliminary experiments have been carried out with a tungsten wire array providing the flow material (Fig. 7.3). Interestingly these did not show the formation of a sub-shock as part of the reverse shock structure during the observed time-scale of $t \leq 250$ns. This may be explained in terms of the higher particle kinetic energy of the plasma which requires a larger opposing pressure force to oppose and decelerate the oncoming ions. Thus a sub-shock may take longer to establish, requiring a greater pile-up of magnetic flux at the obstacle surface, however further investigation and in particular measurements from Thomson scattering are required here.

The shape and geometry of the obstacle shock target remains a further avenue for investigation. Oblique shocks, where the flow and magnetic field direction are aligned at an angle to the shock interface are of great interest in many fields of astrophysical

research, including that of the bow shock of the Earth's magnetosphere. 3D or even magnetised targets could also later be explored.

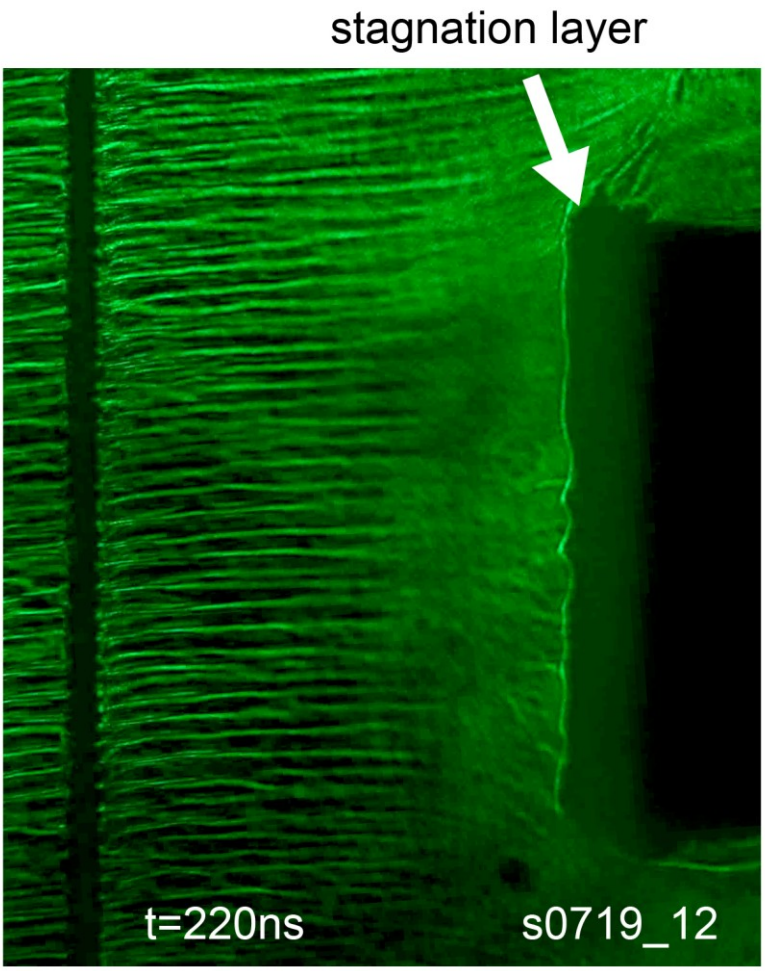


FIG. 7.3 Shadowgraphy image showing the reverse shock structure produced using a tungsten plasma. A thick stagnation layer is seen in front of the obstacle surface but no sub-shock is seen in the upstream flow. The upstream flow does however appear less modulated in line with the obstacle, indicating that a magnetic precursor from the accumulated flow may be having some effect on this material.

7.2.2 Experiments with colliding flows

A modified setup of the inverse array described in this thesis has been designed for future experiments investigating the collision of multiple plasma flows. The modified setup consists of two inverse arrays, with parallel axes, separated by a distance of 20mm. Each of these arrays employs the same paired wire arrangement as described in chapter 4, with oppositely mirrored wire pairs in each array such that the anti-parallel, counter-streaming flows from the two arrays collide head-on in the central region. This results in an interaction where the embedded magnetic fields of these plasmas are

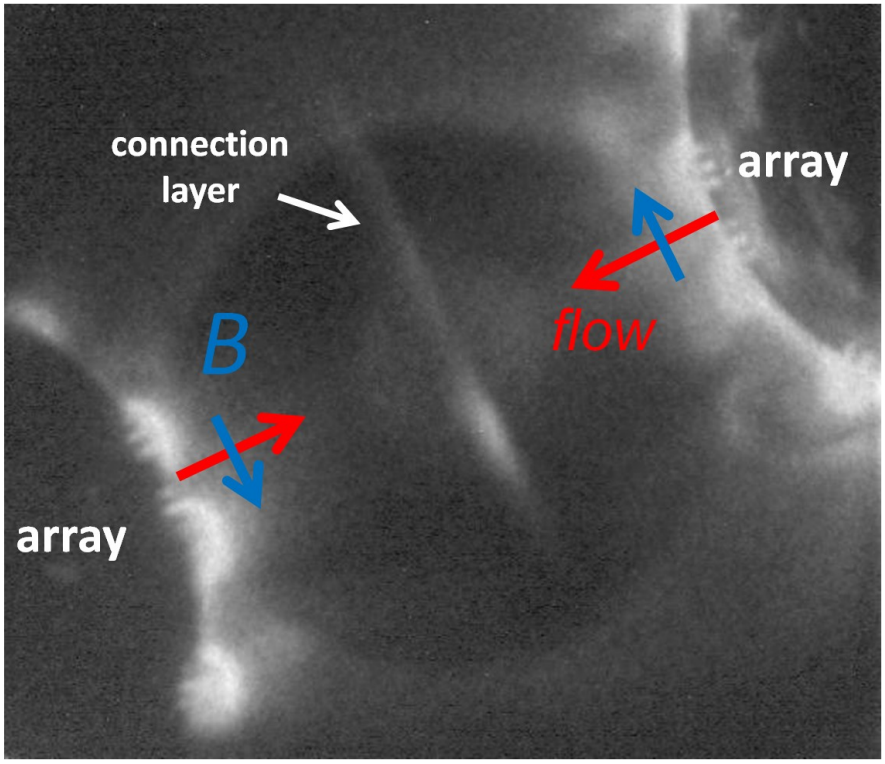


FIG. 7.4 End-on optical emission image of the interaction between two counter-streaming tungsten plasma flows. A bright connection layer is formed in the central region between the two arrays where the opposing advected fields meet.

oppositely aligned and so provide an opportunity to study effects associated with the phenomenon of magnetic reconnection in high beta, and potentially radiatively cooled plasma flows. Fig. 7.4 shows preliminary observations of the dynamics of this interaction from an end-on view, where a central, brightly-emitting reconnection band is observed. Measurements of the reconnection structure and field distribution using interferometry and Faraday rotation are highlighted as key objectives for future experiments. Previous experiments on MAGPIE using converging z pinch geometries [46] have shown that collisionless interpenetrating flows produced by tungsten plasmas give rise to axially collimated ion jets which are believed to be generated by the stagnation of the advected magnetic field. It will therefore also be of interest to make measurements with Thomson scattering in the double array setup to ascertain any possible lateral ion acceleration mechanisms within the interaction.

References

[1] A. Ciardi, Jets from Young Stars IV **50**, 31 (2010).

[2] B. Remington, R. Drake, and D. Ryutov, Rev. Mod. Phys. **78**, 755 (2006).

[3] C. Stehlé, C. Joblin, and L. D'Hendecourt, editors, *European Conference on Laboratory Astrophysics (ECLA)* (EDP Sciences, 2013).

[4] P. M. Hartigan, editor, *High Energy Density Laboratory Astrophysics IX* (Elsevier, 2013).

[5] I. H. Mitchell, J. M. Bayley, J. P. Chittenden, J. F. Worley, A. E. Dangor, M. G. Haines, and P. Choi, Rev. Sci. Instrum. **67**, 1533 (1996).

[6] A. J. Harvey-Thompson, S. V. Lebedev, S. N. Bland, J. P. Chittenden, G. N. Hall, A. Marocchino, F. Suzuki-Vidal, S. C. Bott, J. B. A. Palmer, and C. Ning, Phys. Plasmas **16**, 022701 (2009).

[7] A. Harvey-Thompson, An Experimental Investigation of Inverse Wire Array Z-Pinches, Imperial College London, 2010.

[8] M. Camenzind, Rev. Mod. Astron. **3**, 234 (1990).

[9] P. Hartigan, J. M. Foster, B. H. Wilde, R. F. Coker, P. a. Rosen, J. F. Hansen, B. E. Blue, R. J. R. Williams, R. Carver, and A. Frank, Astrophys. J. **705**, 1073 (2009).

[10] S. D. Drell, H. M. Foley, and M. A. Ruderman, J. Geophys. Res. **70**, 3131 (1965).

[11] P. Thompson, D. J. Southwood, and S. Goodman, J. Geophys. Res. **101**, 19849 (1996).

[12] A. V. Gurevich, A. L. Krylov, and E. N. Fedorov, Sov. Phys. JETP **48**, 1074 (1978).

[13] G. J. Odgers, Dom. Astrophys. Obs. **10**, 393 (1957).

[14] S. Bouquet, E. Falize, C. Michaut, C. D. Gregory, B. Loupias, T. Vinci, and M. Koenig, High Energy Density Phys. **6**, 368 (2010).

[15] R. Coker, *Jets from Young Stars IV* (Springer Berlin Heidelberg, Berlin, Heidelberg, 2010), pp. 1–29.

[16] É. Falize, C. Michaut, and S. Bouquet, Astrophys. J. **730**, 96 (2011).

[17] D. Ryutov, R. P. Drake, J. Kane, E. Liang, B. A. Remington, and W. M. Wood-Vasey, Astrophys. J. **518**, 821 (1999).

[18] D. D. Ryutov and B. A. Remington, Plasma Phys. Control. Fusion **44**, B407 (2002).

[19] D. D. Ryutov and B. A. Remington, Phys. Plasmas **10**, 2629 (2003).

[20] D. D. Ryutov, R. P. Drake, and B. A. Remington, Astrophys. J. Suppl. Ser. **127**, 465 (2000).

[21] D. D. Ryutov, B. A. Remington, H. F. Robey, and R. P. Drake, Phys. Plasmas **8**, 1804 (2001).

[22] M. Sarioglu and T. Yavuz, Turkish J. Eng. Environ. Sci. **24**, 217 (2000).

[23] R. Drake, *High-Energy-Density Physics* (Springer Berlin Heidelberg, 2006).

[24] S. V. Lebedev, F. N. Beg, S. N. Bland, J. P. Chittenden, A. E. Dangor, M. G. Haines, K. H. Kwek, S. A. Pikuz, and T. A. Shelkovenko, Phys. Plasmas **8**, 3734 (2001).

[25] G. F. Swadling, S. V. Lebedev, N. Niasse, J. P. Chittenden, G. N. Hall, F. Suzuki-Vidal, G. Burdiak, A. J. Harvey-Thompson, S. N. Bland, P. De Grouchy, E. Khoory, L. Pickworth, J. Skidmore, and L. Suttle, Phys. Plasmas **20**, 022705 (2013).

[26] S. V. Lebedev, L. Suttle, G. F. Swadling, M. Bennett, S. N. Bland, G. C. Burdiak, D. Burgess, J. P. Chittenden, A. Ciardi, A. Clemens, P. de Grouchy, G. N. Hall, J. D. Hare, N. Kalmoni, N. Niasse, S. Patankar, L. Sheng, R. a. Smith, F. Suzuki-Vidal, J. Yuan, A. Frank, E. G. Blackman, and R. P. Drake, Phys. Plasmas **21**, 056305 (2014).

[27] R. P. Drake, Astrophys. Space Sci. **298**, 49 (2005).

[28] C. Michaut, E. Falize, C. Cavet, S. Bouquet, M. Koenig, T. Vinci, A. Reighard, and R. P. Drake, Astrophys. Space Sci. **322**, 77 (2008).

[29] R. P. Drake, Phys. Plasmas **14**, 043301 (2007).

[30] C. Michaut, E. Falize, C. Cavet, S. Bouquet, M. Koenig, T. Vinci, and B. Loupias, J. Phys. Conf. Ser. **112**, 042013 (2008).

[31] M. Kivelson and C. Russell, *Introduction to Space Physics* (Cambridge University Press, 1995).

[32] C. F. Kennel, J. Geophys. Res. **93**, 8545 (1988).

[33] N. Sckopke, G. Paschmann, S. J. Bame, J. T. Gosling, and C. T. Russell, J. Geophys. Res. **88**, 6121 (1983).

[34] N. L. Kugland, D. D. Ryutov, P.-Y. Chang, R. P. Drake, G. Fiksel, D. H. Froula, S. H. Glenzer, G. Gregori, M. Grosskopf, M. Koenig, Y. Kuramitsu, C. Kuranz, M. C. Levy, E. Liang, J. Meinecke, F. Miniati, T. Morita, A. Pelka, C. Plechaty, R. Presura, A. Ravasio, B. A. Remington, B. Reville, J. S. Ross, Y. Sakawa, A. Spitkovsky, H. Takabe, and H.-S. Park, Nat. Phys. **8**, 809 (2012).

[35] H.-S. Park, D. D. Ryutov, J. S. Ross, N. L. Kugland, S. H. Glenzer, C. Plechaty, S. M. Pollaine, B. A. Remington, A. Spitkovsky, L. Gargate, G. Gregori, A. Bell, C. Murphy, Y. Sakawa, Y. Kuramitsu, T. Morita, H. Takabe, D. H. Froula, G. Fiksel, F. Miniati, M. Koenig, A. Ravasio, A. Pelka, E. Liang, N. Woolsey, C. C. Kuranz, R. P. Drake, and M. J. Grosskopf, High Energy Density Phys. **8**, 38 (2012).

[36] F. Suzuki-Vidal, Experimental Study of Radiatively Cooled Magnetically Driven Plasma Jets, Imperial College London, 2009.

[37] F. Suzuki-Vidal, S. V. Lebedev, S. N. Bland, G. N. Hall, G. Swadling, A. J. Harvey-Thompson, J. P. Chittenden, A. Marocchino, A. Ciardi, A. Frank, E. G. Blackman, and S. C. Bott, Phys. Plasmas **17**, 112708 (2010).

[38] A. Ciardi, S. V. Lebedev, A. Frank, F. Suzuki-Vidal, G. N. Hall, S. N. Bland, A. Harvey-Thompson, E. G. Blackman, and M. Camenzind, Astrophys. J. **691**, L147 (2009).

[39] F. Suzuki-Vidal, S. V. Lebedev, a. Ciardi, S. N. Bland, J. P. Chittenden, G. N. Hall, a. Harvey-Thompson, a. Marocchino, C. Ning, C. Stehle, a. Frank, E. G. Blackman, S. C. Bott, and T. Ray, Astrophys. Space Sci. **322**, 19 (2009).

[40] F. Suzuki-Vidal, S. V. Lebedev, G. Swadling, P. de Grouchy, M. Bocchi, G. Burdiak, S. N. Bland, G. N. Hall, A. J. Harvey-Thompson, E. Khoory, L. Pickworth, J. Skidmore, J. P. Chittenden, M. Krishnan, K. W. Elliot, R. Madden, and A. Ciardi, IEEE Trans. Plasma Sci. **39**, 2830 (2011).

[41] F. Suzuki-Vidal, S. V. Lebedev, M. Bocchi, M. Krishnan, G. Swadling, G. Burdiak, S. N. Bland, P. Grouchy, G. N. Hall, a. J. Harvey-Thompson, E. Khoory, L. Pickworth, J. Skidmore, J. P. Chittenden, K. Wilson-Elliot, R. Madden, and a. Ciardi, Shock Waves **22**, 249 (2012).

[42] F. Suzuki-Vidal, M. Bocchi, S. V. Lebedev, J. Skidmore, G. Swadling, G. Burdiak, a. J. Harvey-Thompson, P. de Grouchy, S. N. Bland, G. N. Hall, E. Khoory, L. Pickworth, L. Suttle, J. P. Chittenden, M. Krishnan, K. Wilson-Elliot, R. Madden, a. Ciardi, and a. Frank, EAS Publ. Ser. **58**, 127 (2013).

[43] P. W. L. de Grouchy, Experimental Studies of the Interaction of Radiatively Cooled Supersonic Plasma Jets with Ambient Plasma, Imperial College London, 2014.

[44] D. J. Ampleford, C. a. Jennings, G. N. Hall, S. V. Lebedev, S. N. Bland, S. C. Bott, F. Suzuki-Vidal, J. B. a. Palmer, J. P. Chittenden, M. E. Cuneo, a. Frank, E. G. Blackman, and a. Ciardi, Phys. Plasmas **17**, 056315 (2010).

[45] G. N. Hall, S. V. Lebedev, F. Suzuki-Vidal, G. Swadling, J. P. Chittenden, S. N. Bland, A. Harvey-Thompson, P. F. Knapp, I. C. Blesener, R. D. McBride, D. a. Chalenski, K. S. Blesener, J. B. Greenly, S. a. Pikuz, T. a. Shelkovenko, D. a. Hammer, and B. R. Kusse, Phys. Plasmas **20**, 022703 (2013).

[46] G. F. Swadling, S. V. Lebedev, G. N. Hall, F. Suzuki-Vidal, G. Burdiak, a. J. Harvey-Thompson, S. N. Bland, P. De Grouchy, E. Khoory, L. Pickworth, J. Skidmore, and L. Suttle, Phys. Plasmas **20**, 062706 (2013).

[47] M. Bocchi, B. Ummels, J. P. Chittenden, S. V. Lebedev, a. Frank, and E. G. Blackman, Astrophys. J. **767**, 84 (2013).

[48] F. Suzuki-Vidal, S. V. Lebedev, S. N. Bland, G. N. Hall, G. Swadling, a. J. Harvey-Thompson, G. Burdiak, P. Grouchy, J. P. Chittenden, a. Marocchino, M. Bocchi, a. Ciardi, a. Frank, and S. C. Bott, Astrophys. Space Sci. **336**, 41 (2010).

[49] E. Salpeter, Phys. Rev. **120**, (1960).

[50] S. V. Lebedev, F. N. Beg, S. N. Bland, J. P. Chittenden, a. E. Dangor, and M. G. Haines, Phys. Plasmas **9**, 2293 (2002).

[51] F. Chen and M. Lieberman, *Introduction to Plasma Physics and Controlled Fusion*, Second Edi (Springer US, 1984).

[52] I. Hutchinson, *Principles of Plasma Diagnostics*, 2nd Editio (Cambridge University Press, 2005).

[53] S. N. Bland, D. J. Ampleford, S. C. Bott, S. V. Lebedev, J. B. a. Palmer, S. a. Pikuz, and T. a. Shelkovenko, Rev. Sci. Instrum. **75**, 3941 (2004).

[54] G. N. Hall, S. a. Pikuz, T. a. Shelkovenko, S. N. Bland, S. V. Lebedev, D. J. Ampleford, J. B. a. Palmer, S. C. Bott, J. Rapley, J. P. Chittenden, and J. P. Apruzese, Phys. Plasmas **13**, 082701 (2006).

[55] *2" Achromatic Doublet Thorlabs, Technical Specifications* (n.d.).

[56] M. K. Matzen, Phys. Plasmas **4**, 1519 (1997).

[57] S. V. Lebedev, R. Aliaga-Rossel, S. N. Bland, J. P. Chittenden, a. E. Dangor, M. G. Haines, and I. H. Mitchell, Phys. Plasmas **6**, 2016 (1999).

[58] S. L. Jackson and U. Shumlak, Rev. Sci. Instrum. **77**, 083502 (2006).

[59] F. S. Felber and N. Rostoker, Phys. Fluids **24**, 1049 (1981).

[60] S. V Lebedev, a Ciardi, D. J. Ampleford, S. N. Bland, S. C. Bott, J. P. Chittenden, G. N. Hall, J. Rapley, C. Jennings, M. Sherlock, a Frank, and E. G. Blackman, Plasma Phys. Control. Fusion **47**, B465 (2005).

[61] A. J. Harvey-Thompson, S. V. Lebedev, S. Patankar, S. N. Bland, G. Burdiak, J. P. Chittenden, A. Colaitis, P. De Grouchy, G. N. Hall, E. Khoory, M. Hohenberger, L. Pickworth, F. Suzuki-Vidal, R. a. Smith, J. Skidmore, L. Suttle, and G. F. Swadling, Phys. Plasmas **19**, 056303 (2012).

[62] M. Busquet, D. Colombant, M. Klapisch, D. Fyfe, and J. Gardner, High Energy Density Phys. **5**, 270 (2009).

[63] V. V. Aleksandrov, G. S. Volkov, E. V. Grabovski, V. I. Zaitsev, G. G. Zukakishvili, S. F. Medovschikov, K. N. Mitrofanov, S. L. Nedoseev, G. M. Oleinik, I. Y.

Porofeev, A. A. Samokhin, P. V. Sasorov, V. P. Smirnov, I. N. Frolov, and M. V. Fedulov, in *AIP Conf. Proc.* (AIP, 2006), pp. 3–8.

[64] J. Greenly, M. Martin, I. Blesener, D. Chalenski, P. Knapp, R. McBride, B. R. Kusse, and D. a. Hammer, in *AIP Conf. Proc.* (AIP, 2009), pp. 53–56.

[65] A. J. Harvey-Thompson, S. V. Lebedev, S. Patankar, S. N. Bland, G. Burdiak, J. P. Chittenden, A. Colaitis, P. De Grouchy, H. W. Doyle, G. N. Hall, E. Khoory, M. Hohenberger, L. Pickworth, F. Suzuki-Vidal, R. a. Smith, J. Skidmore, L. Suttle, and G. F. Swadling, Phys. Rev. Lett. **108**, 145002 (2012).

[66] J. D. Huba, *NRL PLASMA FORMULARY* (Naval Research Laboratory, Washington, DC, 2007), pp. 1–71.

[67] A. V Dmitriev, A. V Suvorova, and I. S. Veselovsky, 65 (2013).

[68] I. Podgorny, Phys. Sol. Planet. Environ. Proc. Int. Symp. Solar-Terrestrial Phys. **7**, (1976).

[69] S. N. Bland, S. C. Bott, G. N. Hall, S. V. Lebedev, F. Suzuki, D. J. Ampleford, J. B. a. Palmer, S. a. Pikuz, and T. a. Shelkovenko, Rev. Sci. Instrum. **77**, 10F326 (2006).

[70] G. N. Hall, G. C. Burdiak, L. Suttle, N. Stuart, G. F. Swadling, S. V. Lebedev, R. A. Smith, S. Patankar, F. Suzuki-Vidal, P. de Grouchy, A. J. Harvey-Thompson, M. Bennett, S. N. Bland, L. Pickworth, and J. Skidmore, Rev. Sci. Instruments (2014).

[71] S. Abas and S. P. Gary, Plasma Phys. **13**, 262 (1971).

[72] I. H. Hahn, http://commons.wikimedia.org/wiki/File:Spherical_aberration_3.svg (2011).